Work Hardening and Latent Hardening of Mg Single Crystals under Uniaxial Deformation at 298K

WORK HARDENING AND LATENT HARDENING OF MG SINGLE CRYSTALS UNDER UNIAXIAL DEFORMATION AT 298K

BY

FUMIAKI HIURA, B.Eng., M.Sc.

A THESIS

SUBMITTED TO THE DEPARTMENT OF MATERIALS SCIENCE & ENGINEERING

AND THE SCHOOL OF GRADUATE STUDIES

OF MCMASTER UNIVERSITY

IN PARTIAL FULFILMENT OF THE REQUIREMENTS

FOR THE DEGREE OF

DOCTOR OF PHILOSOPHY

Doctor of Philosophy (2015) McMaster University

(Materials Science & Engineering) Hamilton, Ontario, Canada

TITLE:	Work Hardening and Latent Hardening of Mg Single Crystals under Uniaxial Deformation at 298K
AUTHOR:	Fumiaki Hiura B.Eng., (Mechanical Engineering) University of Tokushima, Tokushima, JAPAN M.Sc., (Materials Science and Engineering) McMaster University, Hamilton, CANADA
SUPERVISOR:	Dr. Marek Niewczas
NUMBER OF PAGES:	xxix, 317

To my family and friends

Abstract

In this thesis, work hardening and latent hardening behaviours of pure Mg single crystals were mainly studied under uniaxial deformation tests at room temperature, 298K. By uniaxial tensile/compression tests, work hardening behaviours of Mg single crystals with different orientations favoured for single and double basal $< a >$ slip, $\{10\bar{1}2\} < 10\bar{1}1 >$ twin, 2^{nd} order pyramidal $< c + a >$ slip and basal $< a >$ slip + $\{10\bar{1}2\} < 10\bar{1}1 >$ twin were studied. In order to investigate latent hardening behaviours among slip and twin systems, the Jackson-Basinski type latent hardening experiments in Mg single crystals at room temperature have been carried out under different types of dislocation interactions, which included: (i) the self-interactions, (ii) the co-planar interactions on the basal plane, (iii) basal $< a >$ slip/$\{10\bar{1}2\} < 10\bar{1}1 >$ twin dislocation interactions, (iv) $\{10\bar{1}2\} < 10\bar{1}1 >$ twin/basal $< a >$ slip dislocation interactions and (v) basal $< a >$ slip/2^{nd} order pyramidal $< c + a >$ slip dislocation interactions. The microstructure and micro-texture of the deformed single crystals was observed by optical microscopy (OM), scanning electron microscopy (SEM), and SEM/EBSD methods. In addition, micro- and nano-indentation measurements were performed on adjacent matrix and $\{10\bar{1}2\} < 10\bar{1}1 >$ twin regions of deformed Mg single crystals and the hardness values were analyzed by the Oliver-Pharr method.

The results from the Ph.D. work provided framework for the discussion of the

plastic flow in Mg single crystals and quantitative values for hardening parameters used in the crystal plasticity modelling.

Acknowledgements

First of all, the author would like to thank my supervisor Dr. Marek Niewczas for his support and encouragement throughout my Ph.D. work. The author is also grateful to Dr. Raja. K. Mishra at GM R&D center, Warren, MI, USA and Dr. Kaan Inal at Waterloo University, ON, CANADA for their useful discussions as my committee members.

The author is also grateful to Mr. Robert Kubic, Mr. Michael Lukitsch and Ms. Daad Haddad at General Motors R&D center for useful discussion and technical assistance with some experiments: SEM/EBSD analysis and nano-indentation experiments.

This study was supported by funding from Initiative for Automotive Manufacturing Innovation (IMAI) at McMaster University.

Contents

List of Figures

Chapter 1

Introduction

Due to favourable combination of physical properties, the utilization of Mg and its alloys has been continuously increasing in particular in aircraft and automobile industries. The important properties of Mg and Mg-based alloys, which make them attractive materials for structural applications, are (Kainer, 2003):

- Lowest density of all construction metals at $1.8 g/cm^3$;
- High specific strength i.e., highest strength to density ratio;
- Excellent castability and suitability for pressure die casting;
- Easy machining with high cutting speeds;
- Highly improved corrosion resistance;
- Recyclability, including possibility of integrated recycling.

However, Mg and its alloys due to their HCP structure, are characterized by intrinsically poor formability, limiting a range of applications for wrought products,

which often require a complex processing path. Low critical resolved shear stress (CRSS) makes $\{0001\} < 2\bar{1}\bar{1}0 >$ basal $< a >$ slip the dominant deformation mode in Mg. In general, homogeneous deformation in polycrystalline material requires five independent slip systems to accomplish an arbitrary change of the shape, which is known as the Von Mises criterion (Von Mises, 1928). However, basal $< a >$ slip provides only two independent slip systems with the Burgers vector contained in the basal plane, thus incapable of executing a shear perpendicular to the basal plane. This gives rise to poor ductility and formability of polycrystalline Mg and Mg alloys at room temperature, limiting their processing power. This feature is illustrated in Fig.1.1 (a). A rolled Mg alloy sheet develops a strong basal texture. Since the basal plane is aligned parallel to the rolled-sheet surface, basal $< a >$ and prismatic $< a >$ slip systems can provide shear components parallel to the rolling and width directions of the sheet, but they cannot operate parallel to the thickness direction (Fig.1.1 (b)). Therefore, rolled Mg alloy sheets hardly deform in the thickness direction, resulting in a fracture at an initial stage of press-forming process. It has been recognized that press-forming of Mg alloy sheet is extremely difficult at room temperature. Many researchers have attempted to understand how to prevent formation of the strong basal texture and how to improve the ductility and formability of Mg and Mg-based alloys at room temperature. The methods typically used include grain refinements, additions of alloying elements and processing at elevated temperatures (Kainer, 2003).

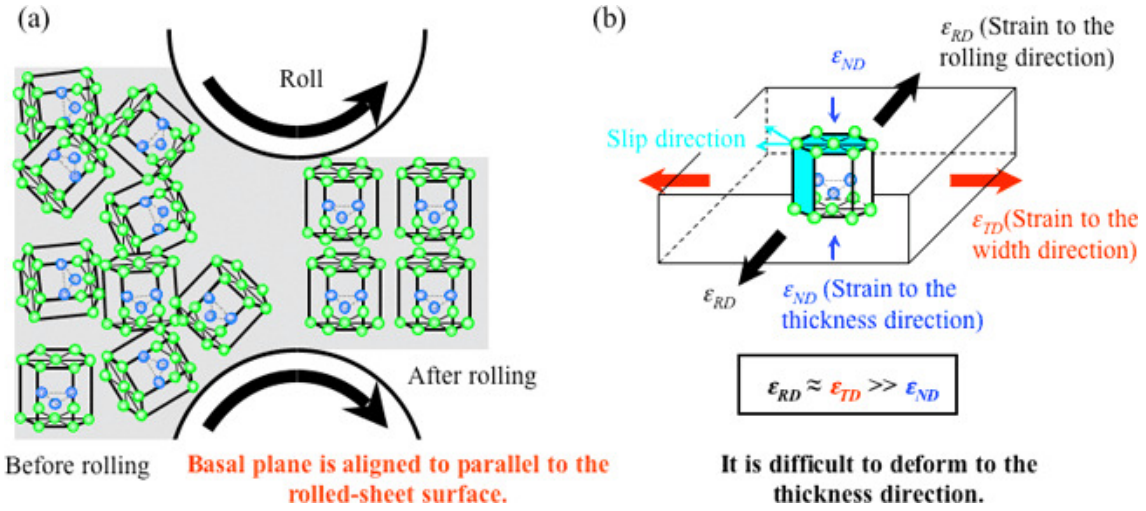

Figure 1.1: Schemiatic illustrations of: (a) basal texture formation in a rolled Mg alloy, (b) effect of texture on press-forming (Advanced industrial science and technology (AIST), 2008).

To be able to use more Mg alloys as structural materials, a better understanding of the plastic deformation mechanisms, which govern the behaviour of these materials during processing is required. The first step is to understand the interactions between various slip and twinning modes and the effect of these interactions on the strength and ductility of Mg. This can be done through systematic studies of the work hardening behaviour on model materials systems such as Mg single crystals in a well-designed experiments which test the hardening effect produced by different slip and twinning systems. The term "work hardening" refers to the phenomenon in which, due to the activity of various slip systems, an ever denser and more complicated network of defects is produced, such that increasingly larger stresses are required to deform the specimen in a process known as work hardening. During work hardening on one slip system, other potential slip systems are largely inactive (latent). However, the latent

(inactive) slip system is also hardened by dislocations' arrangements and dislocation movement on active slip system, which is known as "latent" hardening.

The latent hardening of HCP crystals has rarely been studied and there is not much data available in the literature on this subject. Previous studies in our research group by Bhattacharya (2006) have focused on the work hardening behaviour of Mg single crystals oriented for single basal $< a >$ slip, 2^{nd} order $< c+a >$ pyramidal slip, and $\{10\bar{1}2\} < 10\bar{1}1 >$ twinning in continuous experiments. In subsequent studies Hiura (2010) carried out the Jackson & Basinski type latent hardening tests on Mg single crystals. This work proved to be the first step in understanding the latent hardening behaviour in Mg single crystals and it has been subsequently developing to understand the orientation dependence of the work hardening and the latent hardening in Mg single crystals under the conditions of the interactions between various slip and twinning systems.

The current work deals with the studies of the mechanisms of plastic flow in Mg Single Crystals at 295K and includes following aspects:

- orientation dependence of the work hardening for (section 5.2):
  - single $< a >$ slip;
  - double basal $< a >$ slip;
  - $\{10\bar{1}2\} < 10\bar{1}1 >$ twin; and
  - 2^{nd} order pyramidal $< c + a >$ slip orientations.
- latent hardening experiments under the conditions of:
  - basal $< a >$ slip/basal $< a >$ slip dislocations interactions (section 5.3);

  - basal $< a >$ slip/$\{10\bar{1}2\} < 10\bar{1}1 >$ twin dislocations interactions (section 5.5);
  - basal $< a >$ slip/2^{nd} order pyramidal $< c + a >$ slip dislocations interactions (section 5.6); and
  - $\{10\bar{1}2\} < 10\bar{1}1 >$ twin/basal $< a >$ slip dislocations interactions (section 5.7).

- intermittent deformation/annealing experiments of deformed and annealed samples at 295K and cyclic unloading/reloading tests at 295K (section 5.4).

- the microstructure and micro-texture analysis of deformed single crystals by optical microscopy (OM), scanning electron microscopy (SEM), and SEM/EBSD methods.

The format of the thesis is as follows. In the first part of chapter 2, overview of the elastic and plastic deformation of Mg single crystals is given. In the second part of chapter 2, a general characteristics of latent hardening behaviour in FCC single crystals and a crystal plasticity modelling incorporating latent hardening effects in FCC crystals are reviewed. Chapter 2 includes also a description of the studies related to the latent hardening experiments in HCP crystals. Based on the considerations of the literature data, research objectives of the present work are described in chapter 3. The experimental procedure, results and discussion of the results are presented in chapter 4 through chapter 6. Finally, the conclusions and summary of major findings of this work are given in chapter 7.

Chapter 2

Literature Review

2.1 Elasticity of HCP crystal system

The stress state at a point in a body is defined by nine components of the stress tensor, σ_{ij} in Eq.(2.1). The indexes i and j define a direction and a plane normal for a given i, j component of the stress tensor. When $i = j$, σ_{ij} represents a normal stress and when $i \neq j$, σ_{ij} represents a shear stress. When a body is in statical equilibrium, $\sigma_{ij} = \sigma_{ji}$, i.e., the stress tensor is symmetrical and it has only six independent components.

$$\sigma_{ij} = \begin{bmatrix} \sigma_{11} & \sigma_{12} & \sigma_{13} \\ \sigma_{12} & \sigma_{22} & \sigma_{23} \\ \sigma_{13} & \sigma_{23} & \sigma_{33} \end{bmatrix} \tag{2.1}$$

This is also true of the strain tensor, ϵ_{ij}. One must however distinguish between the relative displacement tensor e_{ij}, the strain tensor and the rotation tensor, ω_{ij}.

The relative displacement tensor is the sum of symmetrical strain tensor ϵ_{ij} and anti-symmetrical rotation tensor ω_{ij}:

$$e_{ij} = \frac{1}{2}(e_{ij} + e_{ji}) + \frac{1}{2}(e_{ij} - e_{ji}) = \epsilon_{ij} + \omega_{ij} \tag{2.2}$$

Components of both tensors are defined in terms of the components of displacement tensor as per Eq.(2.3) and Eq.(2.4) below:

$$\epsilon_{ij} = \begin{bmatrix} \epsilon_{11} & \epsilon_{12} & \epsilon_{13} \\ \epsilon_{21} & \epsilon_{22} & \epsilon_{23} \\ \epsilon_{31} & \epsilon_{32} & \epsilon_{33} \end{bmatrix} = \begin{bmatrix} e_{11} & \frac{1}{2}(e_{12} + e_{21}) & \frac{1}{2}(e_{13} + e_{31}) \\ \frac{1}{2}(e_{21} + e_{12}) & e_{22} & \frac{1}{2}(e_{23} + e_{32}) \\ \frac{1}{2}(e_{31} + e_{13}) & \frac{1}{2}(e_{32} + e_{23}) & e_{33} \end{bmatrix} \tag{2.3}$$

$$\omega_{ij} = \begin{bmatrix} \omega_{11} & \omega_{12} & \omega_{13} \\ \omega_{21} & \omega_{22} & \omega_{23} \\ \omega_{31} & \omega_{32} & \omega_{33} \end{bmatrix} = \begin{bmatrix} 0 & \frac{1}{2}(e_{12} - e_{21}) & \frac{1}{2}(e_{13} - e_{31}) \\ \frac{1}{2}(e_{21} - e_{12}) & 0 & \frac{1}{2}(e_{23} - e_{32}) \\ \frac{1}{2}(e_{31} - e_{13}) & \frac{1}{2}(e_{32} - e_{23}) & 0 \end{bmatrix} \tag{2.4}$$

The engineering shear strain, γ_{ij} (for $i \neq j$) differs from the shear components of the strain tensor. The relationship between the engineering shear strain, the strain tensor and the relative displacement tensor components is:

$$\gamma_{ij} = 2\epsilon_{ij} = e_{ij} + e_{ji} \tag{2.5}$$

In a strained crystal, the stress at any point is linearly related to the strain at that

point, which is known as Hooke's law. The general Hooke's law can be expressed as:

$$\sigma_{ij} = c_{ijkl}\epsilon_{kl} \tag{2.6}$$

The constants c_{ijkl} are called the stiffness constants and the c_{ijkl} in above Eq.(2.6) represents a four-rank tensor with eighty-one components.

The equation (2.6) is extended to nine independent equations describing unique relationship between the components of strain and stress tensors. In practice, the equations have much simpler forms. The symmetry of the stress and strain tensors when the body is in static equilibrium implies that:

$$c_{ijkl} = c_{ijlk} = c_{jikl} = c_{jilk}. \tag{2.7}$$

The conditions above reduces the number of independent constants in c_{ijkl} from eighty-one components to thirty-six. In view of this symmetry, a matrix notation can be employed:

$$\sigma_p = c_{pq}\epsilon_q \tag{2.8}$$

in which p and q run from one to six, i.e.

$$\begin{bmatrix} \sigma_1 \\ \sigma_2 \\ \sigma_3 \\ \sigma_4 \\ \sigma_5 \\ \sigma_6 \end{bmatrix} = \begin{bmatrix} c_{11} & c_{12} & c_{13} & c_{14} & c_{15} & c_{16} \\ c_{21} & c_{22} & c_{23} & c_{24} & c_{25} & c_{26} \\ c_{31} & c_{32} & c_{33} & c_{34} & c_{35} & c_{36} \\ c_{41} & c_{42} & c_{43} & c_{44} & c_{45} & c_{46} \\ c_{51} & c_{52} & c_{53} & c_{54} & c_{55} & c_{56} \\ c_{61} & c_{62} & c_{63} & c_{64} & c_{65} & c_{66} \end{bmatrix} \begin{bmatrix} \epsilon_1 \\ \epsilon_2 \\ \epsilon_3 \\ \gamma_4 \\ \gamma_5 \\ \gamma_6 \end{bmatrix} \tag{2.9}$$

where

$$\begin{bmatrix} \sigma_{11} & \sigma_{12} & \sigma_{13} \\ \sigma_{12} & \sigma_{22} & \sigma_{23} \\ \sigma_{13} & \sigma_{23} & \sigma_{33} \end{bmatrix} = \begin{bmatrix} \sigma_1 & \sigma_6 & \sigma_5 \\ \sigma_6 & \sigma_2 & \sigma_4 \\ \sigma_5 & \sigma_4 & \sigma_3 \end{bmatrix} \tag{2.10}$$

and

$$\begin{bmatrix} \epsilon_{11} & \epsilon_{12} & \epsilon_{13} \\ \epsilon_{12} & \epsilon_{22} & \epsilon_{23} \\ \epsilon_{13} & \epsilon_{23} & \epsilon_{33} \end{bmatrix} = \begin{bmatrix} \epsilon_1 & \frac{1}{2}\epsilon_6 & \frac{1}{2}\epsilon_5 \\ \frac{1}{2}\epsilon_6 & \epsilon_2 & \frac{1}{2}\epsilon_4 \\ \frac{1}{2}\epsilon_5 & \frac{1}{2}\epsilon_4 & \epsilon_3 \end{bmatrix} \tag{2.11}$$

Alternatively, the Hook's law can be written as set of stress - strain equations:

$$\epsilon_{ij} = s_{ijkl}\sigma_{kl} \tag{2.12}$$

The constants s_{ijkl} are called the compliance constants and a similar reduction to matrix notation:

$$\epsilon_p = s_{pq}\sigma_q \tag{2.13}$$

can be carried out, with additional conversion factors such that:

$s_{pq} = s_{ijkl}$ when both p and q are 1, 2, or 3,

s_{pq}=$2s_{ijkl}$ when either p or q are 4, 5, or 6,

s_{pq}=$4s_{ijkl}$ when both p and q are 4, 5, or 6.

Finally, the thermodynamic considerations relating to elastic strain energy lead to (Nye, 1985) :

$$c_{pq} = c_{qp} \tag{2.14}$$

and

$$s_{pq} = s_{qp}. \tag{2.15}$$

which reduces, the thirty-six to twenty-one independent compliances in the stress - strain relationships for elasticity.

The most general matrix of elastic constants with twenty-one independent constants is characteristic of triclinic crystals that have only a centre of symmetry. In materials of higher symmetry, the number of independent elastic constants is further reduced and the compliance matrix is simplified. For hexagonal crystals, the matrices of elastic constants can be expressed as:

$$s_{ij} = \begin{bmatrix} s_{11} & s_{12} & s_{13} & 0 & 0 & 0 \\ s_{12} & s_{11} & s_{13} & 0 & 0 & 0 \\ s_{13} & s_{13} & s_{33} & 0 & 0 & 0 \\ 0 & 0 & 0 & s_{44} & 0 & 0 \\ 0 & 0 & 0 & 0 & s_{44} & 0 \\ 0 & 0 & 0 & 0 & 0 & 2(s_{11} - s_{12}) \end{bmatrix} \tag{2.16}$$

or

$$c_{ij} = \begin{bmatrix} c_{11} & c_{12} & c_{13} & 0 & 0 & 0 \\ c_{12} & c_{11} & c_{13} & 0 & 0 & 0 \\ c_{13} & c_{13} & c_{33} & 0 & 0 & 0 \\ 0 & 0 & 0 & c_{44} & 0 & 0 \\ 0 & 0 & 0 & 0 & c_{44} & 0 \\ 0 & 0 & 0 & 0 & 0 & \frac{1}{2}(c_{11} - c_{12}) \end{bmatrix}. \tag{2.17}$$

Fig. 2.1 shows the form of the matrices for hexagonal symmetry and indicates that hexagonal crystals have five independent elastic constants, $s_{11}, s_{33}, s_{44}, s_{12}$, and s_{13} (or $c_{11}, c_{33}, c_{44}, c_{12}$, and c_{13}), where: $s_{22} = s_{11}$, $s_{23} = s_{13}$, and $s_{66} = 2(s_{11} - s_{22})$ (or $c_{22} = c_{11}$, $c_{23} = c_{13}$, and $c_{66} = \frac{1}{2}(c_{11} - c_{12})$).

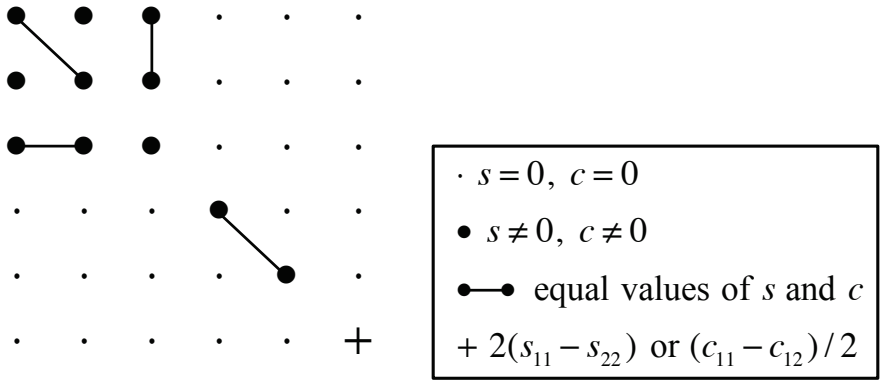

Figure 2.1: Matrix of elastic constants for hexagonal system (Nye, 1985).

The compliance constants for crystals with hexagonal symmetry can be expressed in terms of the stiffness constants and vice versa (Kelly *et al.*, 2000):

$$s_{11} + s_{12} = \frac{c_{33}}{c} \tag{2.18}$$

$$s_{11} - s_{12} = \frac{1}{c_{11} - c_{12}} \tag{2.19}$$

$$s_{13} = -\frac{c_{13}}{c} \tag{2.20}$$

$$s_{33} = \frac{c_{11} + c_{12}}{c} \tag{2.21}$$

$$s_{44} = \frac{1}{c_{44}} \tag{2.22}$$

where

$$c = c_{33}(c_{11} + c_{12}) - 2c_{13}^2 \tag{2.23}$$

Slutsky and Garland (1957) have measured the elastic constants of Mg in the temperate range between 4.2K to 300K by ultrasonic pulse technique. The five stiffness tensor values at 0K, 80K, and 300K are listed in Table 2.1.

Table 2.1: The adiabatic constants, c_{ij} of magnesium in the unit of $dynes/cm^2$x10^{12} (Slutsky and Garland, 1957).

T (K)	c_{11}	c_{33}	c_{44}	c_{12}	c_{13}
0	0.6348	0.6645	0.1842	0.2594	0.2170
80	0.6300	0.6595	0.1820	0.2591	0.2168
300	0.5940	0.6160	0.1640	0.2561	0.2144

2.2 Plasticity of Mg single crystals

2.2.1 Orientation dependence

Fig. 2.2 shows the standard stereographic triangle indicating regions of possible slip systems for basal $< a >$ slip metals such as Be, Mg, Zn, Cd and etc. under an uniaxial tensile deformation (Munroe *et al.*, 1997). The triangle is divided into four regions, A – D. Region A corresponds to the orientation where the crystals deform

primarily by pyramidal $< c+a >$ slip and prismatic $< a >$ slip systems. Twinning is the most favourable deformation mode in region B. Region C is the region of double basal $< a >$ slip and region D represents the region of single basal $< a >$ slip.

When the basal $< a >$ slip metals are subjected to an uniaxial compression test, the deformation behaviour is different from that of the crystals under a tensile deformation. In Fig. 2.2, the favourable deformation modes under the compressive stress are as follows: (i) Region A: brittle fracture in basal $< a >$ slip metals with $c/a > \sqrt{3}$ (Zn, Cd), $\{10\bar{1}2\} < 10\bar{1}1 >$ twinning in basal $< a >$ slip metals with $c/a < \sqrt{3}$ (Be, Mg); (ii) Region B: $\{10\bar{1}2\} < 10\bar{1}1 >$ twinning and $< c+a >$ slip ($c/a > \sqrt{3}$), brittle fracture after some degree of $< c+a >$ slip ($c/a < \sqrt{3}$); (iii) Region C: double basal $< a >$ slip; and (iv) Region D: single basal $< a >$ slip.

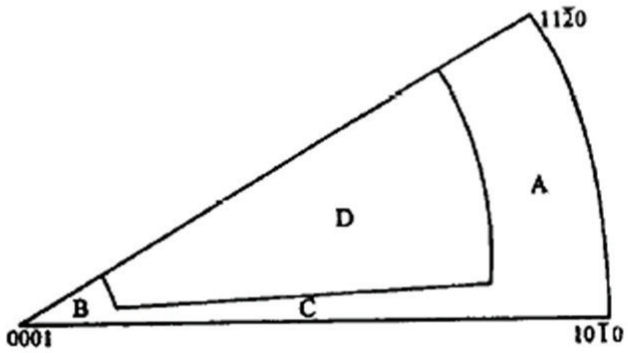

Figure 2.2: Orientation dependence of plastic deformation of basal $< a >$ slip metals at room temperature (Munroe *et al.*, 1997).

2.2.2 Single basal $< a >$ slip orientations

In Mg single crystals, basal $< a >$ slip: $\{0001\} < 2\bar{1}\bar{1}0 >$ is activated dominantly at room temperature. Tensile deformation behaviour of Mg single crystals with single basal orientations was widely reported by various researchers (Burke and Hibbard, 1952; Asada and Yoshinaga, 1959; Basinski, 1960; Yoshinaga and Horiuchi, 1962; Sharp *et al.*, 1965; Hirsch and Lally, 1965; Bhattacharya, 2006; Bhattacharya and Niewczas, 2011; Sułkowski *et al.*, 2011; Sułkowski and Mikułowski, 2012). Burke and Hibbard (1952) reported that when the basal plane is within 6° to 72° of the tensile axis, the basal $< a >$ slip is the main deformation mechanism in Mg. When the Schmid factor for basal $< a >$ slip is close to 0.5, homogeneous deformation by single basal $< a >$ slip occurs. According to Hirsch and Lally (1965), the angle between the slip direction and the tensile axis should be between 40° to 60° to avoid geometrical softening and inhomogeneous deformations.

Fig. 2.3 shows the typical shear stress-shear strain curve for single basal $< a >$ slip obtained from the Hirsch and Lally's experiments. The flow stress characteristic was divided into two stages of deformation according to the similar work hardening rate: Stage A (low work hardening range) and Stage B (rapid work hardening range).

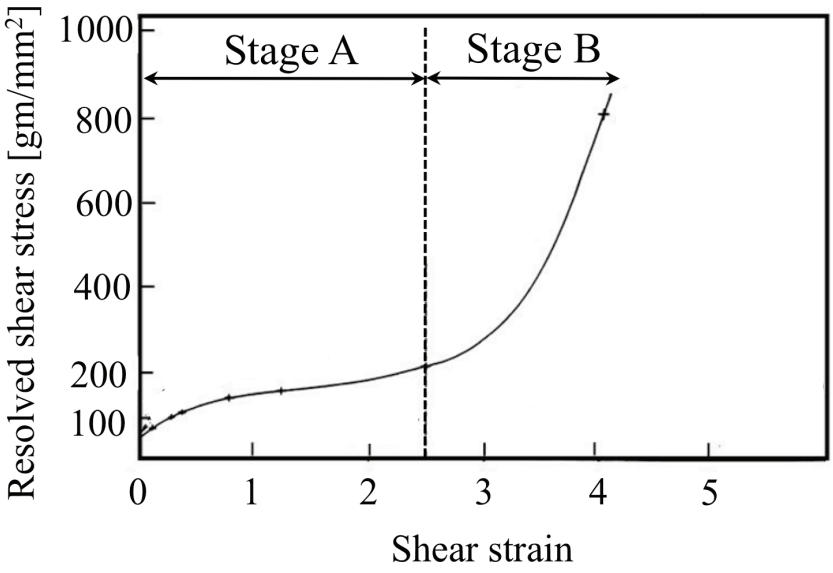

Figure 2.3: Typical shear stress-shear strain curve of Mg single crystal oriented for single basal $< a >$ slip, deformed at 295K (Hirsch and Lally, 1965).

The main features and the mechanism of deformation in these two stages of deformation based on the early works are as follows:

Stage A

- The dislocations from the sources operating simultaneously trap one another and form dipole bands for edges and screws.
- The screw dislocations cross-slip and annihilate leaving the edge dislocation and the excess of the screws of the same sign. The flow stress in this stage is controlled by the internal stress field from edge clusters, residual screw dislocations and dislocations with non-primary Burgers vectors.
- The work hardening rate in stage A is very low because most of the dislocations

annihilate or form dipoles, which have relatively small interaction radii with the mobile dislocation and therefore contribute little to the hardening effect.

- The density of the obstacles in this stage rises very slowly as the deformation proceeds.

Stage B

- Stage B is characterized by formation of twinning, the production of dislocation tangles and the dislocation network in which three basal Burgers vectors are equally represented.

- The hardening is mainly due to the interaction between the dislocations in the basal plane. The glide of non-primary dislocations with Burgers vectors in the basal plane gives rise to the formation of hexagonal networks of dislocations on the basal plane.

- A high density of twins is observed near the fracture surface of the samples.

2.2.3 Double basal $< a >$ slip orientations

When tensile axes are located between $< 0001 >$ and $< 10\bar{1}0 >$, the $\{0001\} < \bar{1}2\bar{1}0 >$ basal $< a >$ slip system, coplanar to the primary basal $< a >$ slip system $\{0001\} < 2\bar{1}\bar{1}0 >$, is activated by reason of symmetry and the double coplanar basal $< a >$ slip will occur. Unlike stress-strain characteristics of Mg single crystals with single basal $< a >$ slip orientations, there is little data available about the single crystals oriented for double basal $< a >$ slip. The only data available in the literatures reports the increase of CRSS for basal $< a >$ slip and larger work hardening in Zn single

crystal with the double basal $< a >$ orientation (Edwards *et al.*, 1953). The present author studied double basal $< a >$ slip in Mg single crystals with the tensile axis of $< 10\bar{1}(1.14) >$ by uniaxial tensile tests and the mechanical behaviour of these Mg single crystals is reported in the thesis.

2.2.4 Inhomogeneous deformation with deformation bands

As described above, there is relatively a narrow range of orientations in which the homogeneous plastic deformation occurs by single basal $< a >$ slip system. In Mg single crystals, inhomogeneous deformation with kink bands and deformation twinning occurs when a single basal $< a >$ slip becomes difficult (Burke and Hibbard, 1952; Yoshinaga and Horiuchi, 1962). Deformation starts locally, typically in the middle part of the sample, with bending and twisting components of the stress being developed due to inhomogeneous deformation. In this case, $\{11\bar{2}0\}$ type kink bands are formed along the boundary of the inhomogeneous deformation. As the inhomogeneous deformation proceeds further, the kink bands are accompanied by many $\{10\bar{1}2\} < 10\bar{1}1 >$ twins. From the perspective of strain hardening, it is very important to understand whether the kink bands are mobile or immobile. At the beginning stage of inhomogeneous deformation, the kink bands are relatively mobile. The kink bands form symmetrical tilt boundaries composed of parallel edge dislocations. It is well known that those dislocations are highly mobile (Washburn and Parker, 1952). In the early stage, the kink bands show little effect on the strain hardening. The kink bands filled up with $\{10\bar{1}2\} < 10\bar{1}1 >$ twins do not migrate during further deformation. Pile-ups of basal dislocations are believed to be sources of $\{10\bar{1}2\} < 10\bar{1}1 >$ twins. However, once the kink bands are locked with the $\{10\bar{1}2\} < 10\bar{1}1 >$ twins,

the kink bands tend to become immobile and act as strong obstacles against gliding dislocations. Fig.2.4 shows the schematic illustration of the kink bands filled up with twins. Formation of kink bands and twins is responsible for rapid hardening stage under conditions of inhomogeneous deformation.

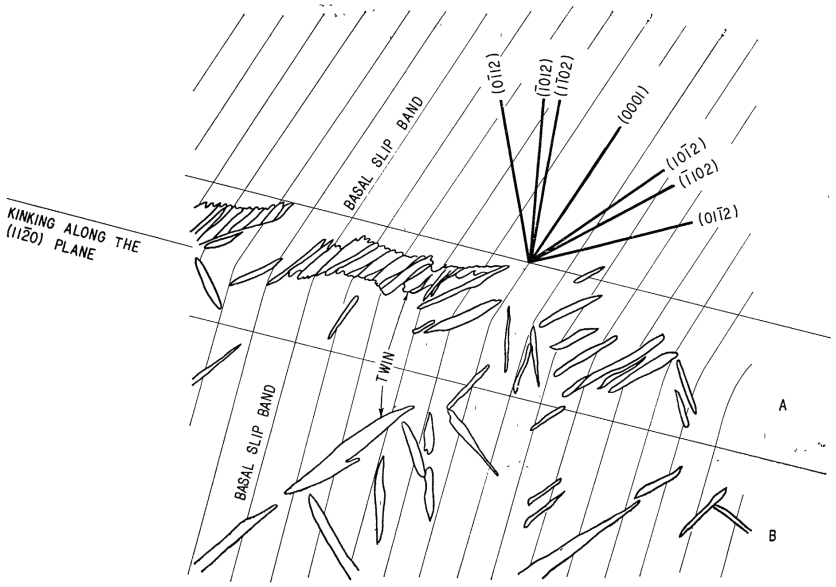

Figure 2.4: Schematic illustration of [11$\bar{2}$0] kink bands with many $\{10\bar{1}2\} < 10\bar{1}1 >$ twins (Yoshinaga and Horiuchi, 1962).

2.2.5 2^{nd} order pyramidal $< c+a >$ slip: [0001] compression and [2$\bar{1}\bar{1}$0] tensile tests

The activation of 2^{nd} order pyramidal $< c+a >$ slip: $\{11\bar{2}2\} < 11\bar{2}3 >$ has been reported in Mg and Mg-Li single crystals under the a-axis tensile tests (Ando *et al.*, 1992) and the c-axis compression tests (Stohr and Poirier, 1972; Obara *et al.*, 1973; Ando and Tonda, 2000; Syed *et al.*, 2012).

Fig. 2.5 shows stress-strain curves for Mg single crystals deformed in compression along the c-axis at various temperatures between 293K and 773K (Obara *et al.*, 1973). Unlike basal $< a >$ slip orientations, the flow curves do not exhibit easy glide stage i.e., rapid hardening stage starts after the yielding by the multiple 2^{nd} order pyramidal $< c + a >$ slip. The crystals fracture after a few percent of strain in the range from 293K to 473K, which is related to the role of $\{10\bar{1}1\} < 10\bar{1}2 >$ twinning (see section 2.2.7). Above 573K, the work hardening decreases rapidly with increasing temperature and the crystal shows unlimited ductility and stress recovery. Yoshinaga (2009) explained the increase of the work hardening at evaluated temperatures by so called Johnston mechanism (Johnston, 1962) attributed to the rapid increase in the $\{10\bar{1}1\} < 10\bar{1}2 >$ twinning and mobile dislocation densities.

The stress-strain curves for Mg single crystals deformed in tension along the a-axis at 77K - 573K show very similar mechanical behaviour to the c-axis compression tests, discussed above (Ando *et al.*, 1992, 2010). However, the small difference between the c-axis compression tests and the a-axis tensile tests can be seen in some aspects of the mechanical properties, e.g., in the value of CRSS for 2^{nd} order pyramidal $< c + a >$ slip and in terms of ductility at lower temperatures (Ando *et al.*, 2010). Ando *et al.* (2010) explained these differences by the effect of sample size between both tests and argued that the activity of 2^{nd} order pyramidal $< c + a >$ slip systems depend on aspect ratio of the specimens.

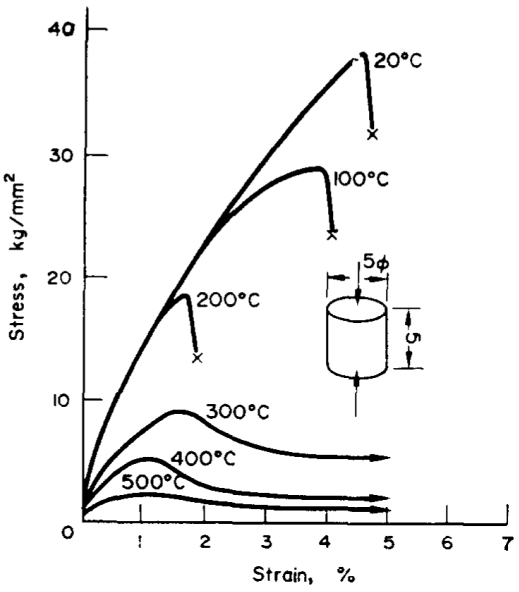

Figure 2.5: Stress-strain curves of the c-axis compression tests in Mg single crystals (Obara *et al.*, 1973).

As seen in the Fig. 2.5, the CRSS for 2^{nd} order pyramidal $< c + a >$ slip in Mg is strongly temperature and it is also strain rate dependent. Fig.2.6 shows the temperature dependence of the CRSS for 2^{nd} order pyramidal $< c + a >$ slip (Yoo *et al.*, 2002). Ando *et al.* (1992) and Ando and Tonda (2000) observed that the yield stress due to 2^{nd} order pyramidal $< c+a >$ slip in Mg single crystals and Mg-Li alloy single crystals follows the same decreasing trend in the low temperature range 77K to 293K. However, the c-axis compression tests on Mg single crystals between 298K - 673K by Obara *et al.* (1973) and 77K - 470K by Stohr and Poirier (1972) have shown that the yield stress due to 2^{nd} order pyramidal $< c + a >$ slip tends to decrease at higher temperatures after reaching the maximum CRSS at around T/T_m∼0.3-0.4.

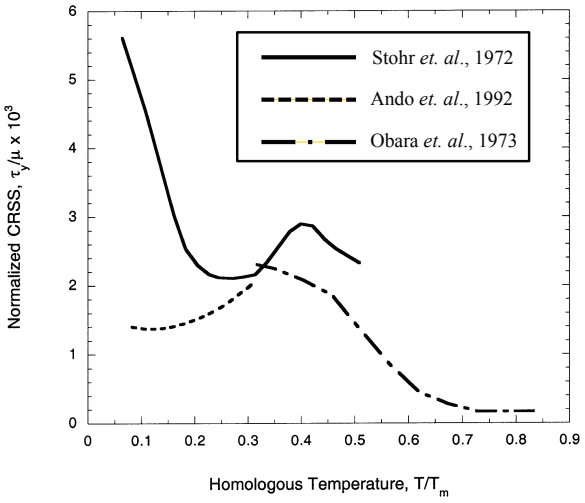

Figure 2.6: CRSS for 2^{nd} order pyramidal $< c + a >$ slip system vs. temperature plots in Mg single crystals (Stohr and Poirier, 1972; Obara *et al.*, 1973; Ando *et al.*, 1992; Yoo *et al.*, 2002).

Fig. 2.7 shows a typical TEM micrograph of Mg single crystals deformed in compression to 2.3% strain in the [0001] direction at 423K (Obara *et al.*, 1973). The analysis have shown $< c + a >$, $< a >$, and $< c >$ types of dislocations in the microstructure. According to another TEM study by Ando *et al.* (1992), $< c + a >$ dislocations with edge component tend to decompose into $< a >$ and $< c >$ perfect dislocations by thermally activated process. The dissociated $< a >$ dislocations, which have extremely high mobility, can slip easily. However, the dissociated $< c >$ dislocation cannot slip by applied stress in the a-axis tension and is left as sessile dislocations on the pyramidal plane. This suggests that the sessile $< c >$ dislocations can act as strong obstacles to other dislocations and influence the mechanical behaviour of the sample. On the other hand, $< c + a >$ dislocations with screw component can

cross-slip onto new slip plane. In comparison to lower temperatures, immobilization of $< c+a >$ dislocations becomes more frequent with increasing temperature. At the same time, $< c+a >$ screw dislocations are forced to double cross slip and propagate in slip bands with the assistance of an applied stress.

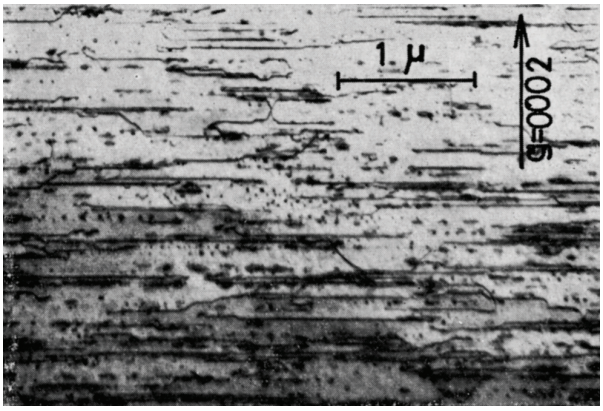

Figure 2.7: Typical dislocation substructures in Mg single crystals deformed in compression to 2.3% strain in the [0001] direction at 423K (Obara *et al.*, 1973).

Ando *et al.* (1996) have studied the core structures of $< c + a >$ edge dislocation by molecular dynamics (MD) simulation based on Lennard-Jones type inter-atomic potential in order to support the mechanism obtained from their TEM observation. As shown in Fig. 2.8, the $< c + a >$ edge dislocation has two stable core structures at 0K: one type is the perfect dislocation and the other is two $\frac{1}{2} < c + a >$ partial dislocations. However, the core of $< c + a >$ edge dislocation becomes sessile due to the core structure change, in which the core extends parallel to the basal plane, as temperature increases, resulting in very low mobility of the $< c+a >$ edge dislocation. The TEM study of Mg single crystals compressed along the c-axis compression by Obara *et al.* (1973) supports the mechanism that Ando and his group have suggested.

They also observed the dissociation of $< c + a >$ edge dislocations into the $< a >$ and $< c >$ perfect dislocations in the c-axis compression sample. However, Stohr and Poirier (1972) observed other kind of partial dislocations in the c-axis compression sample and suggested that they are formed by following dislocation reaction:

$$\frac{1}{3}[11\bar{2}3] \rightarrow \frac{1}{6}[20\bar{2}3] + \frac{1}{3}[02\bar{2}3]. \tag{2.24}$$

Frank and Nicholas (1953) showed the Shockley type reaction on the 2^{nd} order pyramidal plane given by eq. (2.24) based on a hard-sphere model and they also recognized that this dissociation may be sessile due to the corrugated nature of the slip plane.

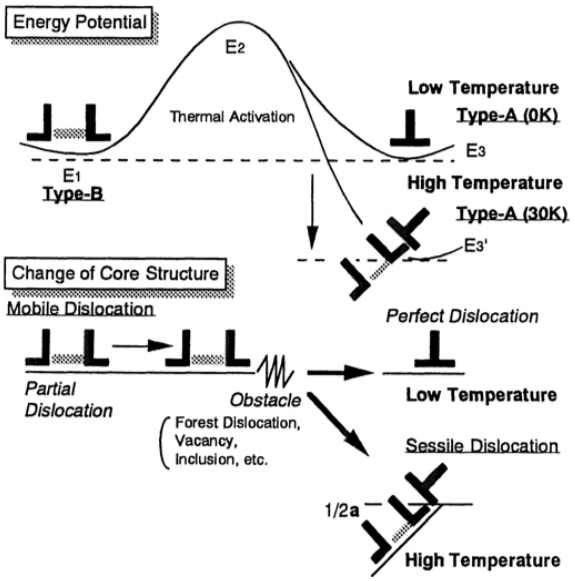

Figure 2.8: Energy potential model of $< c + a >$ edge dislocation immobilization suggested by Ando *et al.* (1996).

2.2.6 Other non-basal slip deformation

Non-basal $< a >$ slip, prismatic $< a >$ slip and 1^{st} order pyramidal $< a >$ slip

When the tensile axis of a single crystal is located between $[2\bar{1}\bar{1}0]$ and $[10\bar{1}0]$, the Schmid factors for prismatic $< a >$ slip: $\{10\bar{1}0\} < 11\bar{2}0 >$ and 1^{st} order pyramidal $< a >$ slip: $\{10\bar{1}1\} < 11\bar{2}0 >$ systems have higher values, than basal $< a >$ slip systems. The activation of prismatic $< a >$ slip and 1^{st} order pyramidal $< a >$ slip is expected to occur in single crystals deformed in tension with these orientations of the tensile axis.

Fig. 2.9 shows stress – strain curves for non-basal $< a >$ slip in Mg single crystals deformed at various temperatures (Yoshinaga and Horiuchi, 1963c). The tensile axis of the single crystals studied by Yoshinaga and Horiuchi (1963c) was 5° off $\{2\bar{1}\bar{1}0\}$ pole towards $\{10\bar{1}0\}$ pole, i.e., paralleled to $\sim [7\bar{4}\bar{3}0]$. As discussed in previous section, Ando *et al.* (1992) found the activations of 2^{nd} order pyramidal $< c+a >$ slip systems in the $[2\bar{1}\bar{1}0]$ tensile deformation. Although there has been no report which deformation mechanisms occur predominately in the $[10\bar{1}0]$ tensile test, the activations of the non-basal slip systems are currently thought to occur in Mg single crystals deformed in tension when the tensile axis is located between $[2\bar{1}\bar{1}0]$ and $[10\bar{1}0]$, excluding exact $[2\bar{1}\bar{1}0]$ orientation.

The flow curves of Mg single crystals with non-basal $< a >$ slip orientations are similar to that of 2^{nd} order pyramidal $< c + a >$ slip. Rapid hardening starts after the yielding without easy glide stage. The crystals fracture is observed after a few

percent of strain deformed at 293K and 373K, while above 473K, the crystals showed excellent ductility and deformation approaching few hundred percent.

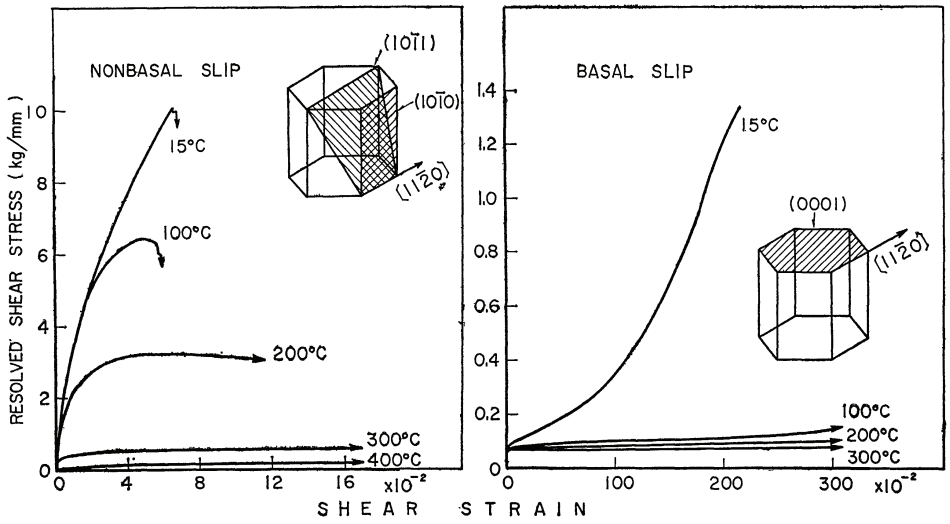

Figure 2.9: Stress-strain curves for non-basal $< a >$ slip in Mg single crystals (Yoshinaga and Horiuchi, 1963c).

Linear patterns corresponded to the prismatic $< a >$ slip, in Mg single crystals in non-basal orientation deformed at 295K are shown in Fig. 2.10(a) (Yoshinaga and Horiuchi, 1963b). At the same time, the slip bands corresponding to the basal plane were observed. One observes that the non-basal slip patterns are very wavy due to the frequent cross-slip of $< a >$ dislocations between $\{10\bar{1}0\}$, $\{10\bar{1}0\}$, and (0001) planes, as seen in Fig.2.10(b) (Yoshinaga and Horiuchi, 1963c). The slip markings show a very similar morphology to $< 111 >$ pencil glide in BCC metals (Gilormini *et al.*, 1988).

The observations can be explained by the formation of the super jogs by cross-slip of the screw $< a >$ dislocations between the non-basal planes and the basal plane

(Yoshinaga and Horiuchi, 1963c). Couret and Caillard (1985a,b) performed $in-situ$ TEM as shown in Fig. 2.11 (a) and suggested kink-pair mechanism based on their observation of prismatic dislocations (Fig.2.11 (b)). The dislocations are assumed to glide by jumps between adjacent valleys through the thermally activated nucleation of a pair of kinks with opposite signs, as shown in Fig. 2.11 (b). The movement of screw dislocations is controlled by the kink-pair mechanism. A dislocation loop formed at a pinning point expands by the rapid movement of its edge parts.

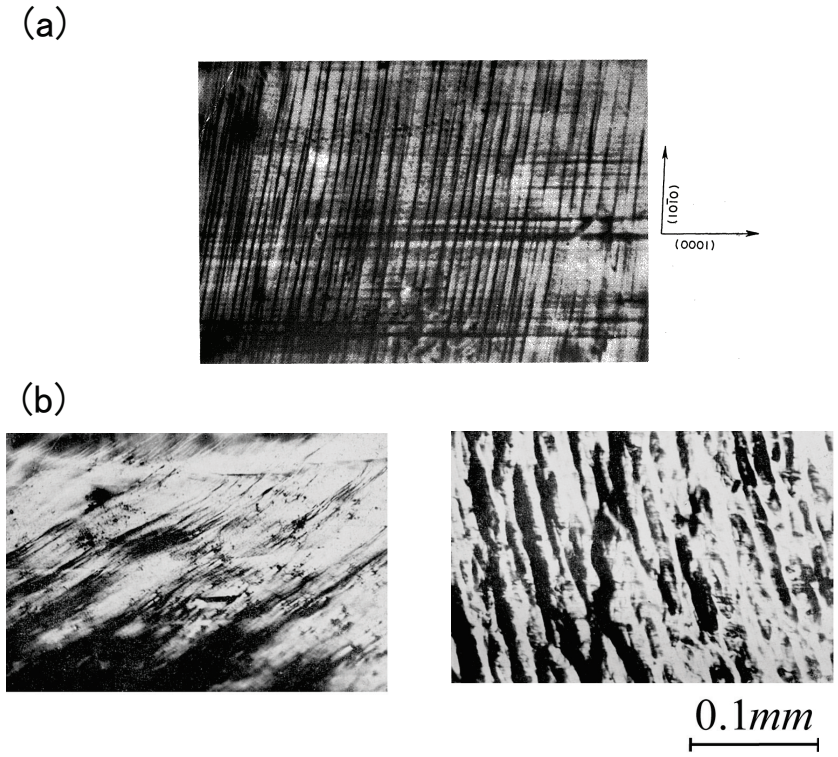

Figure 2.10: Prismatic $< a >$ slip bands in Mg single crystals deformed to fracture (a) at 295K (Yoshinaga and Horiuchi, 1963b) and (b) at 673K (Yoshinaga and Horiuchi, 1963c).

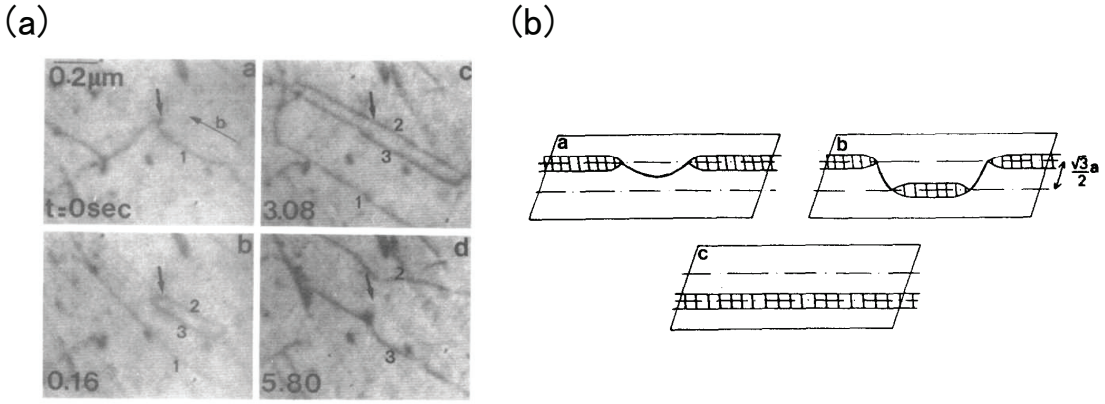

Figure 2.11: (a) TEM observation of prismatic $< a >$ slip in Mg at 300K, and (b) kink-pair mechanism (Couret and Caillard, 1985a).

2.2.7 Higher temperature deformation of Mg single crystals

High temperature deformation behaviour of Mg single crystals in various crystallographic orientations has also been extensively studied (Yoshinaga and Horiuchi, 1962, 1963c; Onaka *et al.*, 1995; Miura *et al.*, 2005). Fig.2.12 shows mechanical properties data of Mg single crystals deformed in tension between 473K and 673K (Miura *et al.*, 2005). Since the CRSS for non-basal slip rapidly decreases in the higher temperatures, slip traces corresponding to prismatic, pyramidal $< a >$ slip and 2^{nd} order pyramidal $< c + a >$ slip were observed in addition to basal $< a >$ slip, even when the tensile axes were located at basal $< a >$ slip orientations such as the A2 and A5 samples in the Fig.2.12.

Miura *et al.* (2005) has argued that dynamic recrystallization (DRX) occurring during high temperature deformation of single crystals plays a very important role in the ductility of the material.

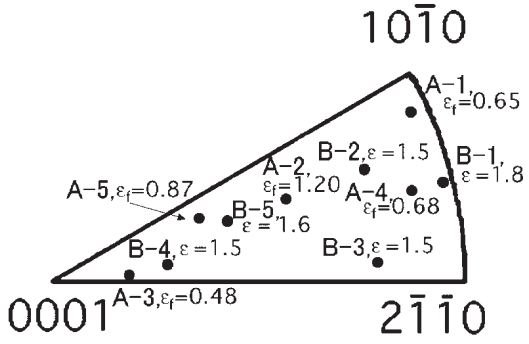

Sample no.	Tensile direction				Elongation to fracture true strain (nominal strain)	Fractured	DRXed	Active slip planes
A-1	27	−1	−26	1	0.65 (92%)	Yes	Yes	Pr + 2Py
A-2	4	−5	1	−3	1.2 (230%)	Yes	Yes	B + Pr
A-3	−1	−1	2	−5	0.48 (62%)	Yes	Yes	B + −
A-4	15	9	−24	−2	0.68 (97%)	Yes	Yes	–
A-5	1	5	−6	5	0.87 (140%)	Yes	Yes	B + Pr
B-1	−11	3	8	−1	1.8 (500%)	No	No	Pr
B-2	25	5	−30	9	1.5 (350%)	No	No	B
B-3	15	21	−36	−14	1.5 (350%)	No	No	B
B-4	−3	2	1	−5	1.5 (350%)	No	No	B
B-5	10	−2	−8	9	1.6 (400%)	No	No	–

Figure 2.12: Crystallogrpahic orientations of tensile directions of Mg single crystals deformed at 573K with the corresponding tensile tests results. The letters 'B', 'Pr', 'Py', and '2Py' indicate basal, prismatic, pyramidal $< a >$ slip and 2 order pyramidal $< c+a >$ slip, respectively. 'DRX' stands for dynamic recrystallization (Miura *et al.*, 2005). Deformation temperature between 473K and 673K.

1^{st} order pyramidal $< c + a >$ slip

1^{st} order pyramidal $< c + a >$ slip, $\{10\bar{1}1\}<11\bar{2}3>$ is rarely observed in Mg single crystals, because the magnitude of the Burgers vector is large and the planes are

atomically rough. This is also true in low-index crystal orientations or at higher deformation temperatures, where other non-basal slip systems such as prismatic $< a >$ slip, 1^{st} order pyramidal $< a >$ slip, 2^{nd} order pyramidal $< c + a >$ slip system are more favourably activated. However, very recently, the activation of the 1^{st} order pyramidal $< c + a >$ slip was reported in the a-axis tensile test of pure Mg and Mg-Al-Zn ternary alloy single crystals at 473K (Ando *et al.*, 2014). According to their report, the CRSS for the 1^{st} order pyramidal $< c+a >$ slip systems had also strongly temperature dependence, as well as other non-basal slip systems.

2.2.8 Twin deformation

$\{10\bar{1}2\} < 10\bar{1}1 >$ **twin**

$\{10\bar{1}2\} < 10\bar{1}1 >$, c-axis extension twin is the most favoured deformation twinning mode in Mg single crystals, because the critical resolved shear stress CRSS for $\{10\bar{1}2\} < 10\bar{1}1 >$ twin is the second smallest among all deformation modes regardless of deformation temperatures and strain rate. According to Koike (2005), CRSS for $\{10\bar{1}2\} < 10\bar{1}1 >$ twin is ∼2-3MPa, second lower after the basal $< a >$ slip. The reason $\{10\bar{1}2\} < 10\bar{1}1 >$ is the most active twinning mode in Mg is that (i) the amount of shear, s=0.130, is significantly smaller compared to other twinning modes and (ii) the shuffling of the layers at the completion of the twinning is very small (Mendelson, 1970). Therefore, $\{10\bar{1}2\} < 10\bar{1}1 >$ twin is an important deformation mode and it assumes many different roles in Mg single crystals' and poly-crystals' plasticity, such as:

- $\{10\bar{1}2\} < 10\bar{1}1 >$ twin introduce additional interfaces and the twin boundaries

can act as barriers to dislocation motion and contribute to ductility and plasticity of Mg through "dynamical Hall-Petch effect", i.e., grain refinement and reduction of mean free path of dislocations.

- The interface act as the origin of fracture (Ando *et al.*, 2006; Somekawa *et al.*, 2009), because the twin interface energy is significantly high.

- $\{10\bar{1}2\} < 10\bar{1}1 >$ twin induces tensile strain parallel to the c-axis and compressive strain perpendicular to the c-axis.

- $\{10\bar{1}2\} < 10\bar{1}1 >$ twin accompany a rotation of the c-axis by 86.3° along the a-axis, which is a major mechanism of deformation-induced texture.

- Basal $< a >$ dislocation with a screw component in the matrix can cross-slip into the basal plane in the $\{10\bar{1}2\} < 10\bar{1}1 >$ twin. Fig. 2.13 shows one example of the cross slip from matrix into twin regions.

- $\{10\bar{1}2\} < 10\bar{1}1 >$ twin can accommodate the stress concentration caused by anisotropic dislocation plasticity due to single basal $< a >$ slip (Yang *et al.*, 2004).

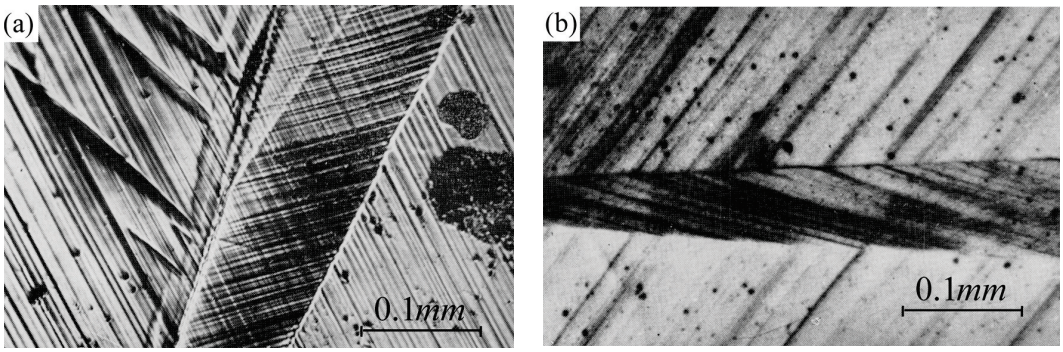

Figure 2.13: Optical microscopic observations of (a) basal $< a >$ slip traces visible inside $\{10\bar{1}2\} < 10\bar{1}1 >$ twin region and (b) the interface of basal $< a >$ slip lines both matrix and twin boundaries (Yoshinaga and Horiuchi, 1963b).

Three independent hardening mechanism due to the $\{10\bar{1}2\} < 10\bar{1}1 >$ twin in Mg have been suggested in the literature. These include: (i) texture strengthening/weakening, (ii) Dynamical Hall-Petch effect, and (iii) the Basinski mechanism (Cáceres *et al.*, 2008; Bhattacharya and Niewczas, 2011).

(i) Texture strengthening/weakening: $\{10\bar{1}2\} < 10\bar{1}1 >$ twinning in Mg reorients the lattice to harder crystallographic orientations. To illustrate concept of texture strengthening/weakening Fig. 2.14 shows flow curves of random and textured Mg polycrystals tested in (a) uniaxial tension and compression tests, and (b) channel-die compression tests cited from several papers by Cáceres *et al.* (2008). Fig. 2.14 shows an example of texture strengthening/weakening in Mg, using compression tests 1c, I, and II. It is well known that there is a high activity of $\{10\bar{1}2\} < 10\bar{1}1 >$ twinning in the first 6-8% of strain of compression tests in Mg and the initial texture affects the total volume fraction of $\{10\bar{1}2\} < 10\bar{1}1 >$ twins. According to Cáceres *et al.* (2008), the final twinned fraction for textured Mg polycrystals is generally larger

than random texture. As seen curves in Fig. 2.14, textured-Mg (curves I and II) exhibit higher work hardening than random-Mg (curve 1c).

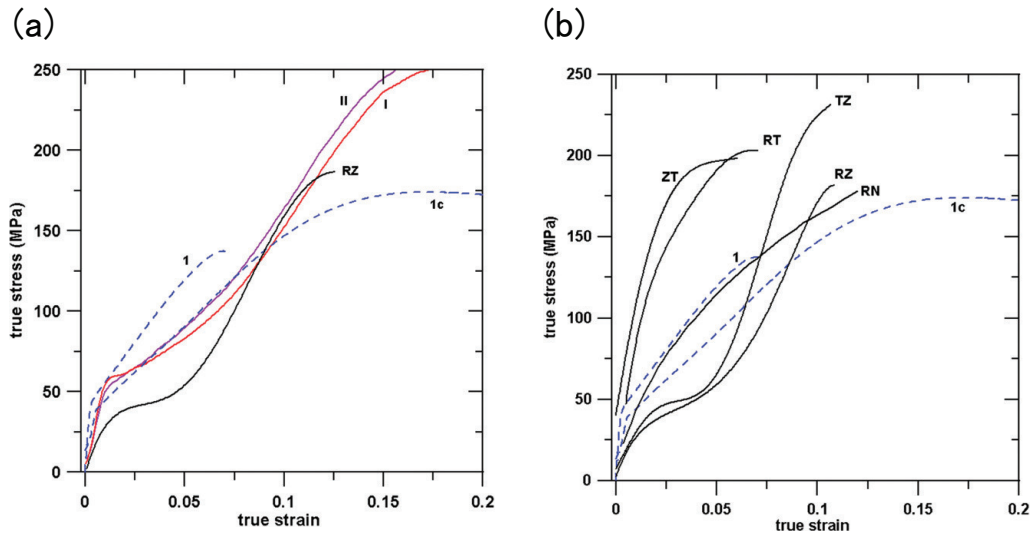

Figure 2.14: Flow curves of random and textured Mg polycrystals tested in (a) uniaxial tension and compression tests, and (b) channel-die compression tests (Cáceres *et al.*, 2008). Curves 1 and 1c represent random Mg polycrystals tested in tension and compression (Cáceres and Blake, 2007); curves I and II represent intense and weak fibre textured Mg polycrystals tested in compression (Klimanek and Pötzsch, 2002) and curve RN represents random Mg polycrystals tested in plane-strain compression (Kelly and Hosford, 1968a); curves ZT, TZ, RZ, RT are textured Mg polycrystals tested in plane-strain compression (Kelly and Hosford, 1968a) (ZT: 'through thickness' compression parallel to the c-axis; TZ and RZ: 'in-plane' compression, perpendicular to the (unconstrained) c-axis, across and parallel to the rolling direction, respectively; RT: compressed perpendicular to the constrained c-axis.)

(ii) Dynamical Hall-Petch effect: the grain refinement and the reduction of the dislocation mean free path due to twins' nucleation and growth during deformation.

The Hall-Petch relationship can be expressed as:

$$\sigma = \sigma_0 + kD^{-1/2} \tag{2.25}$$

where σ is the flow strength, σ_0 the friction stress and k the stress intensity constant. Fig. 2.15 shows Hall-Petch relationsip for polycrystalline Mg with different textures (Cáceres *et al.*, 2008). According to Cáceres *et al.* (2008), the dynamical Hall-Petch hardening has a relatively small effect on the strain-hardening behaviour of Mg polycrystals. In textured polycrystals, this is due to the small value of the Hall-Petch constant, k. For random polycrystals, on the other hand, the k-value is several times larger but, since the fraction of grains undergoing twinning is small, so is the overall hardening effect.

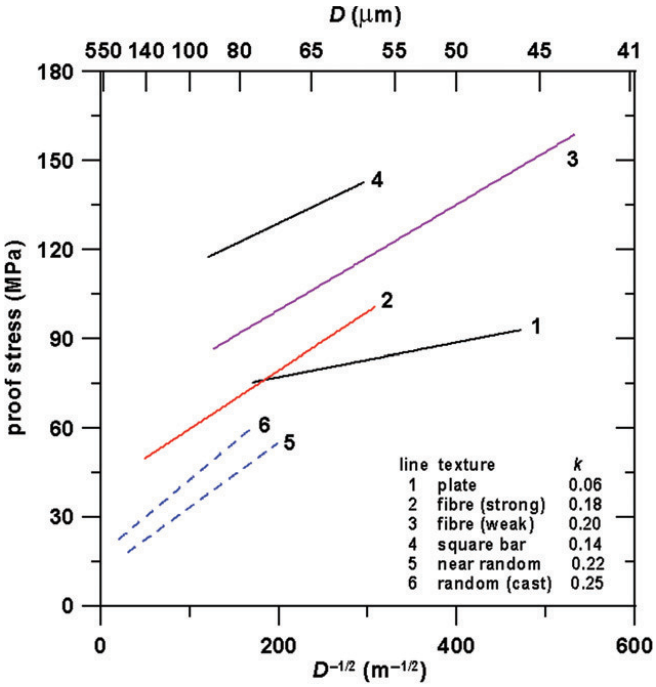

Figure 2.15: Hall-Petch relationship for textured polycrystal Mg determined by tension tests (Cáceres *et al.*, 2008). References to line 1-3 (Wilson and Chapman, 1963), line 4 (Sambasiva Rao and Prasad, 1982), line 5 (Hauser *et al.*, 1956), and line 6 (Andersson *et al.*, 2003).

(iii) The Basinski mechanism: the transformation of dislocations as the twinning front passes through them can lead to the establishment of high hardening rates within the twin interior.

New hardening mechanism proposed by Basinski *et al.* (1997b) predicts that an increment in strength/hardness develops as a result of dislocations transformation from glissile to sessile configurations within twins. Consequently, twins formed in a lightly strained matrix are expected to be harder than the adjacent matrix region.

The micro-hardness values from matrix and twin regions in Cu-8at.% Al single crystal (Basinski *et al.*, 1997b) and α-Ti (Kalidindi *et al.*, 2003; Salem *et al.*, 2006), shown in Table 2.2, indicate that twin is harder than matrix in these materials. In Cu-8at.% Al single crystal, the value of micro-hardness in twin area is almost twice higher than the adjacent matrix region. The micro-hardness measurements in adjacent matrix and twin regions of α-Ti polycrystalline sheet having HCP structure indicate that the twin regions is almost 30% harder than the matrix region.

Table 2.2: Experimental data of micro-hardness tests in matrix and twin regions in the literatures (Basinski *et al.*, 1997b; Kalidindi *et al.*, 2003; Salem *et al.*, 2006).

Materials	Hardness (HV)		Remarks
	Matrix	Twin	
Cu-8at.% Al single crystal (FCC)	16-19	41-43	The onset of twinning was 70% elongation.
α-Ti polycrystalline sheet (HCP)	93±9	123±15	5% strain compression.

It is very important to determine whether the character of dislocations incorporated to the mechanical twin is sessile or glissile in consideration of the Basinski hardening mechanism. In the case of twinned Cu-8at.% Al crystals (Basinski *et al.*, 1997b), TEM observations of dislocation configurations at the twin boundaries showed much complex dislocation substructures. The dislocation transformation to the twin lattice were classified into five groups based on the corresponding matrix method: (i) glissile-to-sessile, (ii) sessile-to-glissile, (iii) glissile-to-glissile, (iv) sessile-to-sessile, and (v) formation of three dimensional structures in the twin including dislocation

loops, jogs and refined debris by conventional TEM works (Niewczas, 2007). Among the dislocation reactions, the sessile dislocation created in twin regions has thought to be the origin of hardening. In contrast, the situation of the incorporation of basal $< a >$ dislocation into $\{10\bar{1}2\} < 10\bar{1}1 >$ twin in pure Mg is different due to HCP structure. The correspondence matrix method proposed by Niewczas (2010) indicates that basal plane in matrix should transform to prism plane in $\{10\bar{1}2\} < 10\bar{1}1 >$ twin. Cáceres *et al.* (2008) assumed that basal $< a >$ dislocation would lie on the harder prism planes whereas prism $< a >$ dislocations would lie on softer basal planes as a result of $\{10\bar{1}2\} < 10\bar{1}1 >$ twinning shear, without any proof from TEM studies.

$\{10\bar{1}1\} < 10\bar{1}2 >$ **twin**

The CRSS for $\{10\bar{1}1\} < 10\bar{1}2 >$, c-axis contraction twin is much higher than that of $\{10\bar{1}2\} < 10\bar{1}1 >$ twin and the reported values are: 76-153MPa (Wonsiewicz and Backofen, 1967) and 114 MPa (Yoshinaga and Horiuchi, 1963a). Unlike $\{10\bar{1}2\} < 10\bar{1}1 >$ twin, the CRSS for $\{10\bar{1}1\} < 10\bar{1}2 >$ has higher temperature and strain rate dependence (Yoshinaga and Horiuchi, 1963a).

The role of the c-axis contraction twin is different from the extension twin and the contraction twins is believed to be responsible for the fracture (Yoshinaga and Horiuchi, 1963a), although there are exceptions from this rule. Very recently Ando *et al.* (2014) reported results of Mg-Al-Zn ternary alloy single crystals deformed by $\{10\bar{1}1\} < 10\bar{1}2 >$ twins in the a-axis tensile test at 298K. The authors observed that additions of Al and Zn elements increases CRSS for 2^{nd} order pyramidal $< c + a >$ slip and decreases for $\{10\bar{1}1\} < 10\bar{1}2 >$ contraction twin.

Strong activity of $\{10\bar{1}1\} < 10\bar{1}2 >$ twins was observed in the c-axis compression

tests of Mg single crystals by Yoshinaga and Horiuchi (1963a); Obara *et al.* (1973); Yoshinaga *et al.* (1973). At 295K the crystal fractured in twinned regions, just after a small number of thin twins were nucleated. Many $\{10\bar{1}1\} < 10\bar{1}2 >$ twins were accompany by fine $\{30\bar{3}4\}$ and $\{10\bar{1}3\}$ habit twins developed during deformation at 373K-473K. Fig. 2.16 shows optical micrograph of $\{10\bar{1}1\} < 10\bar{1}2 >$ twins in Mg single crystals in the c-axis compression tests at 373K (Yoshinaga and Horiuchi, 1963a). The activation of 2^{nd} order pyramidal $< c + a >$ slip prevailed above 573K and the amount of $\{10\bar{1}1\} < 10\bar{1}2 >$ twin was decreased.

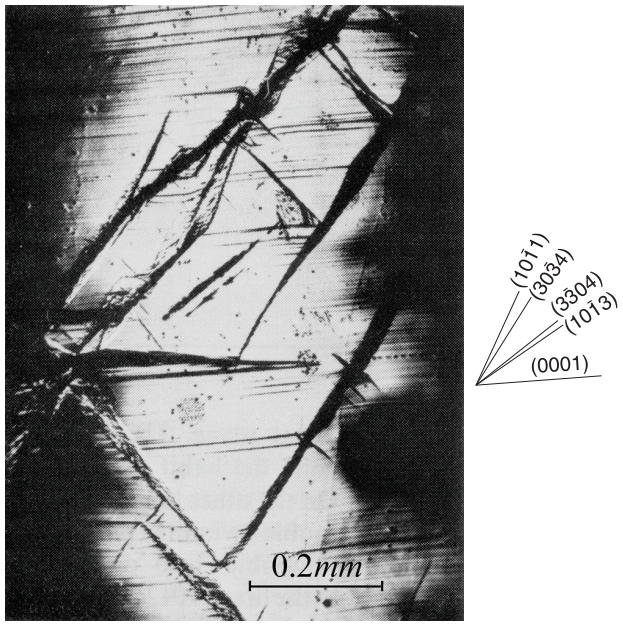

Figure 2.16: $\{10\bar{1}1\} < 10\bar{1}2 >$, c-axis contraction twins observed in Mg single crystals in the c-axis compression tests at 373K (Yoshinaga and Horiuchi, 1963a).

2.3 Latent hardening

Latent hardening experiments have been used to investigate the anisotropy of the flow stresses produced by the corresponding anisotropy of dislocation substructure and properties. Fig. 2.17 shows schematic illustration of a combined uniaxial loading type latent hardening experiment. In this test, two consecutive deformations are carried out on a single crystal. Firstly, an annealed large single crystal termed "parent" crystal, is axially loaded in an initial single slip orientation and is deformed to some predetermined stress levels. After unloading, differently oriented "secondary" samples, are cut from the pre-deformed parent crystal by spark cutter and then subjected to the secondary tensile test or compression test. The orientations of these secondary samples are chosen such that a single slip system is activated during the secondary test and the dislocations of this slip system interact with the dislocations of the slip systems that operated in the parent sample. In order to describe latent hardening behaviour, a latent hardening ratio (LHR) was introduced by Jackson and Basinski (1967) and have been widely used by many researchers. If a parent crystal is predeformed to a flow-stress $\tau_{max}^{(i)}$ and the initial flow-stress on the secondary system is $\tau_0^{(j)}$, as shown in Fig. 2.17(c), the LHR is defined as:

$$LHR = \frac{\tau_0^{(j)}}{\tau_{max}^{(i)}} \tag{2.26}$$

2.3.1 Latent Hardening behaviour of FCC crystals

Latent hardening tests have been extensively studied in FCC single crystals and alloy single crystals such as Cu (Jackson and Basinski, 1967; Franciosi *et al.*, 1980),

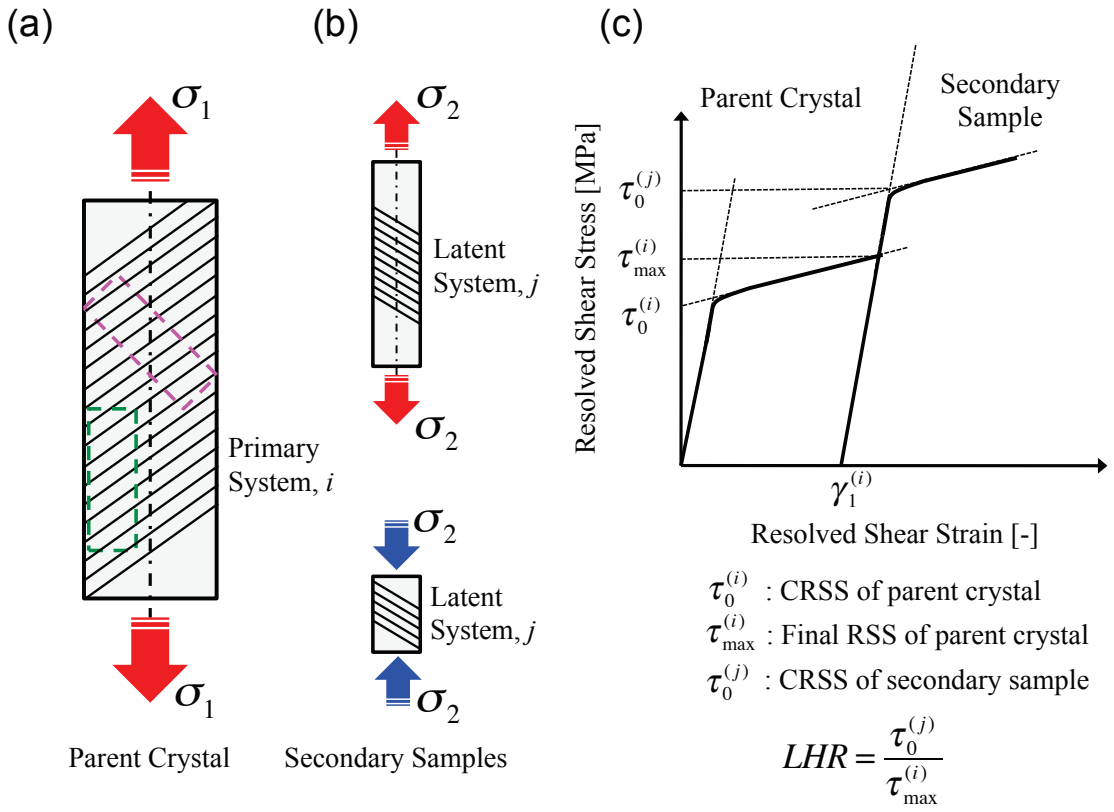

Figure 2.17: Experimental procedure and notation of Jackson and Basinski type latent hardening tests: (a) deformation of parent crystal in tension, (b) deformation of secondary samples in tension and compression, and (c) the definition of latent hardening ratio.

Al (Kocks, 1964; Kocks and Brown, 1966; Lake and Craig, 1972; Miyamoto *et al.*, 1977; Franciosi *et al.*, 1980), Ag (Kocks, 1964; Ramaswami *et al.*, 1965), Cu-Al alloy (Wessels and Jackson, 1969; Wessels and Nabarro, 1971), Ag-Au alloy (Ramaswami *et al.*, 1965), and Al-Mg alloy (Wu *et al.*, 1997). In the following, the latent hardening experiments in FCC crystals and the conclusions arising from these studies are reviewed.

Types of dislocation interactions

To describe the dislocation interactions between the primary and secondary deformation tests and the strength of these interactions, the literature describing the latent hardening behaviour of FCC crystals has used mostly the Schmid and Boas notation (Schmid and Boas, 1935). As well known, in FCC crystals there are four {111} slip planes and three $< 110 >$ directions in each slip plane, giving in total twelve $\{111\} < 110 >$ slip systems. The Schmid and Boas notation (Schmid and Boas, 1935) for the slip systems in FCC crystals and the corresponding crystallographic planes and directions is shown in Fig. 2.18 and Table 2.3.

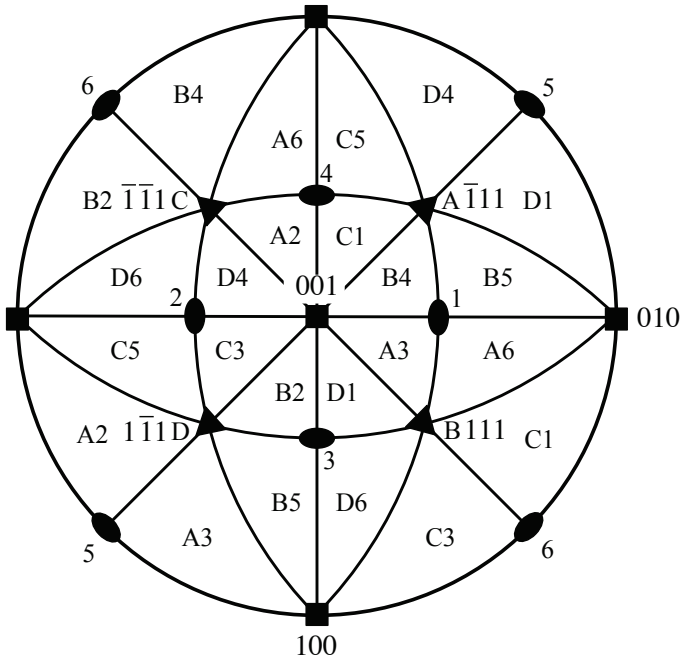

Figure 2.18: (001) stereographic projection with the description of slip systems operating in different standard triangles (Schmid and Boas, 1935).

In this notations, the capital letter denotes the slip plane normal and the number

Table 2.3: Schmid and Boas notation for slip systems in FCC lattice (Schmid and Boas, 1935).

	number	Schmid and Boas notation	slip system
Primary system	1	B4	$(111)[\bar{1}01]$
	2	B5	$(111)[\bar{1}10]$
	3	B2	$(111)[0\bar{1}1]$
Conjugate system	4	C1	$(1\bar{1}\bar{1})[011]$
	5	C5	$(1\bar{1}\bar{1})[1\bar{1}0]$
	6	C3	$(1\bar{1}\bar{1})[101]$
Cross-glide system	7	D4	$(1\bar{1}1)[\bar{1}01]$
	8	D1	$(1\bar{1}1)[011]$
	9	D6	$(1\bar{1}1)[110]$
Critical system	10	A3	$(\bar{1}11)[101]$
	11	A6	$(\bar{1}11)[110]$
	12	A2	$(\bar{1}11)[0\bar{1}1]$

denotes the slip direction. For the orientations inside the standard $[001]-[011]-[\bar{1}11]$ triangle, B4 $(111)[\bar{1}01]$ slip system has maximum Schmid factor and is called the primary slip system. Crystallographic symmetry of cubic crystals reduces the number of possible types of dislocation interactions to six and these types are schematically depicted in Fig. 2.19. The self-interactions (Fig. 2.19(a)) are interactions between two dislocations of the same Burgers vectors gliding in parallel slip planes. The coplanar interactions (Fig. 2.19(b)) occurs between two dislocations of different Burgers vectors in parallel slip planes. Collinear interactions (Fig. 2.19(c)) stand for the reactions

between two dislocations of parallel Burgers vectors gliding in two planes intersecting each other along the direction of the Burgers vector of dislocations. Non-coplanar (forest) interactions (Fig. 2.19(d)) are defined as the reactions between dislocations with different Burgers vectors moving on intersecting planes. Furthermore, three possible types of dislocation reactions exist between non-coplanar slip systems in FCC crystals, producing glissile junctions, the Lomer-Cottrel locks and the Hirth locks (Hirth and Lothe, 1992). Fig. 2.20 shows the part of the [001] standard stereographic projection illustrating possible dislocation reactions that can occur with the primary slip system B4 (Kubin, 2013). "LC", "H", and "G" denote the Lomer-Cottrel locks, the Hirth locks and glissile junctions respectively, formed during these interactions.

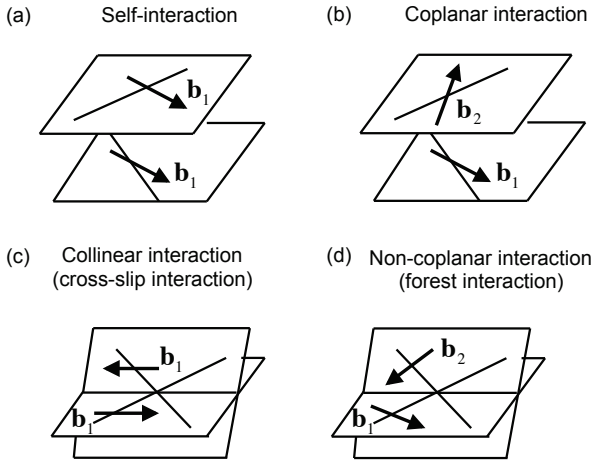

Figure 2.19: The examples of six elementary short-range interactions of perfect dislocations in FCC crystals: (a) Self-interaction; (b) Coplanar interaction; (c) Collinear interaction and (d) Non-coplanar interaction (Kubin, 2013).

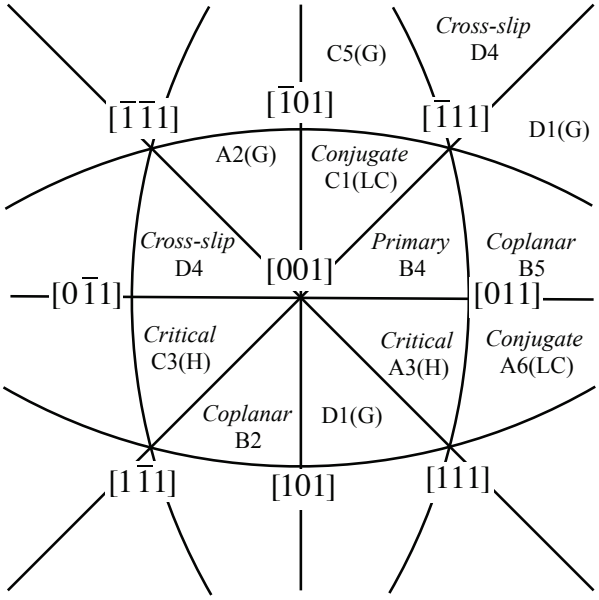

Figure 2.20: [001] stereographic projection illustrating possible interactions of the primary slip system with other slip systems in neighbouring stereographic triangles, having maximum Schmid factors. "LC", "H", and "G" denote the Lomer-Cottrel locks, the Hirth locks and glissile junctions formed during these interactions (Kubin, 2013).

In the following part we review seminal studies of the latent hardening for various coplanar and forest systems in Cu single crystals performed by Jackson and Basinski (1967). Fig. 2.21 is the (001) stereographic projection showing the initial and the final axis orientations of the parent crystal "G_4" strained in tension ($\gamma^{(i)}_{max}$=0.245) and the tensile axis orientations of the secondary specimens in triangles B2, A2, and D1, cut from the parent crystals. Shear stress-shear strain curves for intersecting slip systems B4/A2 and B4/D1 and coplanar systems B4/B2 are shown in Fig. 2.22. When the slip plane in the secondary test is the same as in the primary test, defined

as coplanar interactions, the flow stress is almost unchanged. However, when the slip plane of the secondary slip system is changed, defined as a non-coplanar (forest) slip system, the flow stress is increased, illustrating the effect of the forest interactions on the flow stress and the latent hardening effect arising from these interactions.

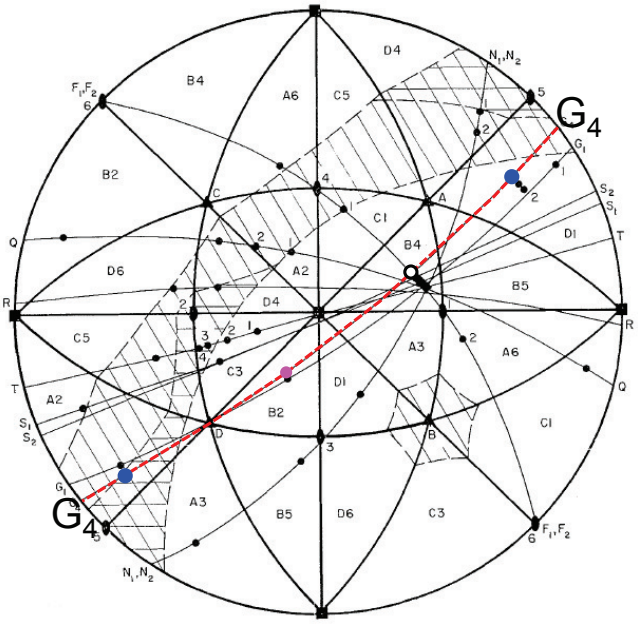

Figure 2.21: Tensile axis positions of Jackson and Basinski's parent and secondary crystals (Jackson and Basinski, 1967).

Other similar type latent hardening experiments published in the literature enabled to obtain general understanding of the strength between different types of dislocation interactions in e.g., Cu (Jackson and Basinski, 1967; Franciosi *et al.*, 1980), Al (Kocks, 1964; Kocks and Brown, 1966; Lake and Craig, 1972; Miyamoto *et al.*, 1977; Franciosi *et al.*, 1980), Ag (Kocks, 1964; Ramaswami *et al.*, 1965), Cu-Al alloy (Wessels and Jackson, 1969; Wessels and Nabarro, 1971), Ag-Au alloy (Ramaswami

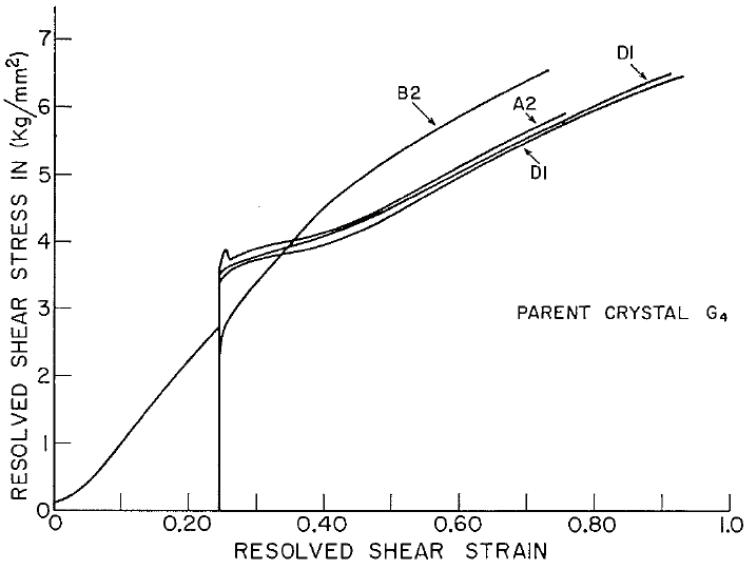

Figure 2.22: Subsequent resolved shear stress-strain curves in secondary crystals of parent crystal G_4. The pre-strain of G_4 crystal was in stage II (Jackson and Basinski, 1967).

et al., 1965), and Al-Mg alloy (Wu *et al.*, 1997). It is revealing that all types of dislocation interactions do not have exactly the same strength and they can be categorized into six groups in terms of the geometrical arrangement of the Burgers vectors of the interacting dislocations, as follows (Franciosi *et al.*, 1980):

1. formation of sessile junction (the Lomer-Cottrell sessile locks) between systems B4/A6 and B4/C1;

2. formation of glissile attractive junctions between systems B4/A2, B4/C5, B4/D1 and B4/D6;

3. formation of the Hirth lock between systems B4/A3 and B4/C3;

4. cross-slip or collinear interactions between system B4/D4;

5. coplanar interactions between systems B4/B2 and B4/B5; and

6. self-interactions between system B4/B4.

Above observations pertinent to the strength of different type dislocation interactions were in good agreement with the forest theory of the flow stress in FCC single crystals. The strength of dislocation interactions and the strength of dislocation junctions was analytically calculated by Baird and Gale (1965) and recent dislocation dynamics (DD) simulations by Kubin *et al.* (2008) confirm the results of latent hardening experiments.

Effect of dislocation density on latent hardening

The anisotropic latent hardening behaviour does not result solely from the type of dislocation interactions between two systems, but also from the anisotropy of the respective dislocation densities of these slip systems. Jackson and Basinski (1967) found that the LHRs on forest systems varied from 2.5 in stage I to 1.4 in late stage II in Cu single crystals, depending on the pre-strain as shown in Fig. 2.23. On the other hand, the LHRs on coplanar system B4/B2 is close to 1.0, regardless of the pre-strain.

In classical forest hardening theories, the flow stresses of both the primary and latent systems were described by:

$$\tau_p = \tau_y + \alpha\mu b\rho_f^{1/2} \tag{2.27}$$

and

$$\tau_f = \tau_y + \alpha\mu b(\rho_p + \rho_f)^{1/2} \tag{2.28}$$

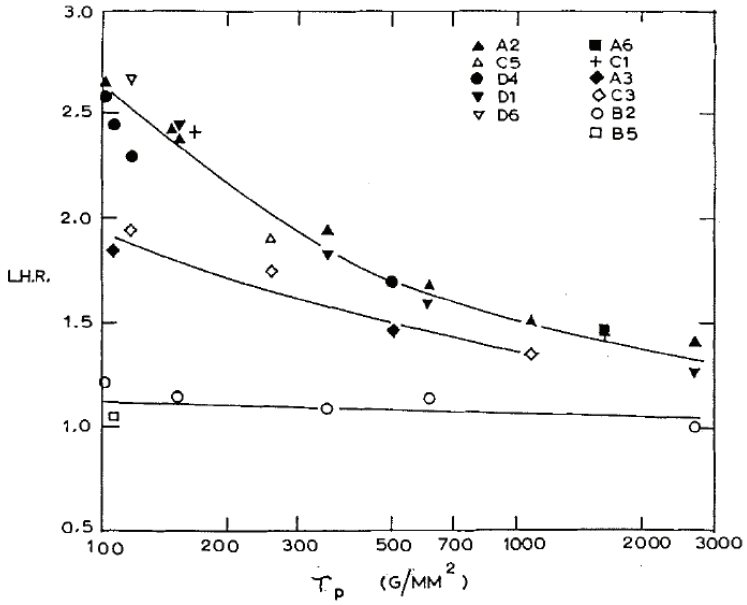

Figure 2.23: Latent Hardening Rations (LHRs) versus shear stress on the primary slip system, after Jackson and Basinski (1967).

respectively (Basinski, 1959; Jackson and Basinski, 1967; Wessels and Jackson, 1969). ρ_f and ρ_p are the density of dislocations of the intersecting and coplanar slip systems, μ is the shear modulus, b is the Burgers vector, and α is the interaction coefficient. The values of the interaction coefficients have been estimated from theoretical calculations. From eqs. (2.27) and (2.28), one can obtain the relative rate of increase of the two flow stresses:

$$\frac{d\tau_f}{d\tau_p} = \left(\frac{\rho_f}{\rho_p + \rho_f}\right)^{1/2} \left(1 + \frac{d\rho_p}{d\rho_f}\right). \tag{2.29}$$

When forest hardening starts to operate between multiple slip systems, the term $\frac{d\rho_p}{d\rho_f}$ should become of the order of unity. Wessels and Jackson (1969) suggested that when the primary shear strain is large enough, the values of LHRs are approximately

expressed as:

$$LHR = \frac{\tau_f}{\tau_p} \approx \left(1 + \frac{\rho_p}{\rho_f}\right)^{1/2}. \tag{2.30}$$

From eq. (2.30), the LHR is proportional to the square root of the ratio of the dislocation density in the primary system to that in the latent system. The saturated value of about 1.4 in late stage II in Cu single crystal (Jackson and Basinski, 1967) has proved that the approximation in eq. (2.30) is valid.

Effect of stacking-fault energy on latent hardening

The stacking-fault energy of crystals has also and influence on the latent hardening behaviour. An equilibrium separation of an extended screw and edge dislocations, d_{screw} and d_{edge} is given by approximate relations derived based on isotropic elasticity theory:

$$d_{screw} = \frac{\mu a^2}{16\pi\Gamma_{SFE}}\left(\frac{2-3\nu}{3(1-\nu)}\right) \tag{2.31}$$

$$d_{edge} = \frac{\mu a^2}{48\pi\Gamma_{SFE}}\left(\frac{2+\nu}{1-\nu}\right) \tag{2.32}$$

where Γ_{SEF} is the stacking-fault energy and ν is the Poisson's ratio. The width of the partial dislocations is inversely proportional to the stacking-fault energy.

Fig. 2.24 shows the LHRs as a function of primary shear strain for different FCC crystals, Al, Cu, Cu-4%Zn and Ag (Franciosi, 1985). It is clear that the LHRs depend on the type of dislocation interactions and on dislocations densities, as discussed above. However, the maximum anisotropy amplitude observed at small primary shear strain, i.e., maximum values of the LHRs, depend on the type of the material. The LHRs maxima for Ag are about 3.5, while the maxima for Al are about 1.5 or so. The different anisotropy amplitude can be interrpretted in terms of the influence of

the stacking fault energy on LHR. Fig. 2.25 shows the LHRs maxima versus the parameter $E/\mu b$, where E is the material stacking fault energy, μ the shear modulus and b the Burgers vector. As seen in Fig. 2.25 representing the LHRs for the forest systems as a function of the stacking-fault energy, the lower the stacking-fault energy of the crystal (i.e., the wider width of dissociated dislocations), the higher is the latent hardening effect. The stacking-fault energy in some selected materials is given in Appendix C (Hirth and Lothe, 1992).

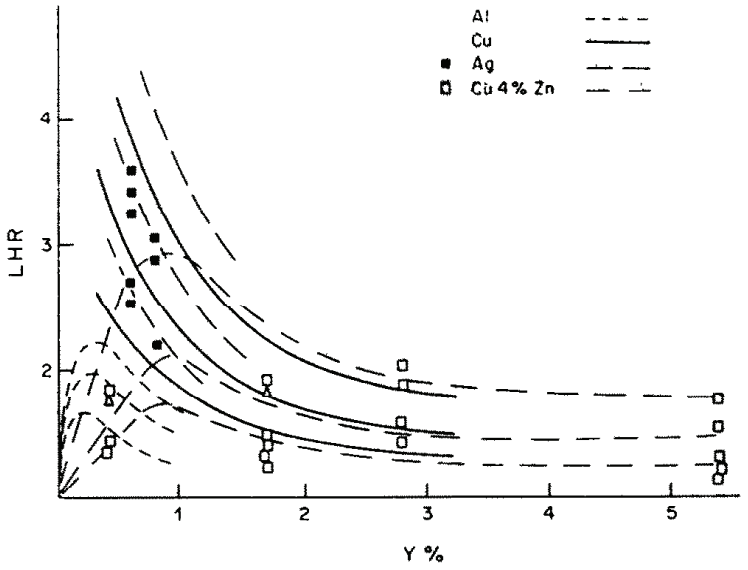

Figure 2.24: LHRs versus primary shear stress plots on forest system in Al, Cu, Cu-4%Zn, Ag single crystals (Franciosi, 1985).

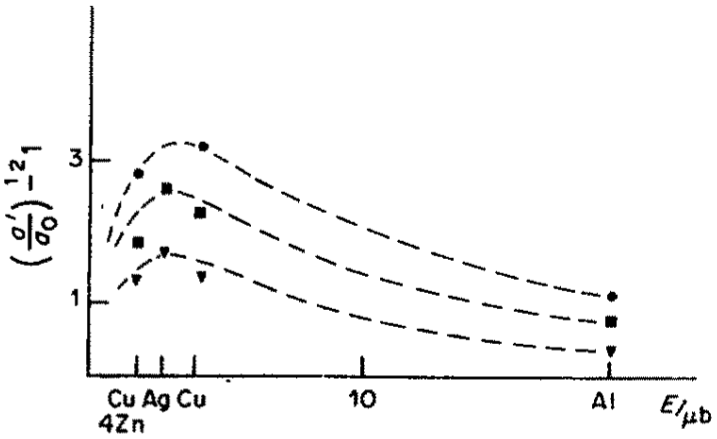

Figure 2.25: LHRs maxima versus the stacking fault energy in Al, Cu, Cu-4%Zn, Ag single crystals (Franciosi, 1985).

2.3.2 Crystal plasticity modelling in FCC single- and poly-crystalline metals

The latent hardening effect is recognized as an important concept required to develop crystal plasticity based hardening models and to predict the texture development during plastic flow (Kocks, 1970; Kocks *et al.*, 1998). In order to describe the latent hardening effects quantitatively, most researchers have assumed a rate-independent hardening rule in the form:

$$d\tau_c^{(\alpha)} = \sum_{\beta} h_{\alpha\beta} d\gamma^{(\beta)} \tag{2.33}$$

Here, $d\tau_c^{(\alpha)}$ is the current yield strength on the α slip system, and $h_{\alpha\beta}$ are the hardening rates. The off-diagonal terms in the matrix **h** represents latent hardening.

In a pioneering crystal plasticity modelling of the flow stress of FCC polycrystalline materials by Taylor and Elam (1925), the authors assumed that the latent hardening rates were equal to self-hardening rates, i.e. $h_{\alpha\beta} = h$ (for all α and β). Later, a number of crystal plasticity models in FCC single- and poly-crystalline metals with latent hardening parameters were proposed. For example, in Zhou *et al.* (1993) model, the $h_{\alpha\beta}$ matrix of the hardening rate in Eq. (2.33), has the following form:

$$h_{\alpha\beta} = h(\Gamma) q_{\alpha\beta}, \tag{2.34}$$

$$q_{\alpha\beta} = \begin{bmatrix} C & L_1 & L_2 & L_3 \\ L_1 & C & L_3 & L_2 \\ L_2 & L_3 & C & L_1 \\ L_3 & L_2 & L_1 & C \end{bmatrix}, \tag{2.35}$$

$$C = \begin{bmatrix} 1 & q_c & q_c \\ q_c & 1 & q_c \\ q_c & q_c & 1 \end{bmatrix}, L_1 = \begin{bmatrix} q_v & q_l & q_l \\ q_l & q_c & q_l \\ q_l & q_l & q_v \end{bmatrix}, L_2 = \begin{bmatrix} q_c & q_l & q_l \\ q_l & q_v & q_l \\ q_l & q_l & q_v \end{bmatrix}, L_3 = \begin{bmatrix} q_v & q_l & q_l \\ q_l & q_v & q_l \\ q_l & q_l & q_c \end{bmatrix}. \tag{2.36}$$

The coefficients, q_c, q_v, and q_l are the latent hardening ratios ($q_c < q_v < q_l$) directly obtained from the latent hardening experiments on single crystals. q_c is the LHR on the coplanar and collinear (cross-slip) systems and its value is closed to unity. q_v is the LHR on the non-coplanar (forest) system responsible for formation of attractive junctions such as the Hirsh lock; q_l is the LHR on the forest system responsible for creating glissile or sessile junctions, such as the LC locks.

Fig. 2.26 shows the difference between true stress-strain curves of Al polycrystal

with latent hardening (curve (1) and curve (2)) and that obtained assuming isotropic hardening (curve (3)). Experimental data was taken from Kocks (1970). From the calculations it is found that the latent hardening model (curve (1)) fits the best the experimental data. In the curve (1), the latent hardening parameters in stage I are higher than in the other stages, while in the curve (2), the latent hardening parameters in stage I are equal to the parameters during other stages.

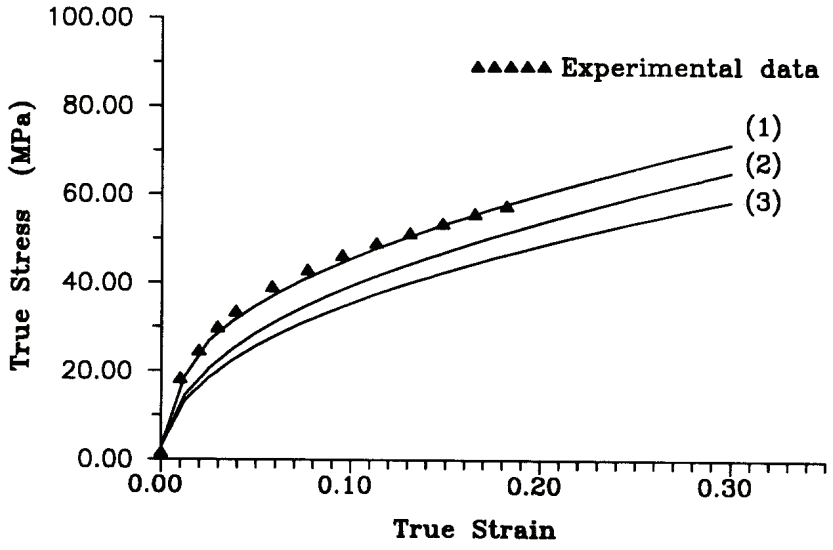

Figure 2.26: True stress-strain curves for pure polycrystalline Al with (1) latent hardening (the LHRs in strain stage I are higher than those in the other stages), (2) latent hardening (the LHRs in strain stage I are equal to those in the other stages), and (3) isotropic hardening. The experimental data are from ref. (Kocks, 1970).

Another strain hardening model was proposed by Franciosi (1985) and it is written in the general form:

$$\tau_c^{(i)} = \mu b \sqrt{\sum_j h_{ij} \rho^{(j)}}. \tag{2.37}$$

In Eq. (2.37), $\tau_c^{(i)}$ is the critical stress for active slip system i and $\rho^{(j)}$ is the dislocation density in slip system j. The coefficients $\sqrt{h_{ij}}$ represent the dislocation interaction strength between slip systems i and j directly obtained from latent hardening tests. Similar to Zhou *et al.* (1993) model, the interaction coefficients h_{ij} are described by 12×12 matrix. The matrix is diagonal and includes six different coefficients, h_k (k=0,1,2,3,4,5) representing each dislocation interaction, as shown in Fig. 2.27. In this model, both mobile dislocation density on primary system i and non-mobile dislocation density on latent system j were taken into account. This approach has successfully given more accurate hardening law in the multi-slip deformation tests than the classic Schmid law (Franciosi and Zaoui, 1982).

	A2	**A3**	**A6**	**B2**	**B4**	**B5**	**C1**	**C3**	**C5**	**D1**	**D4**	**D6**
A2	h_0	h_1	h_1	h_3	h_4	h_4	h_2	h_4	h_5	h_2	h_5	h_4
A3	h_1	h_0	h_1	h_4	h_2	h_5	h_4	h_3	h_4	h_5	h_2	h_4
A6	h_1	h_1	h_0	h_4	h_5	h_2	h_5	h_4	h_2	h_4	h_4	h_3
B2	h_3	h_4	h_4	h_0	h_1	h_1	h_2	h_5	h_4	h_2	h_4	h_5
B4	h_4	h_2	h_5	h_1	h_0	h_1	h_5	h_2	h_4	h_4	h_3	h_4
B5	h_4	h_5	h_2	h_1	h_1	h_0	h_4	h_4	h_3	h_5	h_4	h_2
C1	h_2	h_4	h_5	h_2	h_5	h_4	h_0	h_1	h_1	h_3	h_4	h_4
C3	h_4	h_3	h_4	h_5	h_2	h_4	h_1	h_0	h_1	h_4	h_2	h_5
C5	h_5	h_4	h_2	h_4	h_4	h_3	h_1	h_1	h_0	h_4	h_5	h_2
D1	h_2	h_5	h_4	h_2	h_4	h_5	h_3	h_4	h_4	h_0	h_1	h_1
D4	h_5	h_2	h_4	h_4	h_3	h_4	h_4	h_2	h_5	h_1	h_0	h_1
D6	h_4	h_4	h_3	h_5	h_4	h_2	h_4	h_5	h_2	h_1	h_1	h_0

Figure 2.27: Interaction coefficients, h_{ij} for FCC crystals (Franciosi, 1985).

2.3.3 Latent Hardening behaviour in HCP crystals

In HCP crystals, one have to consider self-interactions, coplanar, collinear, non-coplanar and non-collinear dislocation interactions between these slip and twinning

systems. There are total fourteen possible dislocations interactions when one considers the basal $< a >$ slip, the prismatic $< a >$ slip, and the 2^{nd} order pyramidal $< c + a >$ slip systems and two different Burgers vectors (Capolungo, 2011):

1. self-interactions in the basal plane;
2. self-interactions in the prismatic plane;
3. self-interactions in the second-order pyramidal plane;
4. coplanar interactions in the basal plane;
5. non-coplanar prismatic interactions;
6. collinear basal/prismatic interaction;
7. non-collinear basal/prismatic interaction;
8. pyramidal/basal forest interactions type I;
9. pyramidal/basal forest interactions type II;
10. pyramidal/prismatic forest interactions type I;
11. pyramidal/prismatic forest interactions type II;
12. collinear pyramidal interactions;
13. non-collinear pyramidal interactions type I; and
14. non-collinear pyramidal interactions type II.

Fig. 2.28 shows geometrical relationship of each dislocation interactions (Capolungo, 2011).

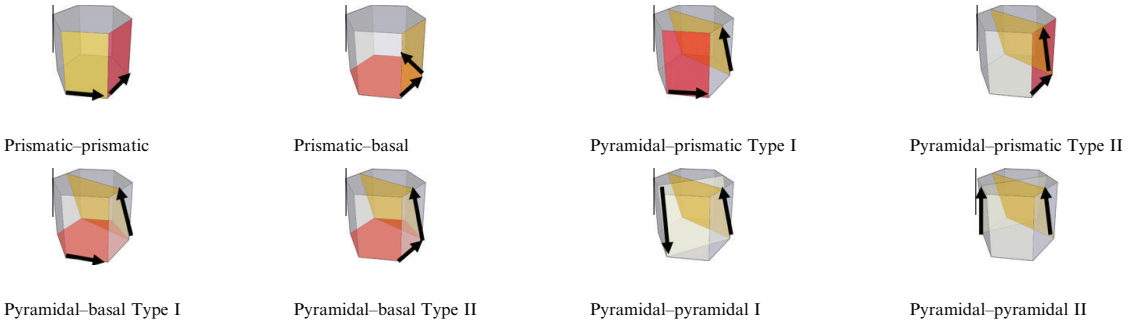

Figure 2.28: Schematic illustrations of different types of dislocation interactions for Mg (Capolungo, 2011).

Furthermore, since the activation of other non-basal slip systems such as 1^{st} order pyramidal $< a >$ and $< c + a >$ slip systems and deformation twinning modes including the c-axis tensile $\{10\bar{1}2\} < 10\bar{1}1 >$ twin and the c-axis contraction $\{10\bar{1}1\} < 10\bar{1}2 >$ twin modes have been commonly observed in deformed Mg alloys, their interactions must also be considered in theoretical models.

HCP single crystals exhibit strong plastic anisotropy due to the hexagonal symmetry and very low critical resolved shear stress (CRSS) of dominant deformation modes at 295K. In Mg single crystals, basal $< a >$ slip is known as the most favored deformation mode from very low to elevated temperatures (Burke and Hibbard, 1952; Asada and Yoshinaga, 1959; Basinski, 1960; Yoshinaga and Horiuchi, 1962; Sharp *et al.*, 1965; Hirsch and Lally, 1965; Bhattacharya, 2006; Bhattacharya and Niewczas, 2011; Sułkowski *et al.*, 2011; Sułkowski and Mikułowski, 2012). However, the activation of non-basal slip systems and deformation twins were reported in Mg single crystals

with low-index orientations of the tensile axis even at 295K, where the Schmid factor for the basal slip systems is zero. In particular, the literature reports the activation of 2^{nd} order pyramidal $< c+a >$: $\{11\bar{2}2\} < \bar{1}\bar{1}23 >$ slip system in the c-axis compression (Stohr and Poirier, 1972; Obara *et al.*, 1973; Syed *et al.*, 2012) and in the a-axis tension (Ando *et al.*, 1992); prism $< a >$: $\{10\bar{1}0\} < 1\bar{2}10 >$ slip system (Yoshinaga and Horiuchi, 1963b); $\{10\bar{1}2\} < 10\bar{1}1 >$ twinning in the c-axis tension; and twinning on $\{10\bar{1}1\}$, $\{10\bar{1}3\}$ and $\{30\bar{3}4\}$ planes and $\{10\bar{1}1\}$-$\{10\bar{1}2\}$ double twinning in the late stage of deformation of the c-axis compression tests (Stohr and Poirier, 1972; Obara *et al.*, 1973; Syed *et al.*, 2012).

Thus, the results suggest that it is possible to determine the strength of dislocation interactions between two interacting slip or twinning systems including collinear and non-coplanar systems, by well-designed experiments on Mg single crystals, where the interactions between slip and twinning systems can be realized during uniaxial tensile tests of specific orientation single crystals. However, in reality, the HCP structure is characterized by highly anisotropic mechanical properties and the ease of the activation of basal $< a >$ slip have made it difficult to measure the strength of interactions between forest systems. Stofel and Wood (1967) attempted to determine the dependence of the flow stress on a basal slip system as a function of the final flow stress on the second pyramidal planes in Zn single crystals. The experimental results were however inconsistent with experimental data for latent hardening on forest systems in FCC crystals and have been considered rather doubtful.

Due to these experimental difficulties, practically no data is available in the literature concerning latent hardening effects in HCP crystals except a few reliable results on the coplanar interactions between two basal slip systems by means of combined pure shear tests in Zn single crystals (Edwards *et al.*, 1953; Edwards and Washburn, 1954; Phillips, 1961), Cd (Edwards *et al.*, 1953) and Mg (Phillips, 1961)and plane-strain compression tests of Mg and Mg alloys (Wonsiewicz and Backofen, 1967; Kelly and Hosford, 1968b). The single crystal samples cut from the sheet were deformed in one of the slip directions in the primary plane and then, shear deformation was continued in other slip directions at 60°, 120° and 180° with respect to the shear direction of the primary deformation. Fig. 2.29 shows that LHRs increase up to 1.24 when shear direction changes to 60° and 120° in the secondary shear test. On the other hand, LHRs are lower than 1.0, when the shear direction changes to 180°, i.e. the crystals shows softening response in the fully reversed shear direction.

Phillips (1961) reported the primary stress (strain) dependence of latent hardening in Mg single crystals. Fig. 2.30 shows increase in shear stress as a result of shifting shear direction to the new direction. Unlike the LHRs behaviour in FCC crystals, the LHRs on coplanar systems are linearly proportional to the primary shear strain.

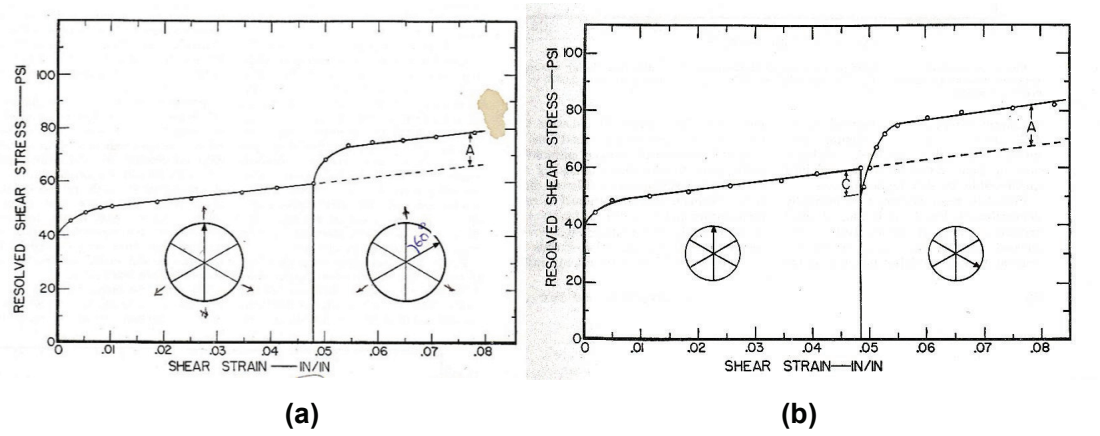

Figure 2.29: Latent hardening characteristics for coplanar slip systems in Mg single crystals obtained from combined pure shear type experiments: (a) represents BI/BII interactions and (b) represents BI/BIII coplanar interactions (Phillips, 1961).

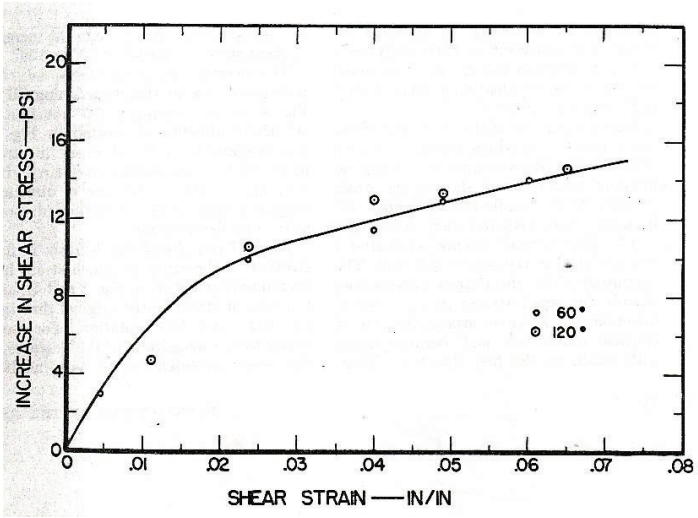

Figure 2.30: Increase in shear stress in Mg as a result of shifting shear direction to the new direction marked on the graph (Phillips, 1961).

Latent hardening experiments have been carried out also by means of plane-strain compression test on Mg and Mg alloy single crystals by Wonsiewicz and Backofen (1967) and Kelly and Hosford (1968b). The authors attempted to measure latent hardening parameters among different interacting systems. Table 2.4 shows experimental conditions including compression direction, direction of forbidden flow and the crystallographic direction of the plastic flow together with the activated slip systems observed in the plane-strain compressive deformation (Kelly and Hosford, 1968b).

Table 2.4: Plane-strain compression tests carried out on Mg single crystal by Kelly and Hosford (1968b) showing the activated systems during the plane-strain compressive deformation. The crystallographic directions of the load axis, forbidden flow direction and extrusion direction are given in the table.

#	Comp. direction	Constraint direction	Elong. direction	Active systems				
				basal	prism	py.	$10\bar{1}2$ T.	$10\bar{1}1$ T.
A	$< 0001 >$	$< 10\bar{1}1 >$	$< 1\bar{2}10 >$	x	x	$\surd$	x	$\surd$
B	$< 0001 >$	$< 1\bar{2}10 >$	$< 10\bar{1}0 >$	x	x	$\surd$	x	$\surd$
C	$< 10\bar{1}0 >$	$< 0001 >$	$< 1\bar{2}10 >$	x	$\surd$	$\surd$	x	x
D	$< 1\bar{2}10 >$	$< 0001 >$	$< 10\bar{1}0 >$	x	$\surd$	$\surd$	x	x
E	$< 10\bar{1}0 >$	$< 1\bar{2}10 >$	$< 0001 >$	x	$\surd$	$\surd$	$\surd$	$\surd$
F	$< 1\bar{2}10 >$	$< 10\bar{1}0 >$	$< 0001 >$	x	$\surd$	$\surd$	$\surd$	$\surd$
G	$< 1\bar{2}12 >$	$< 10\bar{1}0 >$	$< 11\bar{2}2 >$	$\surd$	$\surd$	$\surd$	$\surd$	$\surd$

$*$ Comp. direction represents the crystallographic direction of the applied compressive load. Elong. direction represents the direction of the plastic flow of the single crystal. Constraint directions represents the crystallographic direction of the forbidden flow for single crystal. py. and T. represent pyramidal and Twin modes respectively.

Graff *et al.* (2007) derived the constitutive law for modelling the plastic flow of Mg and Mg alloys, based on Kelly and Hosford (1968b) results with the latent hardening parameters, $q_{\alpha\beta}$ given in Table 2.5. Fig. 2.31(a) shows the experimental results of channel die test of Mg single crystal by Kelly and Hosford (1968b). Fig. 2.31 (b) reveals that the simulation results matched the experimental results quite well.

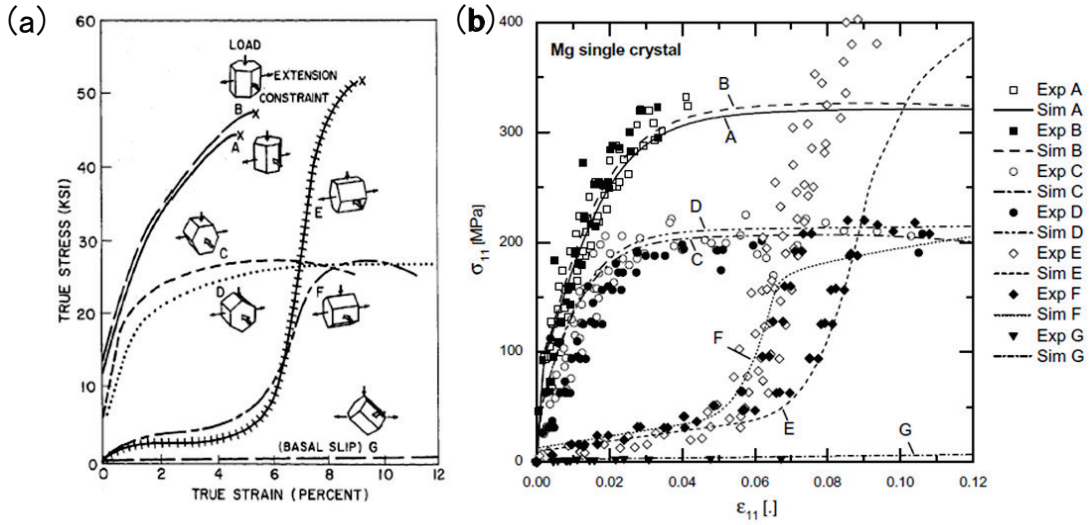

Figure 2.31: (a) True stress-true strain curves of Mg single crystals deformed in plane-strain compression at 295K (Kelly and Hosford, 1968b) and (b) the corresponding simulation results by Graff *et al.* (2007).

Although there have been much research efforts directed to develop various crystal plasticity models for HCP materials, there is still a lack of fundamental understanding of the role of various slip and twinning modes in determining the plastic flow behaviour of HCP materials. The important aspect of it is the understanding of the nature of the interactions between different slip and twinning systems and their effect on the strength and ductility. This work provides an experimental data that helps to gain

Table 2.5: Latent hardening parameters, $q_{\alpha\beta}$ calibrate using experimental data (Kelly and Hosford, 1968a,b).

α	β			
	Basal $< a >$	Prismatic $< a >$	Pyramidal $< c+a >$	Tensile twinning
Basal $< a >$	0.2	0.5	0.5	0.5
Prismatic $< a >$	0.2	0.2	0.2	0.5
Pyramidal $< c+a >$	1.0	1.0	0.2	0.25
Tensile twinning	1.0	1.0	0.2	0.25

insight into dislocation interaction processes in Mg and can be used in developing better models of the plastic flow of HCP materials.

Chapter 3

Research Objectives and Justification

In HCP materials slip and twinning modes operate simultaneously during deformation and the interactions between different slip and twinning dislocations determine the behaviour of HCP materials during plastic flow. Understanding the role of these interactions in the work hardening process is important from both fundamental and practical point of view.

The objective of the present work is to study plastic deformation and work hardening behaviour of Mg single crystals with different crystallographic orientation at room temperature to understand the relationship between the mechanical properties and the mechanism of plastic flow and the role of different modes in strength and ductility of these materials. Four different orientations of single crystals (basal $< a >$ slip, 2^{nd} order pyramidal $< c + a >$ slip, $\{10\bar{1}2\} < 10\bar{1}1 >$ twin orientations) were selected in this study. To obtain an insight into the effect of interactions between

different deformation modes on the plastic flow and the work hardening, the Jackson-Basinski type latent hardening experiments were carried out under the conditions of: (i) basal $< a >$ slip/basal $< a >$ slip, (ii) basal $< a >$ slip/$\{10\bar{1}2\} < 10\bar{1}1 >$ twin, (iii) $\{10\bar{1}2\} < 10\bar{1}1 >$ twin/basal $< a >$ slip dislocations and (iv) basal $< a >$ slip/2^{nd} order pyramidal $< c+a >$ slip dislocations interactions in Mg single crystals at room temperature. The results of these studies provide a framework for the discussion of the latent hardening effects on the plastic flow in single and polycrystalline Mg and provide a quantitative values for hardening parameters that can be used in the crystal plasticity models. SEM/EBSD analysis and indentation measurements were carried out to observe $\{10\bar{1}2\} < 10\bar{1}1 >$ twin evolutions with plastic deformation and evaluate the strength of the matrix and the $\{10\bar{1}2\} < 10\bar{1}1 >$ twin regions in deformed Mg single crystals.

Chapter 4

Experimental Procedures

4.1 Growth of Mg single crystals and sample preparation

High purity 99.995% Mg single crystals were produced by modified Bridgeman technique. The crystals were grown using a split mold made of high purity graphite coated uniformly with boron nitride. Thin boron nitride layer on the mold surface prevents reaction of liquid Mg with the mold surface. Fig. 4.1 shows picture and schematic illustration of the graphite mold. Single crystal nucleus with known orientation was placed at the bottom of the mold and was used to grow a predetermined orientation of the crystals for the experiments. The dimension of nucleus was $3 \times 3 \times 20mm^3$. High purity Mg ingot obtained from Timminco Metals (Ontario, Canada) was placed at the top part of the mold.

Figure 4.1: Picture of the grown Mg single crystal and schematic illustration of the graphite mold used for the crystal growth.

Fig. 4.2 shows pictures of the crystal growth system consisting of a vertical furnace with platinum heating coil, rotary and diffusion vacuum pumps, a thermal controller, an argon gas cylinder and an alumina tube. The temperature in the furnace was controlled by K type thermocouples and the whole heating and cooling cycles of the furnace was controlled by 2416 programmable temperature and process controller (Eurotherm). The system is equipped with a copper stage, the height of which can be adjusted vertically with a screw driven device. The carbon mold was mounted on the height adjustable copper stage and was placed inside a high purity alumina tube. The temperature profile of the furnace was recorded by thermocouples placed in between the inside wall of the furnace and the alumina tube. The height of carbon mold was adjusted to ensure that the middle-height of the nucleus was at 933K, the melting point of Mg. Water-cooling system was used for cooling various elements of the system such as the diffusion pump during heating. The amount of water flowing

in the system can be controlled by a valve attached to the water line.

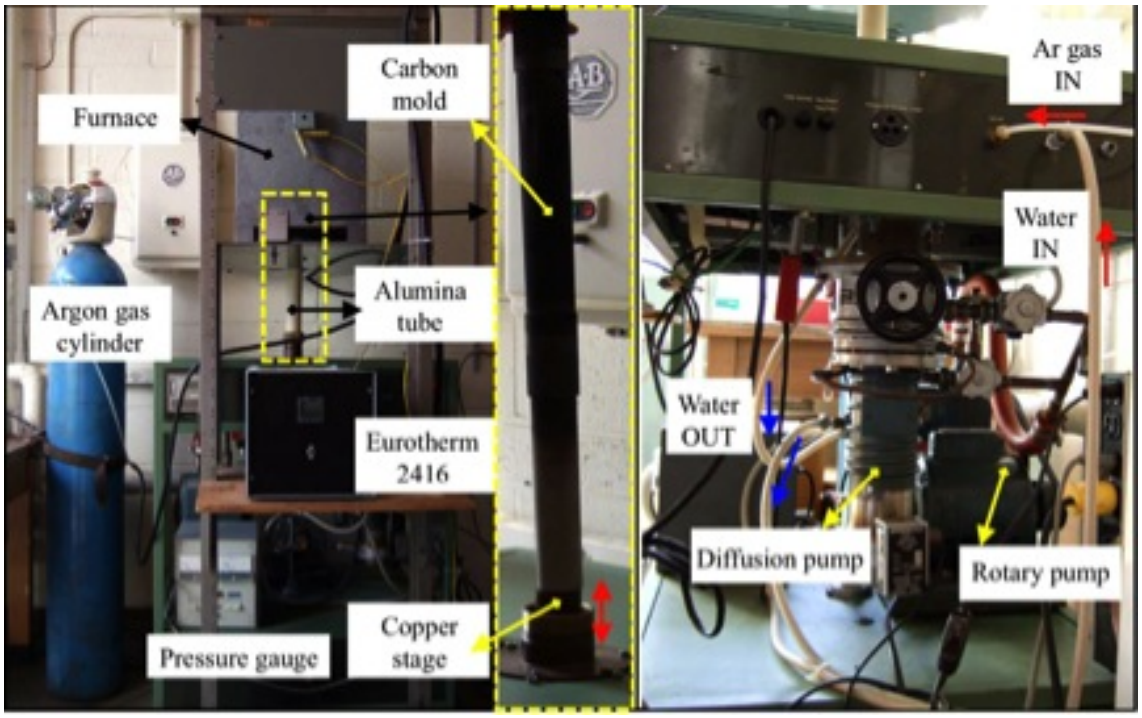

Figure 4.2: Furnace along with the crystal growth unit used for growing Mg single crystals.

Before heating the furnace, the alumina tube was evacuated to a pressure of 10^{-6} torr using rotary and diffusion pumps. The furnace was switched on and the system was heated to 717K at the rate of 1.5K/min and kept at this temperature for 30min. Then, the diffusion pump was switched off and a high purity argon gas was flown into the chamber till the pressure of the system reached 0.5-0.7 atmosphere. The system was heated to 1070K at the rate of 3K/min and maintained at this temperature for 80min. Following this, the system was cooled to 773K at the rate of 0.3K/min and then cooled to room temperature with the natural furnace cooling rate. The

program for heating and cooling cycles with 2416 programmable temperature and process controller (Eurotherm) is shown in Table 4.1.

Table 4.1: Program for heating and cooling cycles with 2416 programmable temperature and process controller (Eurotherm).

Segment	Program	Comments
No.1	Type rmp.r tGt 444°C Rate 1.5°C/min	Heating to 717K at the rate of 1.5K/min.
No.2	Type dwell due 30.0min	Keep 717K during 30min. † Stop diffusion pump and flow in Ar gas in the end of this stage.
No.3	Type rmp.r tGt 797°C Rate 3.0°C/min	Heating to 1070K at the rate of 3.0K/min.
No.4	Type dwell due 80.0min	Keep 1070K during 80min. † Stop rotary pump in the end of this stage.
No.5	Type rmp.r tGt 500°C Rate 0.3°C/min	Cooling to 773K at the rate of 0.3K/min.
No.6	Type tmp.r tGt 20°C	Cooling to 20°C.
No.7	Type END	END one cycle.

One large single crystal of dimensions $3 \times 26 \times 120 - 150 mm^3$ was produced per one cycle. Fig. 4.3 shows schematic illustration of a grown Mg single crystal, where marks 1, 2, and 3 indicate tensile axis face normal, wide face normal, and side face normal, respectively. The orientations of the parent crystals were determined by X-ray back refection Laüe technique. X-rays were generated by Philips PW1729 X-ray generator

with 40kV voltage at 30mA current. Laüe patterns were taken from three parts on the wide side of the parent crystal, 3cm apart, and then the patterns were matched with each other to evaluate the missorientations that could develop within one long crystal. The crystals whose misorientations among three Laüe patterns were less than 2° were selected for the experiments. The Laüe patterns from parent crystals were indexed using OrientExpress 3.4 and stereographic projections indicating the initial orientations of parent crystals were made with OrientExpress 3.4 and WinWulff 1.1.0 softwares.

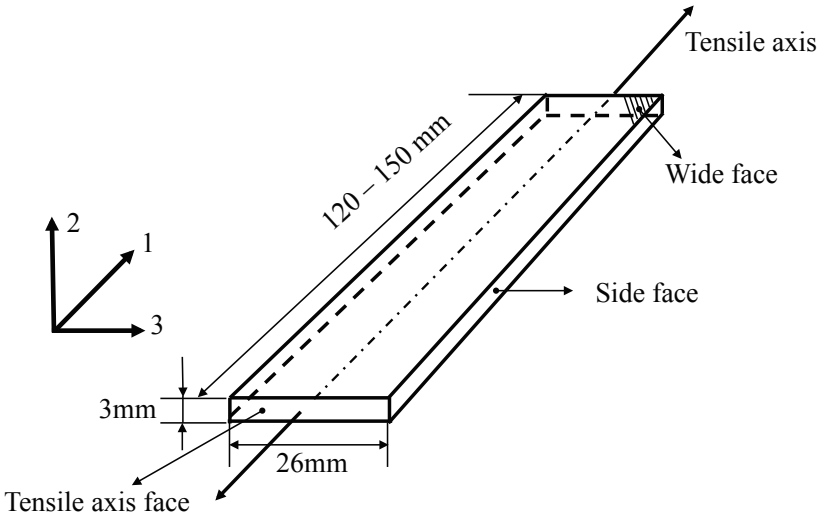

Figure 4.3: Schematic illustration of a Mg crystal with relevant dimensions. 1, 2, and 3 coordinate system marked on the graph show directions of the tensile axis, wide face and side face normal, respectively.

To remove any internal stresses generated during growing and handling, all parent crystals were chemically etched with 10% nitric acid and then annealed in a vacuum of $1.0x10^{-3}$ Pa for 72hrs at 623K. Annealed crystals were cooled very slowly over 12hrs to

room temperature. All the heating and cooling cycles during annealing the crystals were automatically controlled by TEMPSTARTM (Thermo Electric Instruments). The program with TEMPSTARTM is shown in Table 4.2.

Table 4.2: Program for heating and cooling cycles with TEMPSTAR.

Segment	Programs	Comments
Set point 0	373K	Heating to 373K.
Time 1	3h	Heating to 623K at
Set point 1	623K	the rate of 83K/h.
Time 2	72h	Keep 623K
Set point 2	623K	during 72h.
Time 3	12h	Cooling to 295K (R.T.)
Set point 3	295K	at the rate of 27.5K/h.
Time 4	0	END one cycle.

Mirror surfaces of single crystals were prepared by electropolishing just before mounting it to an Instron machine for deformation experiments. The solution of diluted nitric acid (∼10-15%) in water was used for electropolishing. The conditions of electropolishing were selected empirically after performing several electro-polishing with Mg samples, where voltage, temperature and electrolyte concentration were varied to get the best conditions of electropolishing. Selection of electropolishing voltage was crucial for Mg, use of higher voltage leads to formation of pits on the surface. On the other hand, too low voltage would etch the sample. The electrolyte was constantly stirred with a glass rod to avoid formation of bubbles on the surface of the sample, which could lead to the formation of uneven surface or in some cases

micro voids. The samples after polishing were quickly cleaned with methanol and dried to avoid formation of oxide layer on the surfaces.

Samples were spark-cut, ∼1mm/h, by electron spark cutting machine, using 30μm molybdenum wire. The surface layer exposed to the spark operation was removed by mechanical and chemical polishing (orthophosphoric acid).

4.2 Deformation tests

All the crystals used in current studies were deformed in tension or in compression at 295K by the Instron deformation test machine. The strain rate was $10^{-4}s^{-1}$. Fig. 4.4 and Fig. 4.5 show photographs of tensile and compression test setup. Special jigs to hold the samples were used in both tension and compression tests. In compression tests, boron nitride powder was spread on the friction surface as lubricant.

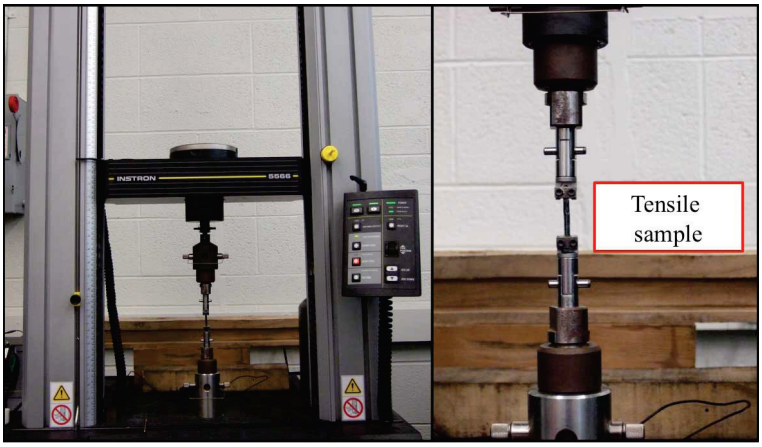

Figure 4.4: Experimental setup for tensile deformation tests.

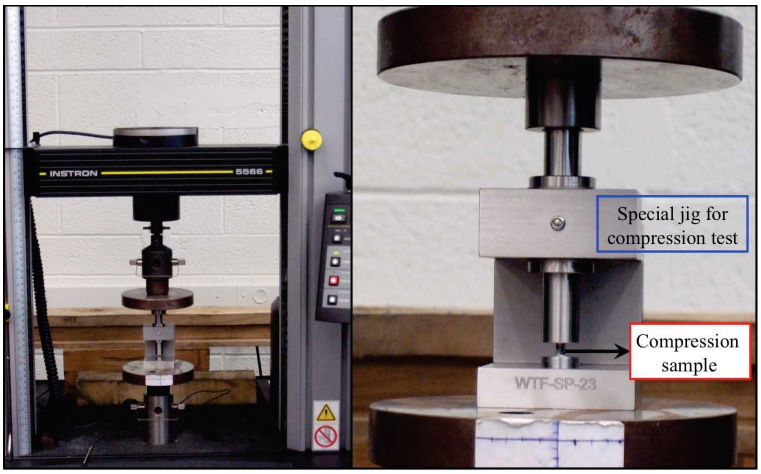

Figure 4.5: Experimental setup for compressive deformation tests.

Mechanical behaviour of Mg single crystals were evaluated by means of (i) true stress-true strain, (ii) work hardening-true stress, (iii) resolved shear stress-shear strain, (iv) work hardening-shear strain, and (v) work hardening-shear stress relations. Engineering stress, σ_0, engineering strain, ϵ_0, true stress, σ, and true strain, ϵ are given by:

$$\sigma_0 = \frac{F}{A_0} \tag{4.1}$$

$$\epsilon_0 = \frac{\Delta l}{l_0} \tag{4.2}$$

$$\sigma = \frac{F}{A} \tag{4.3}$$

$$\epsilon = \ln\left(\frac{l}{l_0}\right) \tag{4.4}$$

where F is the measured load, A_0 is the initial cross-sectional area of the specimen, A is the instantaneous cross-sectional area of the specimen, l_0 is the initial specimen length, and l is the instantaneous specimen length.

The resolved shear stress and resolved shear strain curve was computed from raw data, assuming the rotation of the tensile axis and taking into account the reduction of cross-sectional area with strain. The resolved shear stress, τ and the resolved shear strain, γ were calculated from the geometrical relation shown in Fig. 4.6:

$$\tau = \frac{F\cos\phi_0}{A_0}\left\{1-\left(\frac{l_0}{l}\right)^2\sin^2\lambda_0\right\}^{\frac{1}{2}} \tag{4.5}$$

$$\gamma = \frac{\cos\lambda}{\cos\phi} - \frac{\cos\lambda_0}{\cos\phi_0} \tag{4.6}$$

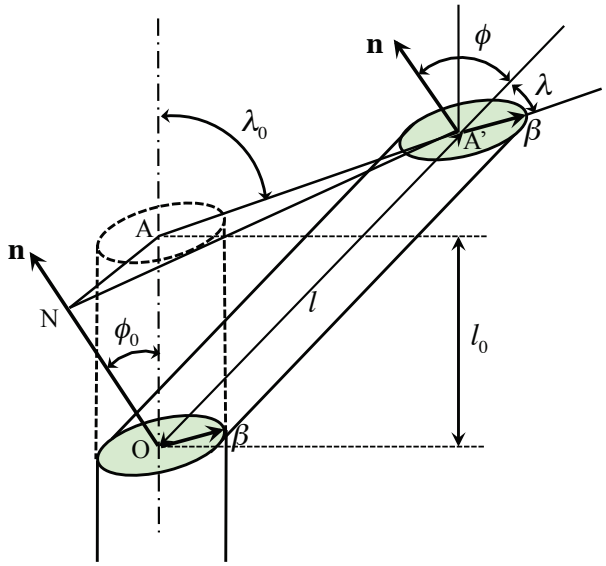

Figure 4.6: Schematic illustration of extension of a single crystal under conditions of a single slip (Kelly *et al.*, 2000).

For compression tests, the resolved shear stress, τ and the resolved shear strain, γ were calculated from the following equations:

$$\tau = \frac{F}{A_0}\left(\frac{h}{h_0}\right)\cos\lambda_0\left\{1-\left(\frac{h}{h_0}\right)^2\sin^2\phi_0\right\}^{\frac{1}{2}} \tag{4.7}$$

$$\gamma = \frac{\cos\phi}{\cos\lambda} - \frac{\cos\phi_0}{\cos\lambda_0} \tag{4.8}$$

4.3 Intermittent deformation/annealing cycle experiments

Intermittent deformation/annealing cycle experiments were carried out on the Mg single crystals oriented initially for basal slip. The tensile axis of the specimens was paralleled to $[2\bar{1}\bar{1}2]$ direction, as shown in Fig. 4.7. These experiments were done by deforming the specimen in tension at 295K to a given stress level, unloading and resting (annealing) it for 0 and 24 hours at 295K and then continuing tensile deformation to the next stress level. The deformation and annealing cycles were repeated several times until the specimen reached the fracture. All uniaxial tensile deformation tests were carried out at 295K in an Instron tensile testing machine, with the strain rate of $1.0 \times 10^{-4}s^{-1}$.

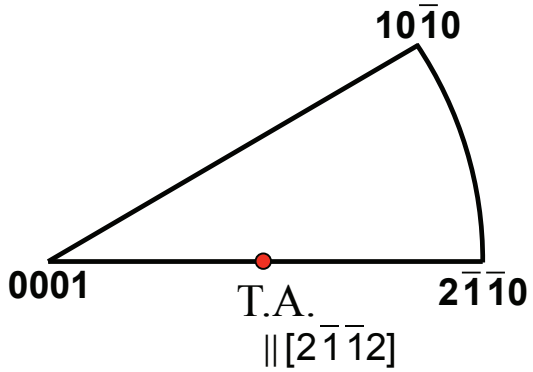

Figure 4.7: Initial orientation of the Mg single crystals under in the intermittent deformation/annealing cycle experiments.

4.4 Surface observations

The slip bands and twinning surface patterns formed on the surfaces of parent crystals and secondary samples during deformation were observed with an optical microscopy with interferential Normarski contrast and Philips SEM515 scanning electron microscopy, operating at 20 kV.

4.5 SEM/EBSD analysis

In order to identify crystallographic nature of twins formed in the single crystals and to measure the orientation of the crystal samples after deformation, deformed single crystals were analyzed by SEM/EBSD technique. A scanning electron microscope LEO, 1455 SEM and Carl ZEISS, NVision40 Crossbeam Workstation equipped with field emission gun and OIM Data collection were used. The surface of the sample was

chemically polished with a solution containing: 60ml of ethanol, 15ml acetic acid, 5ml nitric acid and 20ml of distilled water, for about 10-15 seconds. After the chemical polishing the samples were quickly cleaned in pure ethanol and dried with an air blower. The orientation maps were recorded with a beam step of 0.10-0.20μm. OIM analysis software 5.3 (EDAX-TSL) was used to analyze EBSD results.

Recent developments of SEM/EBSD technique allows not only analysis of the texture but also allows to identify crystallographic nature of deformation twinning based on the determination of a micro-scale orientation of a specimen. There exists well-known crystallographic relationship between matrix and twin regions. $\{10\bar{1}2\} < 10\bar{1}1 >$ twin is associated with the rotation of the c-axis by 86° around $< 2\bar{1}\bar{1}0 >$ axis. $\{10\bar{1}1\} < 10\bar{1}2 >$ twin accompanies the rotation of the c-axis by 56° around $< 2\bar{1}\bar{1}0 >$ axis. The $\{10\bar{1}1\}$-$\{10\bar{1}2\}$ and $\{10\bar{1}3\}$-$\{10\bar{1}2\}$double twin are associated with the rotation of the c-axis by 38° and 22° about $< 2\bar{1}\bar{1}0 >$ axis, respectively. In addition, Fig. 4.8 shows the crystallographic orientation relationship of three pairs of $\{10\bar{1}2\} < 10\bar{1}1 >$ twin planes in HCP metals. This geometrical relations are also determined by EBSD technique. All the geometrical relationships between matrix and various types of twins in Mg are summarized in Table 4.3.

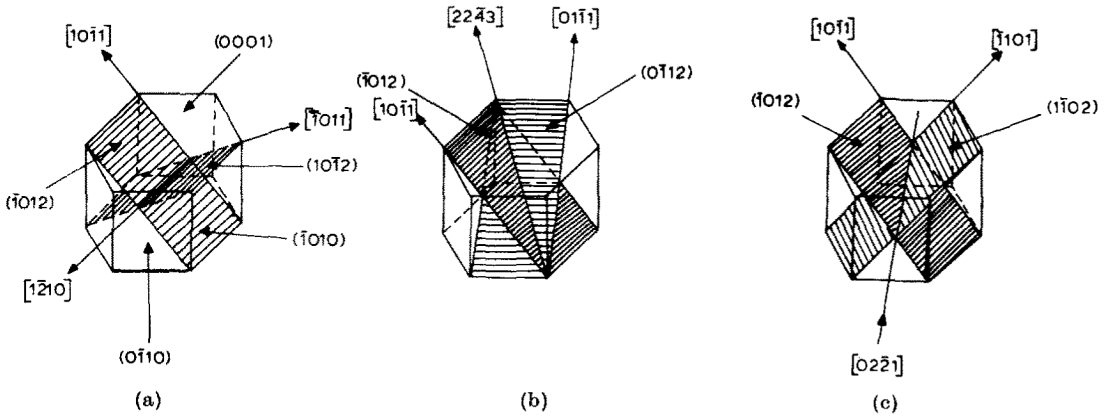

Figure 4.8: The orientation relationship of three pairs of $\{10\bar{1}2\} < 10\bar{1}1 >$ twin planes in HCP metals (Roberts and Partridge, 1966).

Table 4.3: Geometrical factors of twinning in Mg.

Twin type	Crystallographic notation	Rotation axis	Misorientation
Single	$\{10\bar{1}2\} < 10\bar{1}1 >$	$<2\bar{1}\bar{1}0>$	86°
Single	$\{10\bar{1}1\}<10\bar{1}2>$	$<2\bar{1}\bar{1}0>$	56°
Double	$\{10\bar{1}1\}$-$\{10\bar{1}2\}$	$<2\bar{1}\bar{1}0>$	38°
Double	$\{10\bar{1}3\}$-$\{10\bar{1}2\}$	$<2\bar{1}\bar{1}0>$	22°
-	$(10\bar{1}2)$-$(\bar{1}012)$	$<1\bar{2}10>$	7.4°
-	$(10\bar{1}2)$-$(01\bar{1}2)$	$<10\bar{1}0>$	60.0°†
-	$(10\bar{1}2)$-$(0\bar{1}12)$	$<8\bar{1}\bar{7}0>$	60.4°††

† Actual axis is 3.7° off $<10\bar{1}0>$, †† Actual axis is 0.2° off $<8\bar{1}\bar{7}0>$.

4.6 Indentation tests

4.6.1 Micro-indentation

The term micro-hardness test usually refers to static indentations made with loads not exceeding $1kgf$. The indenter is either the Vickers diamond pyramid or the Knoop elongated diamond pyramid. The procedure for testing is very similar to that of the standard Vickers hardness test, except that it is done on a microscopic scale with higher precision instruments. The surface being tested generally requires a metallographic finish; the smaller the load used, the higher the surface finish required. Precision microscopes are used to measure the indentations; these usually have a magnification of around X500 and measure to accuracy of $\pm 0.5\mu$m. Also with the same observer, differences of $\pm 0.2\mu$m can usually be resolved. It should, however, be added that considerable care and experience are necessary to obtain this accuracy.

The Vickers Diamond Pyramid harness number is the applied load (kgf) divided by the surface area of the indentation (mm^2):

$$HV = \frac{2F \sin \frac{136^\circ}{2}}{d^2} \approx 1.854 \frac{F}{d^2} \tag{4.9}$$

where F is load (kgf) and d is the arithmetic mean of the two diagonals, $d1$ (mm) and $d2$ (mm). The Vickers Diamond Pyramid indenter is in the form of a squared pyramid with an angle of 136° between faces. The depth of indentation is about 1/7 of the diagonal length. When calculating the Vickers Diamond Pyramid hardness number, both diagonals of the indentation are measured, the mean of these values and the load are used to determine the value of HV by above formula. A more convenient way to look-up HV values is to inspect appropriate Tables.

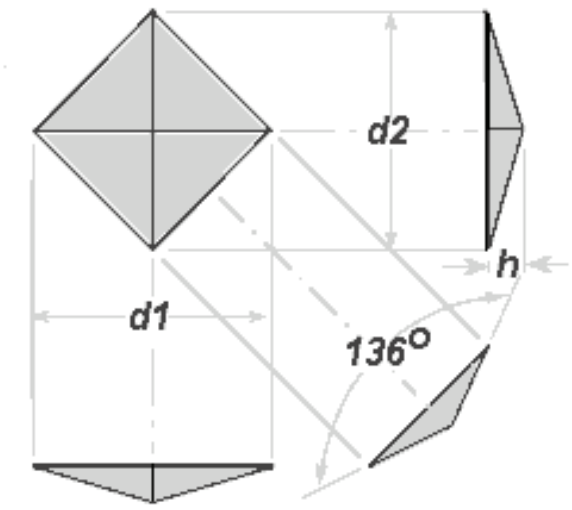

Figure 4.9: Schematic illustration of the geometry of Vickers pyramid diamond indenter.

4.6.2 Nano-indentation

Nano-indentation measurements were carried out on selected single crystals containing matrix and twin regions by a TRIBOINDENTER (HYSITRON Corporation) equipped with a diamond cube corner tip with a tip radius of 50nm. During the nano-indentation measurements, the loading force was increased at a rate of 90N/s to a maximum load of 500N, held for 2 seconds, and then decreased at an unloading rate of 90N/s to 0N/s. 30 measurements in 5×6 rectangular arrays geometry separated by 5μm were carried out at one location, as shown in Fig. 4.10. The indentation curves that deviate from the behaviour of the majority of indentation curves were rejected for the accuracy and reliability of the calibration.

For evaluation the data sets, the Oliver-Pharr method (Oliver and Pharr, 1992,

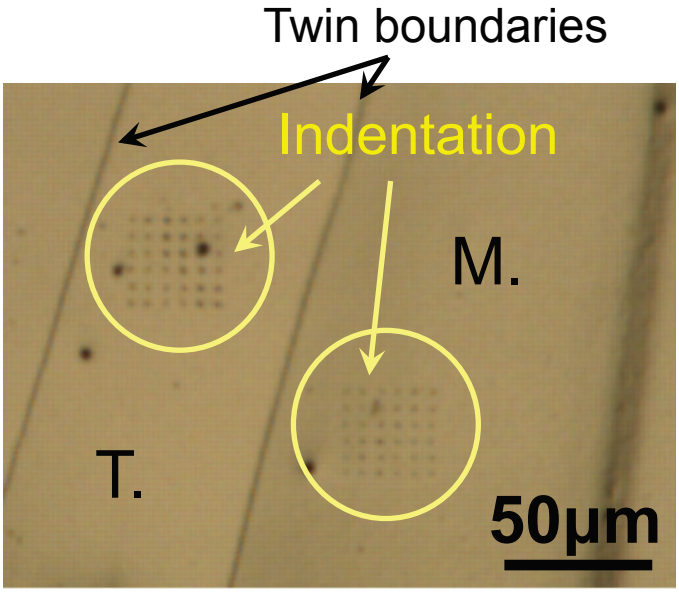

Figure 4.10: Optical microscope (OM) observation at the indentation area.

2004) was used to calculate the hardness of the samples. During an indentation, an indenter probe is driven into a sample and then withdrawn by decreasing the applied force. The applied load P and depth of penetration into the sample h, are continuously monitored. The contact area is determined from a probe area function, $A(h_c)$, where h_c is the contact depth calculated from Eq. (4.10).

$$h_c = h_{max} - \epsilon \frac{P_{max}}{S}. \tag{4.10}$$

To account for edge effects, the deflection of the surface at the contact perimeter is estimated by taking the geometric constant, ϵ as 0.75. Fig. 4.11 illustrates the relationship of P, A, h_c, and h.

The hardness, H is defined as:

$$H = \frac{P_{max}}{A} \tag{4.11}$$

where P is the indentation load and A is the projected contact area of the indenter tip at that load.

The reduced modulus is defined as:

$$E_r = \frac{S\sqrt{\pi}}{2\sqrt{A}} \tag{4.12}$$

where S is the stiffness of the unloading curve and A is the projected contact area. The initial unloading contact stiffness, i.e. the slope of the initial portion of the unloading curve is defined as:

$$S = \frac{dP}{dh} \tag{4.13}$$

Here, the reduced modulus is related to the Young's modulus, E through Eq. (4.14);

$$\frac{1}{E_r} = \left(\frac{1-\nu^2}{E}\right)_{sample} + \left(\frac{1-\nu^2}{E}\right)_{indenter}. \tag{4.14}$$

The diamond indentor probe, $E_{indenter}$ is 1140GPa and the poisson ratio, $\nu_{indenter}$ is 0.07. For pure magnesium, E_{Mg} is 45GPa and ν_{Mg} is 0.29. Rearranging Eq. (4.12) yields

$$A = \frac{\pi}{4}\left(\frac{S}{E_r}\right)^2 \tag{4.15}$$

To determine the area function, a series of indents at various contact depths are performed in a sample of known elastic modulus sample and the contact area, A is calculated from Eq. (4.15). A plot of the calculated area as a function of contact

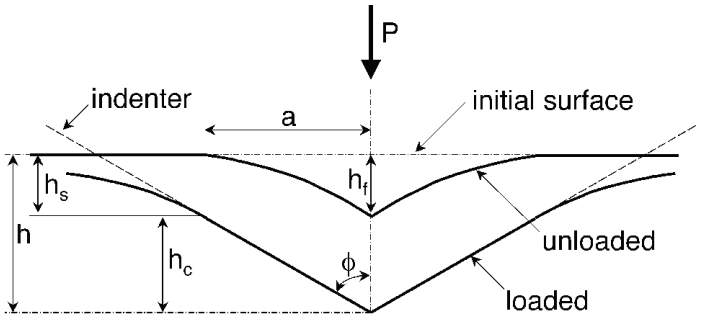

Figure 4.11: Schematic illustration of indentation showing various quantities used in the Oliver-Pharr method (Oliver and Pharr, 1992).

depth is created and the Hysitron software fits the A vs. h_c curve to a sixth order polynomial in Eq. (4.16);

$$A = C_0 h_c^2 + C_1 h_c + C_2 h_c^{1/2} + C_3 h_c^{1/4} + C_4 h_c^{1/8} + C_5 h_c^{1/16}. \tag{4.16}$$

C_0 for an ideal Berkovich probe is 24.5 while a cube corner probe is 2.598 with C_1 through C_5 set equal to 0. To better fit the shape of a real probe, C_1 through C_5 will vary depending on the exact shape of the probe.

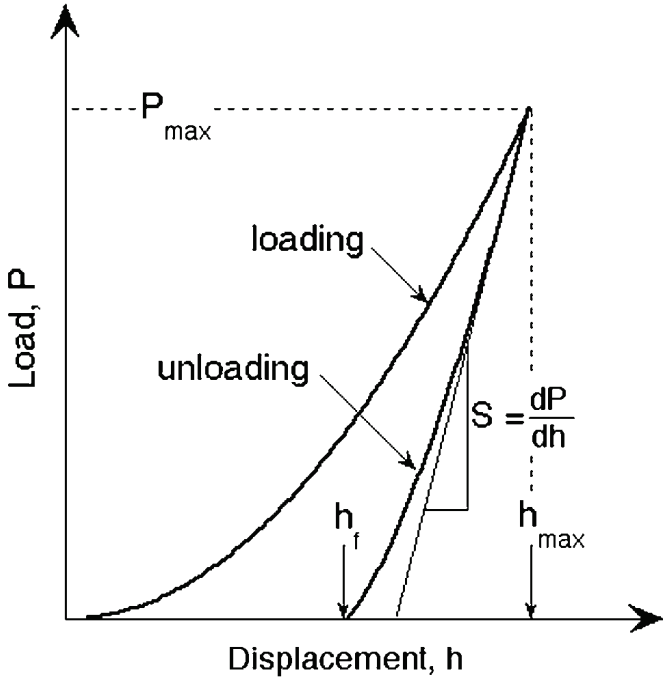

Figure 4.12: Schematic illustration of applied load vs. indenter displacement (Oliver and Pharr, 1992). P_{max}: the peak applied load; h_{max}: the indenter displacement at the peal load; h_f: the final depth of the contact impression after unloading; and S: the initial unloading stiffness.

Chapter 5

Experimental Results

5.1 Notation for slip and twin systems in Mg

At the beginning of this section, the notation for the slip and twin systems activated during deformation is discussed with reference to (0001) stereographic projection shown in Fig.5.1. In this work, we assume that operating slip systems and twin modes are basal $< a >$ slip and $\{10\bar{1}2\} < 10\bar{1}1 >$ twin, respectively. In Mg single crystals, the basal $< a >$ slip is known to be a dominant deformation mode at room temperature, regardless of the crystallographic orientation of single crystals, because of its lowest CRSS among all slip and twinning systems available. The basal $< a >$ slip systems are expressed in terms of the Schmid and Boas notation (Schmid and Boas, 1935), i.e., a combination of slip plane and slip direction. In Fig.5.1, the letter "BI" indicates that the slip occurs on the basal (0001) plane "B" in $[2\bar{1}\bar{1}0]$ direction denoted as "I". Similarly, the letters "BII" and "BIII" represent two other basal $< a >$ slip systems: $(0001)[\bar{1}2\bar{1}0]$ and $(0001)[\bar{1}\bar{1}20]$, respectively. Fig.5.1 shows the (0001) stereographic projection with the Schmid and Boas notation for basal $< a >$

slip systems in Mg single crystals.

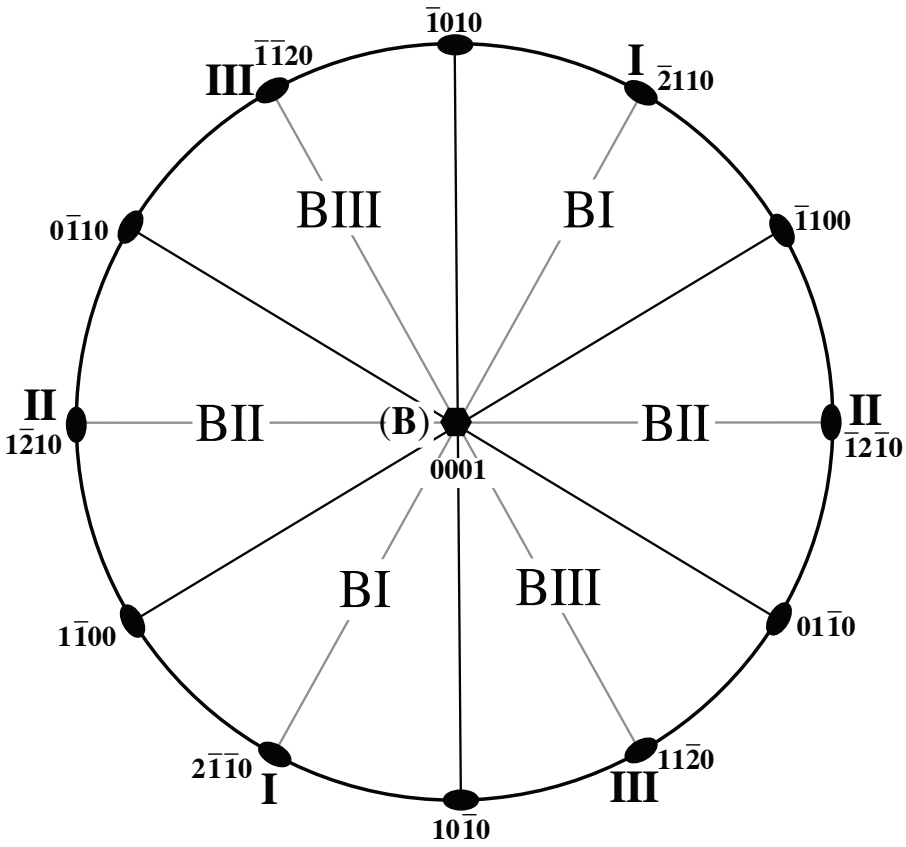

Figure 5.1: Schmid and Boas notation for three basal $< a >$ slip systems in Mg single crystals.

Similar representation for the operating twin modes during deformation is required to systematically evaluate latent hardening characteristics between active slip and twin systems. A new notation for $\{10\bar{1}2\} < 10\bar{1}1 >$ twin systems in HCP crystals is proposed, which involves a combination of twinning planes, A' - F' and twinning directions, 1' - 6'. Here, A'1' represents $(10\bar{1}2)[\bar{1}011]$ twin system, B'2' represents $(01\bar{1}2)[0\bar{1}11]$ twin system, C'3'=$(\bar{1}102)[1\bar{1}01]$, D'4'=$(\bar{1}012)[10\bar{1}1]$, E'5'=$(0\bar{1}12)[01\bar{1}1]$,

and F'6' represents $(1\bar{1}02)[\bar{1}101]$ twin system, respectively. Fig. 5.2 shows the (0001) stereographic projection depicting the Schmid and Boas notation for the twinning systems in HCP crystals where black dots (•) and white dots (○) indicate twinning planes normal and twinning directions, respectively. Note that the relation between the crystallographic plane $(hkil)$ and its normal $[uvtw]$ for hexagonal system is given: $[uvtw]=[hki(l/\lambda^2)]$ or $(hkil)=(uvt(\lambda^2 w))$, where $\lambda^2=2/3(c/a)^2=1.757$ for Mg (see appendix A for other crystallographic relationships in HCP crystal in details). Therefore, $[\bar{1}011]$ direction (depicted 1') lies on the trace of $(10\bar{1}2)$ plane, whereas $(10\bar{1}2)$ plane normal (depicted A') is located on the trance of $(\bar{4}047)$ because $[\bar{1}011]$ direction is perpendicular to $(\bar{1}01(1/1.757))\simeq(\bar{4}047)$ plane, as shown in the figure.

Fig. 5.3 (a) shows contours of the Schmid factors for F'6': $(1\bar{1}02)[\bar{1}101]$ twin system on the stereographic projection. When the tensile axis of the sample is parallel to the c-axis, [0001] direction, the Schmid factor for F'6' system assumes the maximum value of 0.50. As the axis rotates from [0001] pole to the middle of the stereographic projection, the Schmid factor decreases and reaches zero at the traces of $(1\bar{1}02)$ and $(\bar{4}407)$ planes. When the axis rotates further towards neighbourhood of $[\bar{1}100]$, the Schmid factors assume negative values. Positive and negative values of the Schmid factor indicate that the $(1\bar{1}02)[\bar{1}101]$ twin system: F'6' is active under the tensile or compressive deformation, respectively. The domains of the operating $\{10\bar{1}2\} < 10\bar{1}1 >$ twinning systems, A'1' - F'6' under uniaxial tension or compression are represented on the standard stereographic triangle surrounded by $[0001]-[\bar{1}2\bar{1}0]-[\bar{1}100]$ poles (Fig. 5.3 (b)).

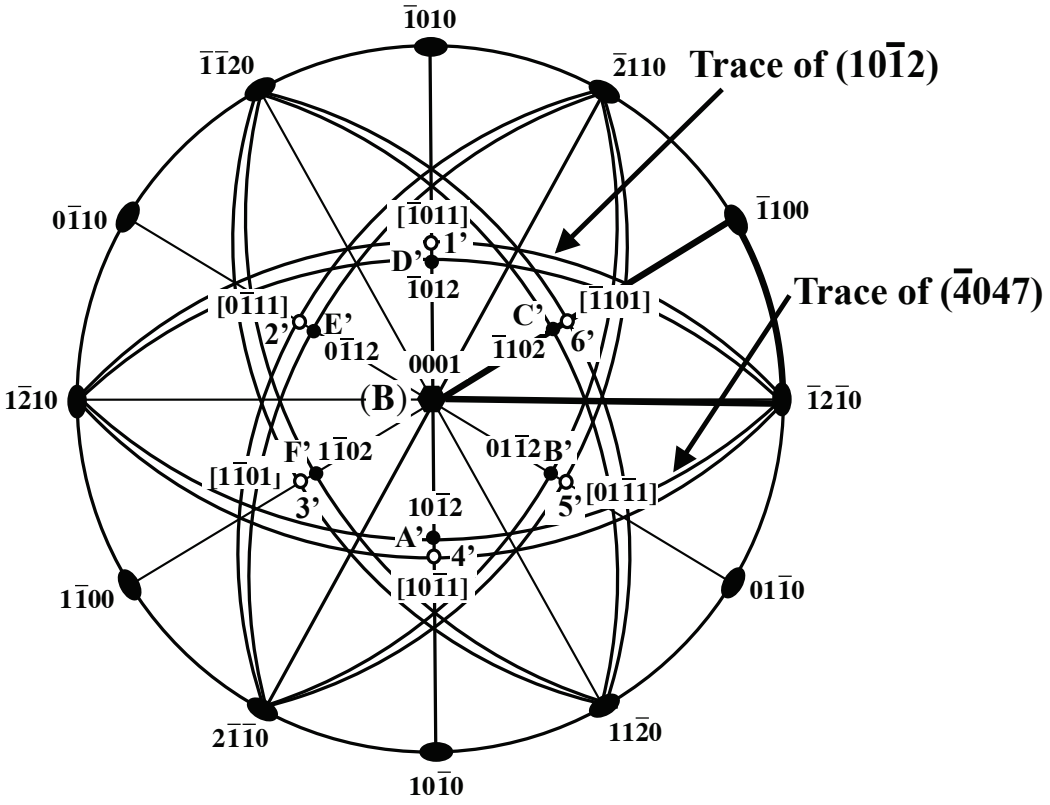

Figure 5.2: Schmid and Boas notation for $\{10\bar{1}2\} < 10\bar{1}1 >$ twin systems with six different variants in Mg single crystals.

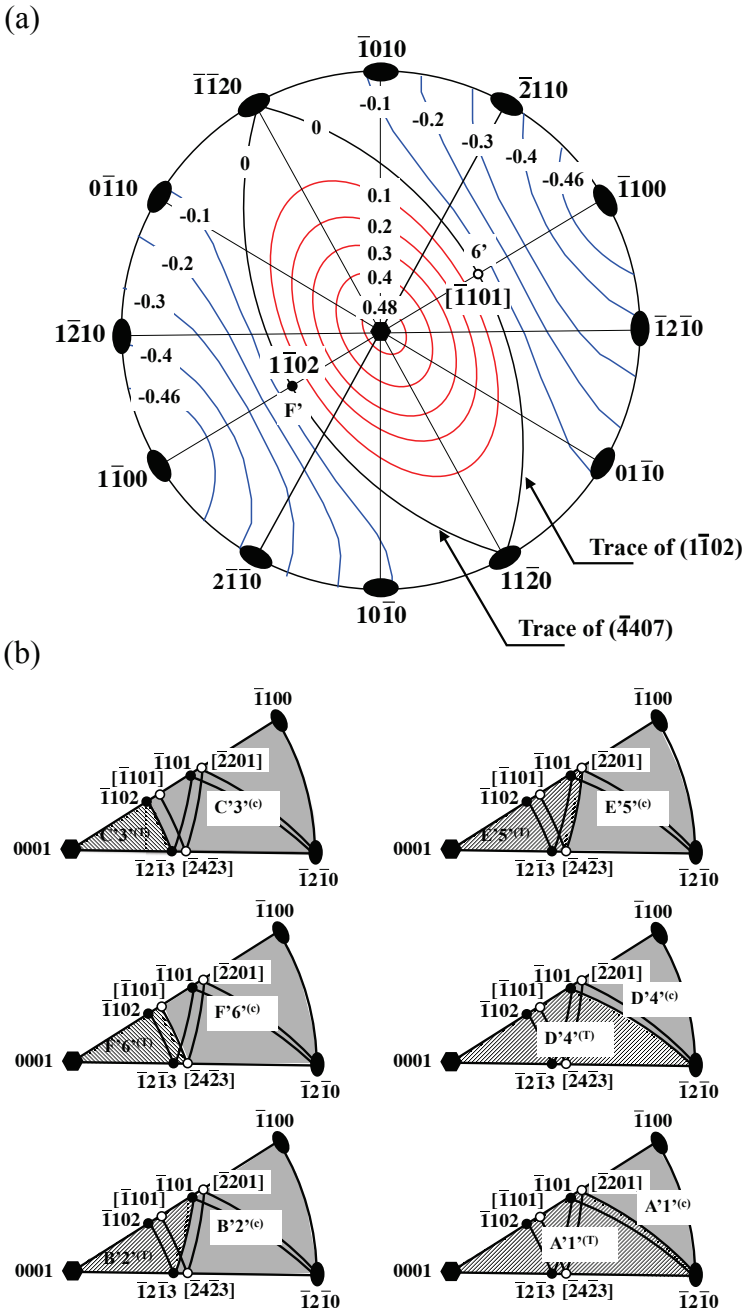

Figure 5.3: (a) Contours of the Schmid factors for F'6': $(1\bar{1}02)[\bar{1}101]$ twin system and (b) standard stereographic triangle indicating orientation dependence of the operative $\{10\bar{1}2\} < 10\bar{1}1 >$ twinning systems under uniaxial tension or compression.

Other slip systems such as, prism $< a >$ slip, 1^{st} order pyramidal $< a >$ slip, 1^{st} order pyramidal $< c + a >$ slip, and 2^{nd} order pyramidal $< c + a >$ slip systems and twin modes such as $\{10\bar{1}1\} < 10\bar{1}2 >$ c-axis compressive twin, have rarely been reported to be active at room temperature deformation of Mg single crystals because of their extremely high values of CRSS, as described in chapter 2. However, above rule does not apply to single crystals with special (low index) orientation of single crystals, such as the c-axis compressive deformation at 295K, where some of these slip and/or twin systems have been observed to be active and contribute to the plastic flow of crystals.

5.2 Work hardening behaviour of Mg single crystals under tension and compression at room temperature

5.2.1 Initial orientations

Figure 5.4 shows orientation of initial tensile and compressive axes of Mg single crystals on the standard stereographic triangle considered in this study. In the figure, contour lines depict the maximum Schmid factor for basal $< a >$ slip systems. Tensile and compressive deformation of Mg single crystals with four different orientations of the axes, labelled as crystals $\#1 - \#4$, have been studied.

For the initial orientation of the tensile and/or compressive axis $[2\bar{1}\bar{1}2]$ of crystal #1, the Schmid factor for basal $< a >$ slip system BI, $(0001)[2\bar{1}\bar{1}0]$, is 0.50 and deformation under both uniaxial tension and compression at room temperature should

proceed in the single basal $< a >$ slip on the BI system.

Crystal #2 represents double coplanar basal $< a >$ slip orientation, with the orientation of the axis $[10\bar{1}(2/\lambda^2)]$[2] and the Schmid factors for basal $< a >$ slip systems BI and BII have the same values, 0.42, as shown in Fig. 5.5.

The initial orientation of crystal #3 predicts deformation in both basal $< a >$ slip systems and $\{10\bar{1}2\} < 10\bar{1}1 >$ twin system, because the Schmid factor for basal $< a >$ slip systems BI and BII is relatively small, 0.19.

The tensile and/or compression axis of crystal #4 is aligned along [0001]. In the c-axis tension, $\{10\bar{1}2\} < 10\bar{1}1 >$ twin mode is the main deformation mode, whereas 2^{nd} order pyramidal $< c + a >$ slip system is favoured deformation mechanism in the c-axis compression.

[2]The relation between the crystallographic plane $(hkil)$ and its normal $[uvtw]$ for hexagonal system is given by: $[uvtw]=[hki(l/\lambda^2)]$ or $(hkil)=(uvt(\lambda^2 w))$, where $\lambda^2=2/3(c/a)^2=1.757$ for Mg. See appendix A for other crystallographic relationships in HCP crystal in details. In this thesis, the tensile axes of all the specimens were represented in terms of the crystal plane index $(hkil)$ and the constant value, λ.

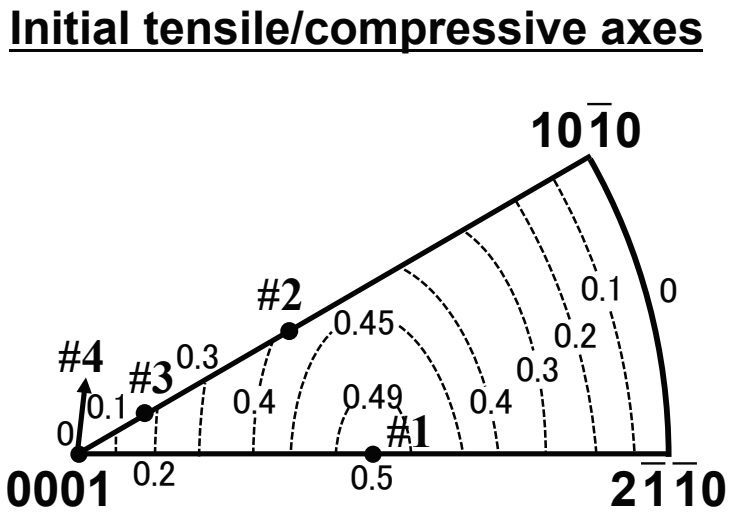

Figure 5.4: Initial tensile and compressive axes of Mg single crystals $\#1 - \#4$ on the standard stereographic triangle.

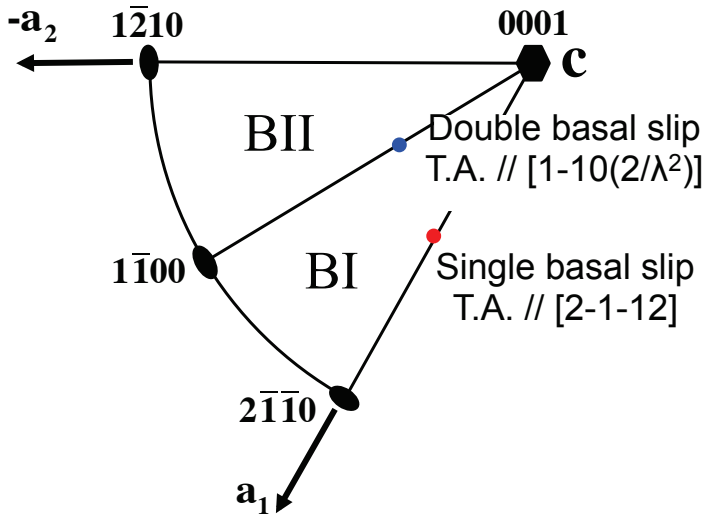

Figure 5.5: A part of standard stereographic projection indicating initial tensile and compression axis for single and double basal $< a >$ slip orientations.

5.2.2 Crystal #1: single basal $< a >$ slip orientation

$[2\bar{1}\bar{1}2]$ tensile deformation

For the tensile axis parallel to $[2\bar{1}\bar{1}2]$, the Schmid factor for BI slip system is 0.50. Figures 5.6 - 5.8 show mechanical properties of Mg single crystals oriented for single basal $< a >$ slip deformed in tension at 295K, which include: (i) resolved shear stress versus resolved shear strain curve $\tau - \gamma$ (Fig.5.6), (ii) work hardening versus resolved shear strain $\theta(= d\tau/d\gamma) - \gamma$ plot (Fig.5.7) and (iii) the normalized with respect to the sheer modulus $\theta/\mu - \tau/\mu$ plot (Fig.5.8), where $\mu = 17$GPa is the shear modulus of Mg. The resolved shear stress and shear strain characteristics were recalculated from raw data, assuming that only single basal $< a >$ slip on the primary BI slip system activates during the plastic deformation. The CRSS for the primary slip system BI was determined by the intersection of the elastic and plastic region of the $\tau - \gamma$ curve and the CRSS value found was 0.70MPa. After the yielding in single basal $< a >$ slip, the plastic flow curve exhibits two stages: easy glide stage (stage I) and rapid hardening stage (stage II). A transition from stage I to stage II occurred gradually and it was difficult to determine a clear transition point. In the present thesis, the transition range was defined by drawing the tangential lines to the stage I and stage II regions and by determining the intersection with the $\tau - \gamma$ curves, as shown in Fig. 5.6 and Fig. 5.7.

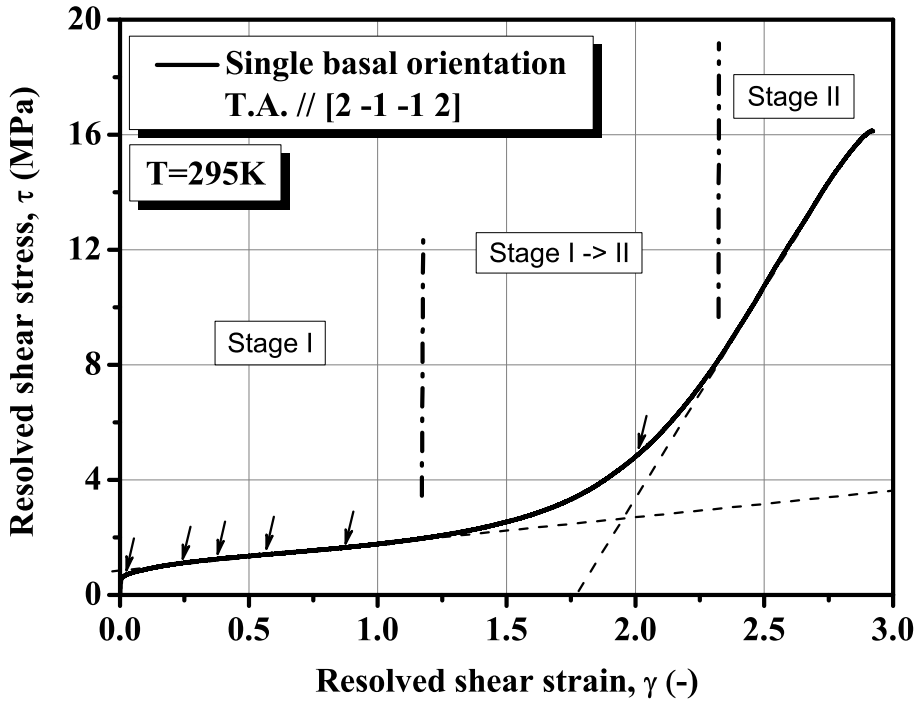

Figure 5.6: Resolved shear stress - shear strain curve of Mg single crystal #1 deformed in tension at 295K.

In Fig. 5.7, the stretch AB represents work hardening of stage I with the almost constant values between $0.60 - 1.50$MPa. The stage I extends until shear strain of ~ 1.2. Then, the work hardening gradually increased by a factor of about 15, identified as the transition region BC in the range of shear strains between $1.2 - 2.3$. The stretch CD represents stage II of work hardening with the value about $14 - 15$MPa. The stage II proceeded until shear strain of $\sim 2.3 - 2.7$.

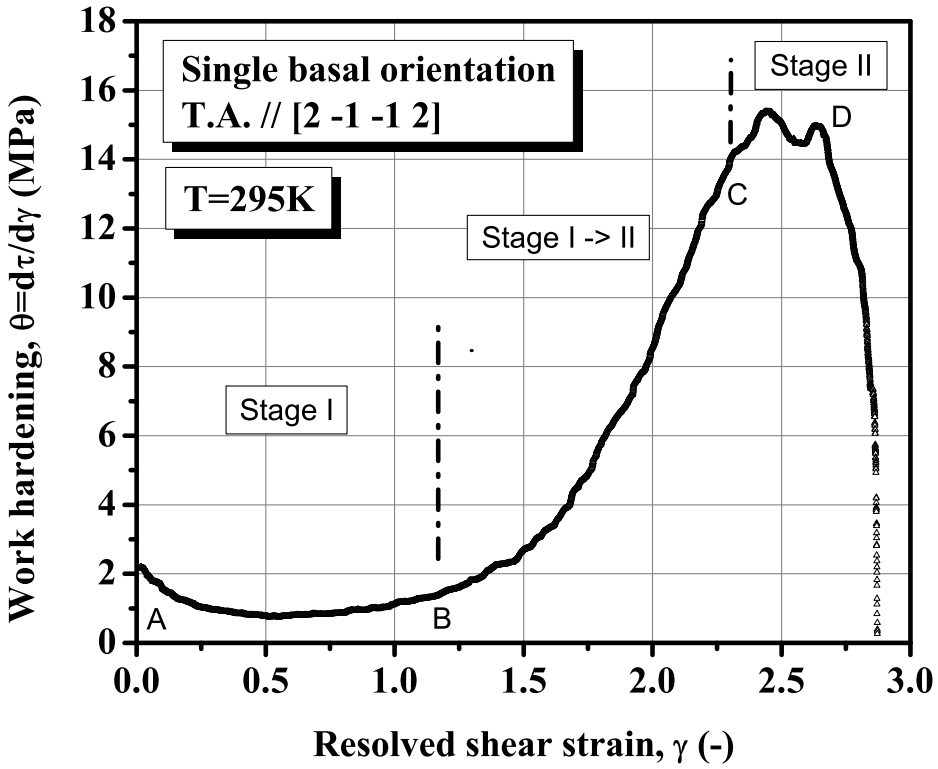

Figure 5.7: Work hardening as a function of shear strain plot for Mg single crystal #1 deformed in tension at 295K.

The work hardening normalized with shear modulus, plotted as a function of normalized shear stress is shown in Fig. 5.8. The rate of work hardening in stage I, θ_I/μ (the stretch A'B') was approximately in the range of $4.70x10^{-5} - 8.30x10^{-5}$. After the initial stage the work hardening increases linearly with the shear stress and approaches θ_{II}/μ values in the range$8.35x10^{-4} - 9.05x10^{-4}$ during stage II defined as the stretch B'C' in the figure. It has been observed that the work hardening during stage II was a factor of $\sim$20 higher than that of stage I. Stage III of work hardening in

FCC singe crystals is characterized by dynamic recovery and have not been observed during tensile deformation of crystal #1. Instead the fracture of the crystal occurred suddenly after the relatively short deformation during stage II.

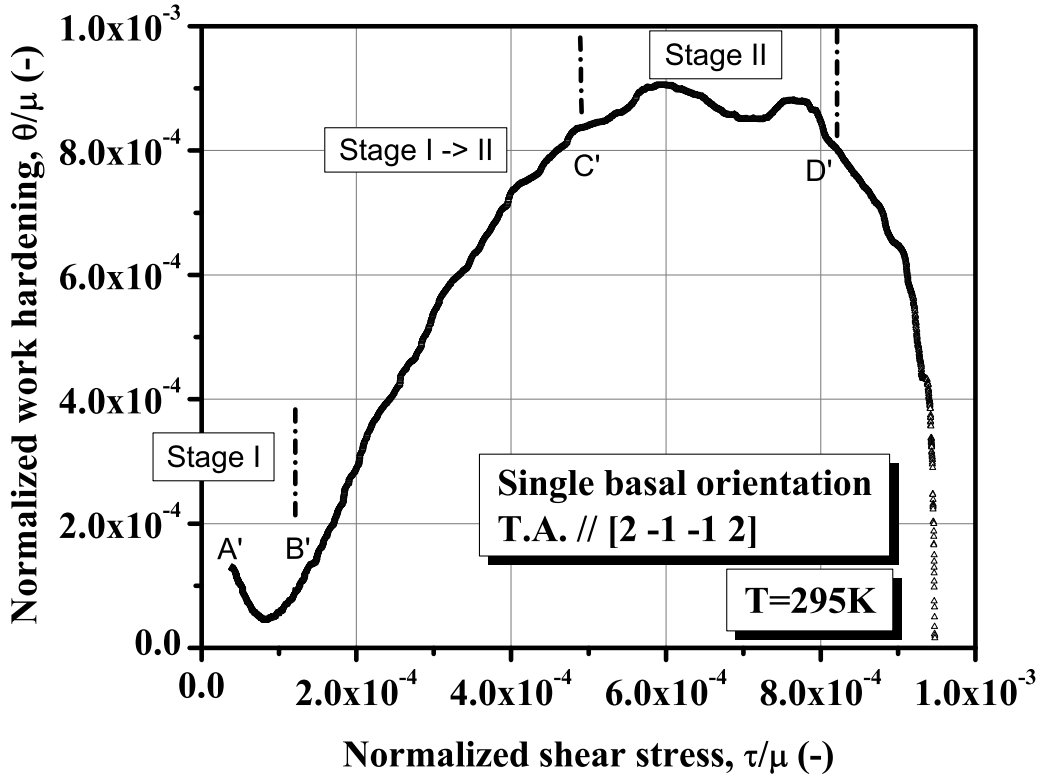

Figure 5.8: Normalized work hardening as a function of normalized shear stress plot for Mg single crystal #1 deformed in tension at 295K.

So far, the work hardening behaviour was represented in terms of resolved shear stress and resolved shear strain on the basal plane, assuming that the only basal $< a >$ slip system BI was activated during the onset of plastic deformation. Since

other deformation modes can also contribute to the plastic low and can play an important role in the work hardening, it is useful to discuss the mechanical properties of single crystals in terms of global properties represented by true stress - true strain data. In the flowing section the properties related to ductility, material strength and fracture stress are discussed in terms of true stress and true strain characteristics.

Figure 5.9 shows true stress - true strain, $\sigma - \epsilon$ curve and work hardening - true strain, $\Theta(= d\sigma/d\epsilon) - \epsilon$ plot of Mg single crystal #1 deformed in tension at 295K on the same graph. In theory, the necking of a specimen occurs when the work hardening is equal to the plastic flow stress i.e., $d\sigma/\epsilon = \sigma$, which is well known as the Considère criterion. However, in the work it was observed that the fracture of crystals occurred at a much higher level of work hardening than predicted by the the Considère point, as shown in Fig. 5.9.

Basinski *et al.* (1997a) introduced Considère ratio (CR) to represent such a sudden onset of instability:

$$R = \frac{\frac{d\sigma_F}{d\epsilon_F}}{\sigma_F} = \frac{\Theta_F}{\sigma_F}. \tag{5.1}$$

In Fig. 5.9, the appearance of instability is indicated by the sudden drop of the work hardening however, the precise measurement of the Considère ratio were difficult and subjected to an error. The stress at the point of fracture was estimated $\sim$65.7MPa and the value of work hardening at this point was $\sim$201MPa. Therefore, the Considère ratio (CR) of crystal#1 oriented for basal $< a >$ slip deformed in tension at 295K was $\sim$3.06.

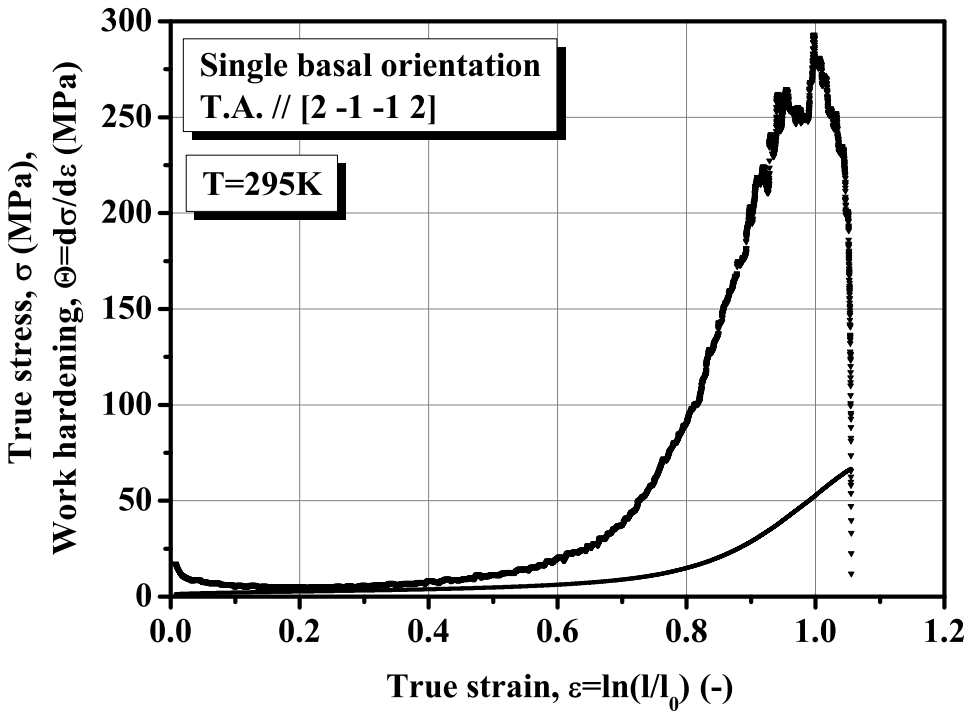

Figure 5.9: The Considère plot (true stress versus true strain and work hardening rate versus true strain characteristics combined on one plot) of Mg single crystal #1 oriented for single basal $< a >$ slip deformed in tension at 295K.

SEM/EBSD analysis was carried out on twin areas developed during tensile deformation of crystal #1 with initially single basal $< a >$ slip orientation. Fig. 5.10 shows low magnification SEM image of crystal #1 deformed in tension until 60% true strain at 295K, which represents the transition range from stage I to stage II. In this stage, the crystallographic orientation rotated out of a single basal $< a >$ slip orientation and the slip traces originally corresponding to the basal (0001) planes assumed the wavy character. Due to the lattice rotation during the tensile test, the basal

Schmid factor decreases and inhomogeneous deformation is induced in the transition from stage I to stage II. As result of it, a certain amount of deformation twinning was observed.

Fig. 5.11 shows inverse pole figure (IPF) maps and pole figures (PFs) constructed from EBSD analysis of locations A and B in Fig. 5.10. From the EBSD analysis, deformation twinning was characterized as $\{10\bar{1}2\} < 10\bar{1}1 >$ extension twinning, corresponding to 86° rotation around $< 2\bar{1}\bar{1}0 >$ orientation relationship.

The orientation of the tensile axis after 60% true strain, as estimated by the PFs in Fig. 5.11 (b) and (d), is close to $[10\bar{6}\bar{4}0]$. Although other slip traces corresponding to non-basal planes could not be detected in the SEM micrographs, coplanar basal $< a >$ slip and non-basal $< a >$ slip are also believed to be activated, in addition to basal $< a >$ slip and $\{10\bar{1}2\} < 10\bar{1}1 >$ twin, since the tensile axis position is located at non-basal $< a >$ slip area.

Note that local hardness measurements by nano-indentation were carried out on deformed matrix and twin regions: area I-VI in Fig. 5.11 (a) and area I-IV in Fig. 5.11 (c). Experimental results for the nano-indentation will be described in section 5.8.

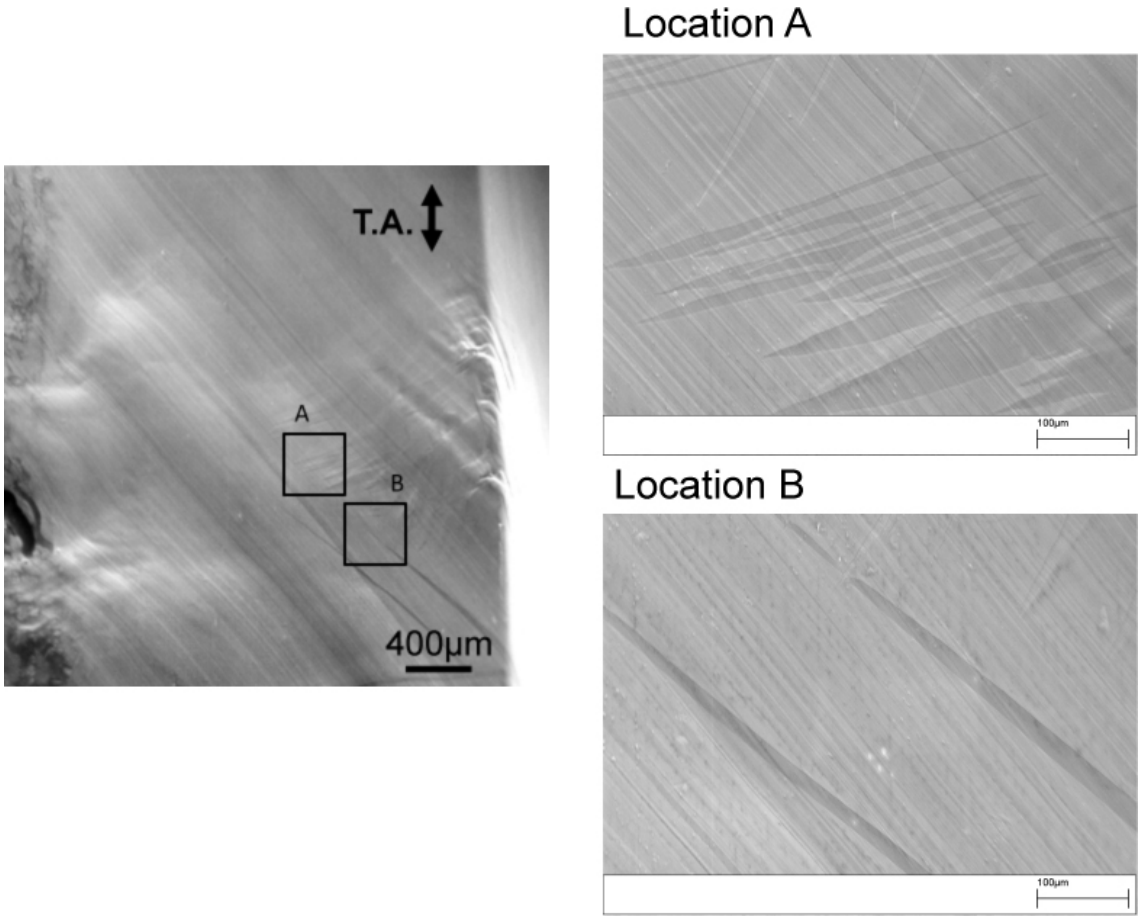

Figure 5.10: Low magnification SEM image of crystal #1 deformed in tension until 60% true strain (transition range from stage I to stage II) at 295K.

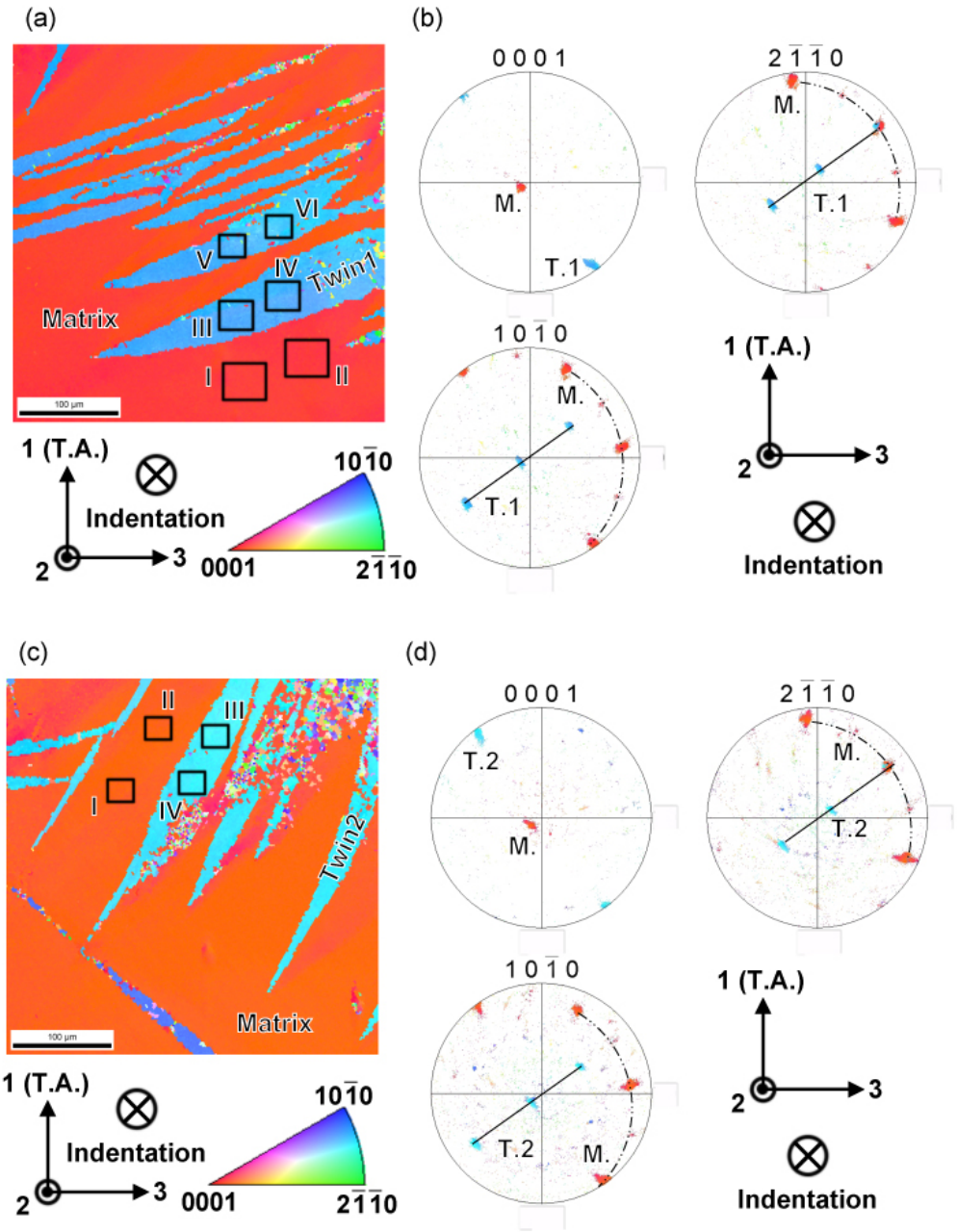

Figure 5.11: (a) Inverse pole figure (IPF) map, (b) pole figures (PFs) constructed from EBSD analysis of location A, (c) IPF map, and (d) PFs of location B in Fig. 5.10.

Fig. 5.12 shows low magnification SEM image of crystal #1 deformed in tension until fracture at 105% of true strain at 295K. The observations were carried out near the fracture surface. In the fracture stage, the crystal was locally twisted and bent due to inhomogeneous deformation accompanied with kink bands formation and deformation twinning. Fig. 5.13 shows IPF maps and PFs constructed from EBSD analysis of locations A and B in Fig. 5.12 near the fracture surface.

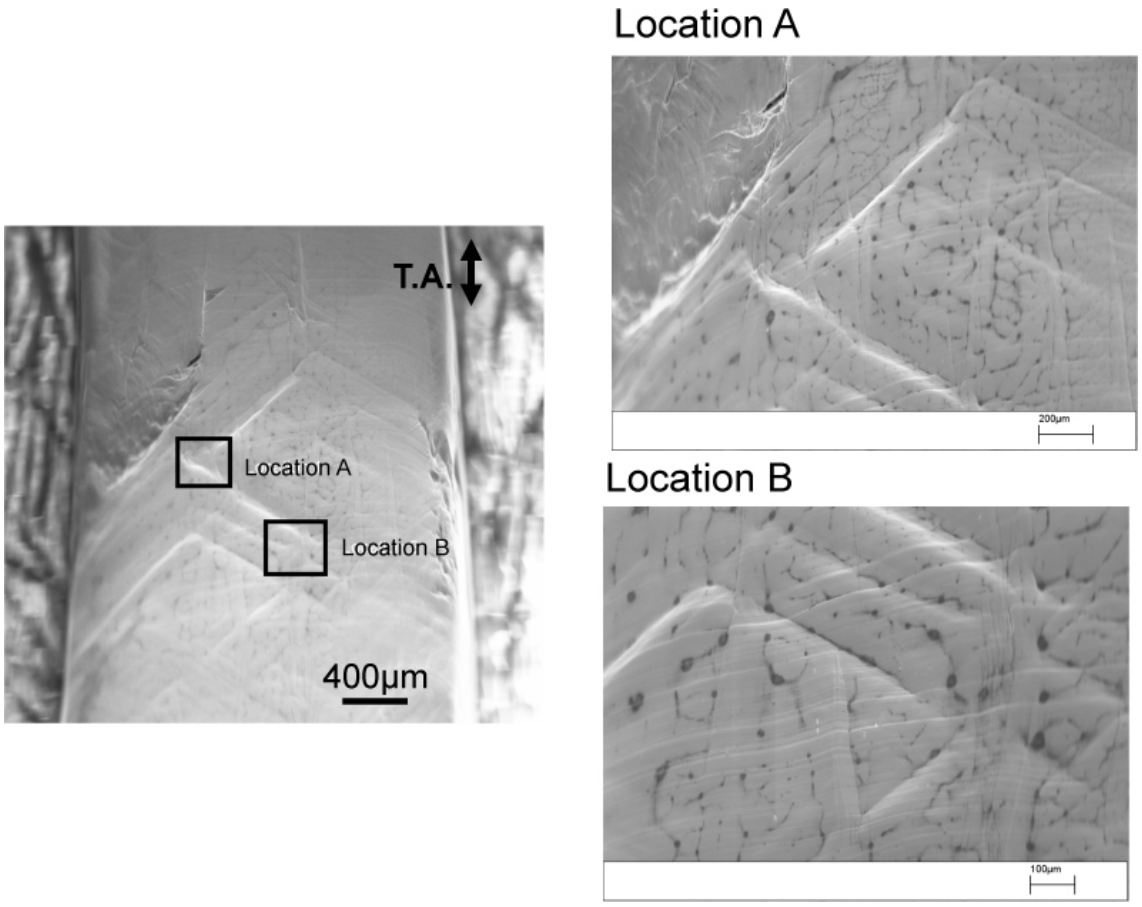

Figure 5.12: Low magnification SEM image of crystal #1 deformed in tension until fracture at 295K.

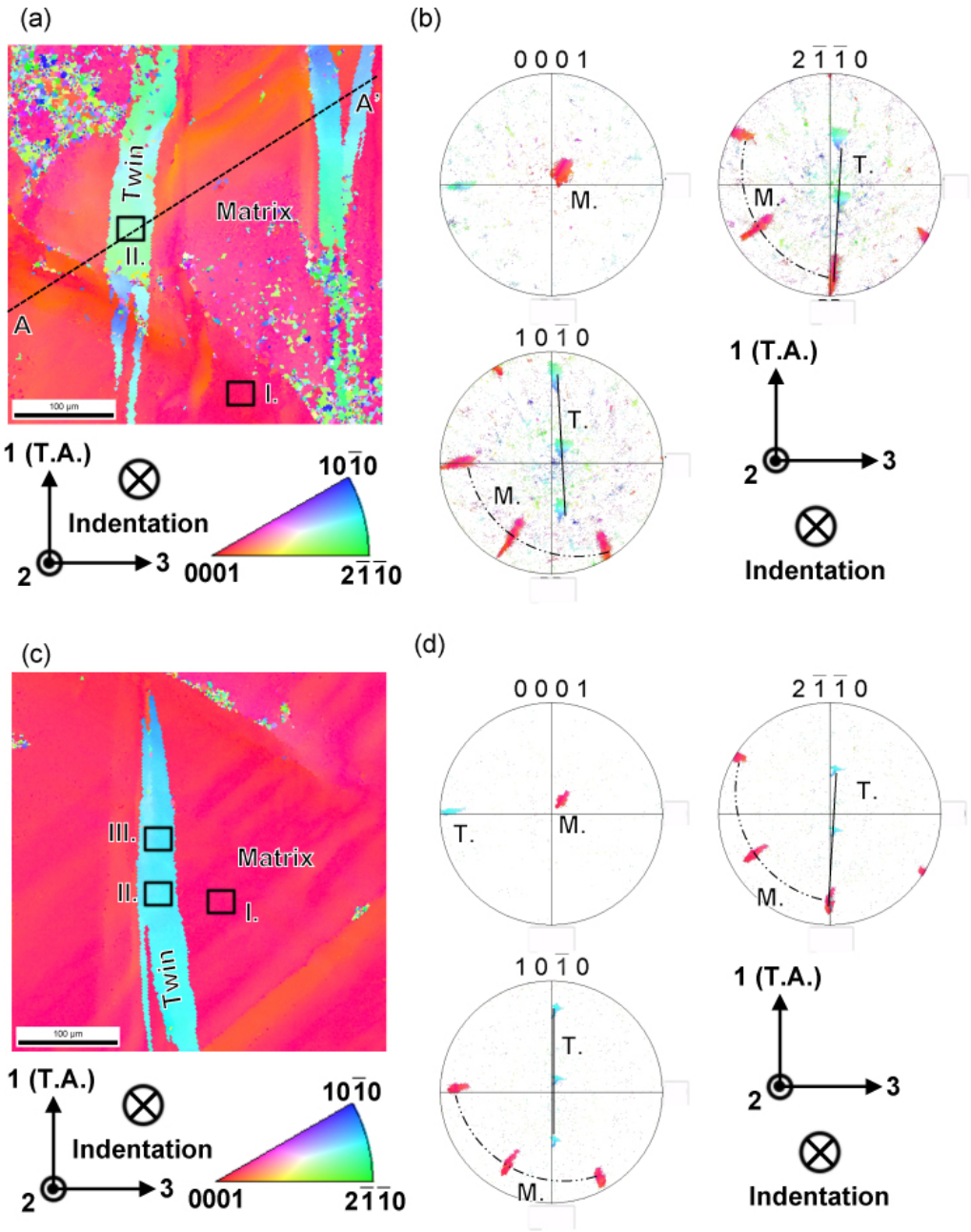

Figure 5.13: (a) Inverse pole figure (IPF) map, (b) pole figures (PFs) constructed from EBSD analysis of location A in the Fig. 5.12, (c) IPF map, and (d) PFs of location B in the Fig. 5.12.

A line misorientation profile along the line A-A' in Fig. 5.13 (a) is presented in Fig 5.14. The misorientation angles were somewhat deviated, maximum of about 15°, from the point A and the accommodation $\{10\bar{1}2\} < 10\bar{1}1 >$ twins were developed in the locally heterogeneous areas. Even in a fractured sample, the volume fraction of $\{10\bar{1}2\} < 10\bar{1}1 >$ twins was not very large.

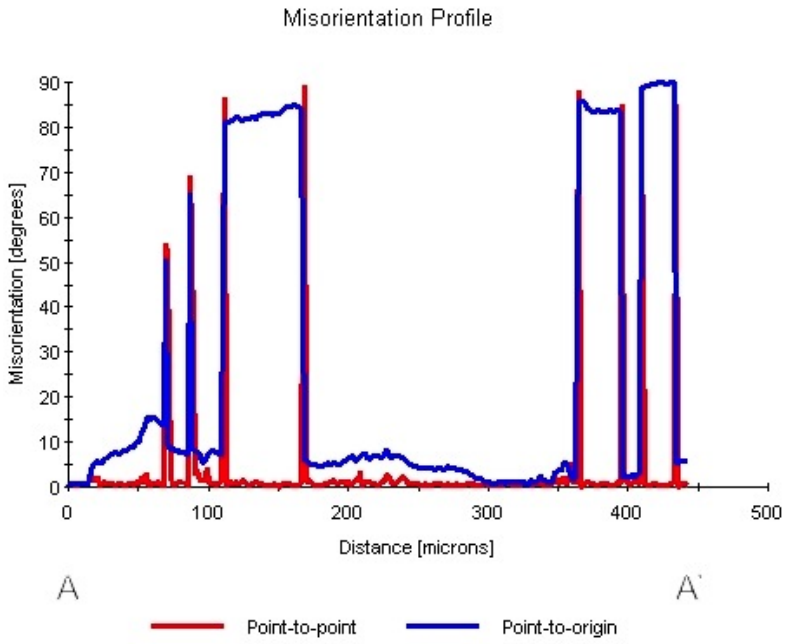

Figure 5.14: misorientation profile along the line A-A' in Fig. 5.13 (a).

Fig. 5.15 shows (a) SEM micrograph, (b) Inverse pole figure (IPF) map, and (c) pole figures (PFs) constructed from EBSD analysis in crystal #1 deformed in tension until fracture at 295K, where the observed location was relatively flat and far from the fracture surface. Accommodation $\{10\bar{1}2\} < 10\bar{1}1 >$ twins of one variant, were developed in this area.

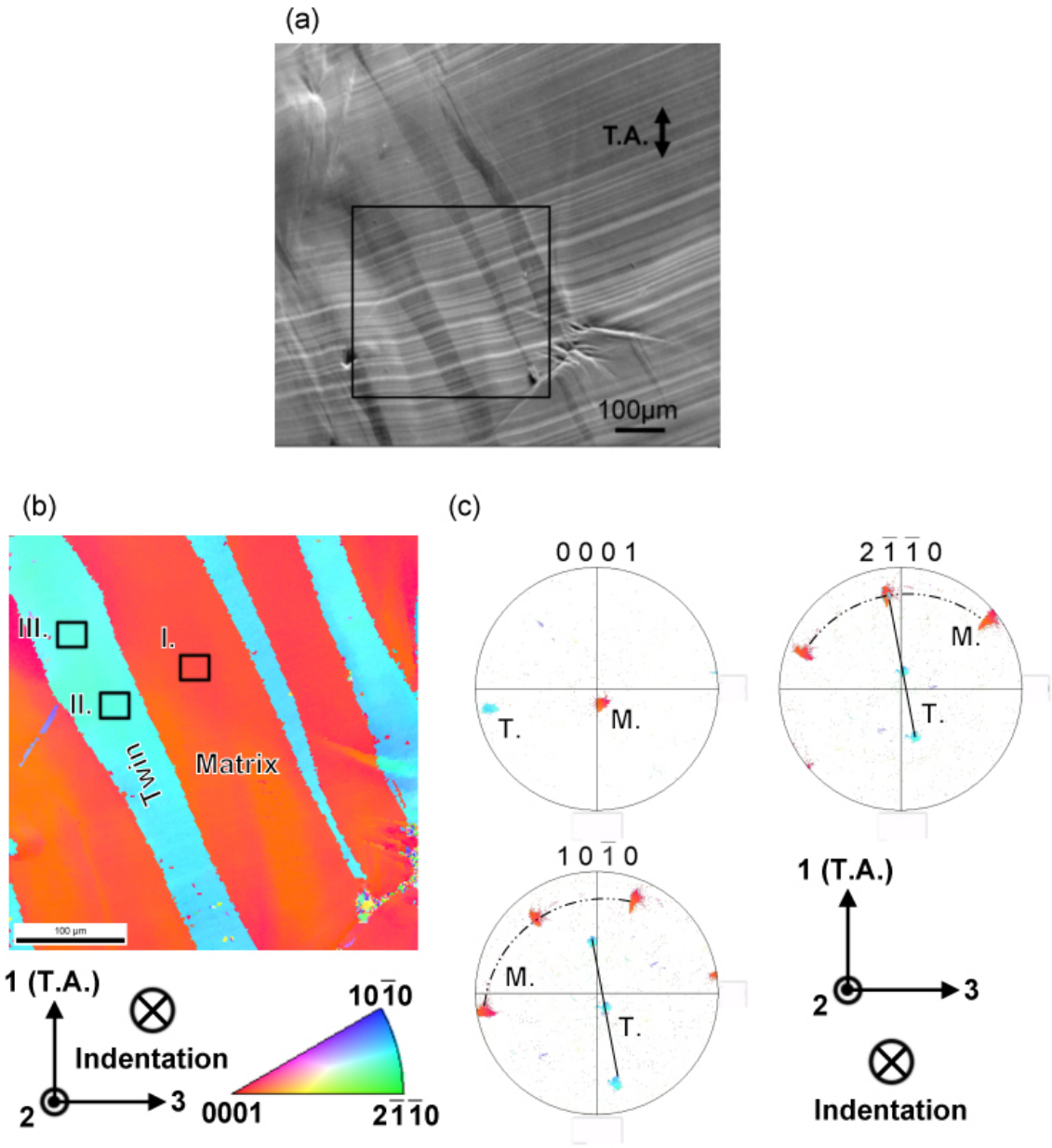

Figure 5.15: (a) SEM micrograph, (b) Inverse pole figure (IPF) map, and (c) pole figures (PFs) constructed from EBSD analysis in crystal #1 deformed in tension until fracture at 295K. The location area was relatively flat and far from the fracture surface.

Note that local hardness measurements by nano-indentation were carried out on deformed matrix and twin regions: area I-II in Fig. 5.13 (a), area I-III in Fig. 5.13 (c), and area I-III in Fig. 5.15 (b). Experimental results of the nano-indentation will be described in section 5.8.2.

$[2\bar{1}\bar{1}2]$ compressive deformation

For the compressive axis of the crystals paralleled to $[2\bar{1}\bar{1}2]$, the Schmid factor for BI slip system is 0.50. Fig. 5.16 shows resolved shear stress - shear strain characteristic of Mg single crystal #1 deformed in compression at 295K. As it was done for the tensile deformation test, the resolved shear stress and shear strain on the basal plane was computed from raw data, assuming that only basal BI slip system operates throughout the onset of deformation under compression. During an uniaxial compression, the lattice rotation associated with activated slip systems occurs towards the normal to the slip plane, i.e., towards [0001] direction, the resolved shear stress and the resolved shear strain has been calculated from eqs. (4.7) and (4.8). The CRSS for the primary slip system, BI was determined by the intersection of the elastic and plastic region of the plastic flow curve. The CRSS for the basal $< a >$ slip system in the compression test was found to be 0.92MPa, which was slightly higher than in the tensile test, 0.70MPa. After the yielding, the compressive deformation characteristics of the crystal #1 exhibited different behaviour, compared to the tensile deformation. Easy glide stage (stage I), transition range from stage I to II and rapid work hardening stage (stage II) were common characteristics in both tensile and compressive deformation tests. In the tensile test, abrupt fracture occurred after very short stage II, while in the compression test, stage III characterized by decreasing

work hardening with shear strain was observed after the stage II. The compression test was stopped just after the work hardening assumed a negative slope.

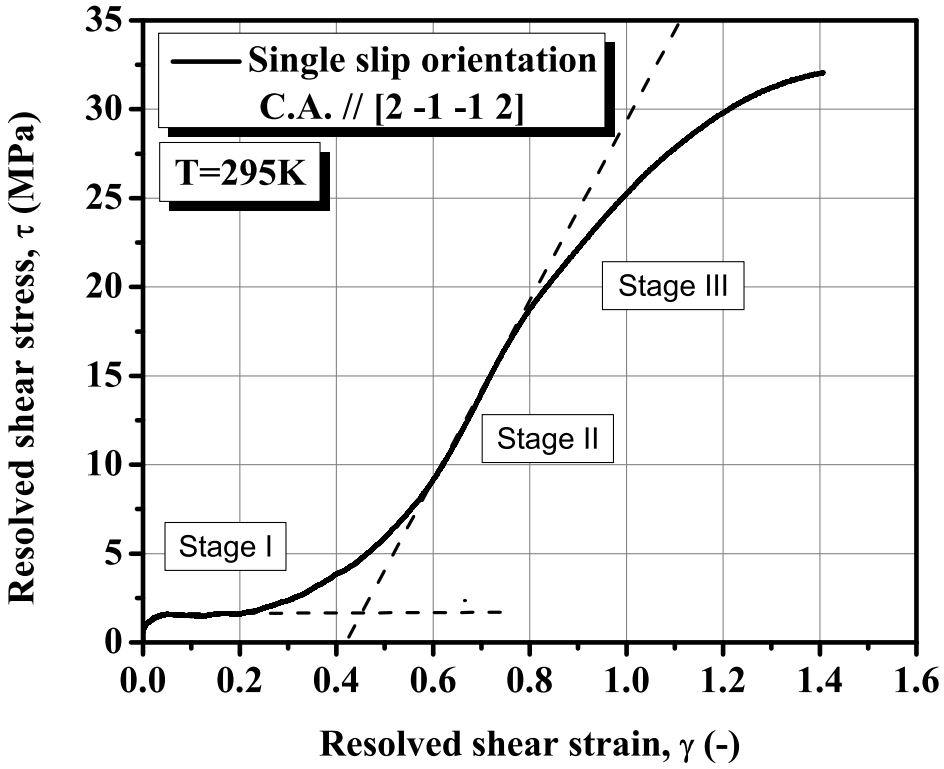

Figure 5.16: Resolved shear stress - shear strain curve of Mg single crystal #1 deformed in compression at 295K.

In Fig. 5.17, the stretch AB represents work hardening of stage I with almost constant values at the level 1-7MPa. The stage I extended until shear strain of ∼0.2. Then, the work hardening gradually increased by a factor of about 6, identified as the transition region in the range of 0.2-0.57 shear strain, depicted as the stretch BC. The stretch CD represents stage II in compression with the hardening rate value of about

38-53MPa. The stage II extends until ∼0.57-0.80 shear strain. Beyond the point D, the work hardening rate gradually decreases in the range of sheer strain 0.8-1.4, down to the level of about 8-38MPa represented by point E in Fig. 5.17. The stretch DE corresponds to the stage III in compression.

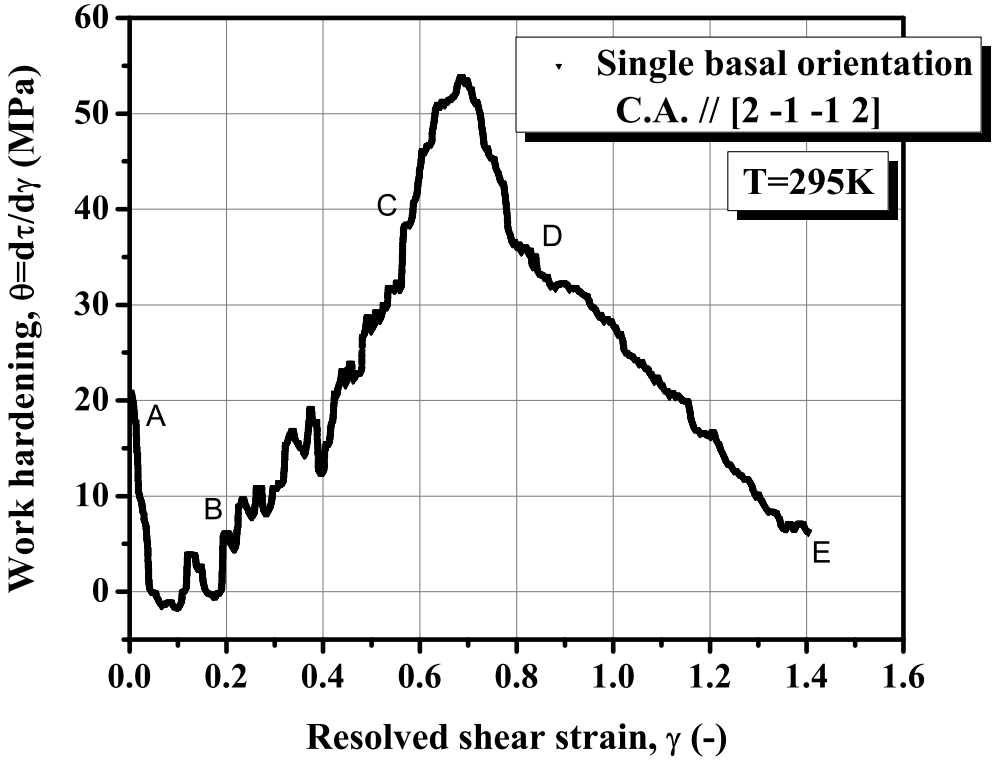

Figure 5.17: Work hardening versus resolved shear strain plot of Mg single crystal #1 deformed in compression at 295K.

The work hardening normalized with shear modulus is plotted as a function of normalized shear stress in Fig. 5.18. The work hardening in stage I, θ_I/μ was approximately in the range of $0 - 5.22x10^{-4}$ (the stretch A'B'). After the stage I, the work

hardening increases with shear stress, defined as the stretch B'C'. The stage II is represented by the stretch C'D' with the rate of work hardening $\theta_{II}/\mu \sim 2.13-3.22x10^{-3}$, a factor of ∼4-6 higher than in the stage I. The rate of work hardening in stage III, represented by the stretch D'E', was in the range of $\theta_{III}/\mu \sim 3.60x10^{-4} - 2.13x10^{-3}$.

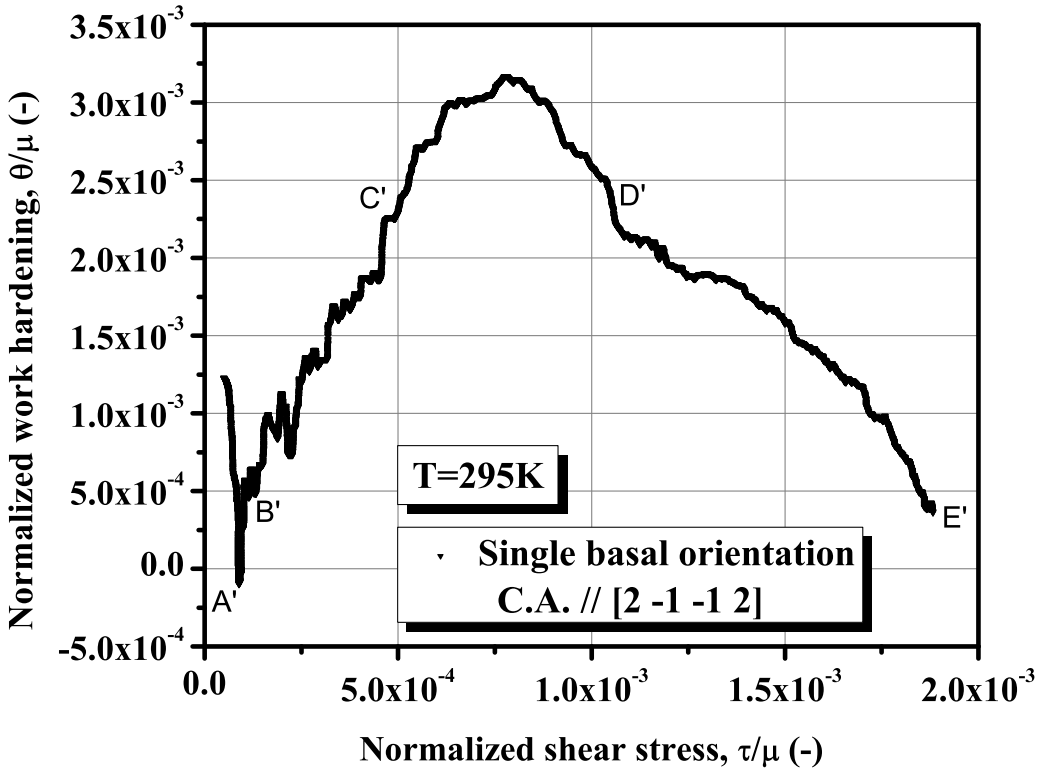

Figure 5.18: Normalized work hardening-normalized shear stress plot with the shear modulus of Mg single crystal #1 deformed in compression at 295K.

Fig. 5.19 shows true stress versus true strain and work hardening rate versus true strain plots of Mg single crystal #1 oriented for single basal $< a >$ slip deformed in compression at 295K, representing the Considère construction of neck instability. It

is seen that the work hardening rate Θ falls below the flow stress σ at the stain level of about 0.65, much before any flow instability was observed in the sample. At about 82% of true strain corresponding to the end of compression test, the work hardening was below the flow stress and the Considère ratio (CR) calculated from Fig. 5.19 was 1.0.

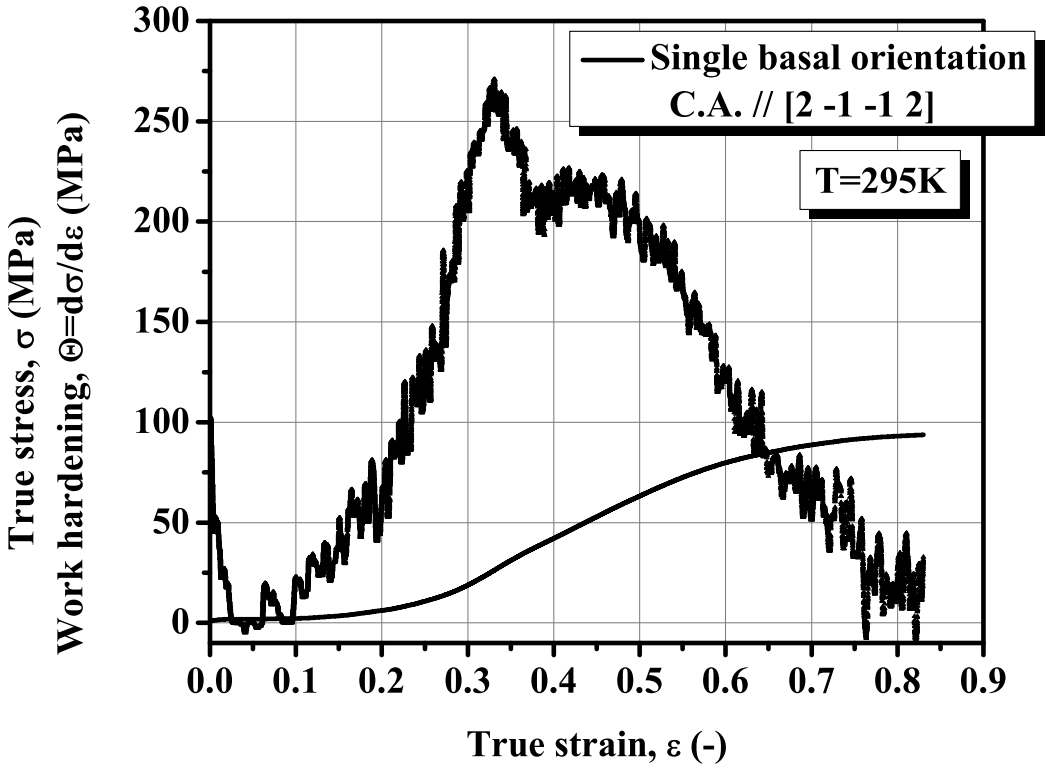

Figure 5.19: The Considère plot encompassing true stress versus true strain and work hardening rate versus true strain characteristics of Mg single crystal #1 oriented for single basal $< a >$ slip deformed in compression at 295K.

5.2.3 Crystal #2: double basal $< a >$ slip orientation

$[10\bar{1}(2/\lambda^2)]$ tensile deformation

The tensile axis in crystal #2 was paralleled to $[10\bar{1}(2/\lambda^2)]$ direction and the Schmid factor for BI and BII systems calculated from the initial orientation was 0.42, indicating that deformation should occur by double basal $< a >$ slip systems. The resolved shear stress and shear strain on the (0001) plane were recalculated from raw data, assuming that only single basal $< a >$ slip on the primary BI (or BII) slip system operates during the onset of plastic deformation. Fig. 5.20 shows Resolved shear stress versus resolved shear strain curve of Mg single crystal #2 deformed in tension at 295K. The CRSS for the primary slip system, BI (or BII) was determined by the intersection of the elastic and plastic region of the plastic flow curve. The CRSS for basal $< a >$ slip was 1.27MPa, slightly higher than the CRSS of crystal #1, 0.70MPa, oriented for single basal slip. The small increase in the CRSS is attributed to the activation of double basal $< a >$ slip on BI and BII systems and their mutual interactions. After the yielding, the plastic flow curve exhibits two stages: easy glide stage (stage I) and rapid hardening stage (stage II). Stress serration due to deformation twinning was observed at the end of stage I and during the transition stage, as shown in the insert in Fig. 5.20.

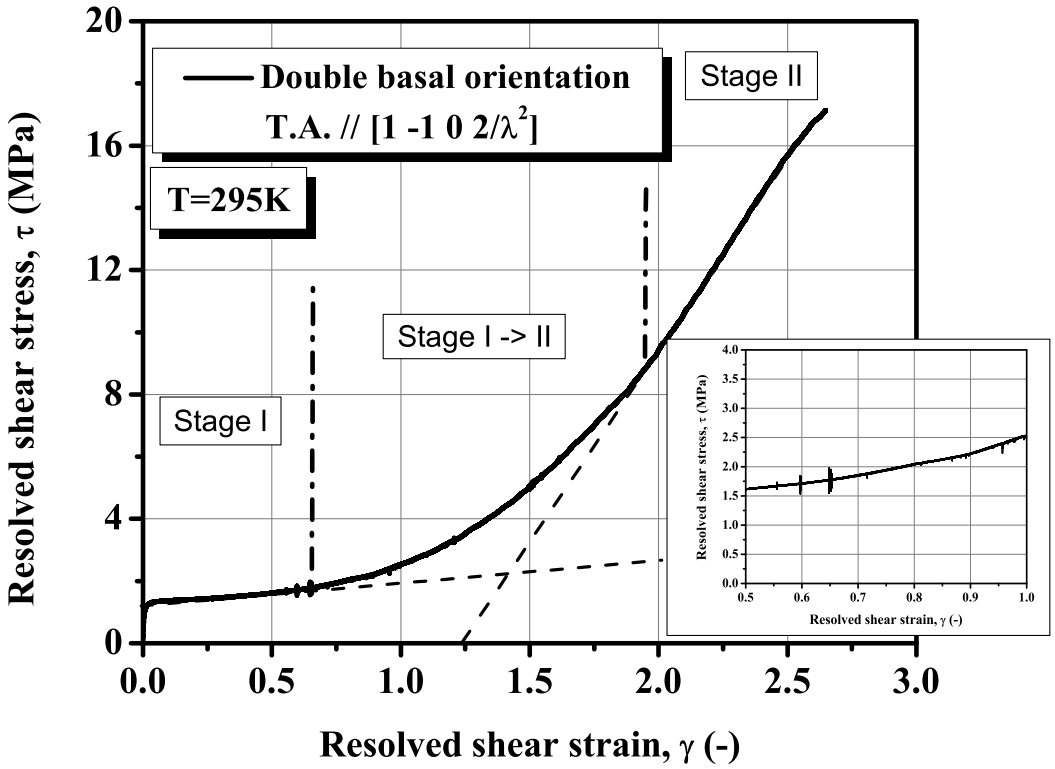

Figure 5.20: Resolved shear stress versus resolved shear strain characteristic of Mg single crystal #2 deformed in tension at 295K.

Fig. 5.21 shows work hardening - shear strain plot of Mg single crystal #2 deformed in tension at 295K. The stretch AB represents stage I with almost constant work hardening rate in a range 0-2MPa. The stage I extends until shear strain of $\sim$0.68. The stage I for the double basal $< a >$ slip orientation is about half long as for the single basal slip orientation. This is attributed to the influence of double basal $< a >$ slip on the dislocation storage, arising from the interactions between BI and BII slip systems. After stage I, from 0.68-1.8 shear strain, the work hardening

gradually increases during the the transition region between stage I and stage II (the stretch BC). The stretch CD represents stage II with the hardening rate between 9-15MPa. The stage II proceeds until ∼1.8-2.3 shear strain.

The work hardening rate normalized with shear modulus as a function of normalized shear stress is shown in Fig. 5.22. The work hardening in stage I, θ_I/μ is in the range $0 - 1.75x10^{-4}$. After the stage I, the work hardening increases linearly with the shear stress, depicted as the stretch B'C', followed by stage II. The rate of work hardening in stage II (the stretch C'D'), is in the range of $\theta_{II}/\mu \sim 5.55 - 8.30x10^{-4}$.

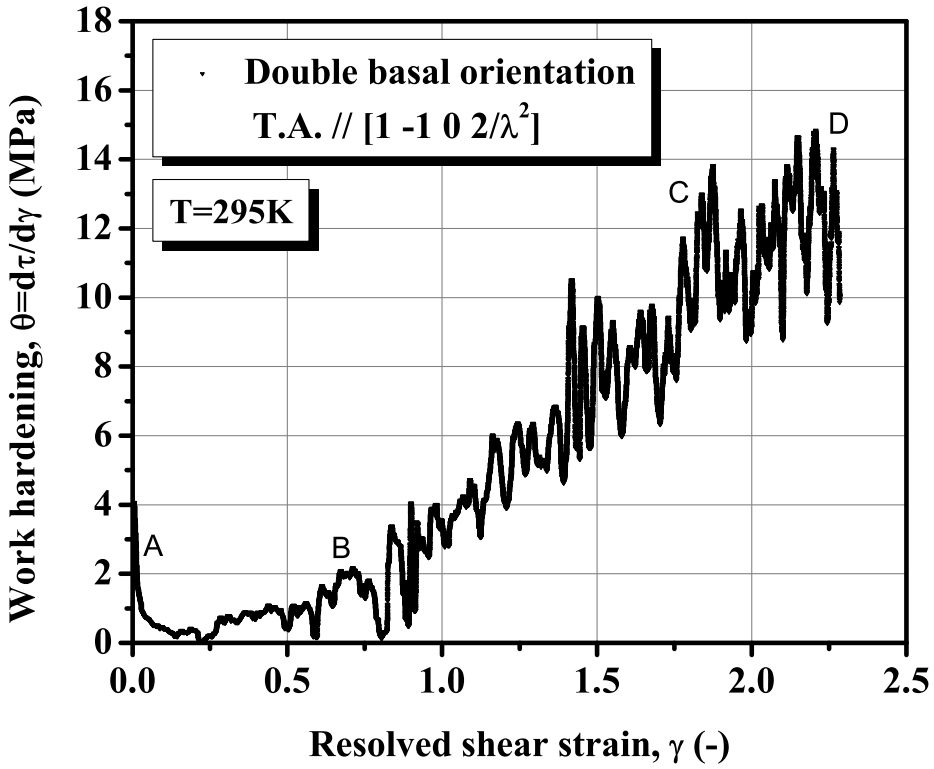

Figure 5.21: Work hardening rate versus shear strain characteristic of Mg single crystal #2 deformed in tension at 295K.

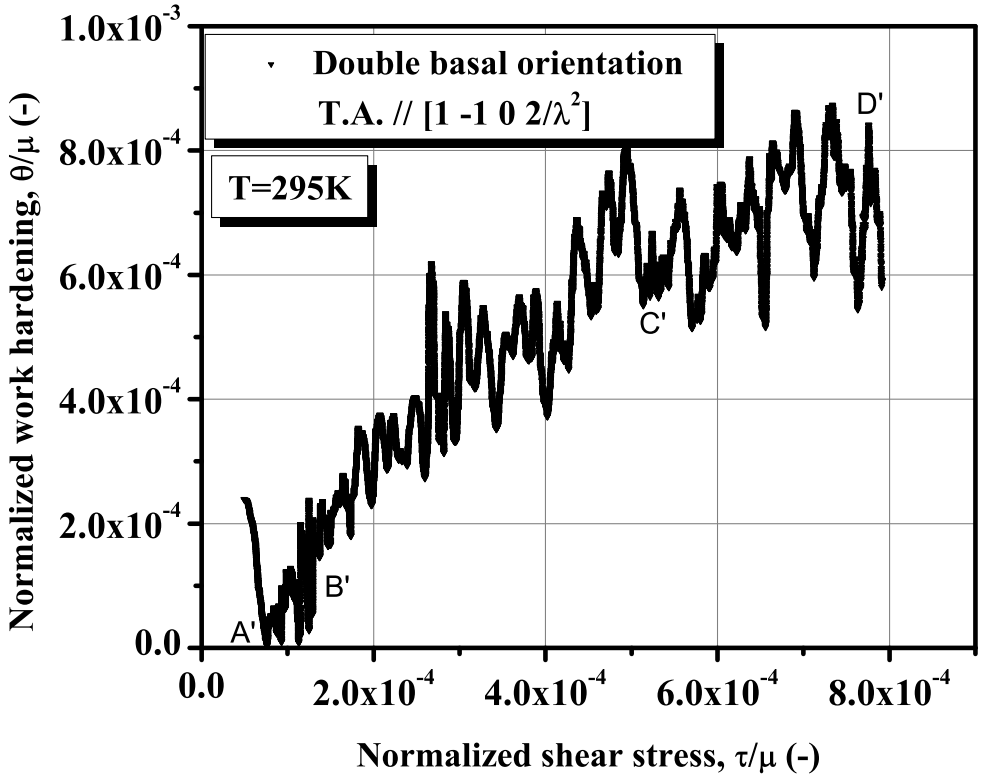

Figure 5.22: Normalized work hardening rate versus shear stress plot of Mg single crystal #2 deformed in tension at 295K.

Fig. 5.23 shows the Considère plot encompassing the true stress versus true strain and work hardening rate versus true strain characteristics of Mg single crystal #2 oriented for double basal $< a >$ slip deformed in tension at 295K. Due to the fluctuations of the work hardening the Considère ratio (CR) for the tensile deformation of crystal #2 cannot be determined precisely however it is in the range of values between 3-5.

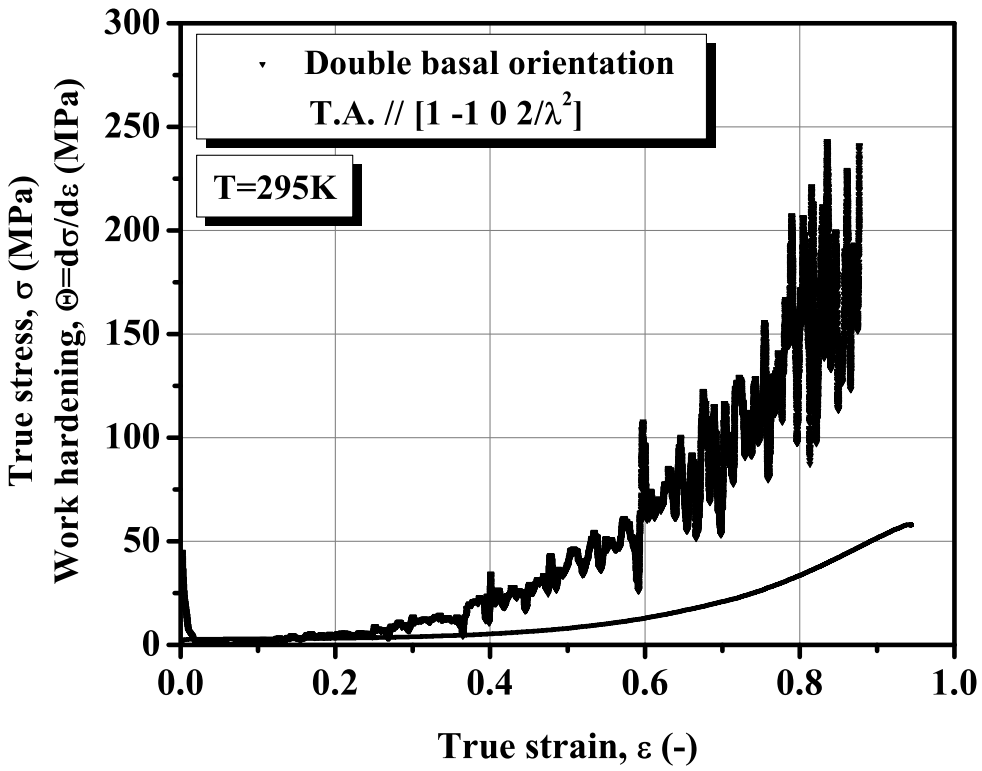

Figure 5.23: The Considère plot, including true stress versus true strain and work hardening rate versus true strain plot characteristics of Mg single crystal #2 oriented for double basal $< a >$ slip deformed in tension at 295K.

$[10\bar{1}(2/\lambda^2)]$ compressive deformation

As in the case of tensile deformation, the Schmid factor for BI and BII systems in the crystal $[10\bar{1}(2/\lambda^2)]$ oriented for double basal slip assumes maximum value of 0.42. The resolved shear stress and resolved shear strain were recalculated from raw data, assuming that only single basal $< a >$ slip on the primary BI (or BII) slip system

operates during plastic deformation. Fig. 5.20 shows resolved shear stress-resolved shear strain curve of Mg single crystal #2 deformed in compression at 295K. The CRSS for the primary slip system, BI (or BII) was determined by the intersection of the elastic and plastic region of the plastic flow curve. The CRSS value was 1.38MPa. After the yielding, the flow curve exhibits two stages: easy glide stage and rapid hardening stage. Stress serrations due to deformation twinning was also seen in the middle of easy glide stage at $\sim$0.25 shear strain. The compression test was stopped before the work hardening rate developed a negative slope.

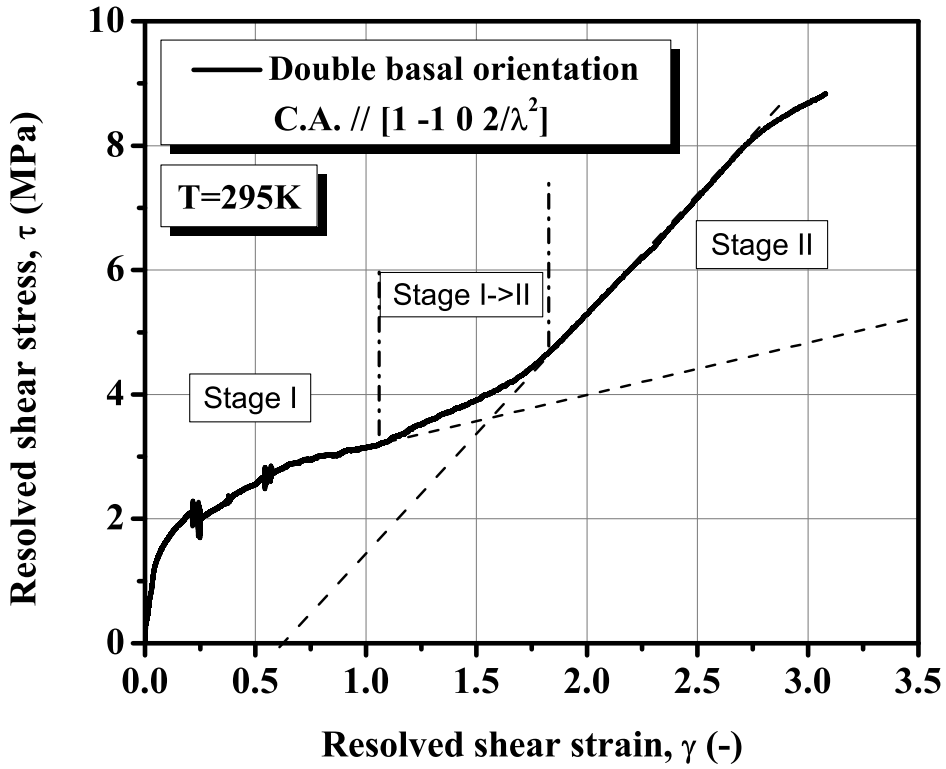

Figure 5.24: Resolved shear stress versus resolved shear strain characteristic of Mg single crystal #2 deformed in compression at 295K.

Fig. 5.25 shows the work hardening - shear strain plot of Mg single crystal #2 deformed in compression at 295K. The work hardening rate in stage I is low and almost constant in the range $0 - 3.7$MPa (stretch AB). The stage I extends until shear strain of $\sim$1.12, followed by the gradual increase of the work hardening rate in the transition region (the stretch BC), between 1.12-1.80 shear strain. The stretch CD represents stage II of work hardening with the work hardening rate at the level about 4MPa. The stage II proceeds until $\sim$1.8-2.75 shear strain.

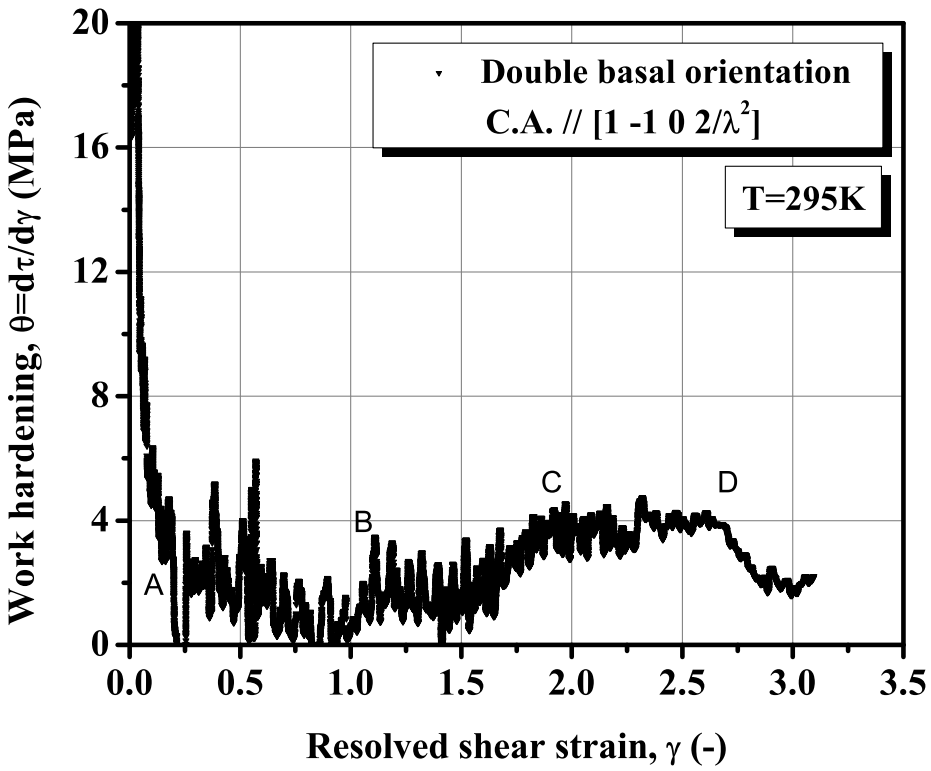

Figure 5.25: Work hardening rate versus shear strain plot of Mg single crystal #2 deformed in compression at 295K.

Fig. 5.26 shows the work hardening normalized with shear modulus as a function of normalized shear stress. The work hardening in stage I is in the range of $\theta_I/\mu \sim 0 - 2.95x10^{-4}$. In stage II of work hardening, represented by the stretch C'D', the crystal exhibits the hardening rate $\theta_{II}/\mu \sim 2.50x10^{-4}$.

Fig. 5.27 shows true stress-true strain and work hardening-true strain characteristics of Mg single crystal #2 oriented for double basal $< a >$ slip deformed in compression at 295K, representing the Considère plot. The Considère ratio (CR)

calculated from Fig. 5.27 was 1.0.

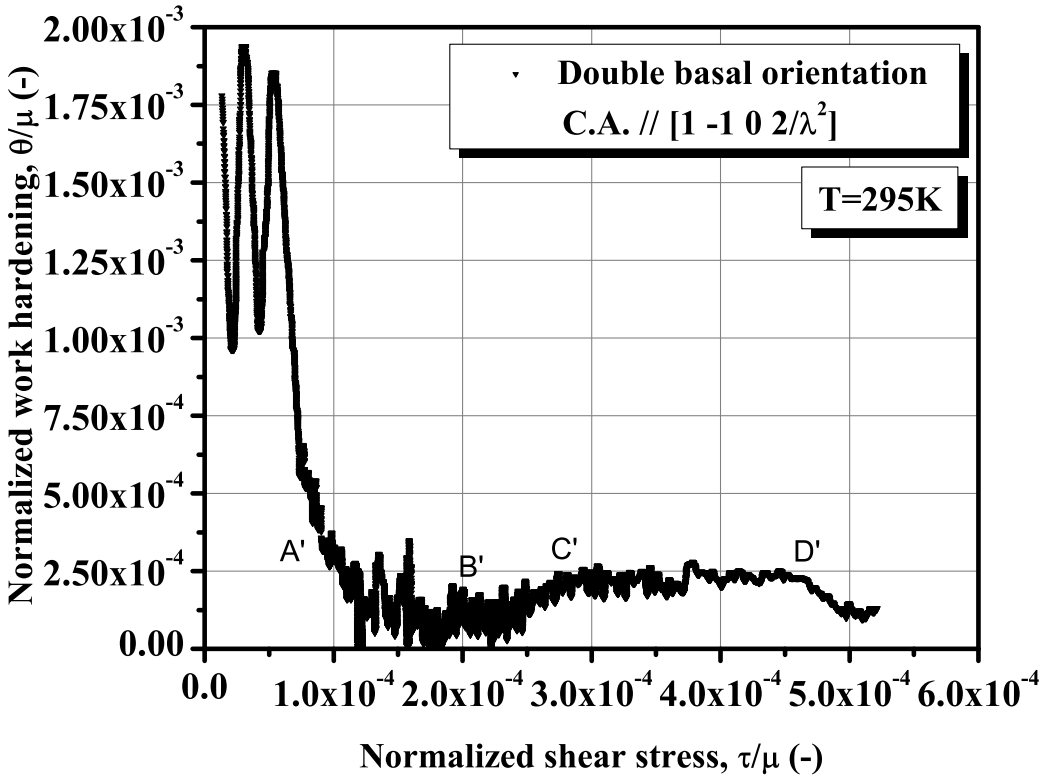

Figure 5.26: Normalized work hardening rate versus normalized shear stress characteristic of Mg single crystal #2 deformed in compression at 295K.

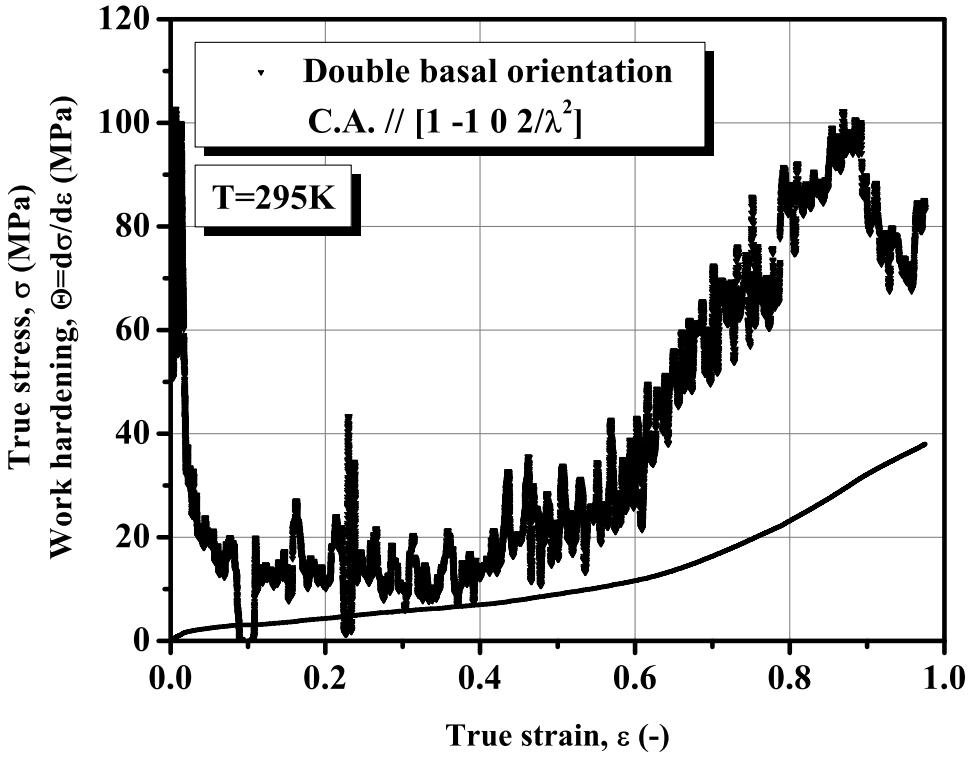

Figure 5.27: The Considère plot for Mg single crystal #2 oriented for double basal $< a >$ slip deformed in compression at 295K.

5.2.4 Crystal #3: basal $< a >$ slip & $\{10\bar{1}2\} < 10\bar{1}1 >$ twin orientation

$[10\bar{1}(8/\lambda^2)]$ tensile deformation

Crystal #3 with tensile axis paralleled to $[10\bar{1}(8/\lambda^2)]$ has relatively low Schmid factor, 0.19, for basal $< a >$ slip systems BI and BII. On the other hand, the Schmid factors

Table 5.1: Schmid factors for basal $< a >$ slip systems, 2^{nd} order pyramidal $< c+a >$ slip systems and $\{10\bar{1}2\} < 10\bar{1}1 >$ twin systems in crystal #3.

Deformatin modes	Notation	Miller-Bravais index	Schmid factor
Basal $< a >$ slip	BI	$(0001)[2\bar{1}\bar{1}0]$	0.19
	BII	$(0001)[\bar{1}2\bar{1}0]$	0
	BIII	$(0001)[\bar{1}\bar{1}20]$	0.19
2^{nd} order pyramidal $< c+a >$ slip	II.Py1	$(11\bar{2}2)[\bar{1}\bar{1}23]$	0.32
	II.Py2	$(\bar{1}2\bar{1}2)[1\bar{2}13]$	0.42
	II.Py3	$(\bar{2}112)[2\bar{1}\bar{1}3]$	0.49
	II.Py4	$(\bar{1}\bar{1}22)[11\bar{2}3]$	0.49
	II.Py5	$(1\bar{2}12)[\bar{1}2\bar{1}3]$	0.42
	II.Py6	$(2\bar{1}\bar{1}2)[\bar{2}113]$	0.32
$\{10\bar{1}2\} < 10\bar{1}1 >$ twin	A'1'	$(10\bar{1}2)[\bar{1}011]$	0.46
	B'2'	$(01\bar{1}2)[0\bar{1}11]$	0.47
	C'3'	$(\bar{1}102)[1\bar{1}01]$	0.46
	D'4'	$(\bar{1}012)[10\bar{1}1]$	0.43
	E'5'	$(0\bar{1}12)[01\bar{1}1]$	0.46
	F'6'	$(1\bar{1}02)[\bar{1}101]$	0.47

for all $\{10\bar{1}2\} < 10\bar{1}1 >$ twin modes are high, as shown in Table 5.1. According to the Schmid factors, the crystals should exhibit inhomogeneous deformation with basal $< a >$ slip and $\{10\bar{1}2\} < 10\bar{1}1 >$ twinning being the dominant modes. Due to the multiple slip and twin activity, there is no reason to analyze the mechanical properties of in terms of resolved shear stress and resolved shear strain characteristics crystal #3. Instead, the tensile deformation of crystal #3 will be characterized in terms of true stress and true strain representations.

Fig. 5.28 shows true stress versus true strain characteristic of Mg single crystal #3 deformed in tension at 295K. Fig. 5.29 shows the Considère plot, which includes $\sigma - \epsilon$ and work hardening - true strain, $\Theta(= d\sigma/d\epsilon) - \epsilon$, curves of single crystal #3 deformed in tension at 295K. The yield stress, $\sigma_0 \sim$3.51MPa, was slightly higher than in single and double basal $< a >$ slip orientations. After the yielding, deformation occurs by basal $< a >$ slip and $\{10\bar{1}2\} < 10\bar{1}1 >$ twins. Serrated flow curve accompany the deformation twinning was seen from the early stage of deformation. Work hardening rate in the early stage of #3 single crystal was ∼2-3 times higher than for single and double basal $< a >$ slip orientations (section 5.2.2 and 5.2.3). On the other hand, homogeneous elongation was about half as long as #1 and #2 tensile samples. The Considère ratio (CR) for the tensile deformation of crystals #2 and #3 cannot be calculated exactly because of the fluctuations of the work hardening rate before the rupture, but rough estimates give CR $\sim 3 - 3.5$.

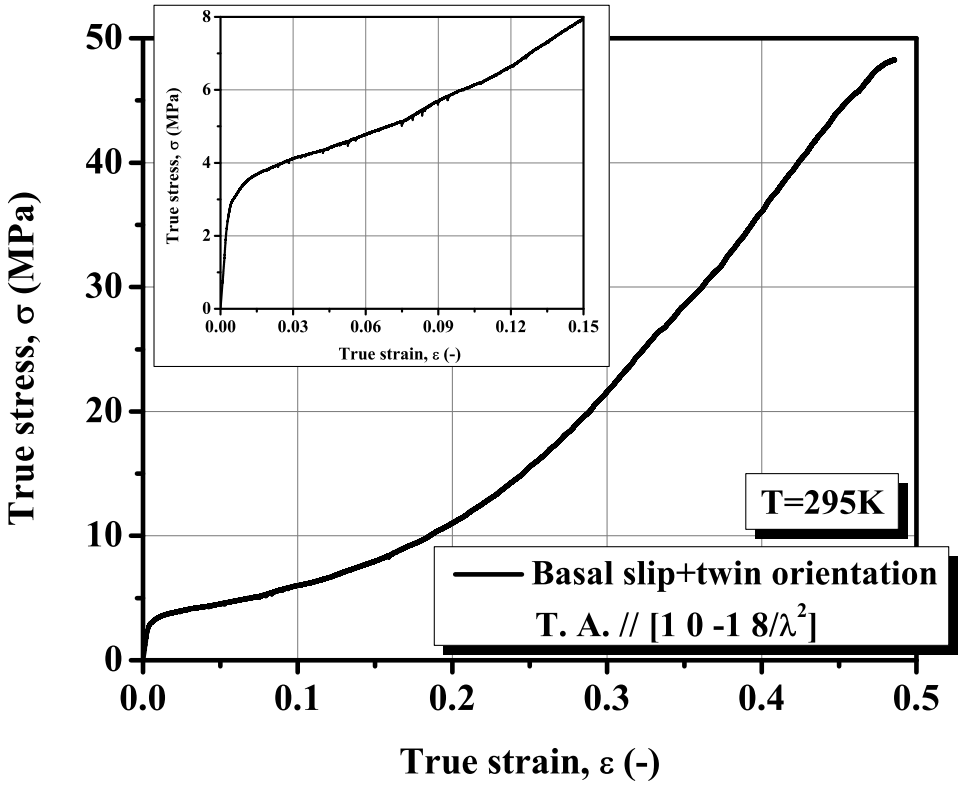

Figure 5.28: True stress versus true strain characteristic of Mg single crystal #3 deformed in tension at 295K.

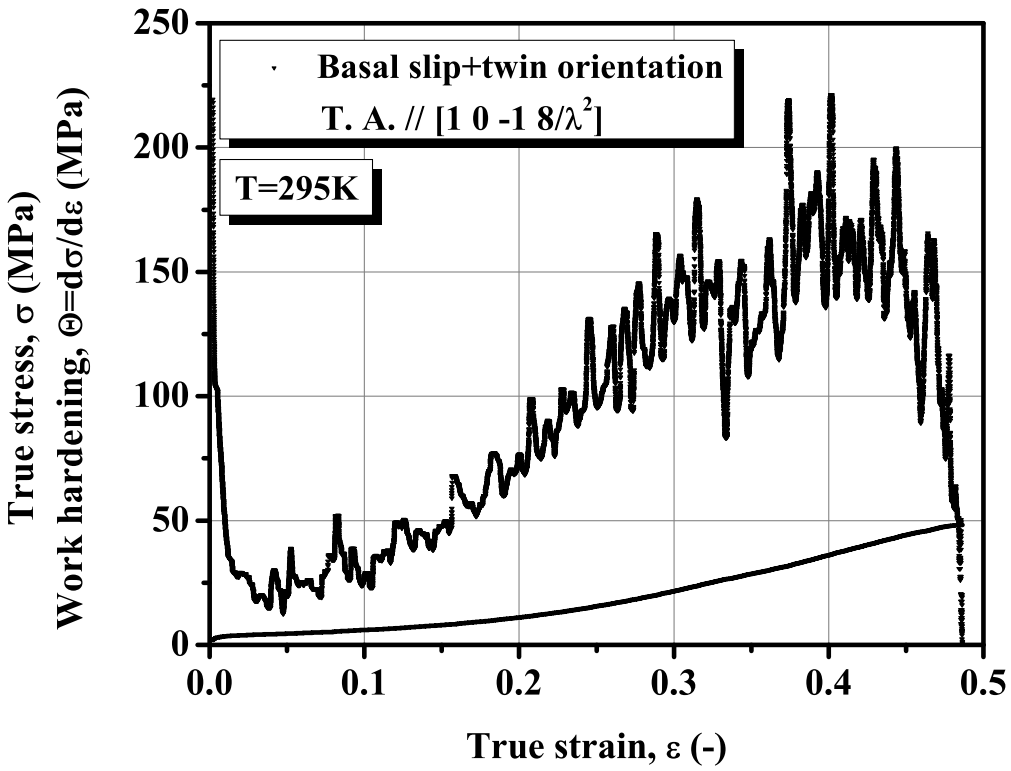

Figure 5.29: The Considère plot of Mg single crystal #3 deformed in tension at 295K.

$[10\bar{1}(8/\lambda^2)]$ compressive deformation

Schmid factors for slip and twin systems of crystal #3 are given in Table 5.1. As in the case of the tensile deformation, the analysis of the stress strain and work hardening properties of crystal #3 is carried out in terms of the true stress and true strain characteristics.

Fig. 5.30 shows true stress versus true strain curve of Mg single crystal #3 deformed in compression at 295K. The corresponding Considère plot, which includes

true stress - strain, $\sigma - \epsilon$ curve and work hardening - true strain, $\Theta(= d\sigma/d\epsilon) - \epsilon$ plot is shown in Fig. 5.31. After the yielding, at $\sigma_0 \sim 2.38$MPa, the crystal deforms with almost zero work hardening between 2-10% strain. In this stage, one observes step-like stress increase. After about 9% strain, an onset of rapid hardening stage is observed with the work hardening increasing dramatically to about 300MPa, followed by the gradual decrease to the level of ~ 50MPa. The compression test was stopped before the work hardening developed a negative slope and the the Considère ratio (CR) for the sample #3 was not determined.

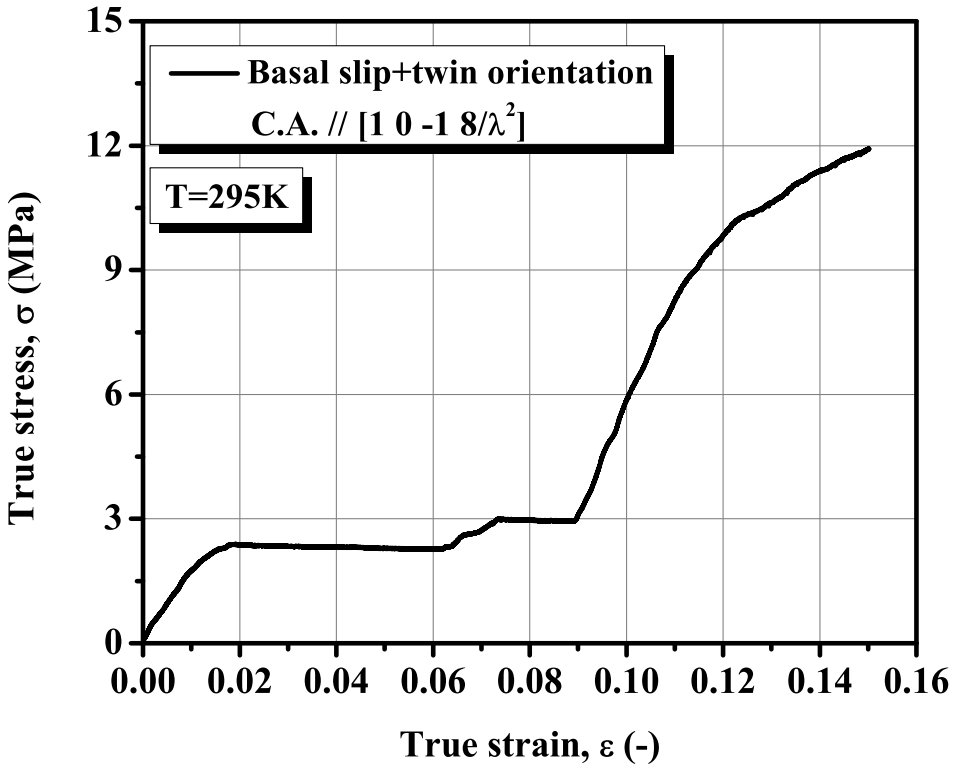

Figure 5.30: True stress versus true strain curve of Mg single crystal #3 deformed in compression at 295K. Note a step-like stress increase in various deformation stages.

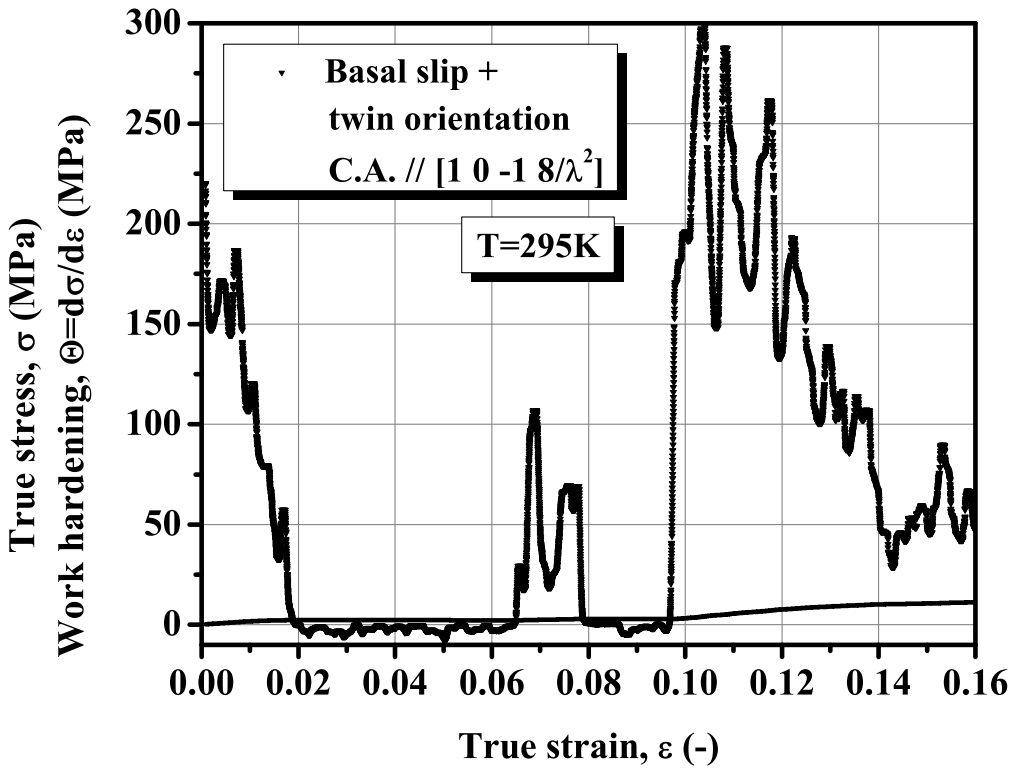

Figure 5.31: The Considère plot of Mg single crystal #3 oriented for basal $< a >$ slip & twinning, deformed in compression at 295K.

5.2.5 Crystal #4 oriented for: $\{10\bar{1}2\} < 10\bar{1}1 >$ twin (tension) & 2^{nd} order pyramidal $< c + a >$ slip (compression)

The Schmid factors for basal $< a >$ slip, 2^{nd} order pyramidal $< c + a >$ slip, and $\{10\bar{1}2\} < 10\bar{1}1 >$ twin systems calculated for the initial [0001] orientation of the axis of crystal #4 are listed in Table 5.2. The Schmid factors for three basal $< a >$ slip systems, BI, BII, and BIII are zero. In the contrary, the Schmid factors for 2^{nd} order

pyramidal $< c+a >$ slip systems, II.Py1 - II.Py6, and $\{10\bar{1}2\} < 10\bar{1}1 >$ twin systems, A'1'-F'6' have high values, because [0001] is the highest symmetrical axis. It is well known that $\{10\bar{1}2\} < 10\bar{1}1 >$ twin deformation occurs predominantly in the c-axis tension test of Mg single crystals, while it was reported that 2^{nd} order pyramidal $< c+a >$ slip system was activated as primary deformation modes when Mg single crystal was deformed in compression paralleled to [0001] direction, as reviewed in section 2.2 of chapter 2.

Table 5.2: Schmid factors for for basal $< a >$ slip and 2^{nd} order pyramidal $< c+a >$ slip systems in crystal #4.

Deformatin modes	Notation	Miller-Bravais index	Schmid factor
Basal $< a >$ slip	BI	$(0001)[2\bar{1}\bar{1}0]$	0
	BII	$(0001)[\bar{1}2\bar{1}0]$	0
	BIII	$(0001)[\bar{1}\bar{1}20]$	0
2^{nd} order pyramidal $< c+a >$ slip	II.Py1	$(11\bar{2}2)[\bar{1}\bar{1}23]$	0.45
	II.Py2	$(\bar{1}2\bar{1}2)[1\bar{2}13]$	0.45
	II.Py3	$(\bar{2}112)[2\bar{1}\bar{1}3]$	0.45
	II.Py4	$(\bar{1}\bar{1}22)[11\bar{2}3]$	0.45
	II.Py5	$(1\bar{2}12)[\bar{1}2\bar{1}3]$	0.45
	II.Py6	$(2\bar{1}\bar{1}2)[\bar{2}113]$	0.45
$\{10\bar{1}2\} < 10\bar{1}1 >$ twin	A'1'	$(10\bar{1}2)[\bar{1}011]$	0.50
	B'2'	$(01\bar{1}2)[0\bar{1}11]$	0.50
	C'3'	$(\bar{1}102)[1\bar{1}01]$	0.50
	D'4'	$(\bar{1}012)[10\bar{1}1]$	0.50
	E'5'	$(0\bar{1}12)[01\bar{1}1]$	0.50
	F'6'	$(1\bar{1}02)[\bar{1}101]$	0.50

[0001] tensile deformation: $\{10\bar{1}2\} < 10\bar{1}1 >$ **twin orientation**

Fig. 5.32 - Fig. 5.34 show mechanical properties, which includes: $\tau - \gamma$, $\theta - \gamma$ and $\theta/\mu - \tau/\mu$ plots of Mg single crystal with the initial orientation of the tensile axis [0001] deformed in tension at 295K. The resolved shear stress and shear strain characteristics were recalculated from experimental raw data, assuming that $\{10\bar{1}2\} < 10\bar{1}1 >$ twinning mode was the only deformation mechanism during plastic flow. Profuse twinning deformation associated with serrated plastic flow was observed due to twins' nucleation and propagation. The onset of $\{10\bar{1}2\} < 10\bar{1}1 >$ twinning was determined as the point of flow stress in which the first stress drop occurred, marked as arrowhead in Fig. 5.32 at the stress value about 2.72MPa.

The work hardening behaviour of Mg single crystal deformed by $\{10\bar{1}2\} < 10\bar{1}1 >$ twin can be divided into two stages. After the yielding, profuse twinning was observed until about 6% shear strain (stage I). After the transition region from stage I to stage II, a rapid hardening stage was observed during stage II, characterized by gross plastic deformation. It can be inferred that the sudden lattice reorientation during twinning would caused the rapid hardening due to dislocation interactions between basal $< a >$ slip and $\{10\bar{1}2\} < 10\bar{1}1 >$ twin systems.

In Fig. 5.33, the stretch AB represents work hardening regime during profuse twinning deformation with the almost constant work hardening rate about 75-150MPa. The profuse twinning stage extends until 7% shear strain. Following the twinning stage, the work hardening rapidly increases by a factor of 3-6, recognized as the transition region between 7-11% shear strain depicted as the stretch BC. The stretch CD in the figure shows rapid work hardening region, with the work hardening $\sim$ 470MPa. The stage II extends from 11-15% shear strain.

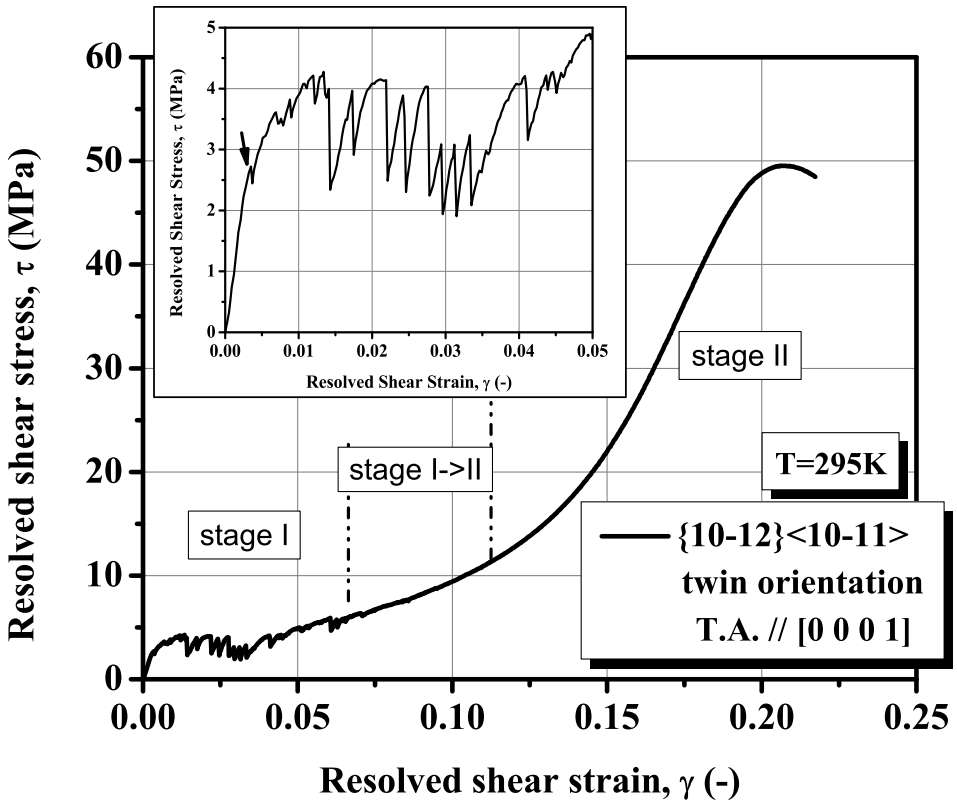

Figure 5.32: Resolved shear stress versus resolved shear strain curve of [0001] Mg single crystal #4 oriented for c-axis tension twinning, deformed in tension at 295K.

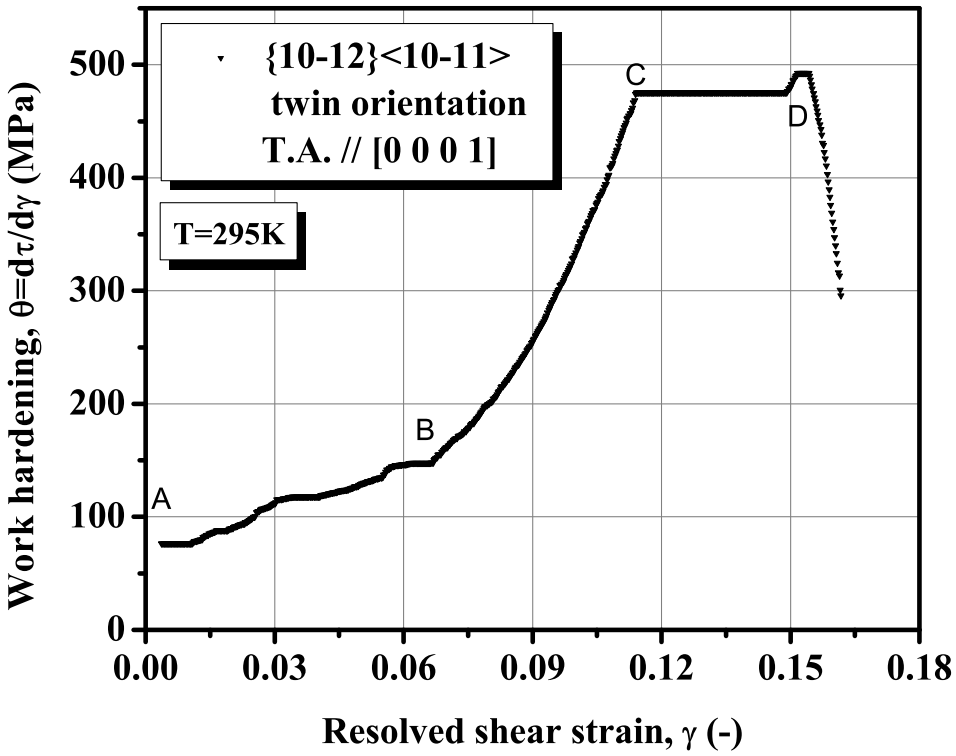

Figure 5.33: Work hardening rate versus shear strain plot of [0001] Mg single crystal oriented for c-axis tension twinning, deformed in tension at 295K.

Fig. 5.34 shows the work hardening normalized with shear modulus plotted as a function of normalized shear stress. During twinning deformation, θ_{Twin}/μ was approximately in the range of $4.48x10^{-3} - 8.70x10^{-2}$, denoted by A'B' in the figure. After the twinning, during B'C' stretch, the work hardening increases approximately linearly with the shear stress until the maximum level of a constant work hardening rate $\theta_{II}/\mu \sim 2.80x10^{-2}$, depicted as the stretch C'D'. It should be mentioned that the Stage III of decreasing work hardening rate due to dynamic recovery characteristic of

FCC singe crystals, has not been observed in the present Mg single crystal and the fracture occurred suddenly after a relatively short stage II, as shown in Fig. 5.34.

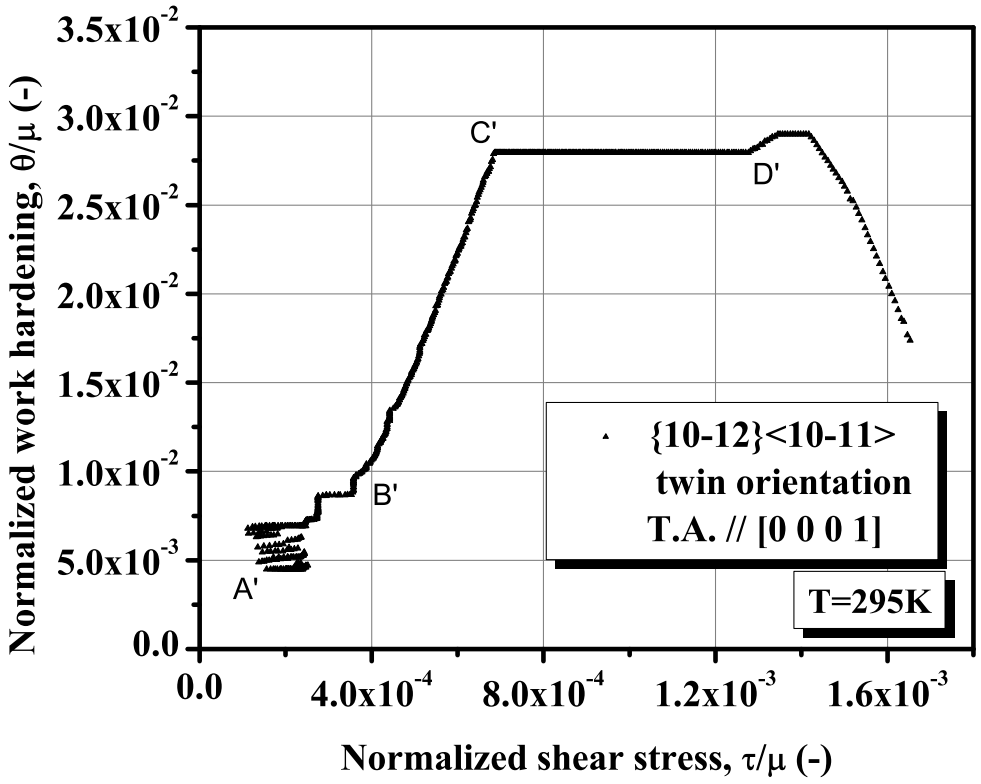

Figure 5.34: Normalized work hardening rate versus normalized shear stress plot of Mg single crystal oriented for c-axis tension twinning, deformed at 295K.

Fig. 5.35 shows true stress - true strain, $\sigma - \epsilon$ curve and work hardening rate versus true strain, $\Theta(= d\sigma/d\epsilon) - \epsilon$ curve of Mg single crystal #4 deformed in tension at 295K, representing the Considère plot. It has been observed that the fracture occurred at a much higher level of work hardening rate than predicted by the the Considère point and the CR was about 16.9 (In Fig. 5.35).

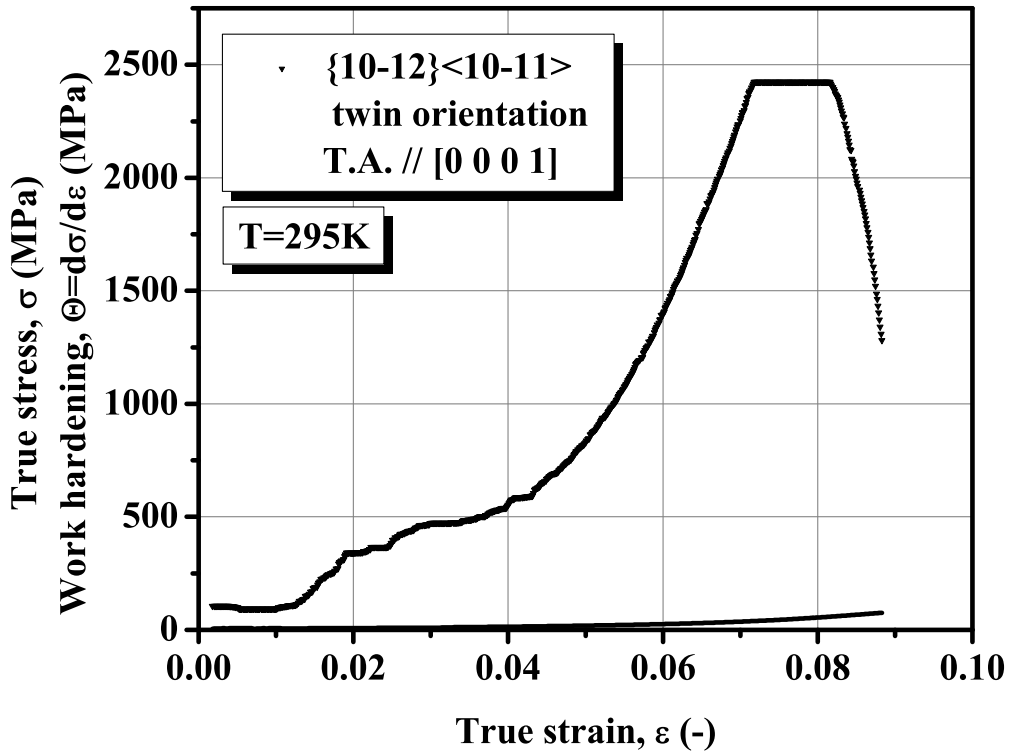

Figure 5.35: The Considère plot of Mg single crystal #4 oriented for $\{10\bar{1}2\} < 10\bar{1}1 >$ twin, deformed in tension at 295K.

[0001] compressive deformation: 2^{nd} order pyramidal $< c + a >$ slip orientation

Fig. 5.36 shows resolved shear stress - resolved shear strain characteristic of Mg single crystals oriented for 2^{nd} order pyramidal $< c+a >$ slip in the c-axis compression test at 295K. The resolved shear stress and shear strain on the $(11\bar{2}2)$ plane were recalculated from experimental raw data, assuming that the 2^{nd} order pyramidal $< c + a >$ slip

systems were the only deformation mechanisms during the compression test. The CRSS for 2^{nd} order pyramidal $< c+a >$ slip observed in this test was 30 MPa. Unlike in basal $< a >$ slip orientations and in $\{10\bar{1}2\} < 10\bar{1}1 >$ twin orientation (crystal #4 tension test), easy glide stage I was not observed in the [0001] compression test. After the yielding, rapid hardening occurred abruptly and it was followed by the sample failure after only 26% shear strain.

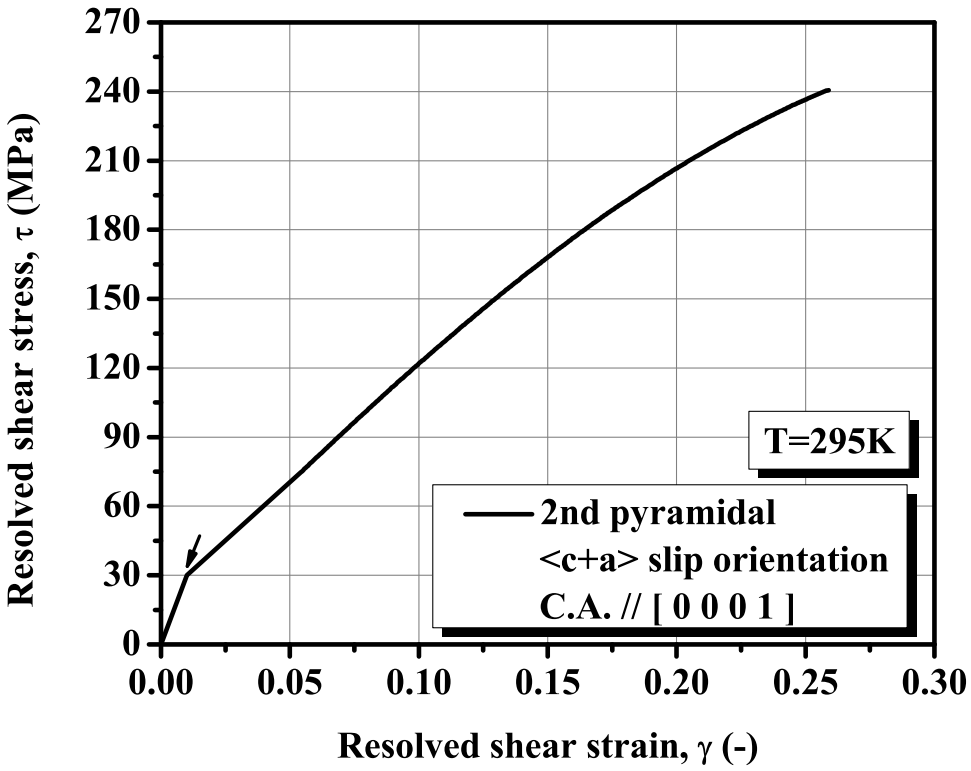

Figure 5.36: Resolved shear stress versus resolved shear strain curve of Mg single crystal deformed in the c-axis compression at 295K.

Fig. 5.37 and Fig. 5.38 show work hardening rate versus shear strain and

normalized work hardening rate versus normalized shear stress plots of Mg single crystal #4 deformed in compression at 295K. The work hardening rate during the rapid hardening stage, θ_{II}, was approximately in the range of $400 - 1050$MPa or $4.48x10^{-3}\mu - 8.70x10^{-2}\mu$.

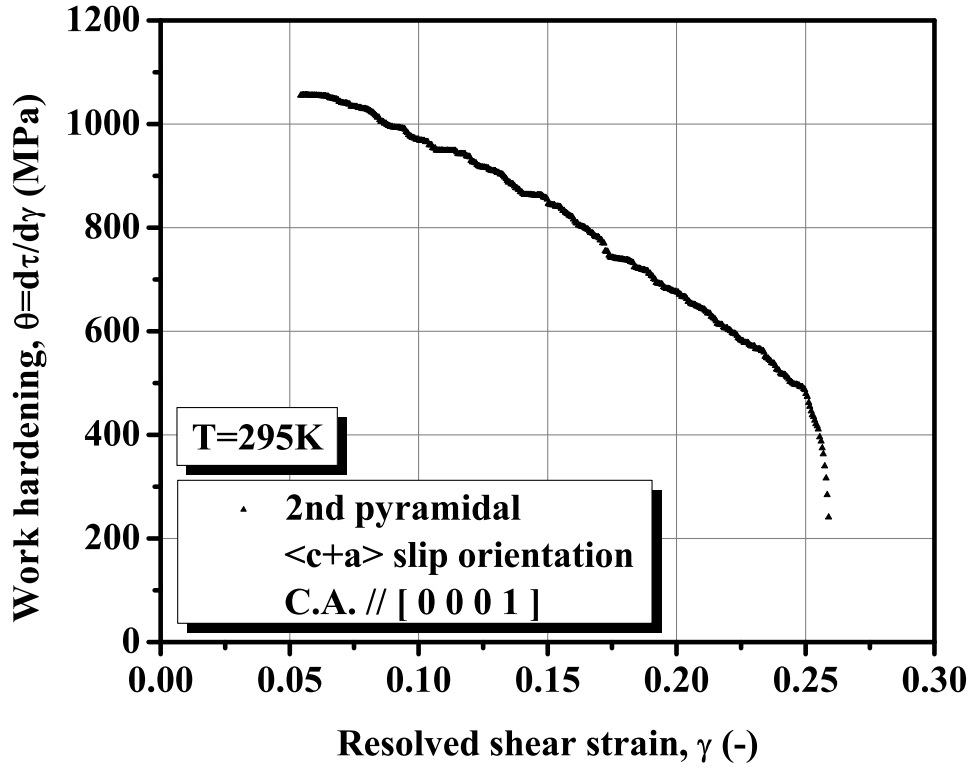

Figure 5.37: Work hardening versus resolved shear strain plot of Mg single crystal #4 deformed in the c-axis compression at 295K.

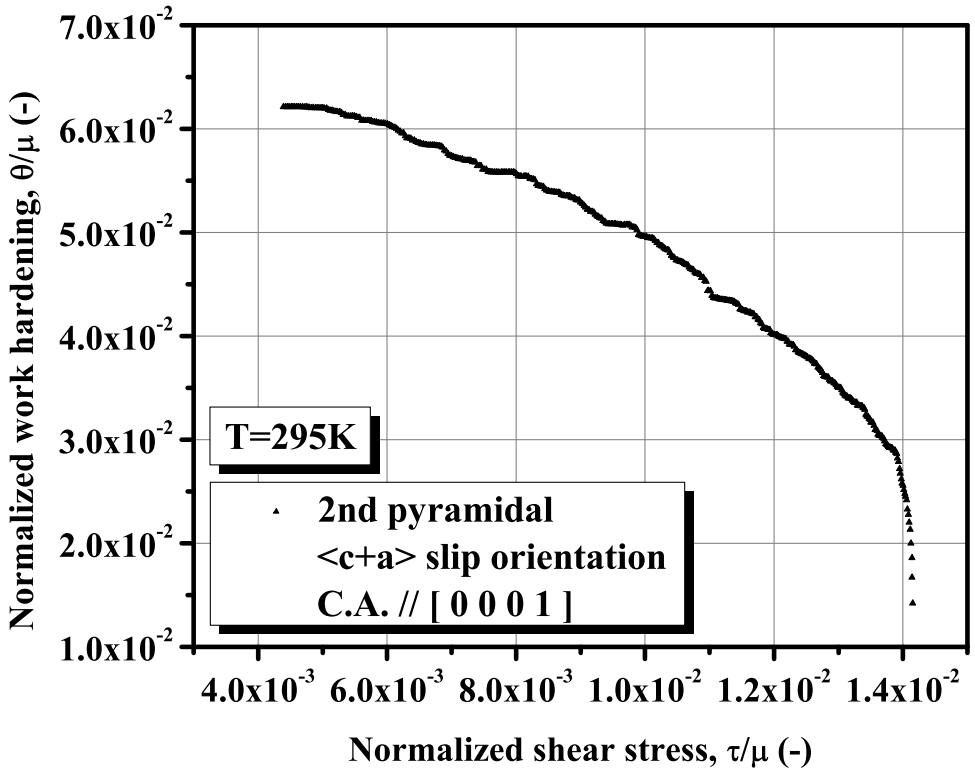

Figure 5.38: Normalized work hardening-shear stress plot of Mg single crystal #4 deformed in the c-axis compression at 295K.

Fig. 5.39 shows the Considère plot including true stress - true strain, $\sigma - \epsilon$ curve and work hardening - true strain, $\Theta(= d\sigma/d\epsilon) - \epsilon$ curve of Mg single crystal #4 deformed in compression at 295K. Unlike during compressive deformation of crystals #1, #2, and #3, present crystal #4 deformed in compression fractured by shear with the CR $\sim$ 3.82 (Fig. 5.39).

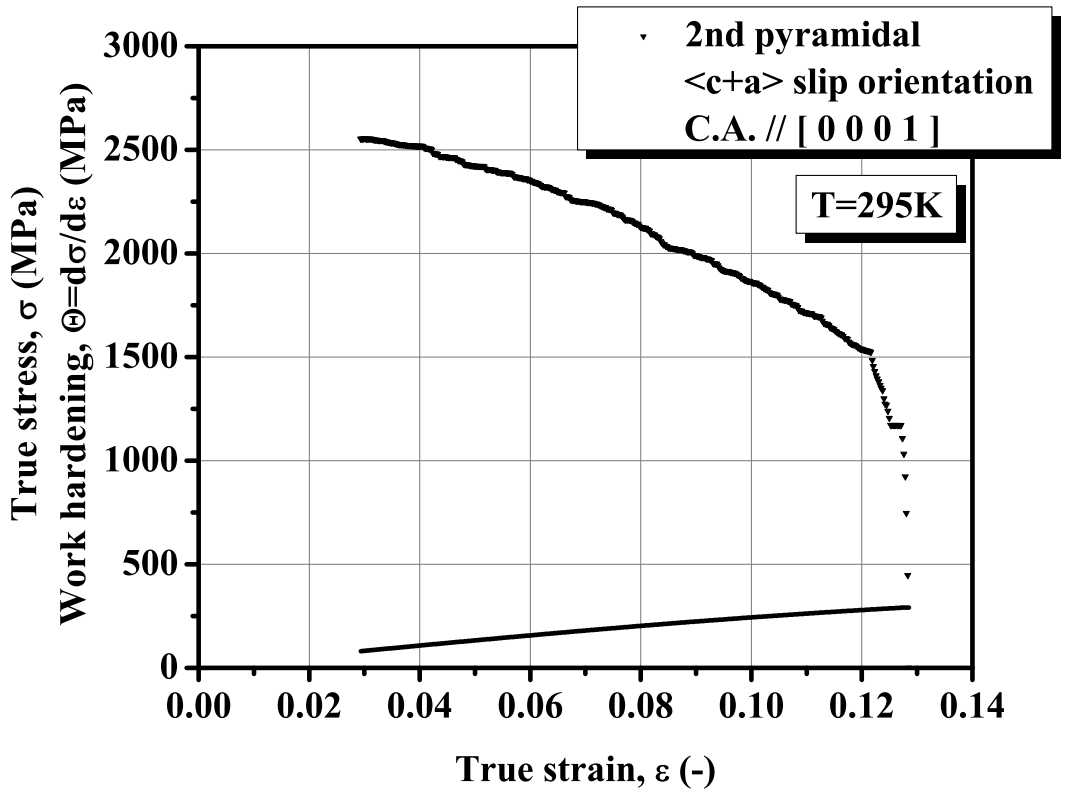

Figure 5.39: The Considère plot of Mg single crystal #4 oriented for 2^{nd} order pyramidal $< c + a >$ slip systems deformed in compression at 295K.

5.3 Latent hardening behaviour under basal - basal dislocation interactions

5.3.1 Orientations of primary and secondary specimens

Fig. 5.40 shows (0001) standard stereographic projection indicating the tensile axis positions of both parent crystals and secondary samples and traces of the wide faces of the parent crystals. Open circles in the figure presents the tensile axis of the parent crystals #a - #e. Maximum Schmid factor for basal $< a >$ slip calculated from the initial orientations was 0.47-0.50 in all the parent crystals #a - #f, whose values were considered to be high enough for homogeneous deformation of the specimens by basal $< a >$ slip only. The secondary samples can be selected along the trace of the wide sides of the parent crystals, labeled as "a - a" to "e - e" on the stereographic projection. In this study, the secondary samples were cut to examine latent hardening behaviour under the conditions of self-interactions, where dislocations with the same Burgers vector are activated in the secondary and primary samples, and under conditions of coplanar interactions, where dislocations of two basal slip systems interact during primary and secondary deformation tests. In Mg single crystals, basal $< a >$ slip is a dominant deformation mode at 295K, regardless of the crystal orientation, because of the lowest CRSS. However, one must note that homogeneous deformation by single basal $< a >$ slip is limited to specific areas of the orientation space. (Hirsch and Lally, 1965) have pointed out that the angle between the slip direction and the tensile axis should be between $40° - 60°$ for the initially single basal $< a >$ slip deformation. If the angle between the tensile axis and the slip direction is too large or too small, inhomogeneous deformation associated with kink bands and deformation twins

occurs in addition to the basal $< a >$ slip. Therefore to conduct the latent hardening experiments under the condition of pure basal $< a >$ dislocation interactions, "safe" regions for the orientations of the crystals were selected with the value of the basal Schimd factor within $0.40 - 0.50$, except the orientations on the symmetry line.

To investigate the hardening effect under conditions of self-interactions between dislocation of the same basal slip system, secondary samples #a1, #b1, #c1, #d1 and #e1 were cut at 0^o from the pre-deformed parent crystals #a - #e, as shown in Fig. 5.40. On the other hand, to inspect the latent hardening effect under conditions of coplanar dislocation interactions, secondary samples #a2, #b2, #c2, #d2 and #e2 were cut at 90^o from the pre-deformed parent crystals #a - #e. It should be noticed that in Fig. 5.40, the tensile axes of all primary and secondary samples are located within "safe zones" of high basal Schmid factor, marked by dashed areas, and they are predicted to deform homogeneously by single basal $< a >$ slip.

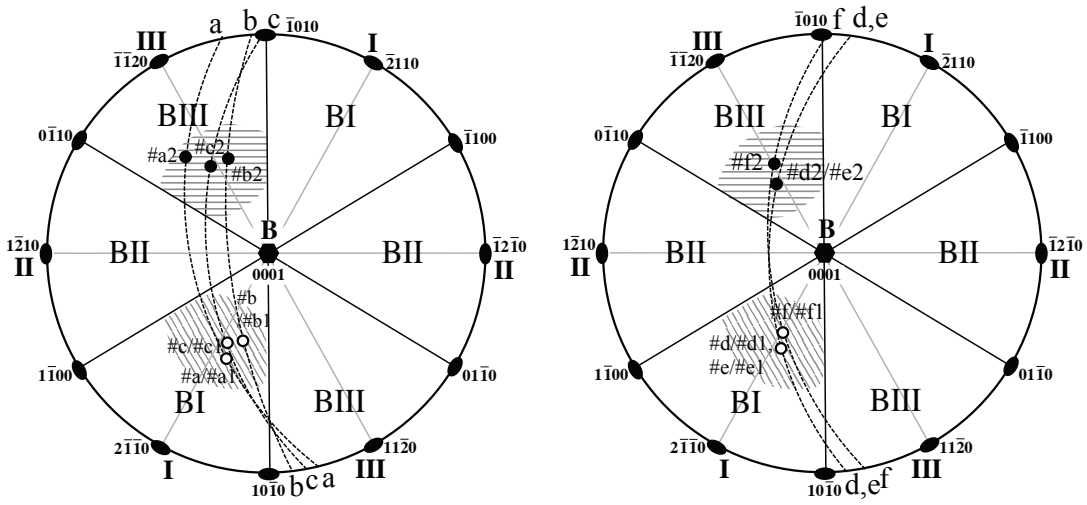

Figure 5.40: The standard (0001) stereographic projection indicating the orientations of the tensile axes of both parent crystals #a - #e and secondary samples (#a1 - #e1, #a2 - #e2) used in latent hardening experiments. Open circles indicate orientations of primary samples, dark circles represent orientation of secondary samples. The traces of the wide surfaces of parent crystals are depicted by dashed great circles (a-a) - (e-e).

Fig. 5.41 shows the variations of basal Schmid factors against the cutting angle on the parent crystal #c and the secondary sample #c1 and #c2, where clockwise direction with respect to the tensile axis of the parent crystal is defined as $+\theta$ and anti-clockwise direction is $-\theta$ angle. In Fig. 5.41, the basal Schmid factor on BI slip system assumes maximum value, -0.48 at 0^o. As the cutting angle increases in the clockwise direction, the Schmid factor for BI slip system decreases and alternatively the Schmid factor for BIII slip system increases. At 90^o, the Schmid factor for BIII

slip system is 0.49. More detailed data for crystallographic orientations, the Schmid factors and possible interaction types between active slip systems are summarized in Table 5.3 and 5.4 with experimental results discussed in next subsection 5.3.2.

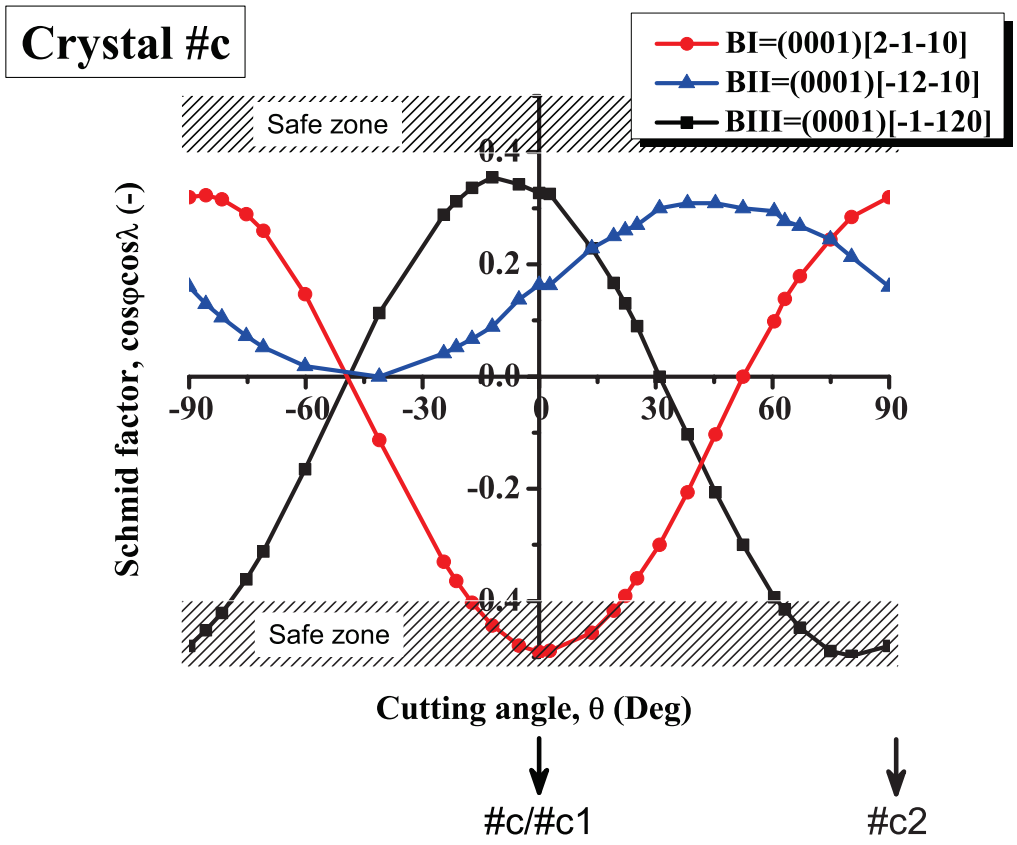

Figure 5.41: Schmid factors variations for basal $< a >$ slip systems, BI, BII, and BIII as a function of cutting angle in crystal #c.

5.3.2 Latent hardening behaviours

The tensile axis of the parent crystal #c was $[5\bar{2}\bar{3}(8/\lambda^2)]$ with the Schmid factor for basal BI system $S.F._{basal}^{BI} = 0.49$. Secondary sample #c1 was cut paralleled to the

tensile axis of the parent crystal #c, while secondary sample #c2 was cut perpendicular to the tensile axis of the parent crystal #c from middle parts of the parent crystal, as shown in Fig. 5.45 (a). The tensile axis of the secondary sample #c1 was the same as the parent crystal i.e., $[5\bar{2}\bar{3}(8/\lambda^2)]$ (S.F.$^{BI}_{basal} = 0.49$), which induced self-interactions of basal dislocations of systems BI and BI on the basal plane. In contrast, the tensile axis of the secondary sample #c2 was $[\bar{3}\bar{4}7(9/\lambda^2)]$ (S.F.$^{BIII}_{basal} = 0.48$), which induced co-planar interactions between systems BI and BIII on the basal plane.

Fig. 5.42 - Fig. 5.44 show typical tensile characteristics of the parent crystal #c and the secondary samples #c1-no.1 and #c2-no.1 including $\tau-\gamma$ and $\theta-\gamma$ plots and normalized work hardening rate versus normalized shear stress, $\theta/\mu - \tau/\mu$ plot. As previously, the $\tau - \gamma$ characteristics were recalculated from raw data, assuming that only single basal $< a >$ slip on the primary BI slip system operates during primary deformation. The plastic flow curve shows an easy glide stage by single basal $< a >$ slip after the yielding. The CRSS for the basal $< a >$ slip was determined by the intersection of the elastic and plastic region of the $\tau - \gamma$ curve and the value was 0.70 MPa, showing good reproducibility with the results reported in section 5.2.2. The work hardening rate for parent crystal #c was in the range $1.0 - 2.5$MPa or $5.0x10^{-5}\mu - 1.5x10^{-4}\mu$. The uniaxial tensile deformation of the parent crystal was stopped at about 22% shear strain, in the middle of easy glide stage and the secondary samples were cut from the crystal.

The CRSS values of sample #c1-no.1 and #c2-no.1, were 1.04MPa and 1.35MPa respectively. The range of work hardening for the secondary samples was between $0.5-2.25$MPa or $4.0x10^{-5}\mu-1.3x10^{-4}\mu$ for crystal #c1-no.1 and between $0.5-2.5$MPa

or $5.0x10^{-5}\mu - 1.4x10^{-4}\mu$ for the secondary sample #c2-no.1. The initial flow stress for co-planar system was somewhat higher than that for self-interaction system. However, the work hardening for both specimens was almost at the same level.

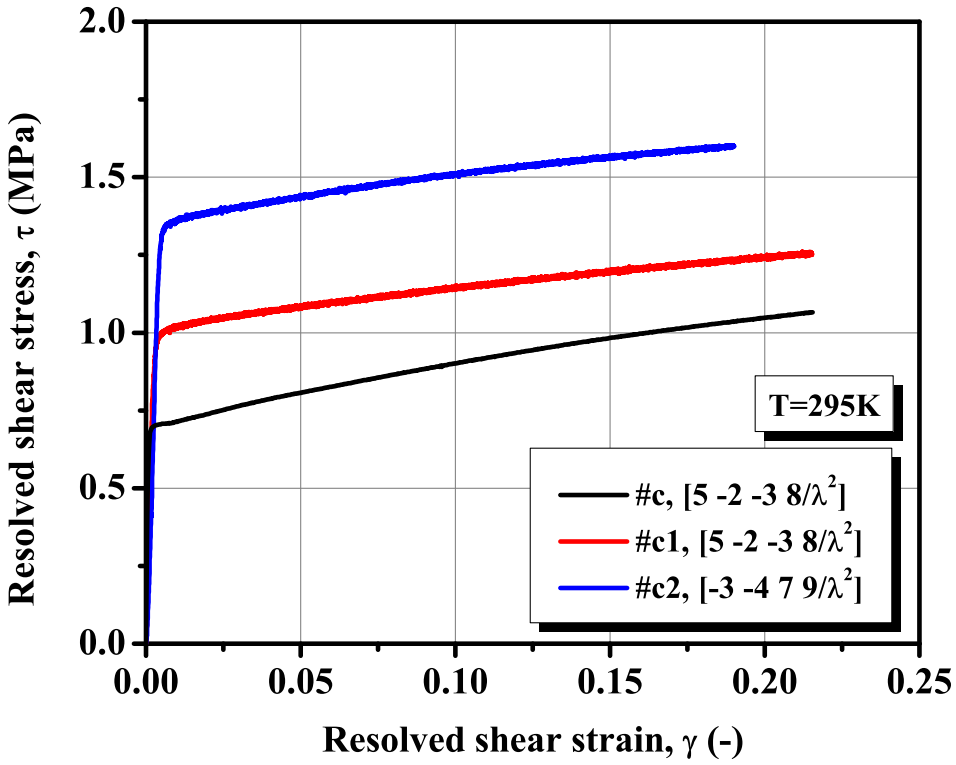

Figure 5.42: Resolved shear stress versus resolved shear strain curves of parent crystal #c and secondary samples #c1 and #c2 deformed in tension at 295K.

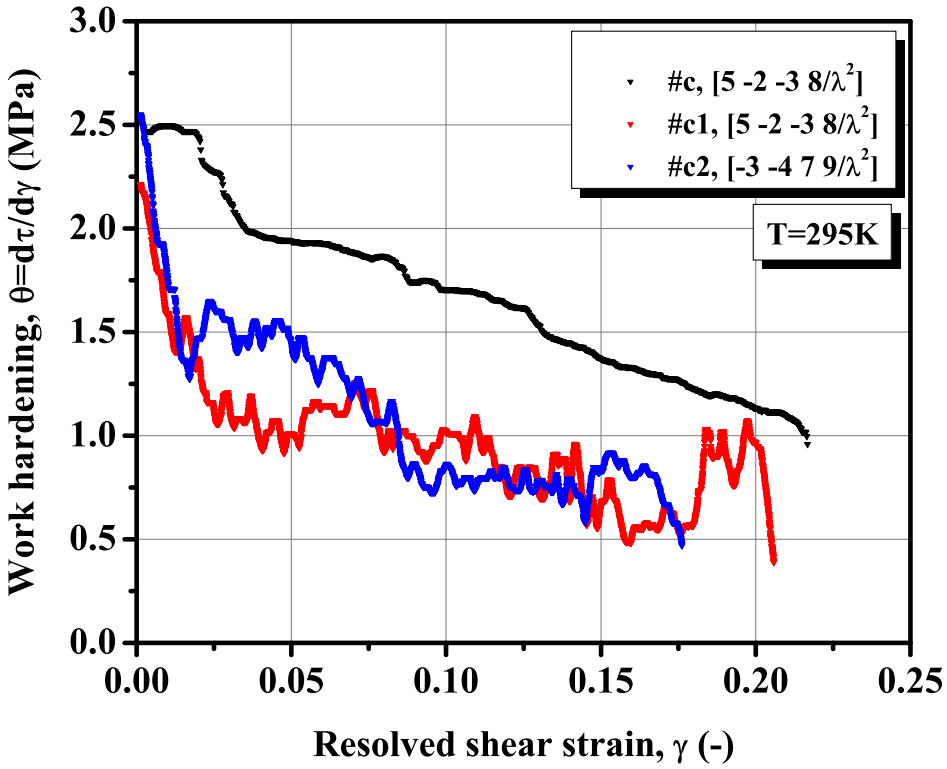

Figure 5.43: Work hardening versus resolved shear strain plots of parent crystal #c and secondary samples #c1 and #c2 deformed in tension at 295K.

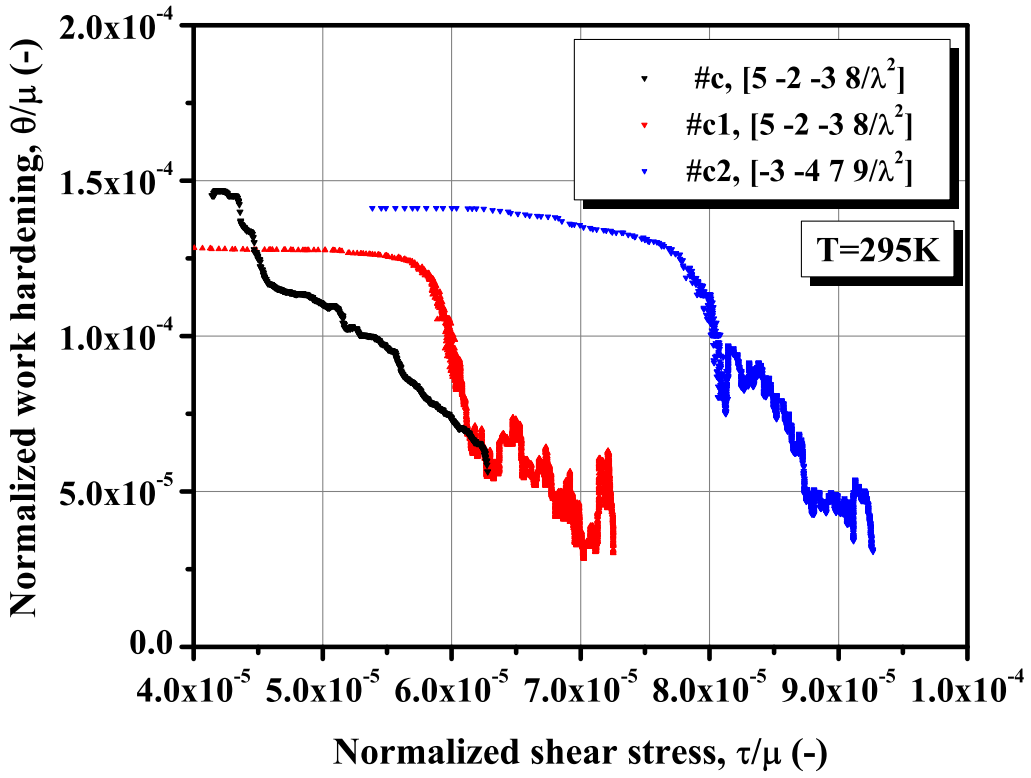

Figure 5.44: Normalized work hardening-normalized shear stress plots of parent crystal #c and secondary samples #c1 and #c2 deformed in tension at 295K.

Fig. 5.45 (a) shows a macroscopic view of the parent crystal #c deformed to 22% shear strain. The figure reveals that macroscopic deformation of the crystals is homogeneous and no formation of kink bands or deformation twins is observed. An optical microscopy observations of slip traces on the wide surface of deformed parent crystal shows slip traces form homogeneous basal $< a >$ slip, as visible in Fig.5.45(b). It is clear that there is no evidence of any inhomogeneous deformation due to kink bands or deformation twining and the plastic flow occurs by single basal

slip. Therefore, the analysis of mechanical properties of parent crystals based on the resolved shear stress and the resolved shear strain data for the BI slip system is valid on the assumption that this slip mode is the only mechanism operating during crystal deformation.

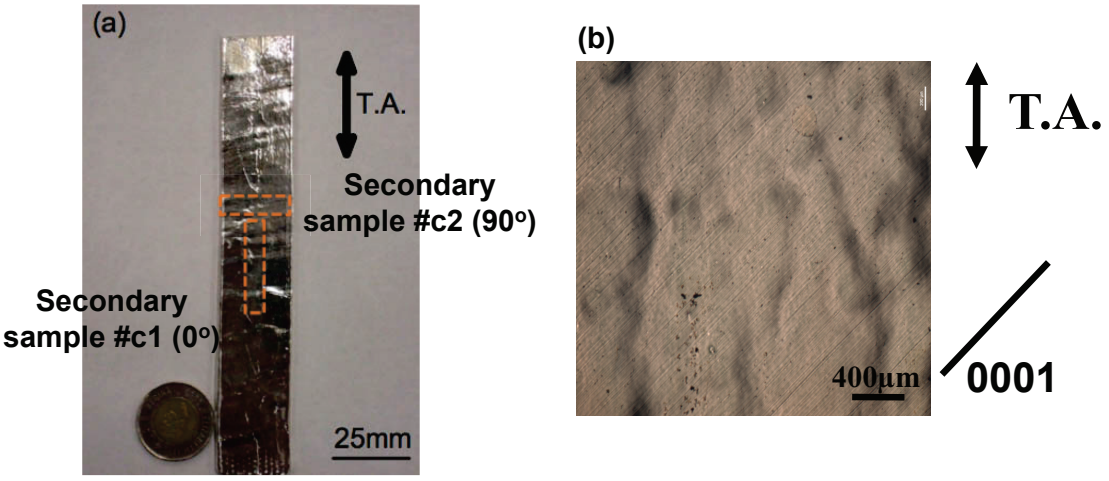

Figure 5.45: OM observations of parent crystal #c deformed in tension to 22% shear strain at 295K.

Fig. 5.46 (a) shows a macroscopic view of secondary samples #c1-no.1 and #c2-no.1 deformed in tension to ∼20% shear strain at 295K. The observations reveal that the crystals deform homogeneously without formation of kink bands or deformation twins. An optical microscopy observation of slip traces on wide surface of the deformed parent crystals in Fig. 5.46(b) shows homogeneous basal $< a >$ slip. No other surface patterns corresponding to kink bands and deformation twins was found in entire surface area. Therefore, the analysis of the mechanical properties of secondary samples based on the resolved shear stress and the resolved shear strain characteristics for the BI slip system was valid based on the assumption that this slip

mode is the only mechanism operating during the crystal deformation.

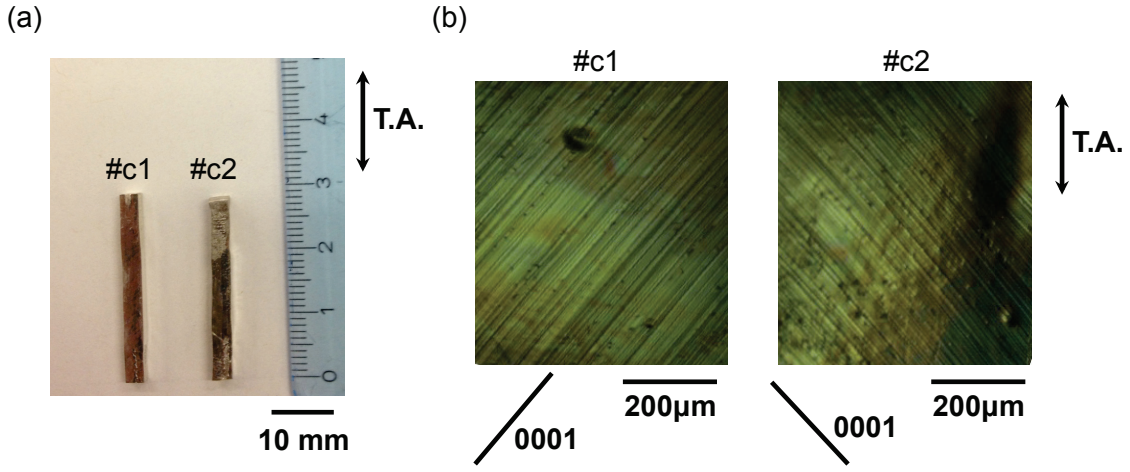

Figure 5.46: OM observations of secondary samples #c1 and #c2 deformed in tension to another 10% strain at 295K.

Latent hardening behaviour are usually characterized by latent hardening ratios (LHRs), which is defined as the ratio of the initial resolved shear stress of secondary sample, $\tau_0^{(j)}$ over final resolved shear stress of parent crystal, $\tau_{max}^{(i)}$, i.e.,

$$LHR = \frac{\tau_0^{(j)}}{\tau_{max}^{(i)}}. \tag{5.2}$$

Latent hardening experiments were carried out with parent samples pre-deformed to the different amounts of primary deformation: 0%, 6%, 11%, 22%, 35%, and 49% shear strain, respectively. Table 5.3 and 5.4 summarizes all the experimental results on the latent hardening tests, which include: crystallographic orientations, Schmid factor of dominant slip system, latent hardening type, pre-deformed strain amount, final flow stress of parent crystals, yield stress of secondary samples, work hardening and latent

hardening ratio (LHR). Latent hardening characteristics with respect to the primary strain and the primary stress are plotted based on the mechanical characteristic data of the parent crystals #a - #e and the secondary samples #a1 - #e1 and #a2 - #e2, listed in Table 5.3 and 5.4. Fig. 5.47 shows LHRs plots as a function of the primary strain, $\tau_0^{(j)}/\tau_{max}^{(i)} - \gamma^{(i)}$ plots, showing latent hardening behaviour under the interaction with self- and coplanar slip systems. Fig. 5.47 shows LHRs plots as a function of the normalized primary stress, $\tau_0^{(j)}/\tau_{max}^{(i)} - (\tau_{max}^{(i)} - \tau_0^{(i)})/\tau_0^{(i)}$ plots, where $\tau_0^{(i)}$ represents the CRSS on system i during the primary deformation. Each data point is a mean value of several measurements and the experimental error is indicated by the standard deviation.

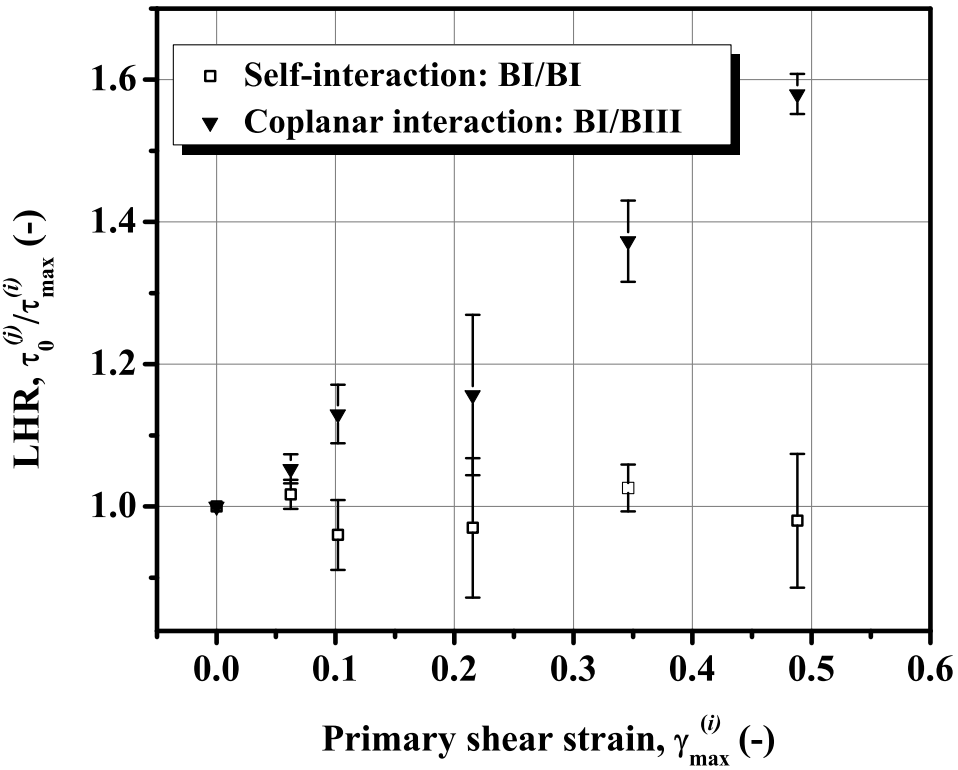

Figure 5.47: LHR values as a function of primary shear strain for self- and coplanar interactions on the basal plane in Mg single crystals.

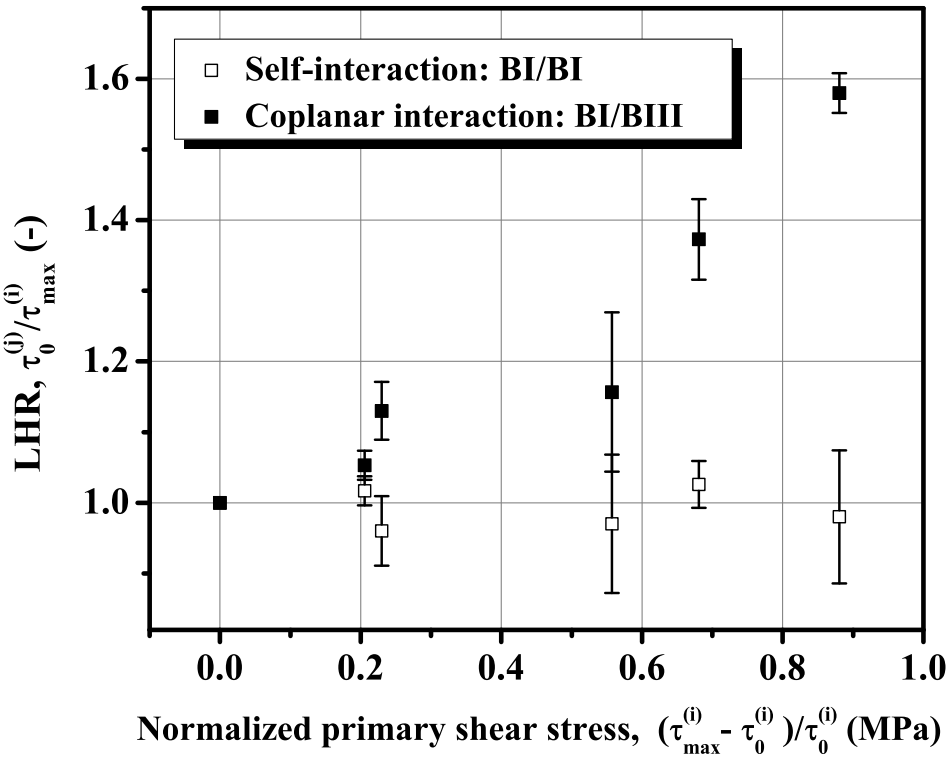

Figure 5.48: LHR values as a function of normalized primary shear stress for self- and coplanar interactions on the basal plane in Mg single crystals.

The results in Figs. 5.47 and 5.48 indicate that three equivalent basal $< a >$ slip systems in well-annealed Mg single crystals have initially the same strength and therefore the LHRs are close to 1.0 in annealed and non-deformed crystals. For all latent hardening tests, coplanar interactions between BI and BIII slip systems induce more hardening than the self-interactions between primary slip system BI and BI. In other words, the LHR in the self-hardening process where the dislocations of the latent slip system BI in the secondary tensile test interact with stored parent

Table 5.3: Primary deformation tests data.

No.	Initial orientation	m [-]	$\gamma_{max}^{(i)}$ [%]	$\tau_0^{(i)}$ [MPa]	$\tau_{max}^{(i)}$ [MPa]	$\theta^{(i)}$ x$10^{-5}\mu$ [MPa]
a	$[7\bar{3}\bar{4}(8/\lambda^2)]$	0.47 (BI)	6	0.68	0.82	8.0-13
b	$[4\bar{1}\bar{3}(7/\lambda^2)]$	0.47 (BI)	11	0.74	0.91	8.0-30
c	$[5\bar{2}\bar{3}(8/\lambda^2)]$	0.49 (BI)	22	0.70	1.09	5.0-15
d	$[7\bar{3}\bar{4}(9/\lambda^2)]$	0.48 (BI)	35	0.72	1.21	7.0-10
e	$[7\bar{3}\bar{4}(9/\lambda^2)]$	0.48 (BI)	49	0.67	1.26	6.0-10
f	$[6\bar{3}\bar{3}(10/\lambda^2)]$	0.49 (BI)	0	0.70	-	-

† m is Schmid factor; $\gamma_{max}^{(i)}$ [%] is the maximum shear strain of parent crystals; $\tau_0^{(i)}$ [MPa] is the critical resolved shear stress (CRSS) of parent crystals; $\tau_{max}^{(i)}$ [MPa] is the maximum shear stress of parent crystal; $\theta^{(i)}(=\mathrm{d}\tau^{(i)}/\mathrm{d}\gamma^{(i)})$ [MPa] is the work hardening of parent crystals.

dislocations of slip system BI, induce no hardening and LHR is close to unity. On the other hand, when dislocations of latent slip system BIII in the secondary sample interact with stored dislocations of primary slip system BI, these interactions lead to the hardening and the LHR for the latent slip direction is higher than that of the self-hardening. Figs. 5.47 and 5.48 reveal that the LHRs for co-planar system BI/BIII increases from 1.0 to 1.6 with increasing the primary shear strain, whereas the LHR for self-interaction between BI/BI slips systems is independent on the pre-strain.

Table 5.4: Secondary deformation tests data.

No.	Initial orientation	m [-]	Interaction type	$\tau_0^{(j)}$ [MPa]	$\theta^{(j)}$ x$10^{-5}\mu$ [MPa]	LHR [-]
a1-no.1				0.81	6.0-20	0.99
a1-no.2	$[7\bar{3}\bar{4}(8/\lambda^2)]$	0.47 (BI)	BI/BI	0.85	6.0-43	1.04
a1-no.3				0.84	8.0-30	1.02
a2-no.1				0.84	7.0-23	1.03
a2-no.2	$[\bar{1}\bar{2}3(3/\lambda^2)]$	0.46 (BIII)	BI/BIII	0.89	9.0-43	1.08
a2-no.3				0.86	4.5-23	1.05
b1-no.1				0.92	8.0-40	1.01
b1-no.2	$[4\bar{1}\bar{3}(7/\lambda^2)]$	0.47 (BI)	BI/BI	0.87	9.0-23	0.96
b1-no.3				0.81	7.0-13	0.89
b2-no.1				1.03	5.0-25	1.13
b2-no.2	$[\bar{3}\bar{3}6(8/\lambda^2)]$	0.49 (BIII)	BI/BIII	0.98	7.0-33	1.08
b2-no.3				1.07	6.0-23	1.18
c1-no.1				1.04	4.0-13	0.97
c1-no.2	$[5\bar{2}\bar{3}(8/\lambda^2)]$	0.49 (BI)	BI/BI	1.17	5.0-25	1.09
c1-no.3				0.91	5.0-30	0.85
c2-no.1				1.35	5.0-14	1.26
c2-no.2	$[\bar{3}\bar{4}7(9/\lambda^2)]$	0.48 (BIII)	BI/BIII	1.29	5.0-40	1.21
c2-no.3				1.07	5.0-45	1.00
d1-no.1				1.29	5.0-35	1.07
d1-no.2	$[7\bar{3}\bar{4}(9/\lambda^2)]$	0.48 (BI)	BI/BI	1.23	4.0-55	1.02
d1-no.3				1.20	6.5-45	0.99
d2-no.1				1.67	5.0-35	1.38
d2-no.2	$[\bar{3}\bar{4}7(13/\lambda^2)]$	0.49 (BIII)	BI/BIII	1.74	6.0-35	1.44
d2-no.3				1.57	6.0-40	1.30
e1-no.1				1.07	6.0-30	0.85
e1-no.2	$[7\bar{3}\bar{4}(9/\lambda^2)]$	0.48 (BI)	BI/BI	1.35	5.0-35	1.07
e1-no.3				1.29	5.0-37	1.02
e2-no.1				1.96	8.0-35	1.56
e2-no.2	$[\bar{3}\bar{4}7(13/\lambda^2)]$	0.49 (BIII)	BI/BIII	2.04	9.0-40	1.62
e2-no.3				1.97	8.5-40	1.56
f1-no.3	$[6\bar{3}\bar{3}(10/\lambda^2)]$	0.49 (BI)	-	0.70	-	1.00
f2-no.3	$[\bar{3}\bar{3}6(8/\lambda^2)]$	0.49 (BIII)	-	0.70	-	1.00

† $\tau_0^{(j)}$ [MPa] is CRSS of secondary samples; $\theta^{(j)}(=\mathrm{d}\tau^{(j)}/\mathrm{d}\gamma^{(j)})$ [MPa] is the work hardening of secondary samples; LHR$=\tau_0^{(j)}/\tau_{max}^{(i)}$ [-] is the latent hardening ratio.

5.4 Intermittent annealing experiments and unloading/reloading cyclic tests in Mg single crystals

Intermittent annealing experiments at room temperature were carried out to determine effect of unloading and sample resting on the flow stress and work hardening behaviour after unload. These data are critical to understand the amount of stress relaxation due to dislocations' rearrangements occurring in the sample on the flow stress. The crystals were oriented for basal $< a >$ slip with the tensile axis parallel to $[2\bar{1}\bar{1}2]$ direction. Fig. 5.49 shows true stress-true strain curves for samples deformed to a given strain, unloaded and subjected to intermittent annealing at 295K, with the resting time of 24 hours. The intermittent stress-strain curve exhibit behaviour typical for tensile deformation of Mg single crystals with single basal $< a >$ slip orientation (crystal #1), which exhibits easy glide stage (stage I), transition range from stage I to II, and short rapid hardening stage (stage II). From Fig. 5.49 it is seen that certain amount of stress recovers after each annealing treatment, depicted by points A - F.

In order to quantitatively evaluate the stress recovery $\Delta\sigma$, stress - strain curve of single crystal is processed as explained in Fig. 5.50. A crystal is strained to the point A on the stress - strain curve and is unloaded. After a certain resting (annealing) time at 295K, a smaller value of the yield stress is observed on reloading. The yield stress σ_2 is determined by the intersection of the elastic and plastic region of the $\sigma - \epsilon$ curves (Fig. 5.50). The stress recovery, $\Delta\sigma^{(i)}$ is expressed as the difference between the final flow stress of $(i-1)^{th}$ tensile deformation test and the yield stress of i^{th}

deformation test such that:

$$\Delta\sigma^{(i)} = \sigma_1^{(i-1)} - \sigma_2^{(i)}. \tag{5.3}$$

Using above definition, the stress recovery was calculated for every intermittent deformation and is summarized in Table 5.5. The table reveals that $\Delta\sigma$ increases with flow stress σ throughout the deformation.

Fig. 5.51 shows true stress versus true strain curves of Mg single crystal after cyclic unloading/reloading tests at 295K, without additional annealing at room temperature. Even if the crystal was reloaded without any annealing process, a similar stress recovery was observed during after each unloading/reloading cycle, i.e., at points A-E. However, the extent to stress recovery in large deformation stage was somewhat smaller than the intermittent deformation/annealing tests.

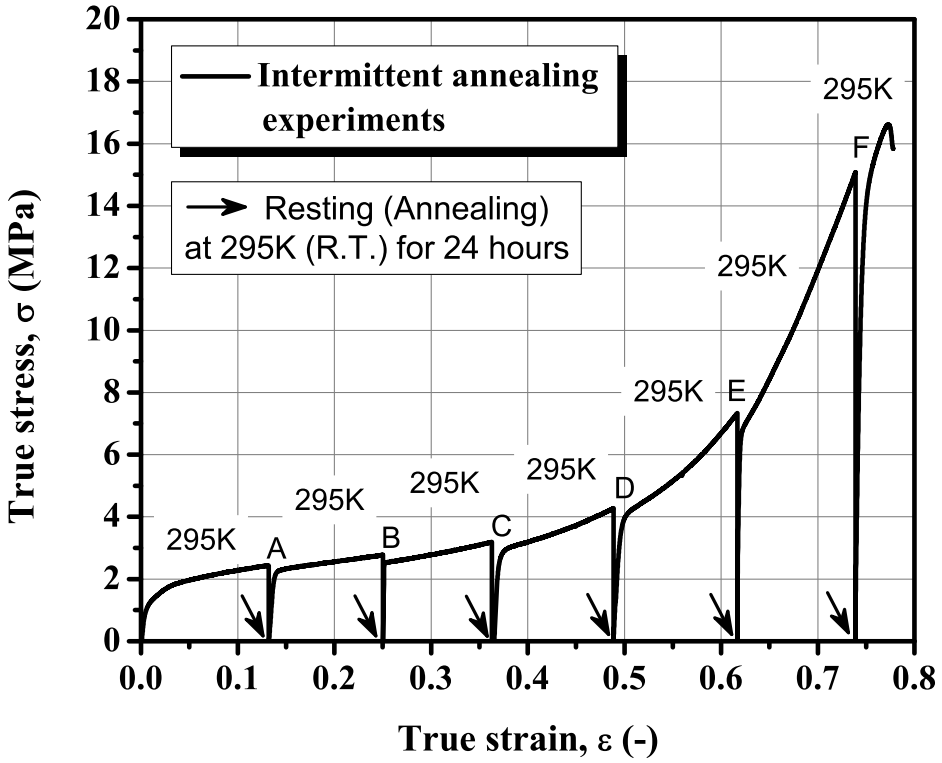

Figure 5.49: True stress versus true strain curve for the intermittent deformation/annealing test on Mg single crystal with single basal slip orientation at 295K.

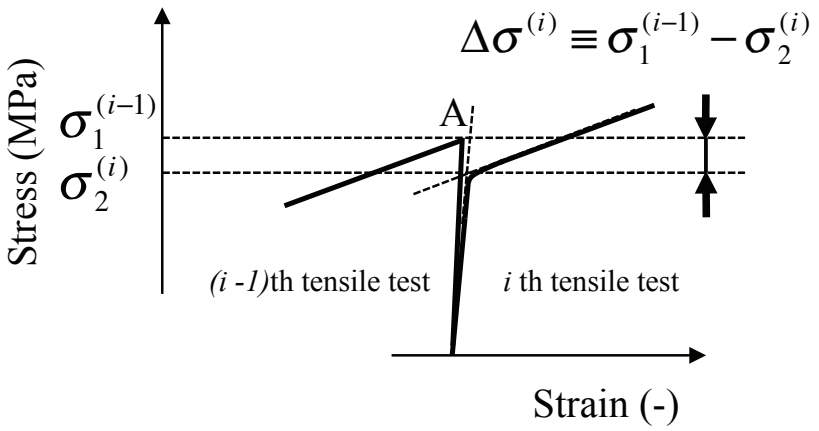

Figure 5.50: The definition of stress recovery effect, $\Delta\sigma^{(i)} = \sigma_1^{(i-1)} - \sigma_2^{(i)}$.

Table 5.5: Stress recovery data.

Points	σ_1 [MPa]	σ_2 [MPa]	$\Delta\sigma$ [MPa]	$\Delta\sigma/\sigma_1$ [-]
A	2.432	2.263	0.169	0.0695
B	2.762	2.515	0.247	0.0895
C	3.184	2.972	0.212	0.0666
D	4.271	3.992	0.279	0.0653
E	7.324	6.758	0.566	0.0773
F	15.083	13.834	1.249	0.0828

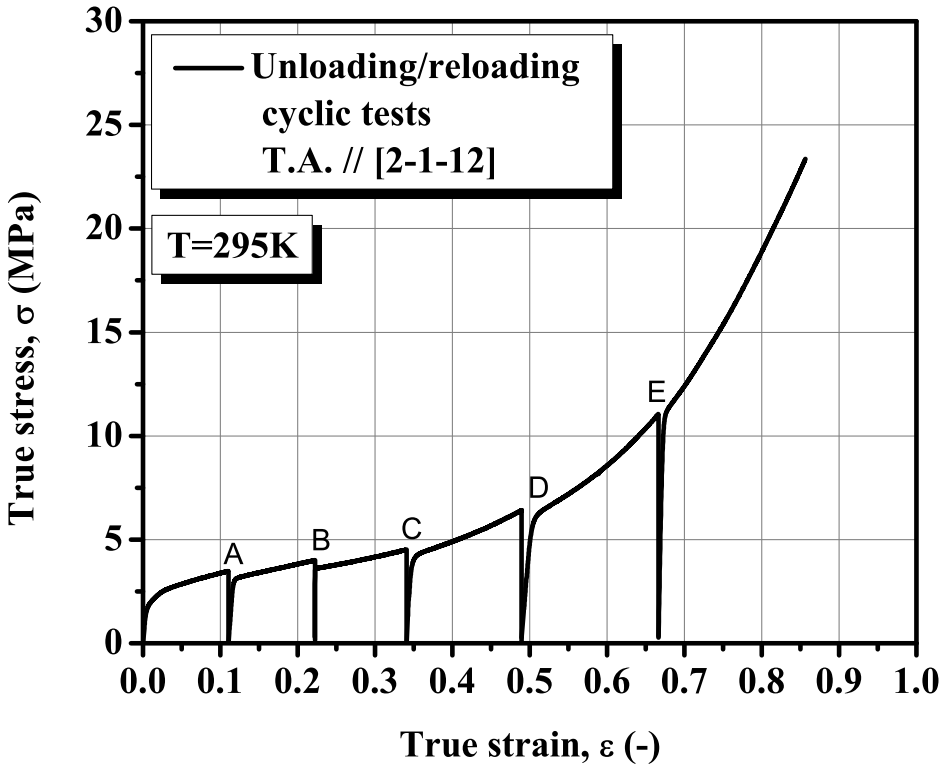

Figure 5.51: True stress versus true strain curve for the unloading/reloading test without annealing, on Mg single crystal with single basal slip orientation at 295K.

A large number of intermittent deformation/annealing experiments and unloading/reloading cyclic tests were carried out on Mg single crystals with the same conditions and they have been represented in terms of $\Delta\sigma$ as a function of σ. Fig. 5.52 shows $\Delta\sigma - \sigma$ plot obtained from many intermittent deformation/annealing experiments and unloading/reloading cyclic tests of Mg single crystals oriented for single basal slip at 295K. When the flow stress σ is low, within stage I, the stress recovery

$\Delta\sigma$ assumes a constant value $\sim$0.2MPa. However, when the deformation of the primary sample enters the stage II of work hardening, $\Delta\sigma$ increases roughy parabolically with substantial rate. Similarly, the stress recovery $\Delta\sigma$ for the unloading/reloading tests was approximately constant $\sim$0.2MPa, when the deformation was limited to the stage I and the flow stress σ was low. However, for more advanced deformation when the flow stress σ increases, $\Delta\sigma$ increases quadratically, but a rate of increase is considerably smaller, in comparison to the samples subjected to the intermittent deformation/annealing experiments.

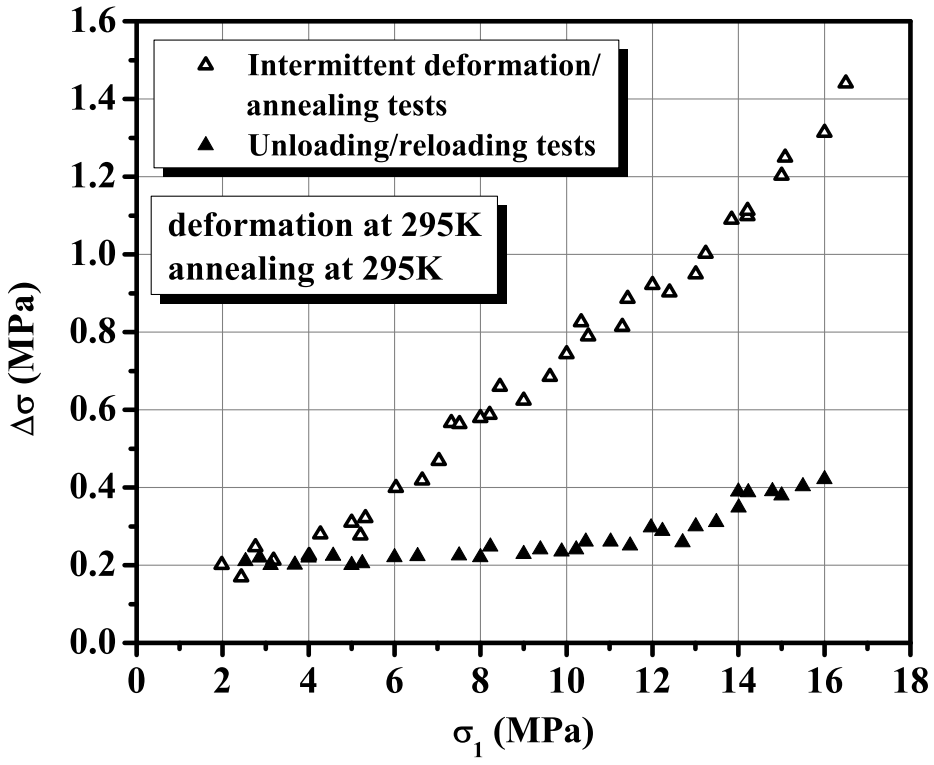

Figure 5.52: $\Delta\sigma$-σ_1 plots obtained from several intermittent deformation/annealing cyclic deformation tests of Mg single crystal with single basal slip orientation at 295K.

Fig. 5.53 shows normalized with respect to the reference flow stress, stress recovery as a function of reference stress, $\Delta\sigma/\sigma - \sigma$ plots obtained from intermittent deformation/annealing and unloading/reloading cyclic tests on Mg single crystals, which permit to determine if the Cottrel-Stokes law (Cottrell and Stokes, 1955) is obeyed or not. It is seen that as the reference stress σ increases, $\Delta\sigma/\sigma$ for intermittent deformation/annealing test decreases, reaches a minimum value of about 0.06, and then gradually increases throughout deformation, following response predicted

by the Cottrell-Stokes law. On the other hand, the unloading/reloading cyclic tests seems to violate the Cottrel-Stokes law through entire onset of plastic flow; the values of $\Delta\sigma/\sigma$ decrease continuously from 0.08 to 0.02, where some kind of saturation is observed.

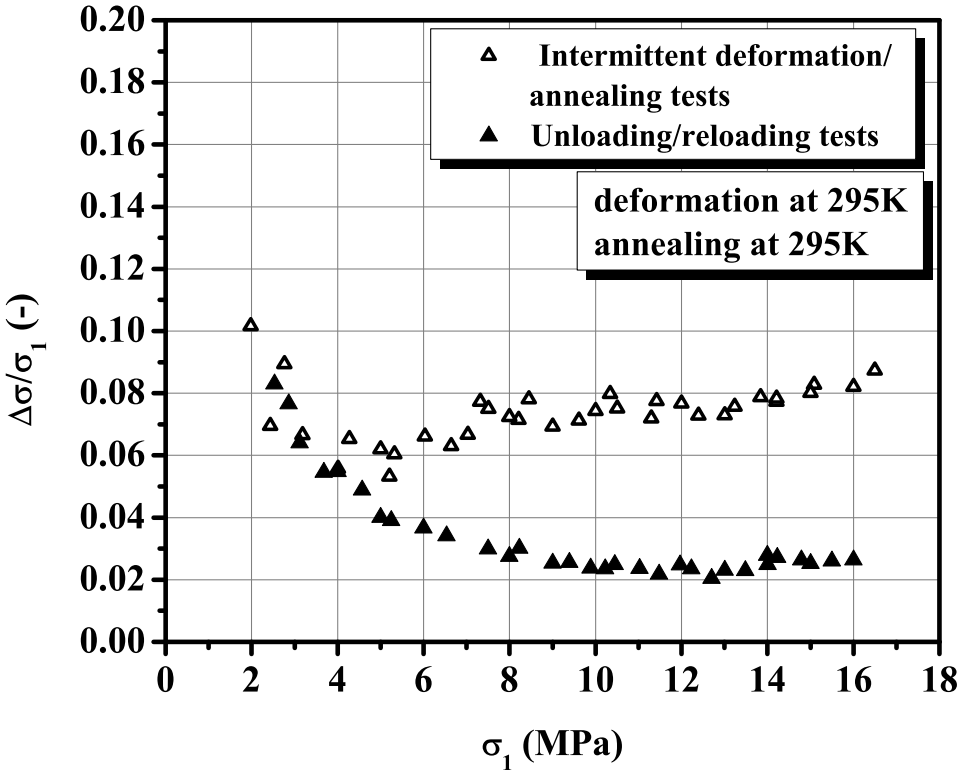

Figure 5.53: $\Delta\sigma/\sigma_1$-σ_1 plots obtained from several intermittent deformation/annealing cyclic deformation tests of Mg single crystal with single basal slip orientation at 295K.

5.5 Latent hardening behaviour under basal $< a >$ slip/$\{10\bar{1}2\} < 10\bar{1}1 >$ twin interactions

5.5.1 Orientations of primary and secondary specimens

Fig. 5.54 shows (0001) stereographic projection indicating tensile axis of parent crystal #x and secondary sample #x'. The tensile axis of the parent crystal #x was close to $[5\bar{1}\bar{4}15/\lambda^2]$, with the Schmid factor for BI system 0.37. Secondary samples has been cut along the trace of wide face of the parent crystals, labeled as x-x on the stereographic projection in Fig.5.54. The secondary sample #x' was selected at -30^o with respect to the tensile axis of the parent crystal #x. The Schmid factors for basal $< a >$ slip, 2^{nd} order pyramidal $< c+a >$ slip, and $\{10\bar{1}2\} < 10\bar{1}1 >$ twin systems in parent crystal #x and secondary sample #x' are listed in Table 5.6. The tensile axis of secondary sample #x' is exactly parallel to [0001] and $\{10\bar{1}2\} < 10\bar{1}1 >$ twining should be the operating deformation mode when the crystal is deformed in tension. As a result, latent hardening behaviour due to basal $< a >$ slip/$\{10\bar{1}2\} < 10\bar{1}1 >$ twin interactions has been evaluated.

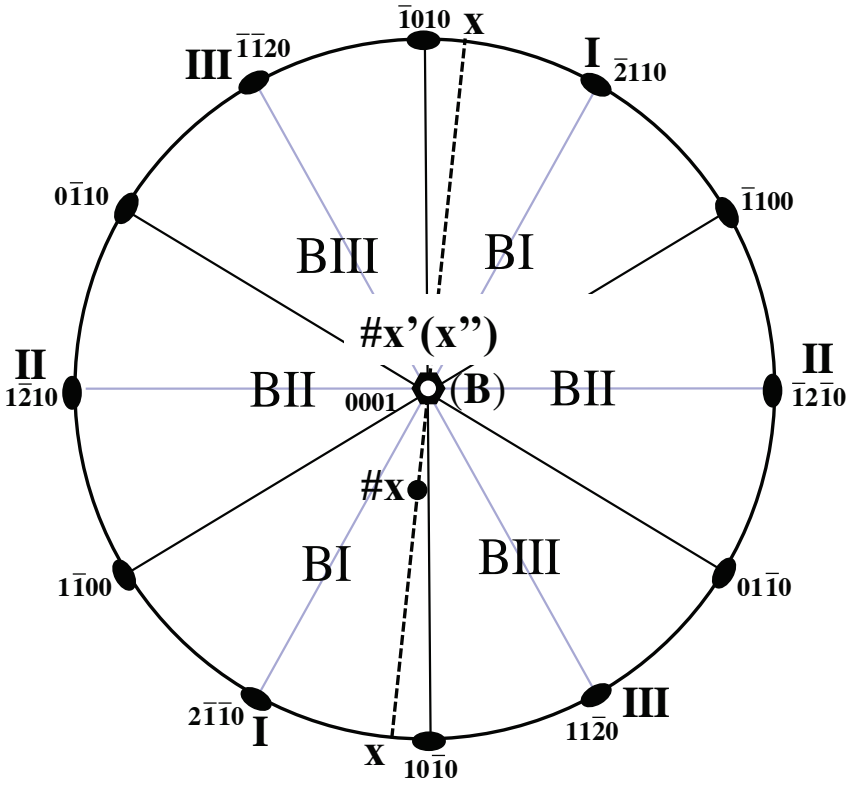

Figure 5.54: The (0001) standard stereographic projections indicating tensile axis of the parent crystal #x and the secondary sample #x' (#x").

5.5.2 Mechanical properties of parent #x and secondary sample #x'

Fig. 5.55 - Fig. 5.57 show typical mechanical behaviour of the parent crystal #x and the secondary sample #x'-No.4 (fractured) deformed in tension at 295K represented by $\tau - \gamma$, $\theta - \gamma$ and θ/μ-τ/μ plots.

Table 5.6: Schmid factors for basal $< a >$ slip, 2^{nd} order $< c + a >$ pyramidal slip, and $\{10\bar{1}2\} < 10\bar{1}1 >$ twin systems in parent crystal #x and secondary sample #x' (#x").

Deformatin modes	Notation	Miller-Bravais index	Schmid factors	
			#x	#x'
Basal $< a >$ slip	BI	$(0001)[2\bar{1}\bar{1}0]$	0.41	0
	BII	$(0001)[\bar{1}2\bar{1}0]$	0.08	0
	BIII	$(0001)[\bar{1}\bar{1}20]$	0.33	0
2^{nd} order pyramidal $< c + a >$ slip	II.Py1	$(11\bar{2}2)[\bar{1}\bar{1}23]$	0.42	0.45
	II.Py2	$(\bar{1}2\bar{1}2)[1\bar{2}13]$	0.30	0.45
	II.Py3	$(\bar{2}112)[2\bar{1}\bar{1}3]$	0.05	0.45
	II.Py4	$(\bar{1}\bar{1}22)[11\bar{2}3]$	0.13	0.45
	II.Py5	$(1\bar{2}12)[\bar{1}2\bar{1}3]$	0.37	0.45
	II.Py6	$(2\bar{1}\bar{1}2)[\bar{2}113]$	0.42	0.45
$\{10\bar{1}2\} < 10\bar{1}1 >$ twin	A'1'	$(10\bar{1}2)[\bar{1}011]$	0.30	0.50
	B'2'	$(01\bar{1}2)[0\bar{1}11]$	0.35	0.50
	C'3'	$(\bar{1}102)[1\bar{1}01]$	0.34	0.50
	D'4'	$(\bar{1}012)[10\bar{1}1]$	0.28	0.50
	E'5'	$(0\bar{1}12)[01\bar{1}1]$	0.37	0.50
	F'6'	$(1\bar{1}02)[\bar{1}101]$	0.30	0.50

In the parent crystal, the plastic flow after the yielding initiates by single basal $< a >$ slip. The CRSS for the basal $< a >$ slip was determined to be 0.47 MPa. The work hardening rate of parent crystal #x was in the range $8.0x10^{-5}\mu - 1.6x10^{-4}\mu$. The uniaxial tensile deformation of the parent crystal was stopped at 22% shear strain, in the middle of easy glide stage and the secondary samples were cut from the deformed parent crystal.

In the secondary sample, the resolved shear stress and shear strain on the $(10\bar{1}2)$

plane were recalculated from experimental raw data, assuming that $\{10\bar{1}2\} < 10\bar{1}1 >$ twinning was the only deformation mechanism operating during the deformation. Twinning deformation is associated with stress instabilities resulting from repeated twin nucleation and propagation. The onset of $\{10\bar{1}2\} < 10\bar{1}1 >$ twinning was determined as the point of flow stress in which the first stress drop occurred, marked as arrowhead in Fig. 5.55 with the CRSS value of 3.01MPa. Similar to the tensile deformation of crystal #4, profuse twinning deformation was observed after the yielding until 8-9% shear strain, followed by the transition stage and rapid hardening stage. The crystal was fractured at around 20 % shear strain, as visible in Fig. 5.55.

The stretch AB represents work hardening rate during profuse twinning deformation (stage I) at the almost constant values about 50MPa. The stage I was extended until about 6% shear strain. Following the twinning stage, the work hardening rapidly increased by a factor of about 6, recognized as the transition region between $7\% - 11\%$ shear strain, depicted as the stretch BC. The stretch CD in the figure shows rapid work hardening stage characterized by gross plastic deformation and the $\theta \sim 300$MPa. The stage II proceeded from 14% to 16% shear strain.

During twinning deformation, the curve was quite noisy due to the stress serration with $\theta_{twin}/\mu \sim 1.7x10^{-3} - 4.0x10^{-3}$, denoted as stretch A'B' in the figure. With rising shear strain, the work hardening rate increases linearly defined as the stretch B'C', achieving the maximum value $\theta_{II}/\mu \sim 1.8x10^{-2}$ during the stretch C'D'. Fracture of the crystal occurred suddenly after the relatively short deformation in stage II.

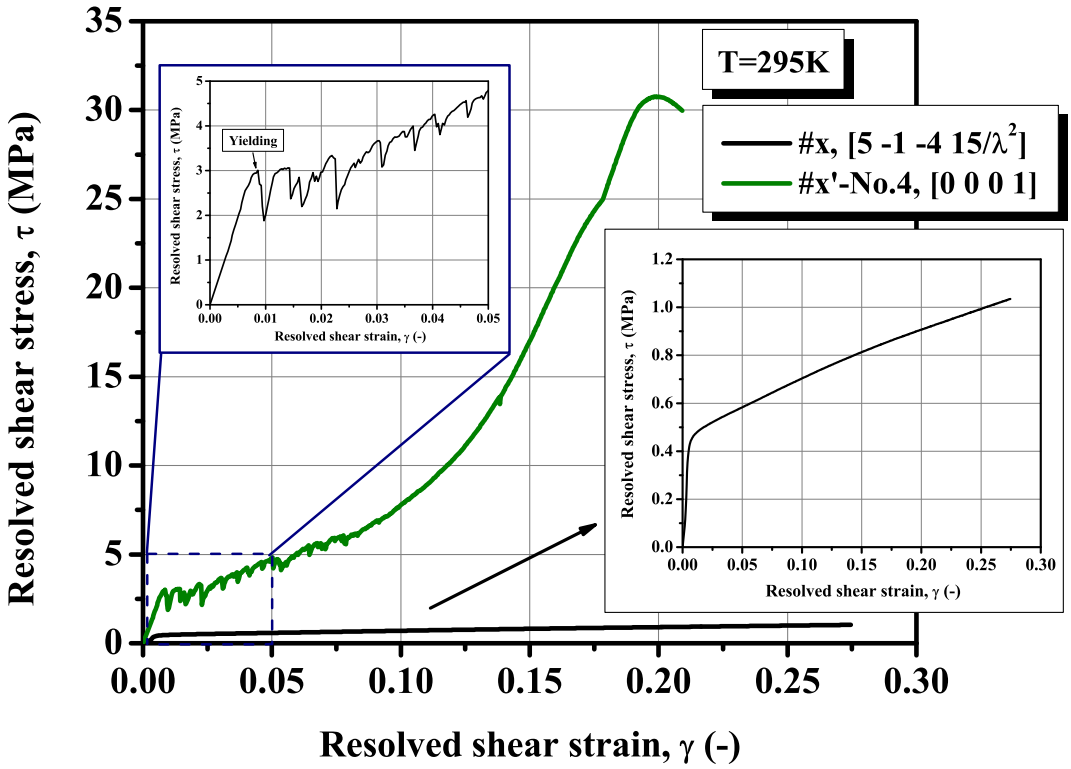

Figure 5.55: Resolved shear stress versus shear strain curves of parent crystal #x and secondary sample #x' deformed in tension at 295K.

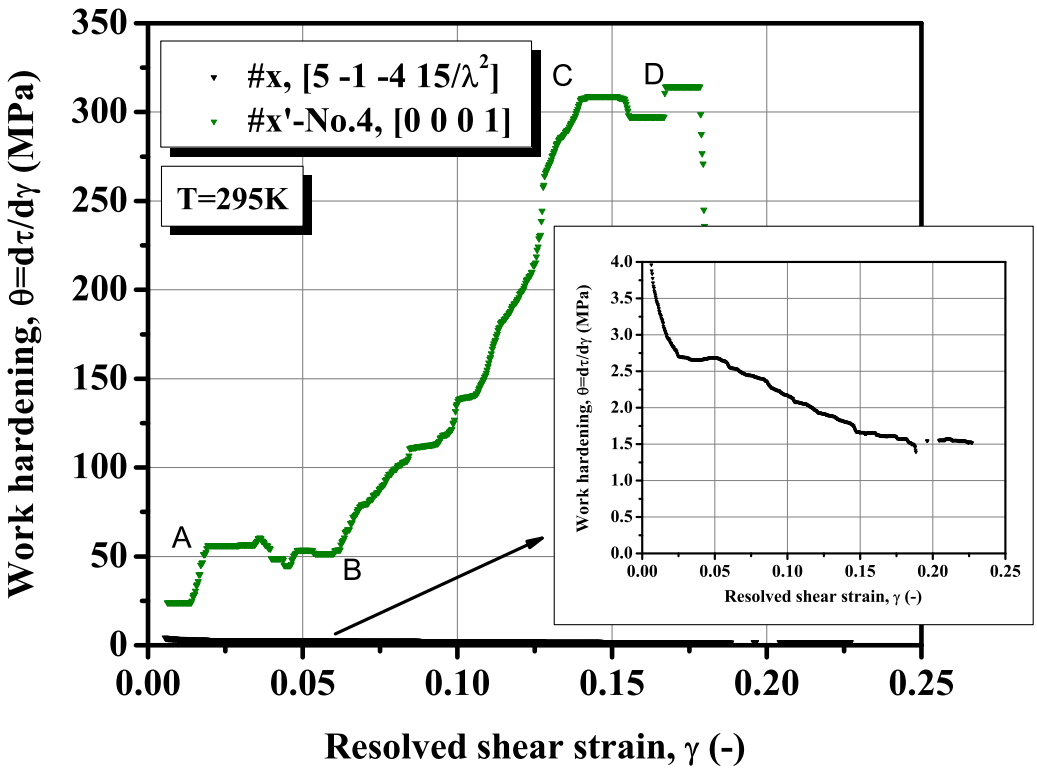

Figure 5.56: Work hardening rate versus shear strain plots of parent crystal #x and secondary sample #x' deformed in tension at 295K.

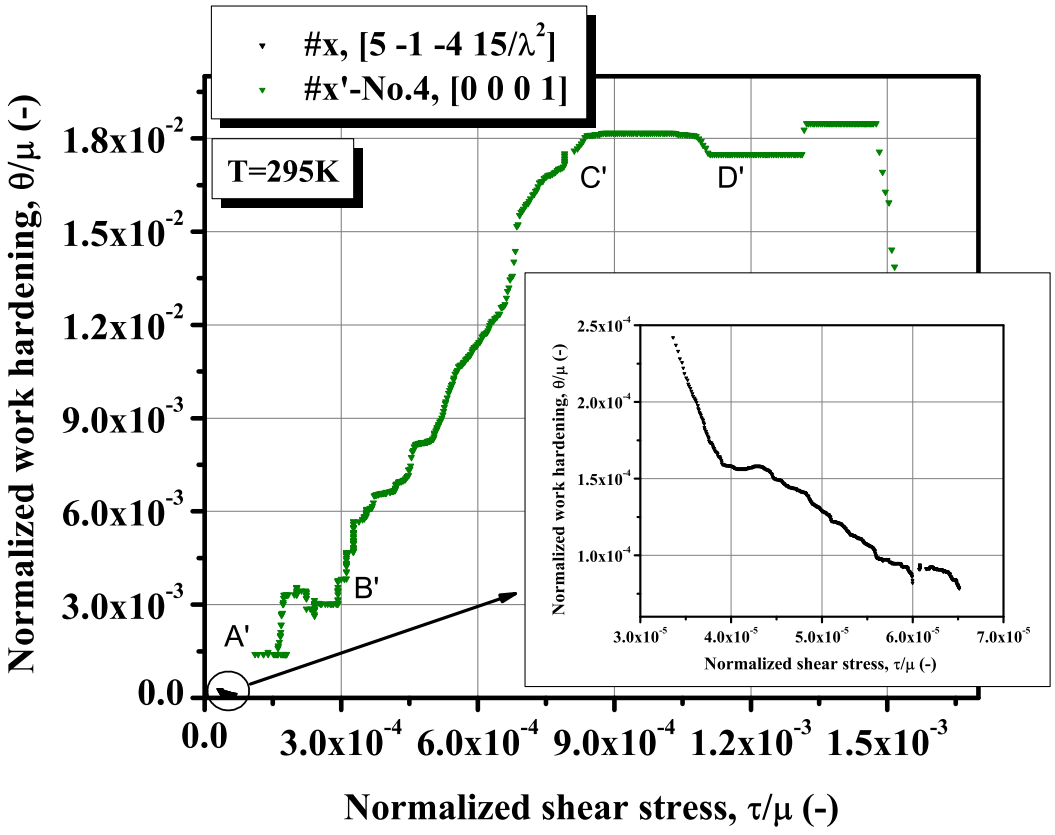

Figure 5.57: Normalized work hardening rate as a function of normalized shear stress characteristic of parent crystal #x and secondary sample #x' deformed in tension at 295K.

5.5.3 $\{10\bar{1}2\} < 10\bar{1}1 >$ twinning stress

In this section, we analyze the mechanical behaviour of the secondary samples #x' with respect to the behaviour of crystal #4 oriented for $\{10\bar{1}2\} < 10\bar{1}1 >$ twin to understand better the interactions of basal dislocations with mechanical twins and the effect of basal dislocations on twinning in Mg. Fig. 5.58 shows resolved

shear stress versus resolved shear strain curves of [0001] tensile test (crystal #4) and secondary samples #x'-No.1-4 deformed at 295K. All secondary samples yielded by $\{10\bar{1}2\} < 10\bar{1}1 >$ twinning, as evident by the stress drops associated with twin formation. However, basal dislocation configurations and the lattice rotation due to the primary deformation influenced the twin formation during the secondary deformation.

Table 5.7 summarizes the CRSS for $\{10\bar{1}2\} < 10\bar{1}1 >$ twinning in [0001] tensile sample #4 and secondary samples #x'-No.1-4. The twinning stress is plotted as a function of the primary stress in Fig. 5.59. Evaluation of the latent hardening tests under the conditions of basal $< a >$ slip/$\{10\bar{1}2\} < 10\bar{1}1 >$ twin dislocation interactions in Mg single crystals, permitted to determine a new latent hardening ratio (LHR*, Table 5.7), where LHR* was defined as the ratio of $\{10\bar{1}2\} < 10\bar{1}1 >$ twinning stress of a secondary sample over final flow stress of a parent crystal i.e.,

$$LHR^* = \frac{\tau_0^{(T.twin)}}{\tau_{max}^{(basal)}}. \tag{5.4}$$

As seen in Fig. 5.59, the $\{10\bar{1}2\} < 10\bar{1}1 >$ twinning stress in the secondary samples varied in the range between $1.28 - 3.01$MPa depending on the state of the initial substructure and the orientation of the crystals. The corresponding LHR*s were between $1.24 - 2.92$.

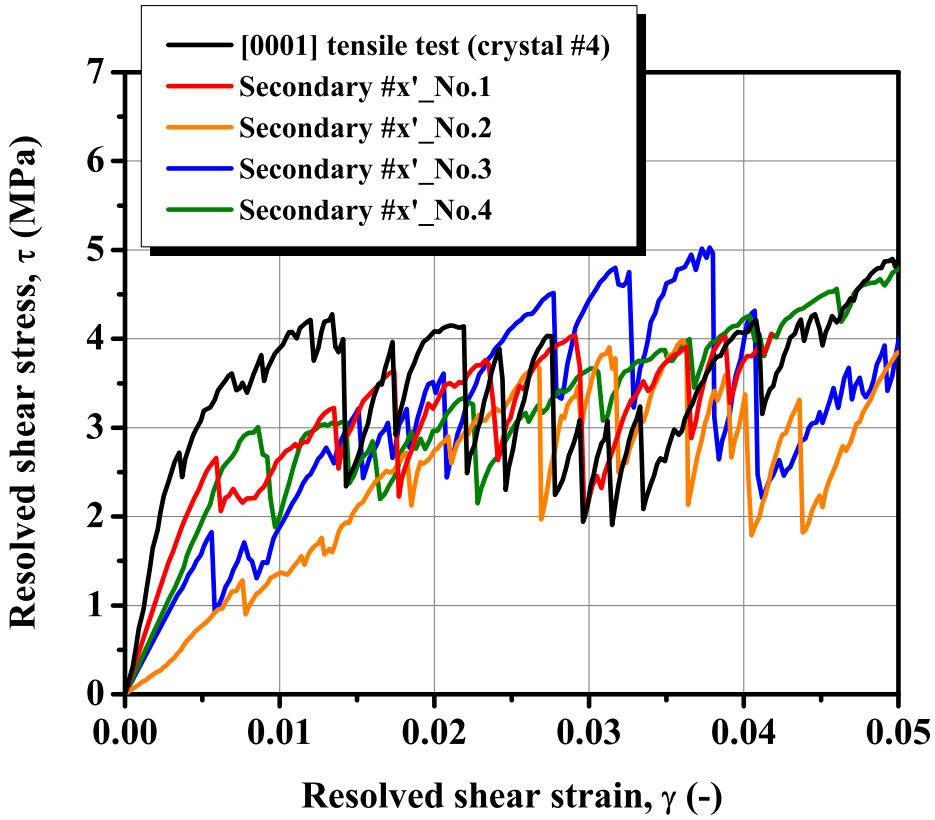

Figure 5.58: Resolved shear stress versus resolved shear strain curves of [0001] single crystal #4 and secondary samples #x'-No.1-4 deformed in tension at 295K.

Table 5.7: Twinning stress and LHR* for the secondary samples #x' and [0001] single crystal #4 during tensile test.

Sample #	#x'-No.1	#x'-No.2	#x'-No.3	#x'-No.4	#4T.
Primary shear strain (-)	27%	27%	27%	27%	0%
Primary shear stress (MPa)	1.03	1.03	1.03	1.03	0
Twinning stress (MPa)	2.66	1.28	1.82	3.01	2.72
LHR* (-)	2.58	1.24	1.77	2.92	-

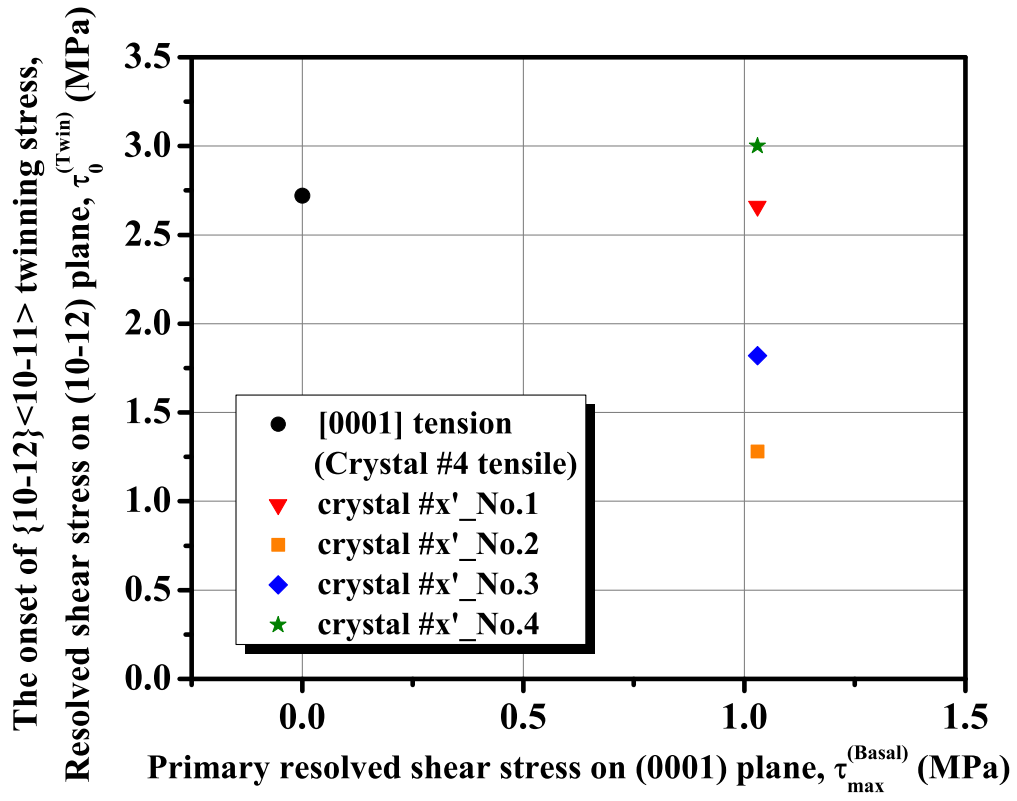

Figure 5.59: $\{10\bar{1}2\} < 10\bar{1}1 >$ twinning stress as a function of primary stress obtained from Fig. 5.58.

5.5.4 OM observation and SEM/EBSD analysis

The analysis of slip traces and deformation twins on wide (2) and side (3) surfaces of the secondary sample #x'-No.1 to No.4 were carried out by an optical microscopy (OM) with interfacial Nomarski contrast, as shown in Fig. 5.60 and Fig. 5.61. The slip bands corresponding to the basal plane can be seen almost perpendicular to the tensile axis. Schmid factor for basal $< a >$ slip system calculated from Laüe pattern after the primary deformation was ∼0.10 and the tensile axis of the secondary samples was $\sim 5-6^o$ tilted from the c-axis. The activation of basal $< a >$ slip was confirmed in spite of a low Schmid factor value ∼0.10, in all the secondary samples. Relatively large twins with preferred one variant were developed as primary twins in 2% strain sample (No.1), although all six $\{10\bar{1}2\} < 10\bar{1}1 >$ twin variants, A'1'-F'6' had largest Schmid factors 0.50 in the c-axis tensile deformation. With increasing strain, many twins with five variants nucleated and developed, e.g., see the OM micrograph after 7% (No.3) and 11% (No.4) strain. Observations by an optical microscopy at higher magnifications revealed that much smaller twins of higher order, nucleated and grew inside the primary twins. The activation of basal $< a >$ slip in both matrix and twin regions, interpreted as the cross-slip of basal $< a >$ dislocations from matrix to twin lattice, were also observed (Fig. 5.62).

In Fig. 5.60 and Fig. 5.61, the traces of (0001) plane and all six $\{10\bar{1}2\}$ planes are included to facilitate analysis of the deformation modes. These have been constructed from X-ray Laüe patterns obtained after the primary deformation of the crystal #4. Note that the direction of observed traces from slip and twin variants was slightly different compared to the predicted trace of (0001) plane and six $\{10\bar{1}2\}$

twin planes, due to the change of local crystallographic orientation during the secondary deformation. Laüe analysis from the secondary samples were not available because of the difficulty to solve these patterns due to the diffuse character of the matrix-twin mixture. Instead, the local crystallographic orientations in the crystals after the secondary deformation were determined by SEM/EBSD technique.

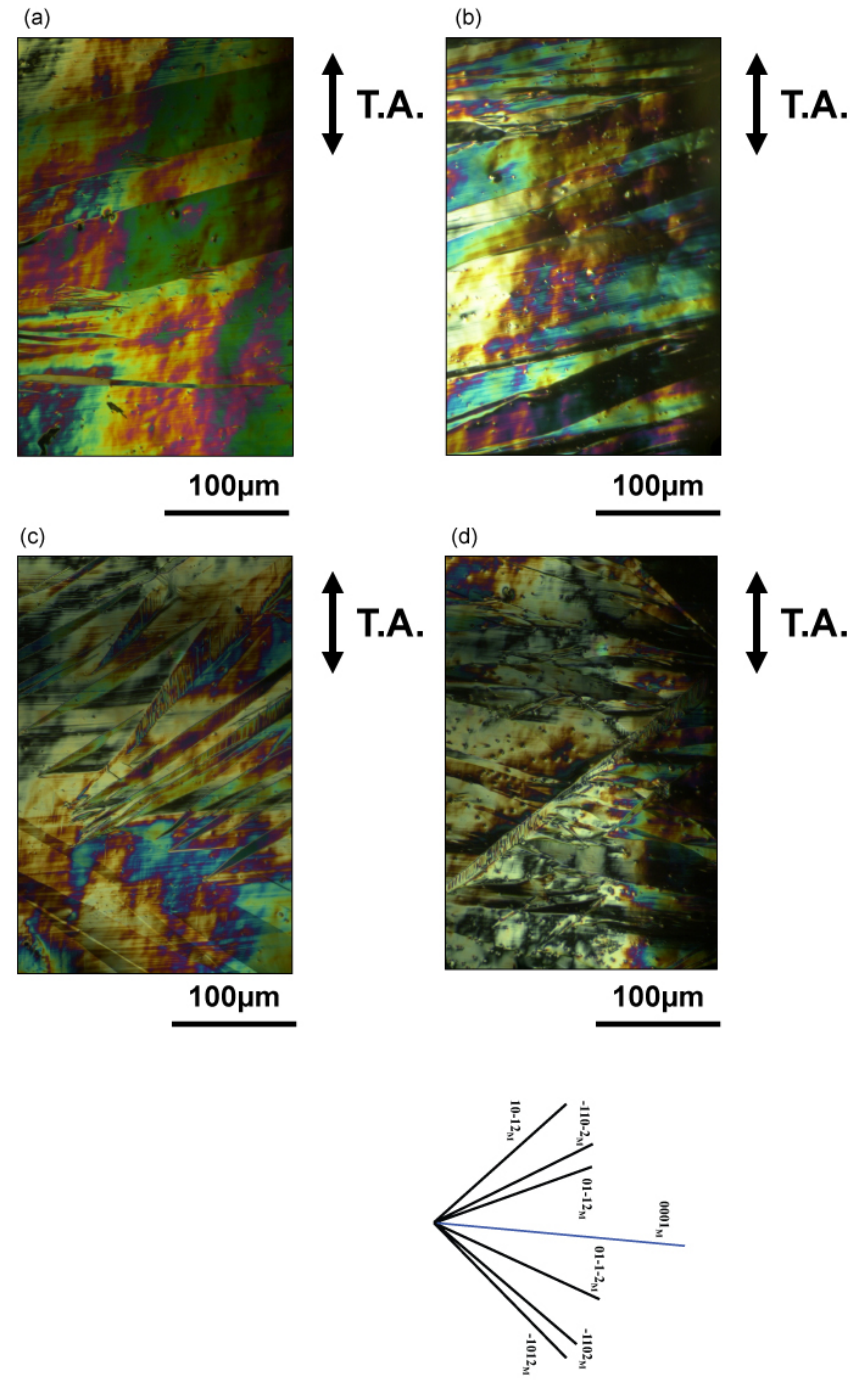

Figure 5.60: OM images from wide surface of the secondary samples #x' stretched to: (a) 2%, (b) 4%, (c) 7%, and (d) 11% strain.

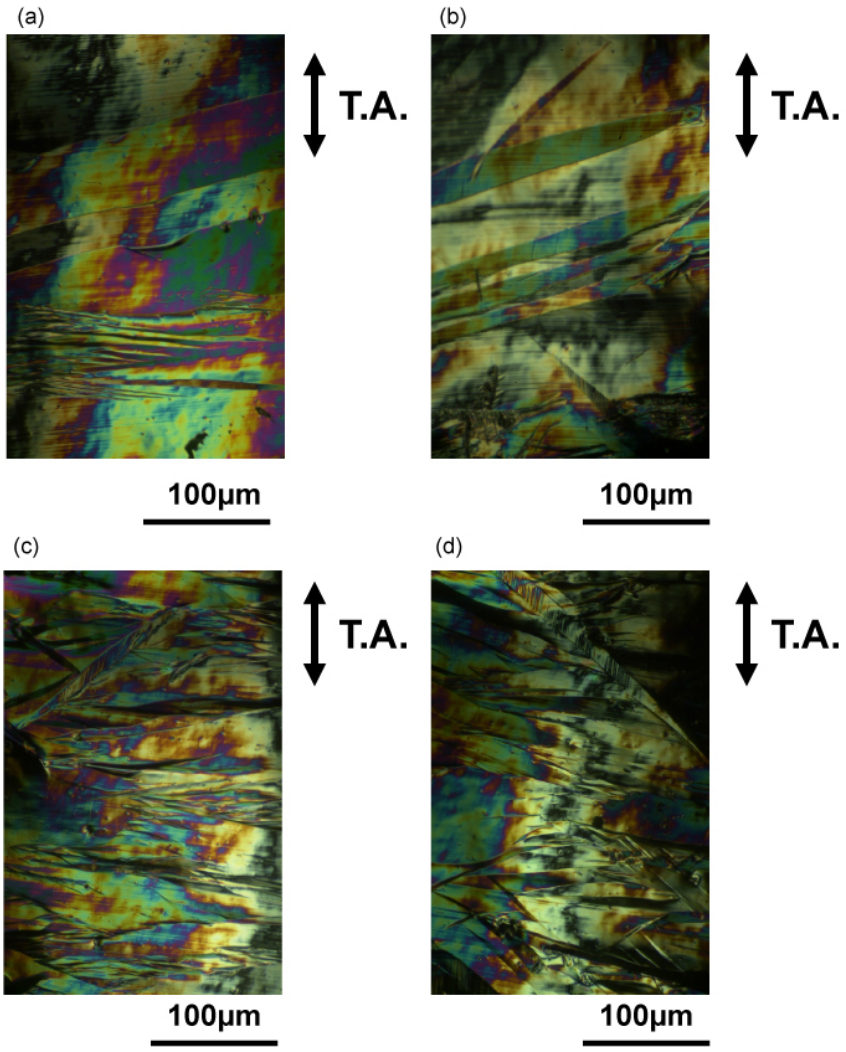

Figure 5.61: OM images from side surface in the secondary samples #x' stretched to: (a) 2%, (b) 4%, (c) 7%, and (d) 11% strain.

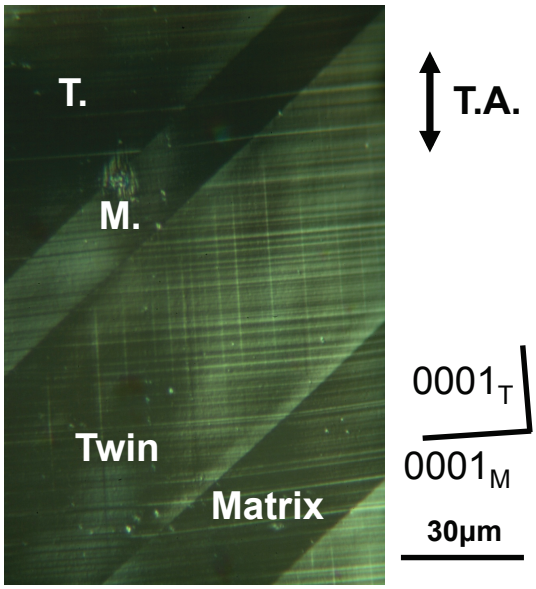

Figure 5.62: OM images from side surface in the secondary samples #x' stretched to: (a) 2%, (b) 4%, (c) 7%, and (d) 11% strain.

SEM/EBSD analysis was carried out on the secondary sample #x'-No.2 (4% strain), No.3 (7% strain), and No.4 (11% strain (fracture)). The side surface with normal (3) (Fig. 6.15) had better surface qualities than other surfaces and it was used for SEM/EBSD analysis and nano-indentation measurements as discussed in section 5.8.

Fig. 5.63 shows low magnification SEM images of the side surface (3) on the crystals #x'-No.2, deformed to 4% of strain in stage I, where profuse twinning deformation occurs. Fig. 5.64 shows inverse pole figure (IPF) maps and pole figures (PFs) constructed from EBSD data in the area A and B in Fig. 5.63. SEM/EBSD analysis revealed that the twinning developed during the secondary deformation was $\{10\bar{1}2\} < 10\bar{1}1 >$ type. Since the tensile axis of the secondary samples #x' was a few

degree off from the c-axis, dense $\{10\bar{1}2\} < 10\bar{1}1 >$ twins developed from the beginning of deformation. Although Schmid factors for all six $\{10\bar{1}2\} < 10\bar{1}1 >$ twin variants, A'1'-F'6' had the highest values of 0.49, it was observed that $\{10\bar{1}2\} < 10\bar{1}1 >$ twins with only four variants were developed. Fig. 5.64 shows three different types of $\{10\bar{1}2\} < 10\bar{1}1 >$ twins, $\text{Twin}_{(I)}$, $\text{Twin}_{(II)}$, and $\text{Twin}_{(III)}$, with relatively large size. At different locations, another twin variant was found, but $\{10\bar{1}2\} < 10\bar{1}1 >$ with remaining two variants could not be found in the analysis, suggesting that only four out of six $\{10\bar{1}2\} < 10\bar{1}1 >$ twin variants was formed.

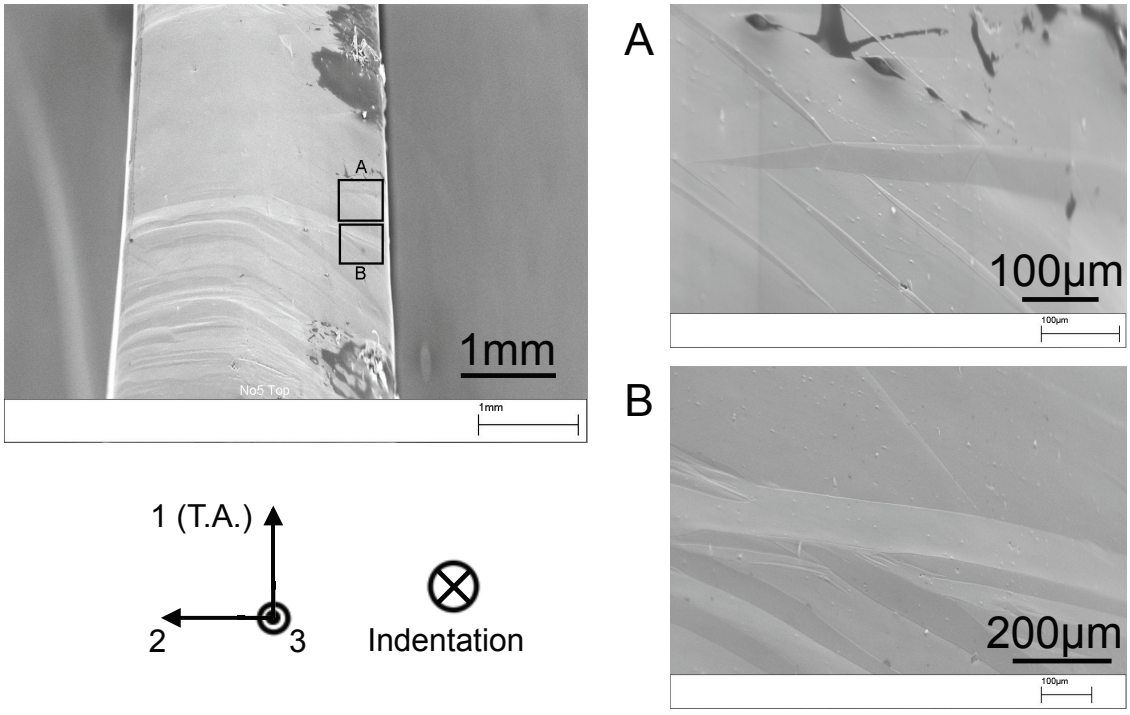

Figure 5.63: Low magnification SEM images of the side surface (3), in the secondary sample #x'-No.2, deformed to 4% strain.

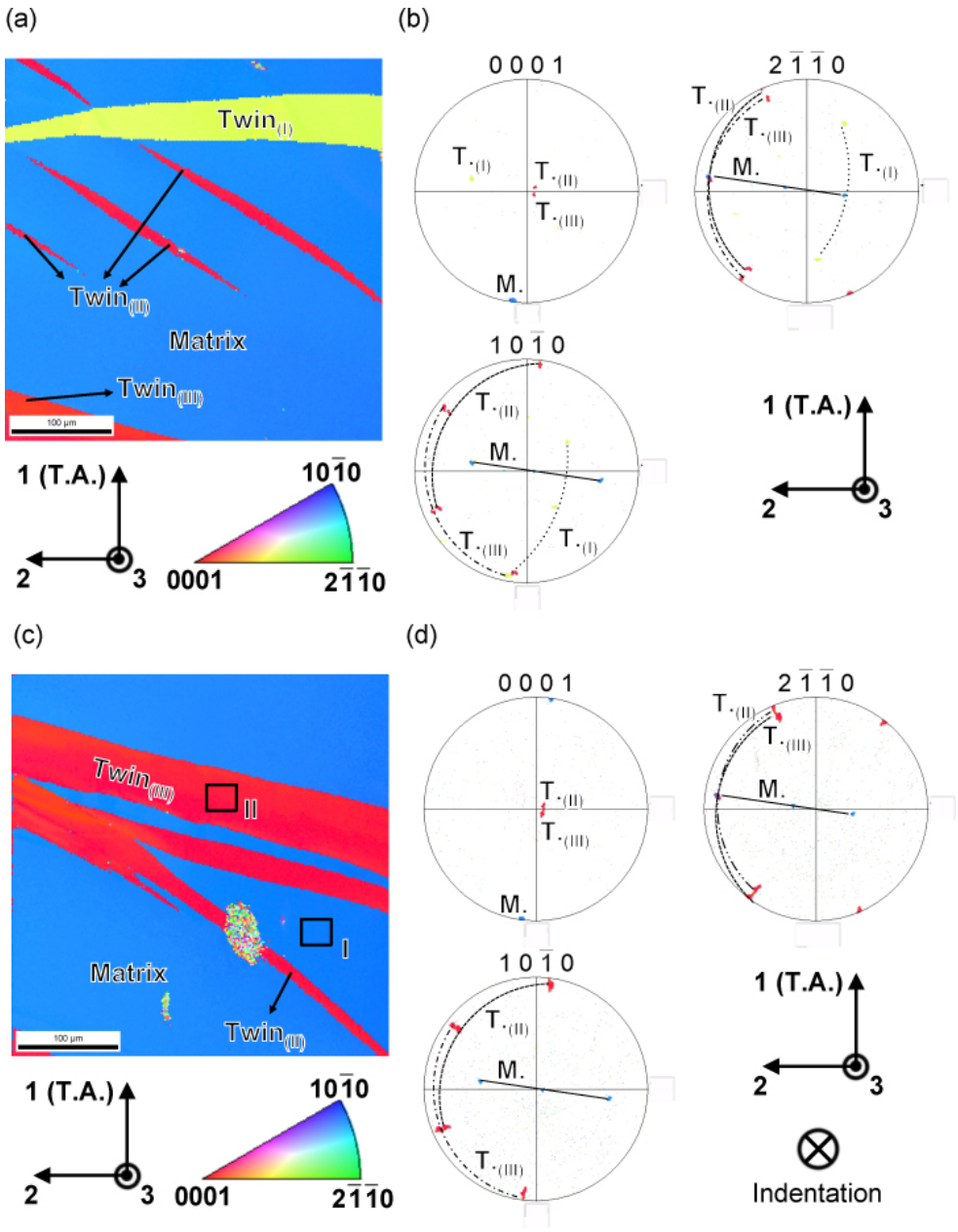

Figure 5.64: (a) Inverse pole figure (IPF) map, (b) pole figures (PFs) constructed from EBSD data in the area A of Fig. 5.63, (c) IPF map, and (d) PFs in the area B of Fig. 5.63.

Fig. 5.65 shows low magnification SEM images of the side surface (3) in the crystal #x'-No.3, deformed to 7% strain in the transition stage from stage I to stage II. Fig. 5.66 shows IPF maps and PFs constructed from EBSD data in the area A and B of Fig. 5.65. In this sample, the observed twinning type was $\{10\bar{1}2\} < 10\bar{1}1 >$. $\{10\bar{1}2\} < 10\bar{1}1 >$ twins with all six variants, Twin1 - Twin6, were observed, as shown in Fig. 5.65.

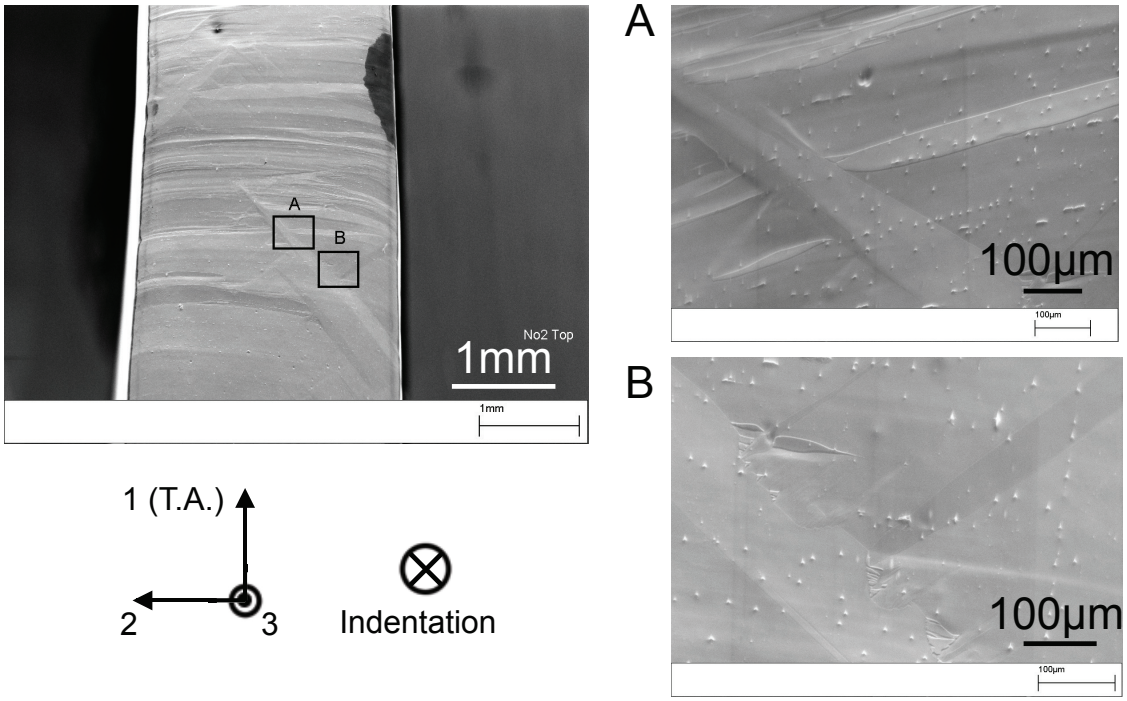

Figure 5.65: Low magnification SEM images of the side surface (3) on the secondary sample #x'-No.3, deformed to 7% strain.

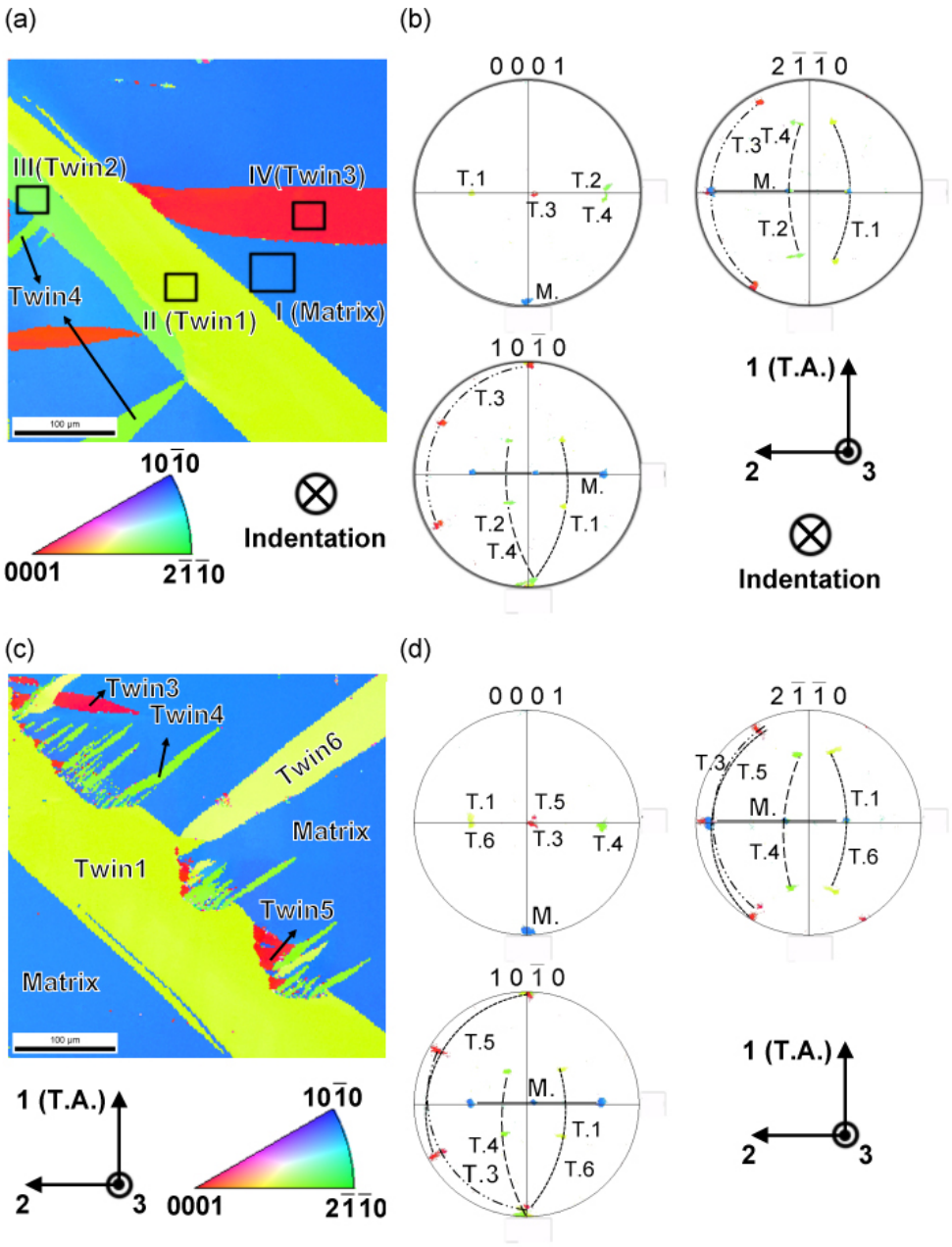

Figure 5.66: (a) Inverse pole figure (IPF) map, (b) pole figures (PFs) constructed from EBSD data in the area A of Fig. 5.65, (c) IPF map, and (d) PFs in the area B of Fig. 5.65.

Fig. 5.67 shows low magnification SEM images of the side surface (3) in the crystals #x'-No.4, deformed to fracture. Fig. 5.68 and Fig. 5.69 show IPF maps and PFs constructed from EBSD data in the area A, B, and C of Fig. 5.67. In this sample, the observed twinning type was also only $\{10\bar{1}2\} < 10\bar{1}1 >$. Higher order twins with much finer size were developed inside/around the primary twins in the secondary sample #x'-No.4.

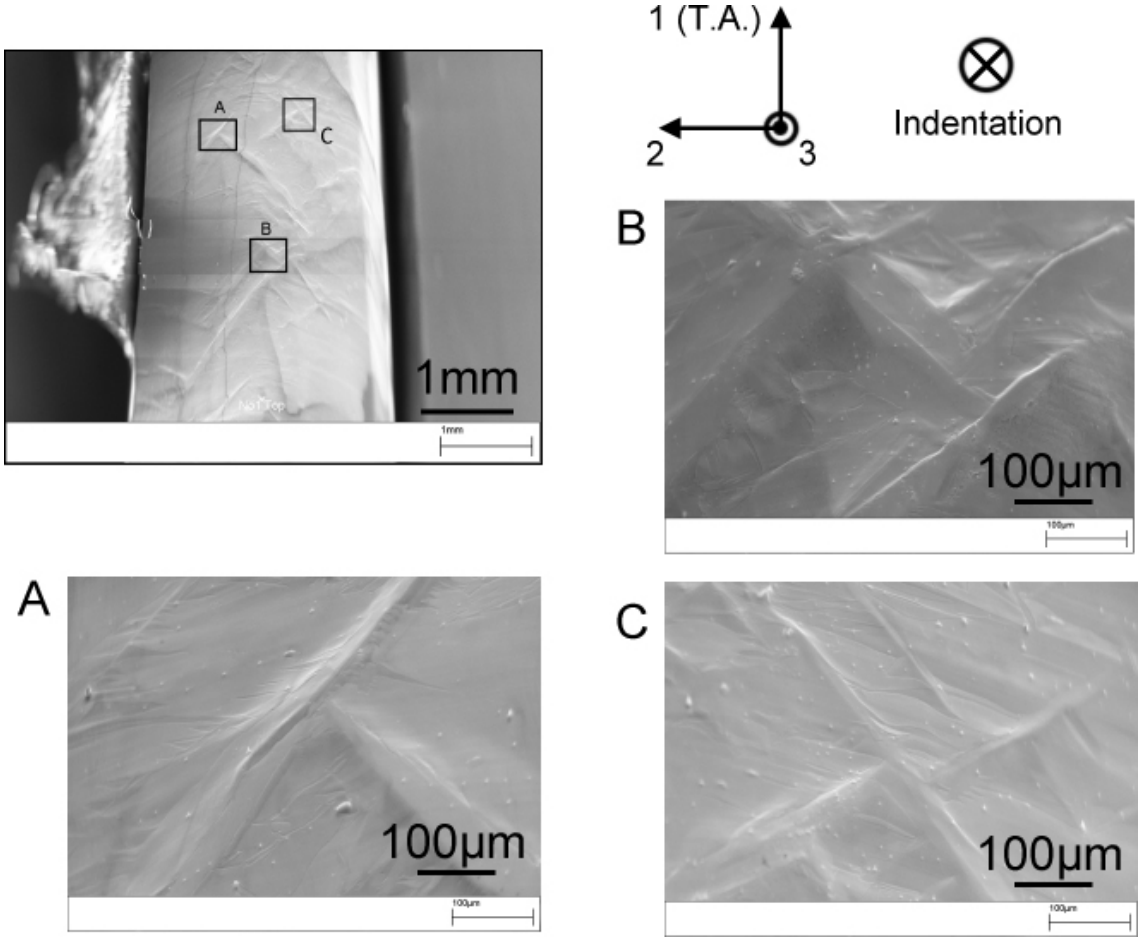

Figure 5.67: Low magnification SEM images of the side surface (3) in the crystal #x'-No.4.

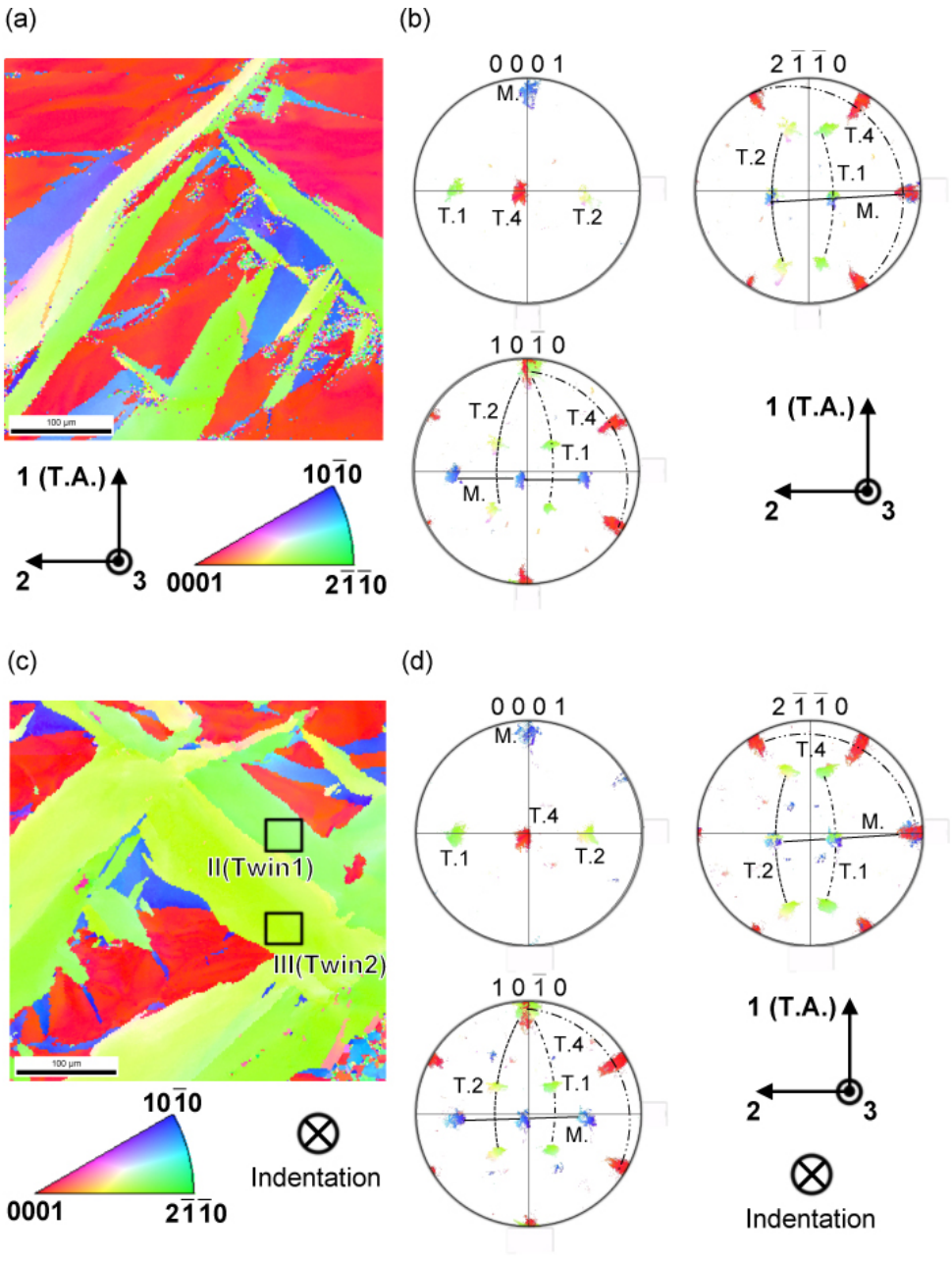

Figure 5.68: (a) Inverse pole figure (IPF) map, (b) pole figures (PFs) constructed from EBSD data in the area A of Fig. 5.67, (c) IPF map, and (d) PFs in the area B of Fig. 5.67.

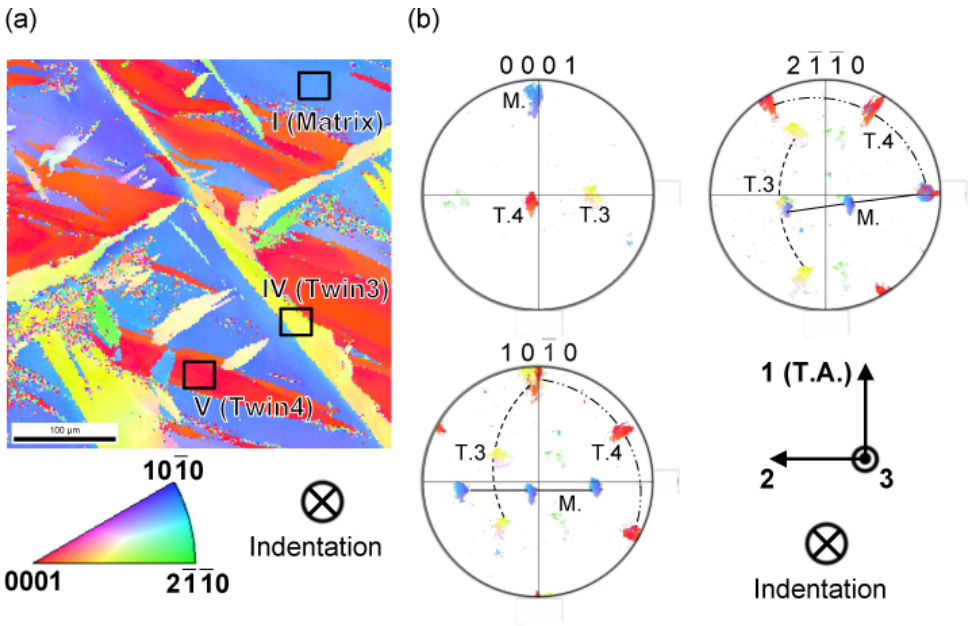

Figure 5.69: (a) Inverse pole figure (IPF) map, and (b) pole figures (PFs) constructed from EBSD data in the area C of Fig. 5.67.

5.6 Latent hardening behaviour under basal $< a >$ slip/2^{nd} order pyramidal $< c + a >$ slip interactions

5.6.1 Orientations of primary and secondary specimens

The initial crystallographic orientations and the corresponding Schmid factors for single crystals used to investigate latent hardening behaviour under conditions of basal $< a >$ slip/2^{nd} order pyramidal $< c + a >$ dislocation interactions have been described in section 5.5 in Table 5.6 and Fig. 5.54. Secondary compression samples,

denoted as #x", were cut at -30^o from the pre-deformed parent crystal #x with dimensions of $\sim$3x3x5mm^3 such that the compression axis of the secondary sample #x" was exactly paralleled to [0001] direction. As discussed in section 5.2.5, the c-axis compression deformation of Mg single crystals induces the 2^{nd} order pyramidal $< c+a >$ slip. Thus, a combination of $[2\bar{1}\bar{1}2]$ tensile test and [0001] compression test permits to study the latent hardening characteristics under interactions of pre-existing basal $< a >$ dislocations with 2^{nd} order pyramidal $< c+a >$ dislocations.

5.6.2 Mechanical properties of the secondary sample #x"

Careful SEM/EBSD analysis revealed that $\{10\bar{1}2\} < 10\bar{1}1 >$ twins and basal $< a >$ slip were activated during the secondary compression test. One expects that the crystallographic rotation during the primary tensile deformation of crystal #x may influence the mechanical behaviour of the secondary compression sample #x". In order to investigate which deformation modes were primarily activated during the crystal #x" compression test, OM and SEM observations and SEM/EBSD analysis of the lateral surfaces of deformed sample were carried out. Fig. 5.70 and Fig. 5.71 show (a) SEM micrographs, (b) inverse pole figure (IPF) maps and (c) pole figures (PFs) constructed from EBSD data of the matrix and twin regions developed during the secondary compression tests of #x" sample. Colours in the IPF map and PFs relate to the crystallographic orientations in the standard triangle. Twinning with several variants and slip traces almost perpendicular to the compression axis, $2-3^o$ off from the compression axis, are observed in the SEM micrographs. Misorientations between matrix/twin I, matrix/twin II, matrix/twin III, and matrix/twin IV were found to be 86^o around $[2\bar{1}\bar{1}0]$ axis, as seen in Fig. 5.70(b) and (c) and Fig.

5.71(b) and (c).This indicates that the twins developed during compression test are $\{10\bar{1}2\} < 10\bar{1}1 >$ extension type twins.

However, both OM and SEM observations have not revealed the presence of slip marking patterns form 2^{nd} order pyramidal $< c + a >$ slip systems, suggesting that $< c+a >$ slip is not a primary deformation modes in the secondary compression tests of crystal #x", despite the fact that sample had favourable orientation for $< c + a >$ slip. Instead, the results indicated that the extension twins were the dominant mode of deformation.

In order to investigate the effect of pre-strain on the onset of twinning deformation under compression, the resolved shear stress and resolved shear strain characteristics were recalculated from the raw data, assuming that the $\{10\bar{1}2\} < 10\bar{1}1 >$ twin system is the only deformation mode.

Fig.5.72 and Fig.5.73 show resolved shear stress versus resolved shear strain and work hardening rate versus resolved shear strain plots for the crystal #x" deformed in compression at 295K. The data reveal that the crystal deforms with zero work hardening stage until $\sim$0.35 of shear strain. In this stage, the stress increases in a step-like way due to the $\{10\bar{1}2\} < 10\bar{1}1 >$ twin nucleation and growth, as shown by arrowheads in Fig. 5.72. The CRSS for the twinning was around $1.75 - 1.9$MPa.

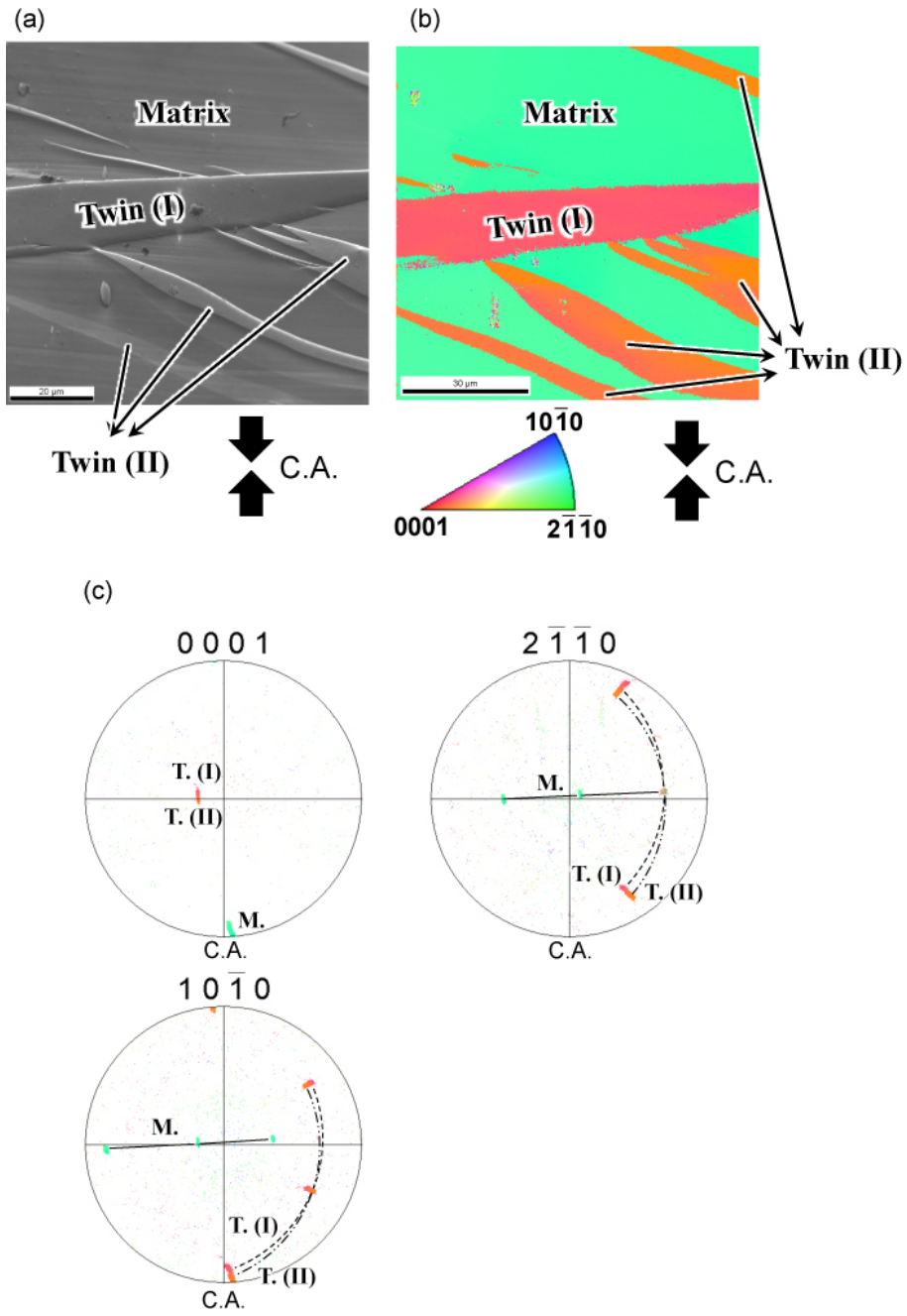

Figure 5.70: (a) SEM image, (b) IPF map, and (c) pole figures constructed from EBSD data of the matrix and twin region 1 developed during secondary compression tests in Mg single crystal #x".

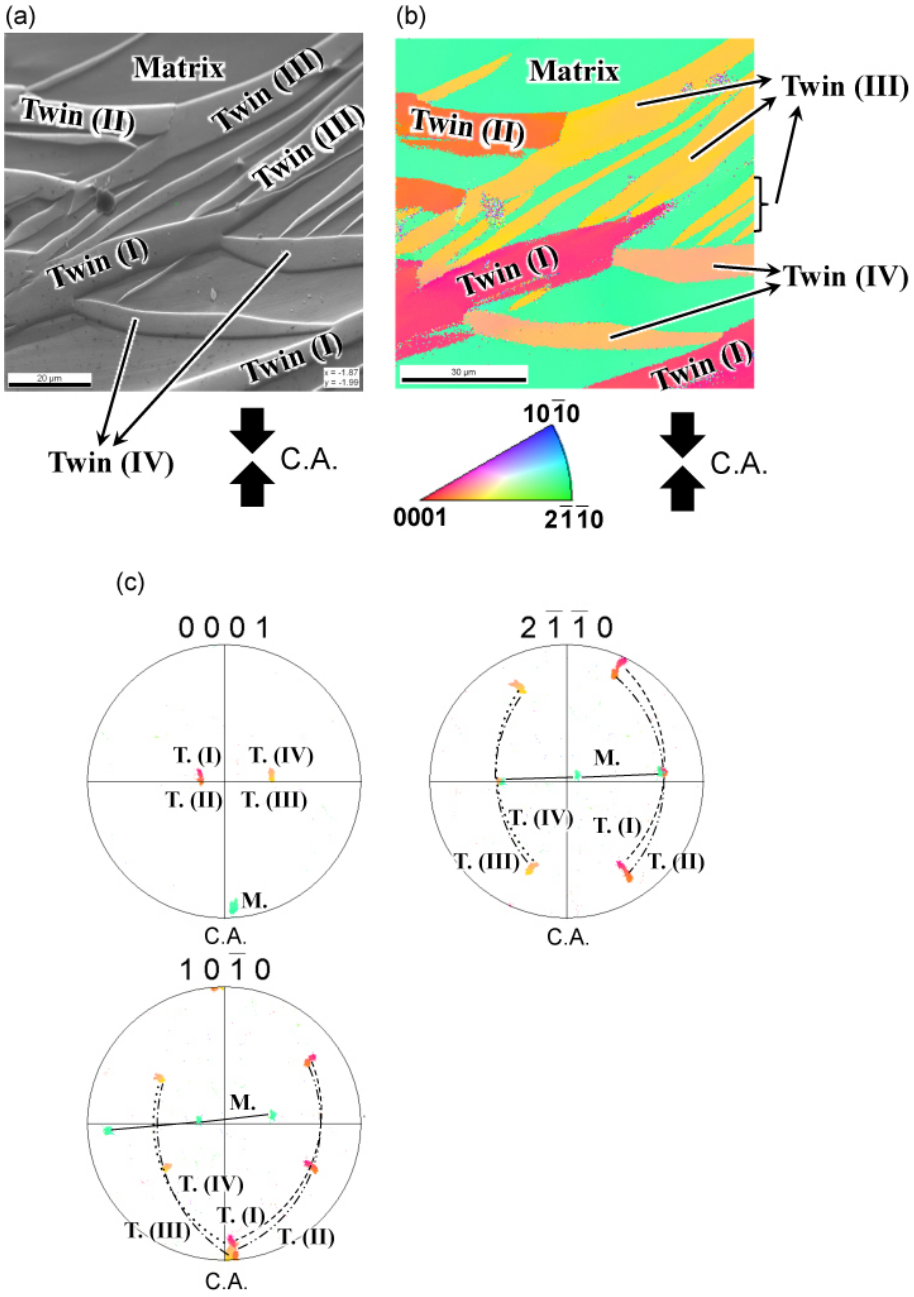

Figure 5.71: (a) SEM image, (b) IPF map, and (c) pole figures constructed from EBSD data of the matrix and twin region 2 developed during secondary compression tests in Mg single crystal #x".

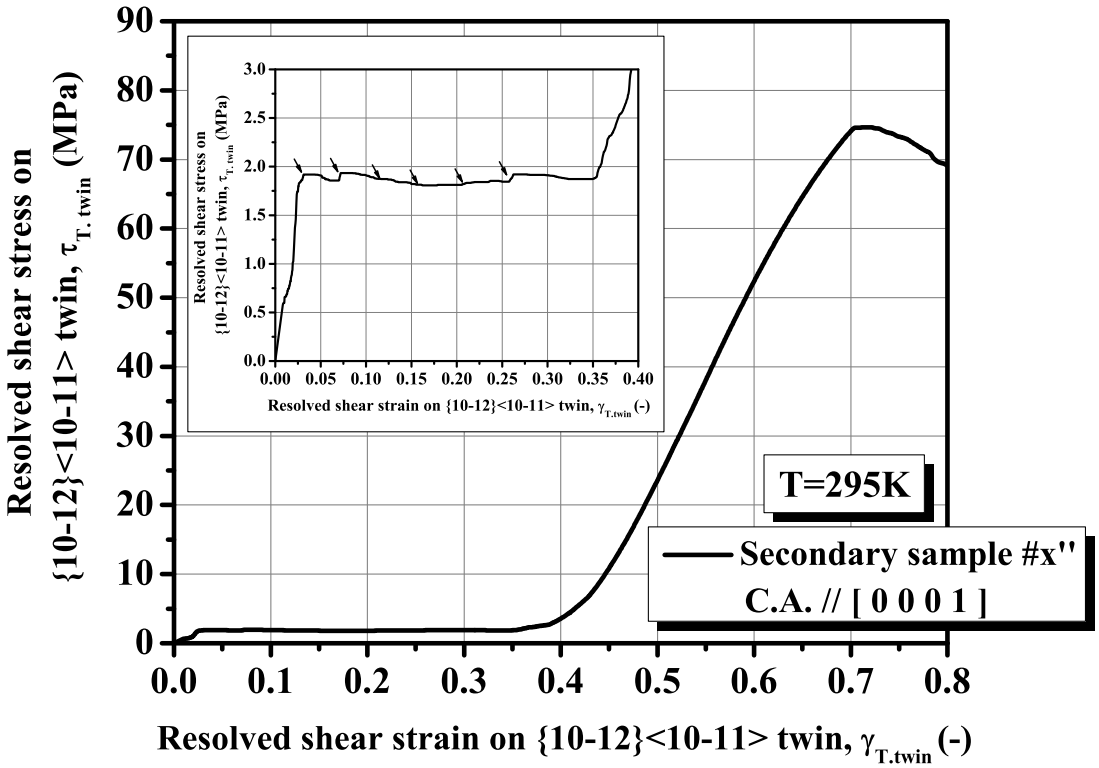

Figure 5.72: Resolved shear stress versus resolved shear strain curve on $\{10\bar{1}2\} < 10\bar{1}1 >$ twin system for secondary sample #x" deformed in compression at 295K.

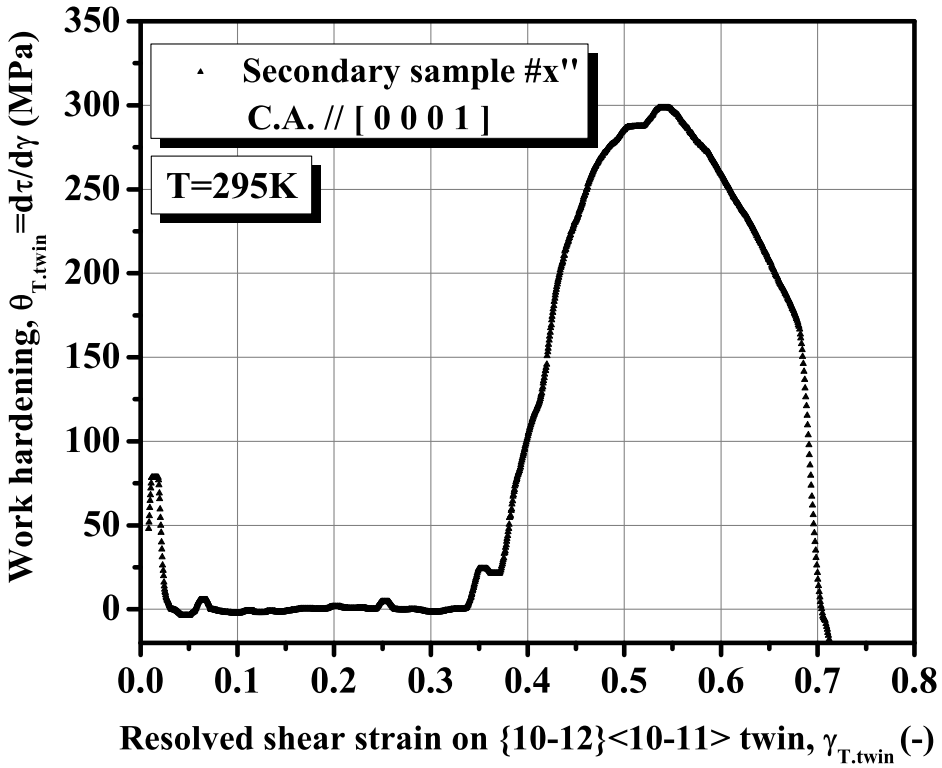

Figure 5.73: Work hardening rate versus resolved shear strain plot for the secondary sample #x" deformed in compression at 295K, under conditions of operating $\{10\bar{1}2\} < 10\bar{1}1 >$ twin system.

5.7 Latent hardening behaviour under $\{10\bar{1}2\} < 10\bar{1}1 >$ twin/basal $< a >$ slip interactions

5.7.1 Orientations of primary and secondary specimens

Fig. 5.74 shows the standard (0001) stereographic projection indicating the initial orientations of parent crystal #y and final orientations of secondary samples #y'1 and #y'2. Secondary samples #y'1 and #y'2 were cut at 0° and 90° angles with respect to the tensile axis of the parent crystal #y. Schmid factors for basal $< a >$ slip, 2^{nd} order pyramidal $< c+a >$ slip and $\{10\bar{1}2\} < 10\bar{1}1 >$ twin systems calculated from the initial orientation of the parent crystal #y and the secondary samples #y'1 and #y'2 are summarized in table 5.8. Schmid factors for BII and BIII systems for crystal #y are relatively low ~ 0.19, as seen in table 5.8.

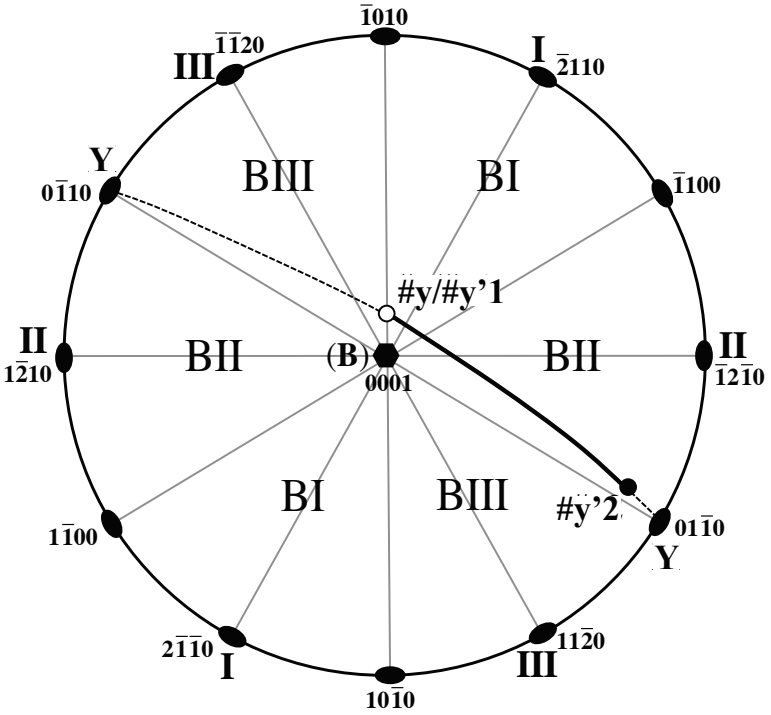

Figure 5.74: The (0001) stereographic projection indicating initial and secondary tensile axes positions of parent crystal #y and secondary samples #y'1 and #y'2.

5.7.2 Primary deformation

The tensile axis of parent crystal #y was paralleled to $[10\bar{1}(8/\lambda^2)]$ and it had a relatively low basal Schmid factor of 0.19 for basal slip systems. Consideration of the Schmid factor suggest the the crystal should deform by inhomogeneous deformation involving $\{10\bar{1}2\} < 10\bar{1}1 >$ twinning and kink bands' formation in addition to basal slip. Therefore, the mechanical properties of parent crystal #y are characterized in

Table 5.8: Schmid factors for basal $< a >$ slip, 2^{nd} order pyramidal $< c + a >$ slip and $\{10\bar{1}2\} < 10\bar{1}1 >$ twin systems in parent crystal #y and secondary samples #y'1 and #y'2. Crystals #y and #y'1 have the same crystallographic orientations of the tensile/compression axis.

Deformatin modes	Notation	Miller-Bravais index	Schmid factor	
			#y (#y'1)	#y'2
Basal $< a >$ slip	BI	$(0001)[2\bar{1}\bar{1}0]$	0.19	0
	BII	$(0001)[\bar{1}2\bar{1}0]$	0	0.10
	BIII	$(0001)[\bar{1}\bar{1}20]$	0.19	0.10
2^{nd} order pyramidal $< c + a >$ slip	II.Py1	$(11\bar{2}2)[\bar{1}\bar{1}23]$	0.32	0.28
	II.Py2	$(\bar{1}2\bar{1}2)[1\bar{2}13]$	0.42	0.28
	II.Py3	$(\bar{2}112)[2\bar{1}\bar{1}3]$	0.49	0.01
	II.Py4	$(\bar{1}\bar{1}22)[11\bar{2}3]$	0.49	0.37
	II.Py5	$(1\bar{2}12)[\bar{1}2\bar{1}3]$	0.42	0.37
	II.Py6	$(2\bar{1}\bar{1}2)[\bar{2}113]$	0.32	0.01
$\{10\bar{1}2\} < 10\bar{1}1 >$ twin	A'1'	$(10\bar{1}2)[\bar{1}011]$	0.46	0.12
	B'2'	$(01\bar{1}2)[0\bar{1}11]$	0.47	0.49
	C'3'	$(\bar{1}102)[1\bar{1}01]$	0.46	0.12
	D'4'	$(\bar{1}012)[10\bar{1}1]$	0.43	0.11
	E'5'	$(0\bar{1}12)[01\bar{1}1]$	0.46	0.48
	F'6'	$(1\bar{1}02)[\bar{1}101]$	0.47	0.11

terms of the true stress and true strain relations.

Fig. 5.75 and Fig. 5.76 show true stress versus true strain curve and work hardening rate versus true strain plots for parent crystal #y deformed in tension at 295K. The yielding stress, around 2.6MPa, was slightly higher than that of single basal $< a >$ slip orientation. After the yielding, stage of zero work hardening rate was observed during initial 0-2% of strain. Subsequently, the crystals deform at constant work hardening rate at the level $\sim 8 - 12$MPa, until the deformation was terminated at 10% of true strain.

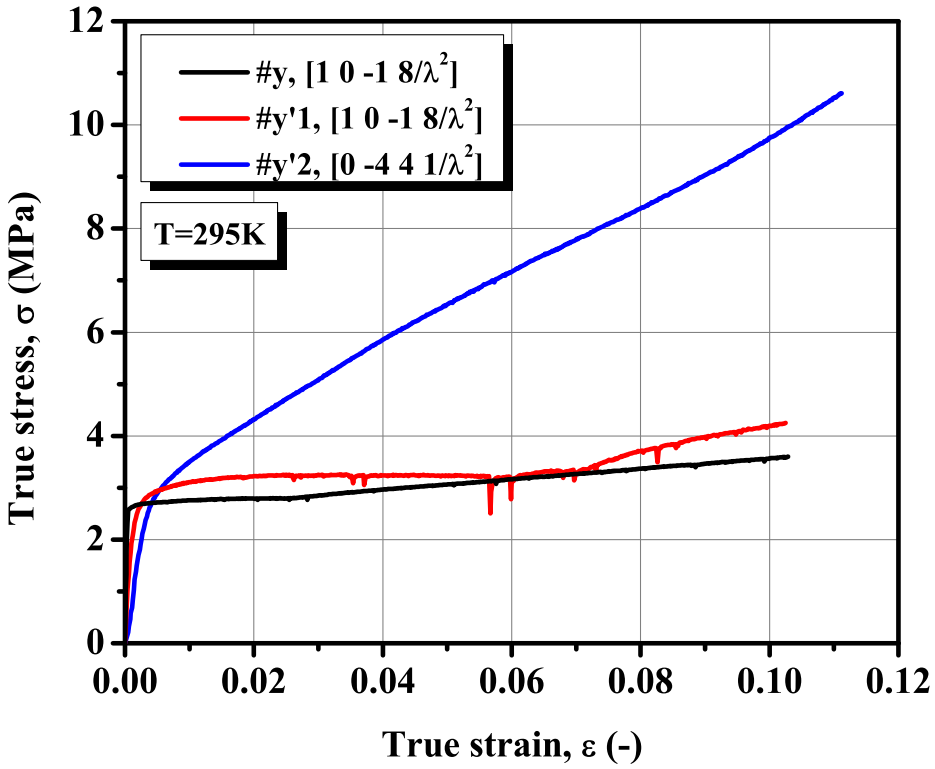

Figure 5.75: True stress versus true strain characteristic of parent crystal #y and secondary samples #y'1 and #y'2 deformed in tension at 295K.

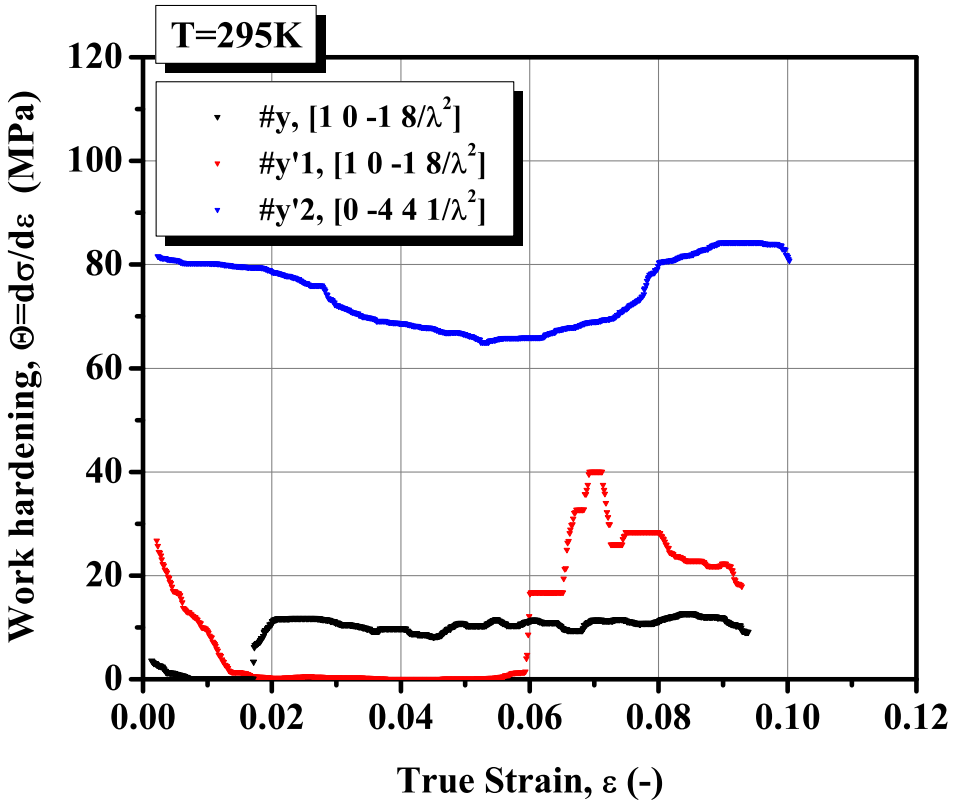

Figure 5.76: Work hardening rate versus true strain characteristic of parent crystal #y and secondary samples #y'1 and #y'2 deformed in tension at 295K.

Fig.5.77 (a) shows a macroscopic view of the parent crystal #y deformed to about 10% of true strain. The macroscopic shape change of the crystal was inhomogeneous and the crystal was slightly bent and twisted during the primary deformation. Optical microscopy (OM) observation on the wide surface of the parent crystal #y presented in Fig. 5.77 revealed that the inhomogeneous area contained kink bands and deformation twins. Kink bands are defined as deformation bands with boundary normal to the primary slip plane. The boundaries of the kink bands observed in the

deformed crystal was almost perpendicular to the trace of (0001) plane. This type of deformation bands was termed as $\{11\bar{2}0\}$ kink bands.

Optical microscopy of the wide surface of deformed parent crystal #y reveal the formation of slip bands corresponding to basal plane, kink bands and deformation twins. As discussed previously, kink band deformation occurs more often in crystals with lower Schmid factors for the basal $< a >$ slip systems. In the present work the "kinking" occurred along $\{11\bar{2}0\}$, i.e., normal to the active basal $< a >$ slip plane, similar to the case reported by Burke and Hibbard (1952) and Yoshinaga and Horiuchi (1962). Thus, the present observations suggest that deformation of crystal #y proceeds by kink bands formation and $\{10\bar{1}2\} < 10\bar{1}1 >$ twin propagation during the initial stage of deformation. The work hardening rate showed sudden increase after about 3% strain (Fig.5.76). The crystallographic orientation of the sample was changed as a result of twinning, combined with twisting and bending, resulting in the increase in the Schmid factor for basal $< a >$ slip. After 3% strain, deformation of crystal proceeds by basal $< a >$ slip and twin propagation. From slip trace analysis, the angle between basal plane normal and tensile axis was $\sim 20^o - 30^o$.

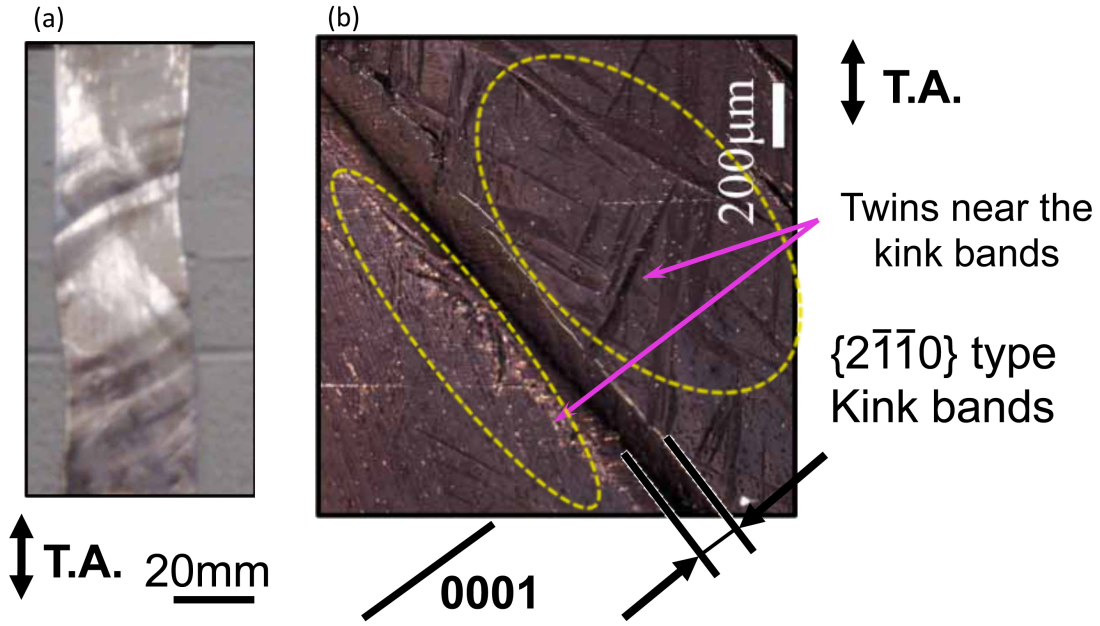

Figure 5.77: (a) Macroscopic view of parent crystal #y and (b) optical microscopy (OM) observation on the wide surface of parent crystal #y deformed to around 10% of true strain at 295K.

Due to the complex nature of the plastic flow of parent crystal #y, the sample is in essence a composite containing parent and twin phases in a spectrum of orientations. The location of secondary samples, plays a critical role in analysis of the twin/slip interactions. As shown in Fig. 5.78, the secondary sample #y'1 was selected from relatively flat/homogenelus area of the parent crystal, containing a small amount of twins and kink bands due to the primary deformation. Secondary sample #y'2 was also selected from relatively homogeneous area and it contained only a pair of twin boundaries.

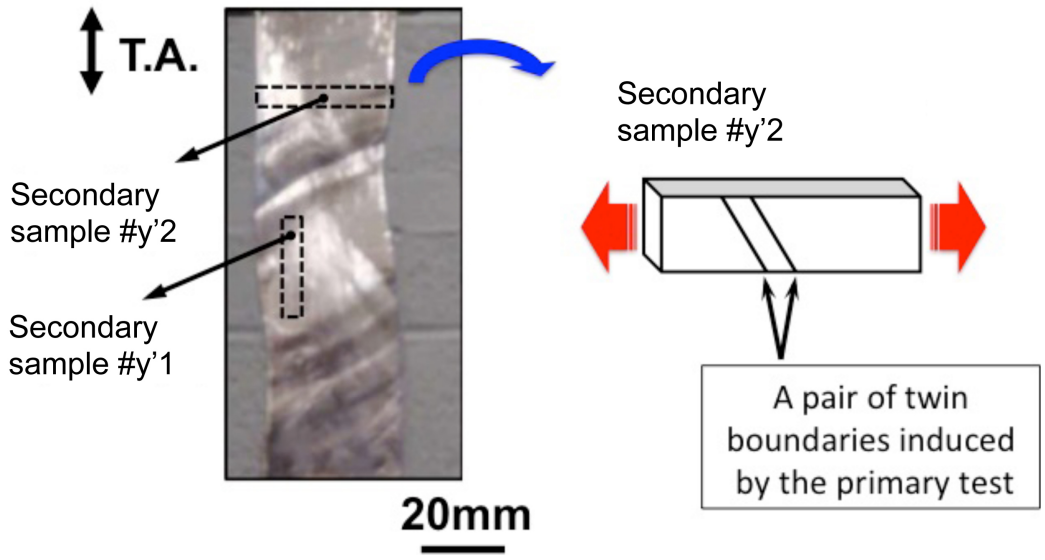

Figure 5.78: Schematic illustrations of the selection of secondary samples #y'1 and #y'2 from the pre-deformed parent crystal #y.

In order to represent the increase of work hardening rate quantitatively, a hardening parameter LHR** expressed in terms of the ratio of true stresses, is calculated from the plastic flow curves of #y, #y'1 and #y'2 crystals as:

$$LHR^{**} = \frac{\sigma_0^{(j)}}{\sigma_{max}^{(i)}} \tag{5.5}$$

here, $\sigma_{max}^{(i)}$ is the final flow stress of the parent crystal and $\sigma_0^{(j)}$ is the yield stress of the secondary sample. In addition, the ratio of the work hardening rates (WHR) was also introduced to evaluate the hardening responses of primary and secondary samples:

$$WHR^{*} = \frac{ave.\theta^{(j)}}{ave.\theta^{(i)}}. \tag{5.6}$$

Table 5.9: LHR** and WHR* for the secondary samples #y'1 and #y'2.

Sample #	$\sigma_{max}^{(i)}$ (MPa)	$\sigma_0^{(j)}$ (MPa)	$\theta^{(i)}$ (MPa)	$\theta^{(j)}$ (MPa)	LHR** (-)	WHR* (-)
#y	3.59	-	8-12	-	-	-
#y'1	-	2.99	-	20-40	0.83	∼3
#y'2	-	3.01	-	62-82	0.84	∼7

where: $ave.\theta^j$ and $ave.\theta^i$ are work hardening rates on primary and secondary systems, respectively

In table 5.9, the values of LHR** and WHR* calculated from the secondary samples #y'1 and #y'2 were summarized. For both samples, latent softening (LHR** < 1) was observed. The WHR* ~ 7 for the secondary sample #y'2, is significantly higher compared to the secondary sample #y'1, (WHR* ~ 3).

Fig. 5.79 shows macroscopic views of secondary samples #y'1 and #y'2 after deformed to 10% of true strain. Secondary sample #y'1 exhibits the same shape change as the parent crystal #y, locally bended and twisted, suggesting the same modes of plastic deformation operate in both crystals. The secondary sample #y'2 deformed homogeneously except the small part deformed by primary twinning.

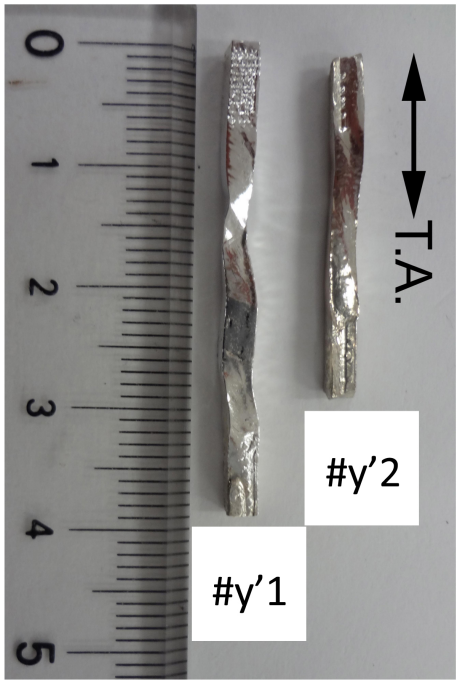

Figure 5.79: Macroscopic view of secondary samples #y'1 and #y'2 deformed to true strain of about 10% at 295K.

5.7.3 SEM/EBSD micro-texture analysis of the secondary sample #y'2

Fig. 5.80 shows SEM image from the wide surface of the secondary sample #y'2. Fig. 5.80 (a) depicts diagrammatically deformed state of the sample #y'2 with region X deformed by the primary twin during primary deformation and region Y containing no twin band. As seen in Fig. 5.80 (b), much smaller size secondary twins, were developed inside the primary twin boundaries during the secondary deformation of #y'2 crystal. Slip lines corresponding to the (0001) plane were also observed in the matrix, primary and secondary twin regions. In the region Y, which has not been

swept by the propagating twin front, slip bands corresponding to the basal plane were observed, as shown in Fig. 5.80 (c).

In order to evaluate the twinning type developed during the secondary deformation, SEM/EBSD analysis was carried out in this region. Fig. 5.81 shows (a) inverse pole figure (IPF) map, (b) grain boundaries map, and (c) pole figures (PFs) map constructed from the EBSD data of the developed secondary twin regions on the secondary sample #y'2. The colouring of the IPF and PF maps corresponds to the crystallographic orientations depicted in the standard triangles. The EBSD analysis revealed that smaller twins, hereafter called "secondary twin", with four different variants developed inside the twin boundary induced by the primary deformation in this region. Primary twin (II) was also observed excepting the primary twin boundary.

Fig. 5.82 shows PFs representing the crystallographic orientation relationship among matrix, primary twins and secondary twins. In the pole figures, the misorientation between matrix (M.) and primary twin (P.T.$_{(I)}$) along the common (rotation) axis was 86^o, indicating that the primary twin type was $\{10\bar{1}2\} < 10\bar{1}1 >$ extension twin. Similarly, the misorientation between primary twin (P.T.$_{(I)}$) and secondary twins (S.T.$_{(I)}$-S.T.$_{(IV)}$) along the common (rotation) axis was 86^o, indicating that secondary twins were also $\{10\bar{1}2\} < 10\bar{1}1 >$ extension twins.

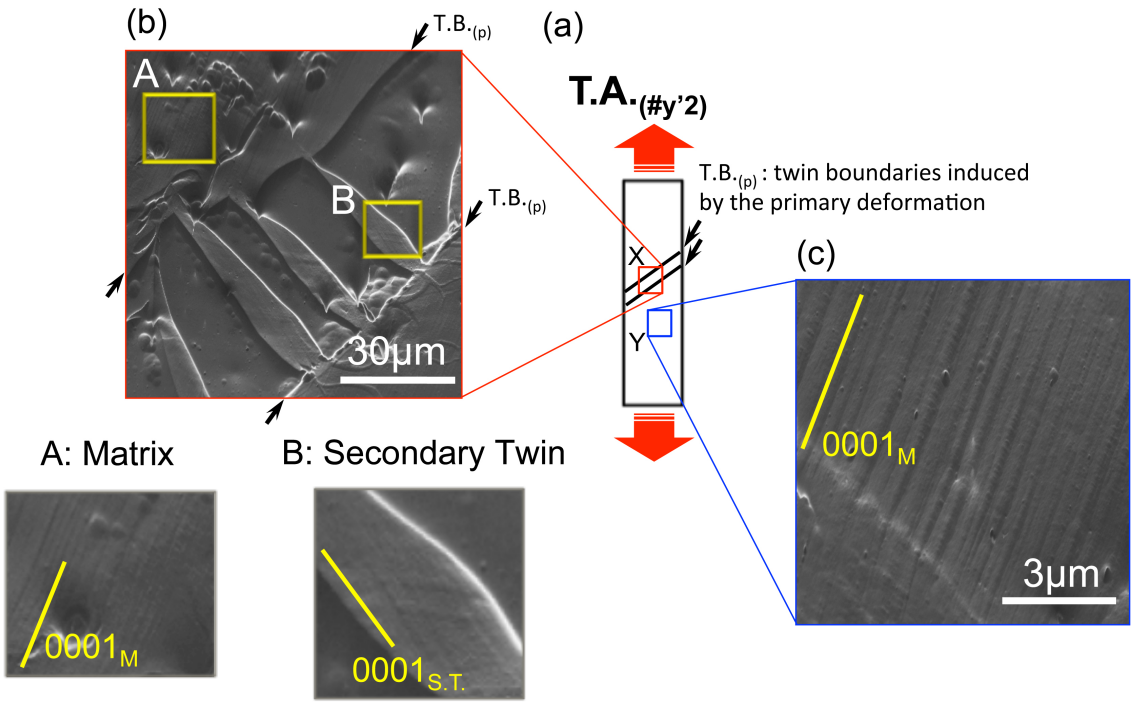

Figure 5.80: (a) Schematic illustration of the secondary sample #y'2, (b and c) SEM images from the regions X and Y, where the region X contains the primary twin boundary area and the region Y contains no primary twin.

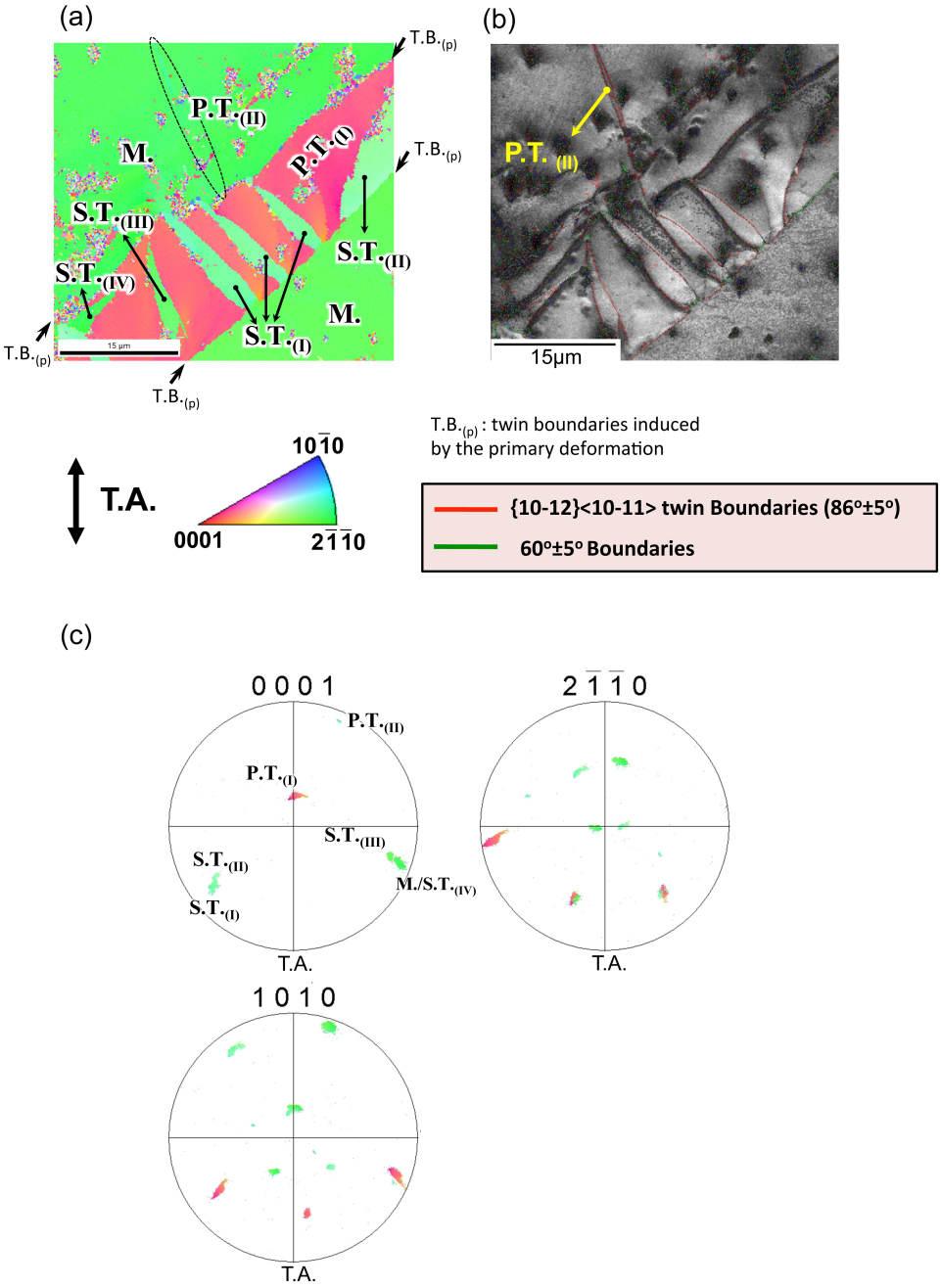

Figure 5.81: (a) Inverse pole figure (IPF) map, (b) grain boundaries map and (c) pole figures (PFs) map of the secondary twin regions developed in the secondary sample #y'2.

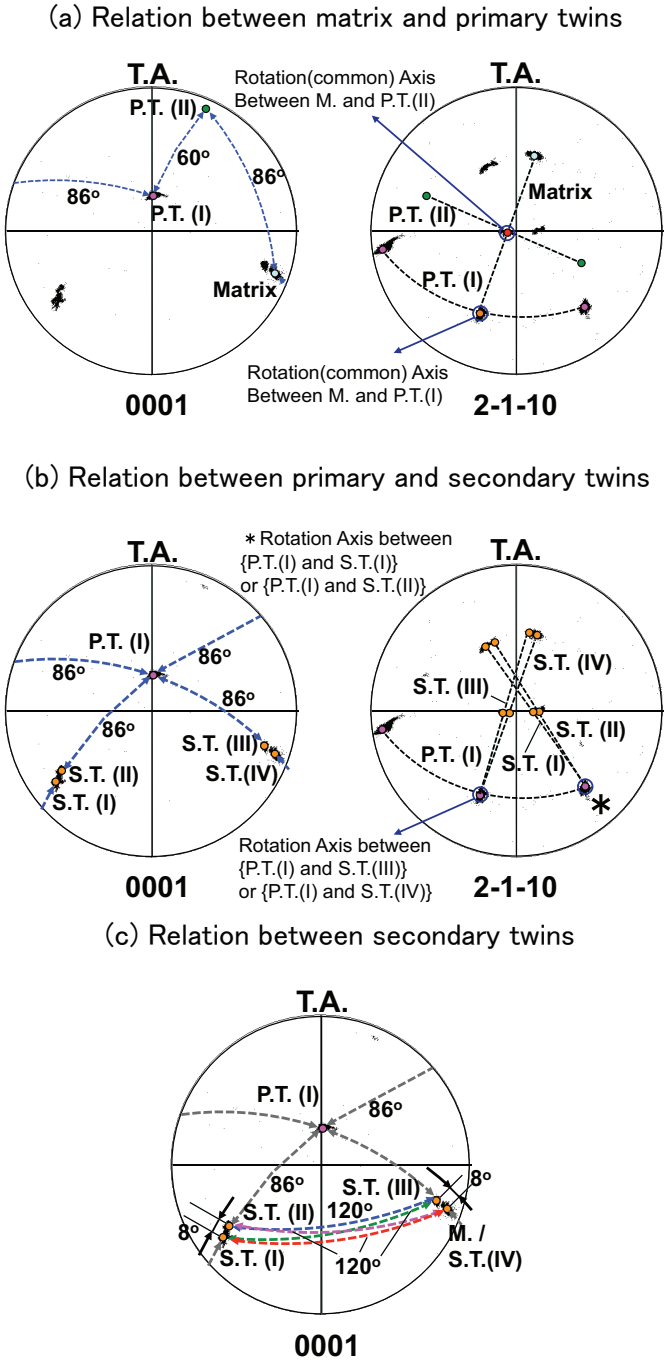

Figure 5.82: Orientation relationship between (a) matrix and primary twins, (b) primary and secondary twins and (c) secondary twins.

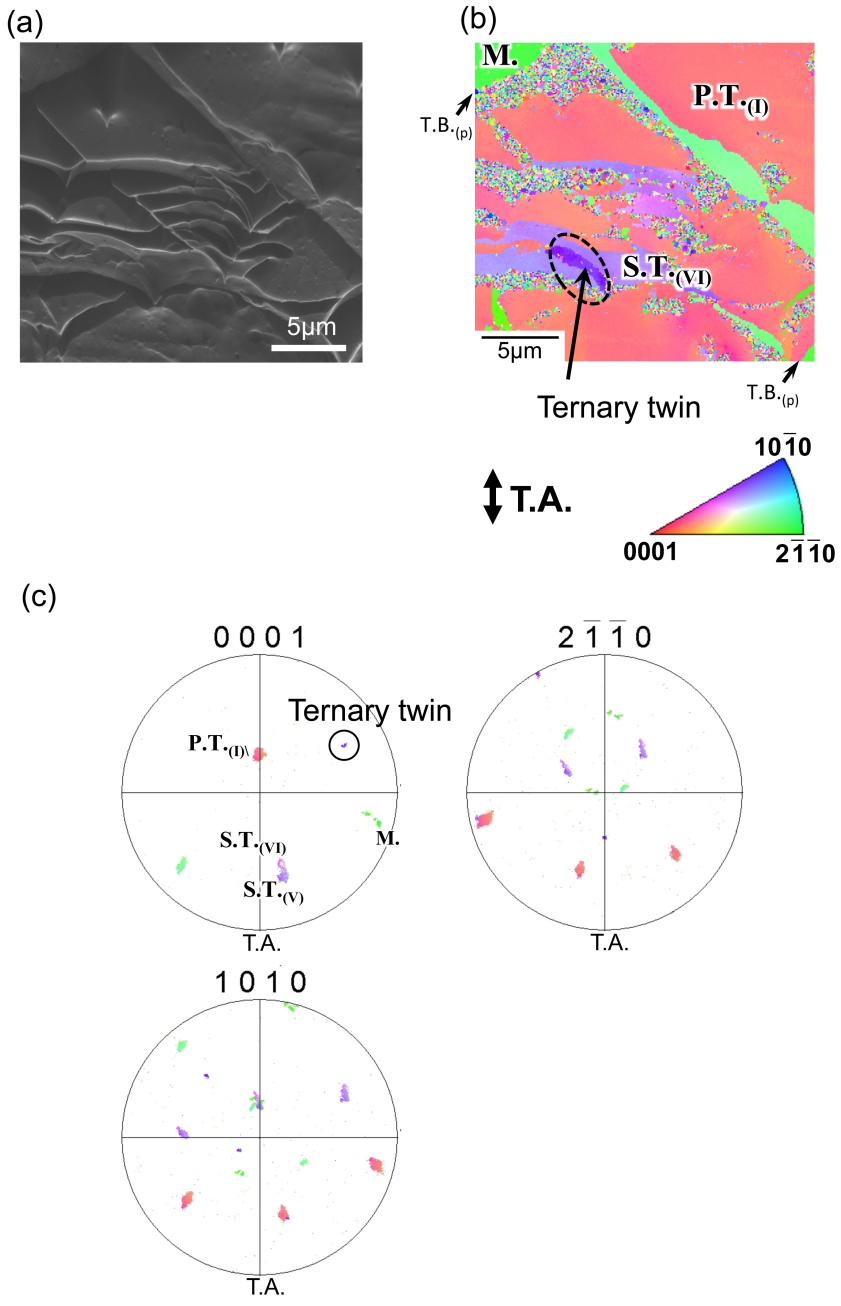

Figure 5.83: (a) SEM micrograph (b) Inverse pole figure (IPF) map and (c) pole figures (PFs) map in the ternary twin regions developed in the secondary sample #y'2.

Fig. 5.83 shows (a) higher magnification SEM image from the area inside the primary twin, (b) inverse pole figure (IPF) map, and (c) pole figures (PFs) map from the same area constructed from EBSD data. $\{10\bar{1}2\} < 10\bar{1}1 >$ twins with other two variants, S.T.$_{(V)} - S.T._{(VI)}$, were also observed in this area. Furthermore, much smaller twin, called "ternary twin" was developed inside the secondary twin (VI). The twinning type of the ternary twin was $\{10\bar{1}2\} < 10\bar{1}1 >$ extension twin. The analysis of the orientation relationship between secondary and ternary twins in sample #y'2 has been shown on the stereographic projection in Fig.5.84.

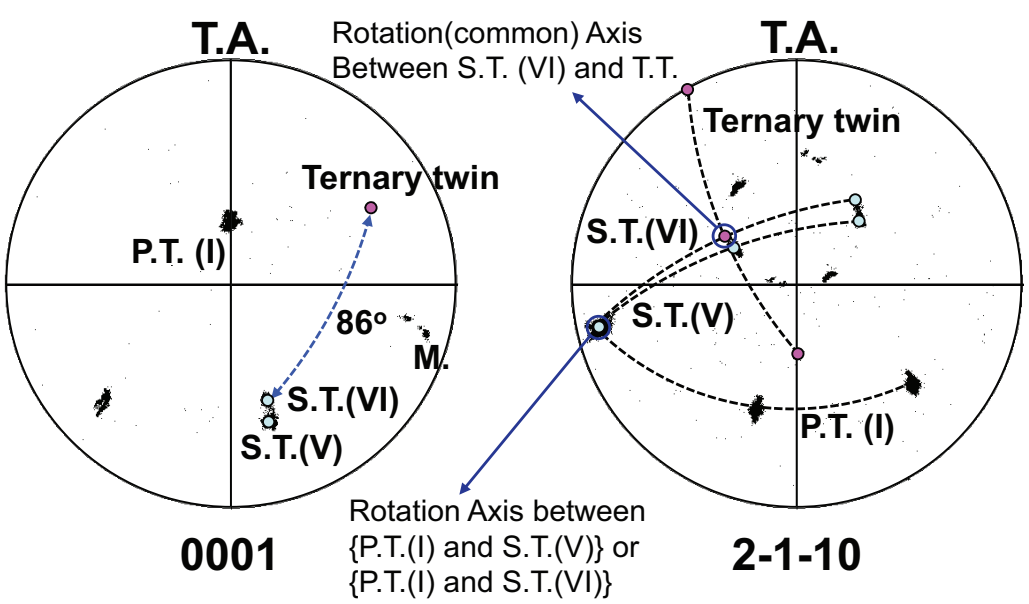

Figure 5.84: Orientation relationship between secondary and ternary twins in sample #y'2.

5.8 Indentation studies

5.8.1 Micro-indentation

Micro-hardness measurements from adjacent matrix and twin areas in secondary sample #x'-No.1-4 were carried out to determine the hardness of both phases. The primary purpose of these measurements was to understand the fundamental mechanisms by which twin phase may harden or soften as a results of plastic flow. More than 20 measurement points under the condition of $25gf$ force and 10s indentation time was applied to different areas of homogeneous parent and twin. Fig. 5.85 shows optical microscopy images from micro-hardness indents in (a) matrix and (b) twin regions. During the measurements, twins nucleated and grew from the tip of diamond as shown in Fig. 5.85. In a very soft pure Mg single crystal, twinning could not be avoided even by setting up the smallest load during the micro-indentation. The micro-hardness values recorded from matrix and twins regions in secondary samples #x' are listed in Table 5.10. The micro-hardness in both matrix and twin is rising slightly with increasing strain, but there is no large differences in the micro-hardness values between matrix and twin regions in all secondary samples, regardless of the amount of strain that the samples experienced. It should be emphasized that the micro-hardness in twin regions was measured from the twinned area large enough compared to the diamond tip. Therefore, these measurement were limited to relatively large regions of the primary twins.

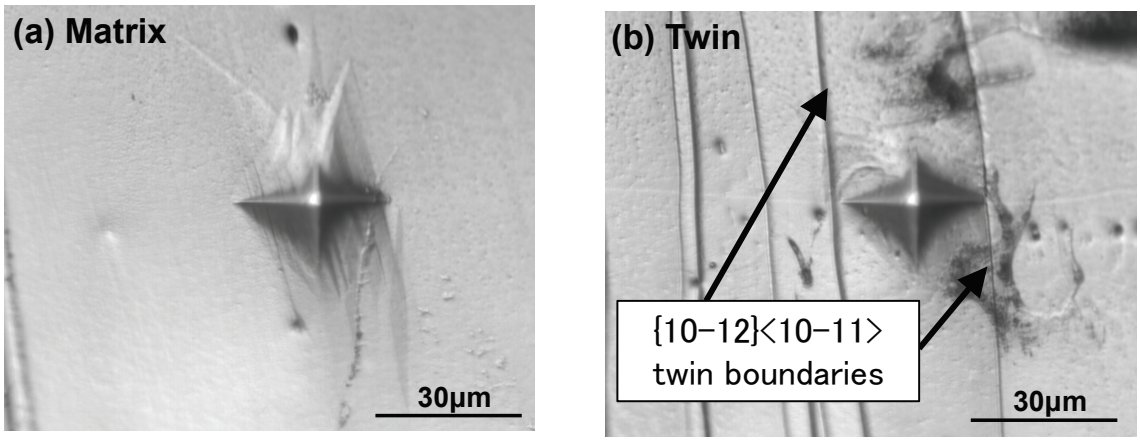

Figure 5.85: Optical microscopy (OM) images from micro-indentation regions: (a) Matrix and (b) Twin of Mg single crystal #x'.

Table 5.10: Micro-hardness data from the matrix and twin regions in crystals #x'-No.1-4.

Crystals #	Micro hardness (HV)		Remarks
	matrix	twin	
#x'-No.1	33 ± 4	36 ± 2	10% primary strain + 2% secondary strain
#x'-No.2	32 ± 2	34 ± 4	10% primary strain + 4% secondary strain
#x'-No.3	37 ± 1	39 ± 3	10% primary strain + 7% secondary strain
#x'-No.4	39 ± 2	42 ± 4	10% primary strain + 11% secondary strain

5.8.2 Nano-indentation

Micro-hardness data may reflect an average hardness value for the twinned areas, twin boundaries, and the matrix, covered by indenter. To obtain an information about local hardens values, the nano-indenation studies with the radius of an intenter of 50nm were also carried out. In this case the tip of the indenter is significantly smaller than the width of both primary and higher order twins and the advantage of using the nano-indentation test is that hardness measurements can be carried out in a homogeneous twin far from twin boundaries. Before the nano-indentation experiments, local crystallographic orientation and the twin types in inspected matrix and twins areas were determined by SEM/EBSD technique and the local hardness was measured by the Oliver and Pharr (1992) method, discussed in details in chapter 4.

Secondary samples #x'

Fig. 5.86 shows typical load versus depth, *P-h* curves obtained from the nano-indentation measurements on matrix and twin regions of the secondary sample #x'-No.4. Loading and unloading curves for matrix and twin regions exhibit very similar behaviour. Displacement bursts, i.e., "pop-in" behaviour marked as arrowheads in Fig. 5.86 were observed on the *P-h* characteristics of both matrix and twin regions. The phenomenon has been observed in several bulk and thin-film materials and it arises from the nucleation and propagation of dislocations when the shear stress is equal to the theoretical strength of the indented material (Gouldstone *et al.*, 2007).

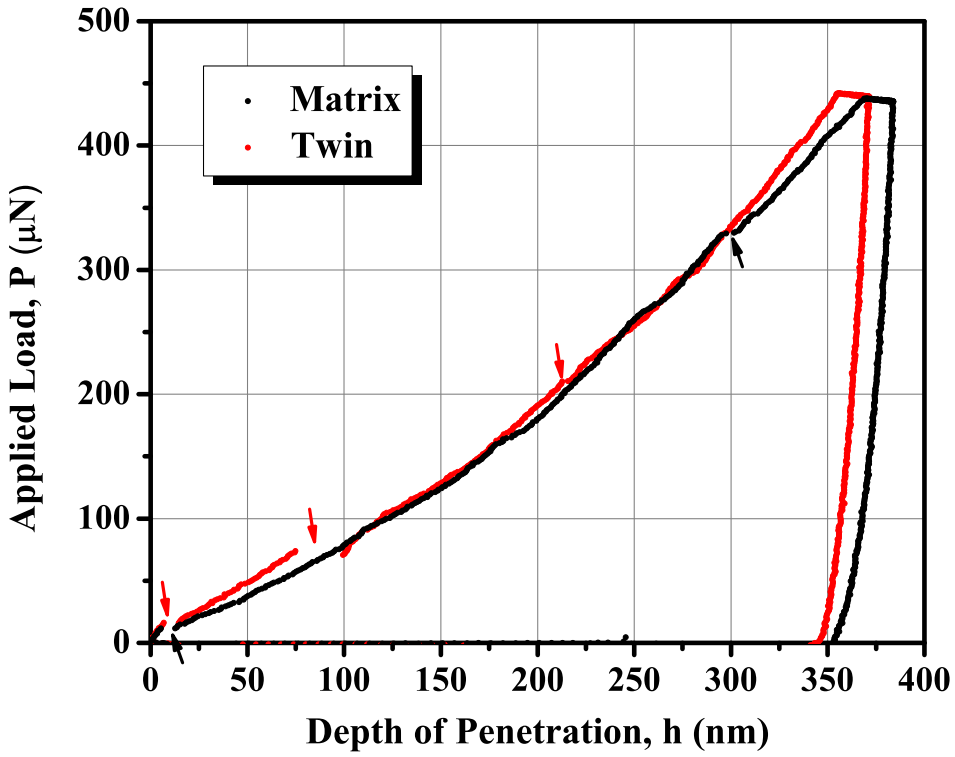

Figure 5.86: Typical load versus depth curves from the matrix and twin regions of the latent samples #x'.

As discussed in the previous section 5.5, the SEM/EBSD analysis from several areas of the secondary samples #x' No.1-No.4 revealed that the dominant deformation mode in these crystals was $\{10\bar{1}2\} < 10\bar{1}1 >$ extension twinning. Nano-indentation experiments were carried out in regions I and II of the secondary sample #x'-No.2, regions I-IV of the secondary sample #x'-No.3 and regions I-V of the secondary sample #x'-No.4, located at matrix and several variants $\{10\bar{1}2\} < 10\bar{1}1 >$ twins. The observations of these areas were shown in Fig.5.64 (c), Fig.5.66 (a), Fig.5.68 (c) and

Fig. 5.69 (a).

Table 5.11 summarizes the values of hardness and Schmid factors for basal $< a >$ slip systems under the indentation. It must be emphasized that the calculations of Schmid factor under the indentation are given by more complex equations than for the calculations of Schmid factor under uniaxial tension or compression. The indentation Schmid factor (ISF) for NiAl single crystals with FCC structure has been calculated by Li *et al.* (2011). However, as far as the author is aware, the ISF for HCP materials has not been calculated yet. In this study, the nano-indentation test was treated as an uniaxial compressive deformation on the side surfaces and the Schmid factor for an uniaxial tensile/compression test was used to rationalize activity of slip and twinning systems during nano-hardness measurements.

Very recently, a combination of TEM and nano-indentation on Mg single crystals revealed that the "pop-in" events in (0001), $(10\bar{1}2)$, and $(10\bar{1}0)$ orientations is due to the homogeneous $< a >$ dislocation's nucleation and motion (Catoor *et al.*, 2013). Even for indentation on (0001) plane, where the 2^{nd} order pyramidal $< c + a >$ slip is favoured, $< a >$ dislocations nucleate and move prior to the 2^{nd} order pyramidal $< c + a >$ dislocations. For those reasons, the hardness values obtained from the nano-indentation were analyzed in terms Schmid factor for basal $< a >$ slip, i.e., the ease of activation of basal $< a >$ dislocations.

In the secondary sample #x', the matrix region coloured in blue in the IPF map had a hard-orientation, close to $\{10\bar{1}0\}$ and the Schmid factor for basal $< a >$ slip was

Table 5.11: Nano-indentation data for latent specimens #x'.

Sample	Region	Hardness [MPa]	S.F.$_{basal}$ [-]	Remarks
#x'-No.2 Location B	I (Matrix)	825±24	0.08	10% primary strain + 11% secondary strain. Refer to Fig. 5.64 (c).
	II (Twin)	828±19	0.06	
#x'-No.3 Location A	I (Matrix)	838±40	0.06	10% primary strain + 7% secondary strain. Refer to Fig. 5.66 (a).
	II (Twin1)	824±33	0.49	
	III (Twin2)	747±28	0.42	
	IV (Twin3)	888±23	0.07	
#x'-No.4 Locations B, C	I (Matrix)	832±47	0.08	10% primary strain + 11% secondary strain. Refer to Fig. 5.68 (c) and Fig. 5.69 (a).
	II (Twin1)	774±28	0.46	
	III (Twin2)	752±31	0.49	
	IV (Twin3)	751±24	0.49	
	V (Twin4)	798±28	0.05	

† S.F.$_{basal}$ denotes the maximum Schmid factor for basal $< a >$ slip systems.

$\sim$0.08. $\{10\bar{1}2\} < 10\bar{1}1 >$ twinning rotates lattice by 86^o with respect to the parent region and it is seen that twinned regions were rotated towards softer orientations, e.g. twin1(yellow) and twin2 (green) in the sample #x'-No.3 and twin1 (green), twin2 (yellow-green) and twin3 (yellow) in the sample #x'-No.4. After transformation these twins have the orientations favouring basal $< a >$ slip, because of high Schmid factors for basal system between 0.42-0.49. On the other hand, other twinned regions were rotated towards harder orientations, close to [0001] and inherited low basal Schmid factors between 0.05-0.08. These include: red twin in the sample#x'-No.2, twin3

(red) in the sample#x'-No.3 and twin4 (red) in the sample#x'-No.4.

The local hardness values measured by the nano-indentation are represented as a function of the Schmid factor for basal $< a >$ slip. Fig. 5.87 shows hardness h versus Schmid factor for basal $< a >$ slip. Fig. 5.88 shows corresponding hardness distributions on the standard triangle with contours of the Schmid factors for basal $< a >$ slip measured by the nano-indentation in the secondary samples #x'. The hardness values clearly correlate with the orientation of the region tested. Matrix and twin regions with harder orientations (Matrix, Twin (No.2), Twin3 (No.3), and Twin 4 (No.4)) show somewhat higher hardness values, whereas twin regions with softer orientations (Twins1,2 (No.3) and Twins1,2,3 (No.4)) showed somewhat lower values.

If the Basinski hardening mechanism operates during $\{10\bar{1}2\} < 10\bar{1}1 >$ twinning deformation in Mg, the increase in the hardness of twin regions due to the effect of the structural transformation should be observed regardless of their orientations. However, as it is evident in the Fig. 5.87, the Basinski hardening mechanism can not be confirmed in the present $\{10\bar{1}2\} < 10\bar{1}1 >$ twinning in Mg.

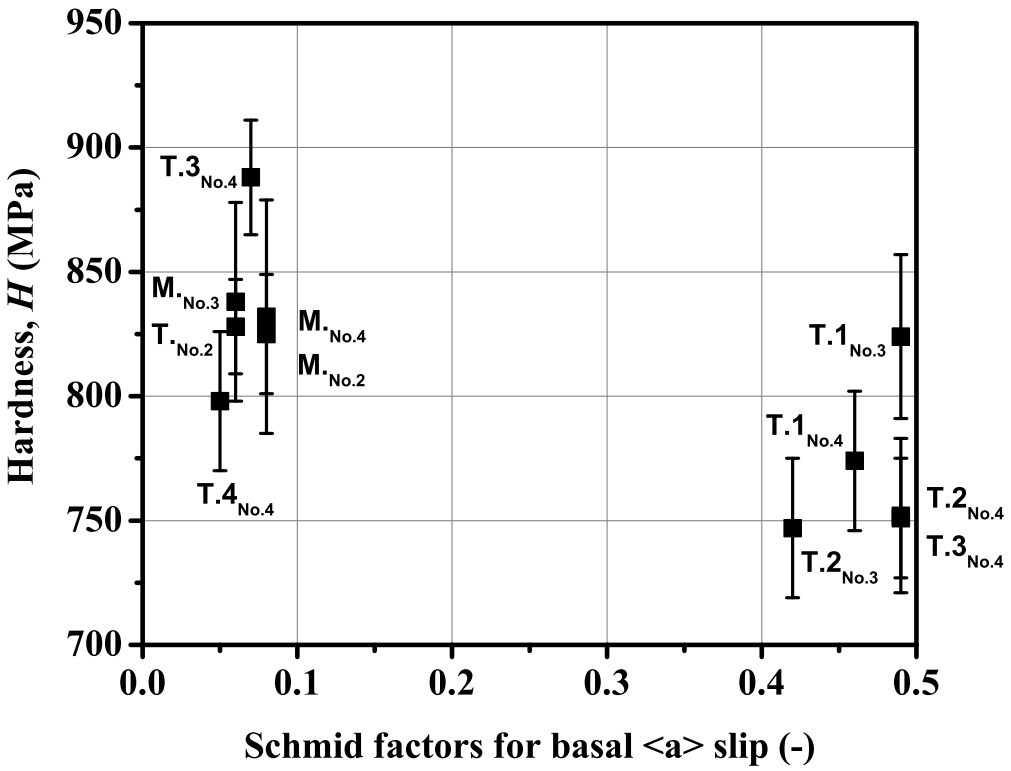

Figure 5.87: Hardness measured by the nano-indentation in the secondary samples #x' as a function of Schmid factor for basal $< a >$ slip.

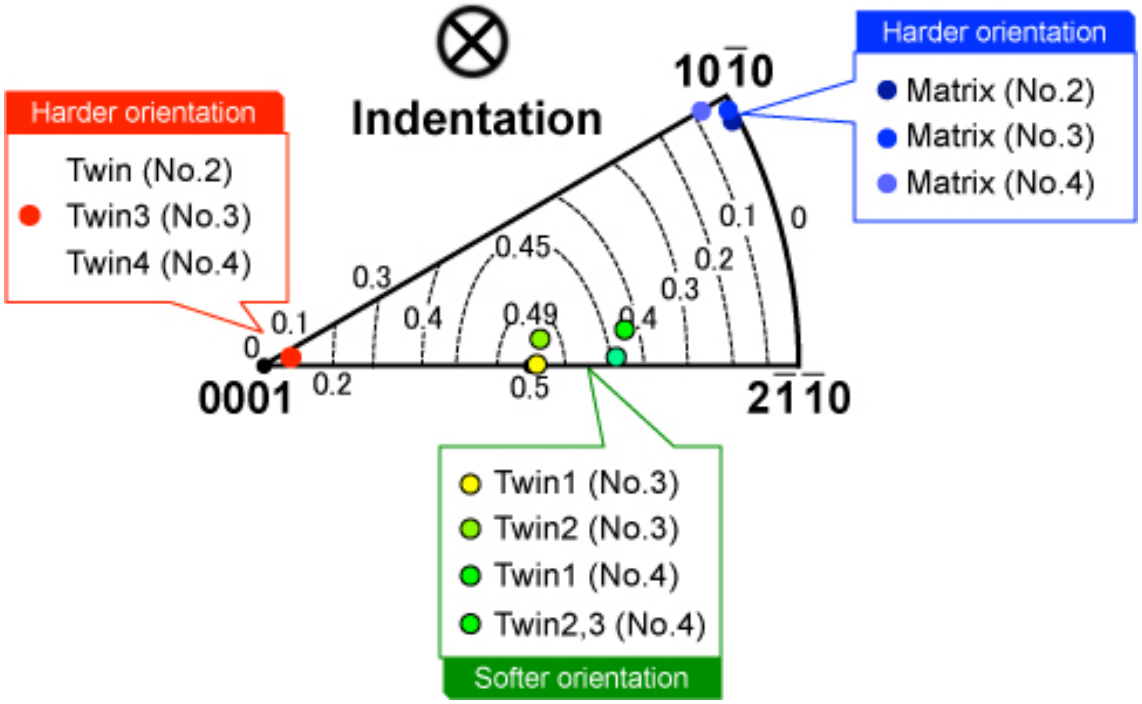

Figure 5.88: Hardness distributions on the standard triangle with contours of the Schmid factors for basal $< a >$ slip.

Similar nano-hardness measurements were carried out on crystal #1 (single basal $< a >$ slip orientation) deformed in tension to stage B (∼60% strain) and till fracture at 295K for which much higher density of basal $< a >$ dislocations was accumulated in the sample than in the secondary samples #x'.

The nano-indentation experiments were carried out on regions I-VI on location A, regions I-IV on location B in the tensile sample #1 deformed to 60% strain (Fig.5.10), regions I and II on location A, regions I-III on location B and regions I-III on location C in the tensile sample #x'-No.4 deformed to fracture (Fig.5.15).

Matrix region which is coloured in red-orange in the IPF map had a hard-orientation, close to $\{2\bar{1}\bar{1}0\}$ and the Schmid factor for basal $< a >$ slip ∼0.05. Twinned regions

were rotated towards harder orientations, highlighted by blue colours with Schmid factor for basal slip S.F.$_{basal} \sim 0.06$. Table 5.12 and Fig. 5.89 summarizes the values of hardness and Schmid factors for basal $< a >$ slip systems under the indentation. The results showed that the hardness values in twinned regions were a little bit smaller than matrix regions for all the

In summary, no experimental evidence for the Basinski hardening mechanism during $\{10\bar{1}2\} < 10\bar{1}1 >$ twinning in the secondary samples #x' was obtained and instead the hardness values showed orientation dependence, following the Schmids law in both matrix and $\{10\bar{1}2\} < 10\bar{1}1 >$ twins regions, regardless of the twin's size and their variants. Furthermore, neither the texture hardening/softening nor the Basinski hardening mechanisms were observed during the hardness measurements on deformed crystal #1. The current results are in direct conflict with the proposed hardening mechanisms due to $\{10\bar{1}2\} < 10\bar{1}1 >$ twinning in Mg and suggest that the hardness correlates with the basal Schmid factor in the parent and twin regions of deformed crystal.

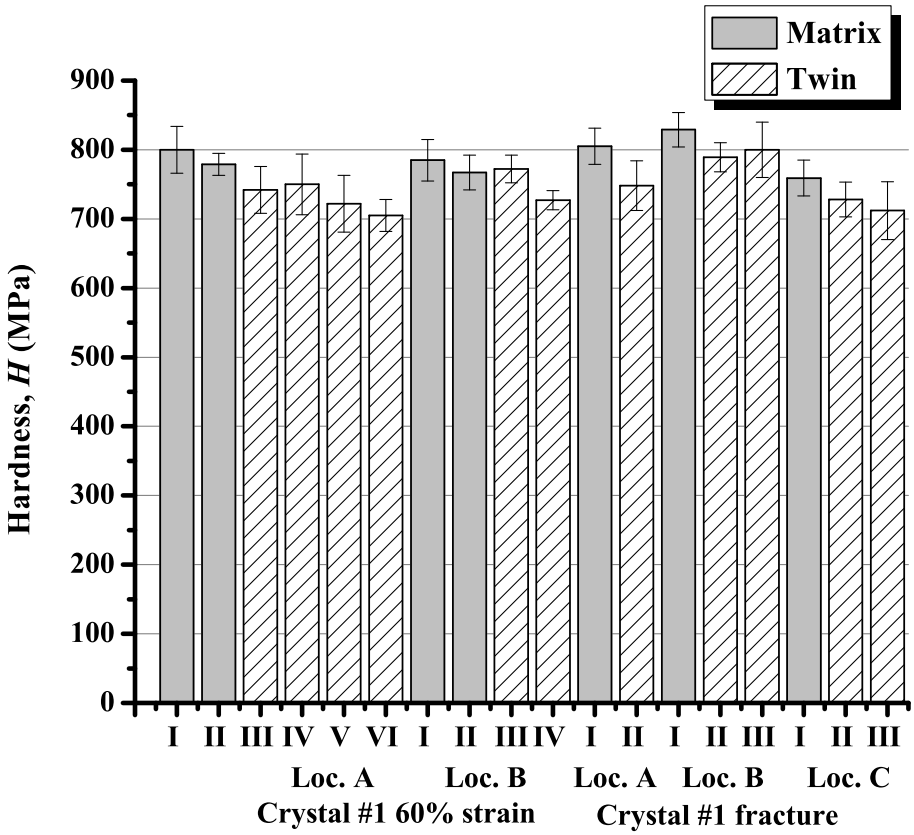

Figure 5.89: Hardness values measured by nano-indentation in crystal #1 subjected to tension.

Table 5.12: Nano-indentation data on crystal #1 deformed in tension at 295K.

Sample	Region	Hardness (MPa)	S.F.$_{basal}$ (-)	Remarks
	I (Matrix)	800±34	0.05	
	II (Matrix)	779±16	0.05	
Crystal #1	III (Twin)	742±34	0.06	
60% strain	IV (Twin)	750±44	0.06	Refer to Fig. 5.10 and Fig. 5.11.
Location A	V (Twin)	722±41	0.06	Single basal $< a >$ slip orientation.
	VI (Twin)	705±23	0.06	Transition range from
Crystal #1	I (Matrix)	785±30	0.05	stage I to stage II.
60% strain	II (Matrix)	767±25	0.05	
Location B	III (Twin)	772±20	0.06	
	IV (Twin)	727±14	0.06	
Crystal #1	I (Matrix)	805±26	0.05	
fracture	II (Twin)	748±36	0.06	Refer to Fig. 5.12-Fig. 5.15.
Location A				Single basal $< a >$ slip orientation.
Crystal #1	I (Matrix)	829±25	0.05	>105% strain (fracture).
fracture	II (Twin)	789±21	0.06	Locations A and B:
Location B	III (Twin)	800±40	0.06	near fracture surface.
Crystal #1	I (Matrix)	759±26	0.05	Location C:
fracture	II (Twin)	728±25	0.06	far from fracture surface.
Location C	III (Twin)	712±42	0.06	

† S.F.$_{basal}$ denotes the maximum Schmid factor for basal $< a >$ slip systems.

Chapter 6

Discussions

6.1 Tensile and compressive deformation behaviour of Mg single crystals

In this thesis, room temperature tensile and compressive deformation characteristics of Mg single crystals with four different crystallographic orientations were investigated: crystal #1 (oriented for single basal $< a >$ slip system), crystal #2 (oriented for double basal $< a >$ slip), crystal #3 (oriented for basal and twin deformation), and crystal #4 (oriented for $\{10\bar{1}2\} < 10\bar{1}1 >$ twin under tension and 2^{nd} order pyramidal $< c+a >$ slip under compression). Table 6.1 summarizes important mechanical characteristics data obtained from these studies: yield stress, critical resolved shear stress (CRSS), fracture stress, homogeneous elongation, and Considère ratio (CR) (Basinski *et al.*, 1997a).

Table 6.1: Tensile and compressive deformation characteristics data of Mg single crystals #1-#4 at 295K.

Crystal #	Yield stress, σ_0 (MPa)	CRSS, τ_0 (MPa)	Fracture stress, σ_F (MPa)	Homogeneous elongation, ϵ_F (%)	CR^* (-)	Deformation modes
#1T	1.40	0.70	65	105	3.06	Single basal $< a >$
#1C	1.88	0.92	-	-	1.00	Single basal $< a >$
#2T	1.98	1.27	59	94	-	Double basal $< a >$
#2C	2.25	1.38	-	-	1.00	basal+twin
#3T	3.51	-	48	49	-	basal+twin
#3C	2.38	-	-	-	1.00	basal+twin
#4T	5.32	2.72	75	8.83	16.9	$\{10\bar{1}2\}$ twin
#4C	80.5	30	290	12.7	3.82	2^{nd} py. $< c+a >$

* CR=Considère ratio (Basinski *et al.*, 1997a). Note: The CR for #2T and #3T cannot be calculated because the work hardening before fracture is fluctuating sharply.

6.1.1 Critical resolved shear stress (CRSS)

Fig. 6.1 shows the comparisons of stress – strain characteristics for Mg single crystals oriented for basal $< a >$ slip, 2^{nd} order pyramidal $< c+a >$ slip, and $\{10\bar{1}2\} < 10\bar{1}1 >$ twin systems during initial stage of plastic flow at 295K, where the elasto – plastic transition and the differences between the values of the critical resolved shear stress (CRSS) of individual orientations are clearly visible. The CRSS at room temperature decrease in the order of basal $< a >$ slip, $\{10\bar{1}2\} < 10\bar{1}1 >$ twin, and 2^{nd} order pyramidal $< c + a >$ slip as reported in the literatures, e.g. see Fig. (B.5) in the

Appendix for the values of CRSS of each deformation modes.

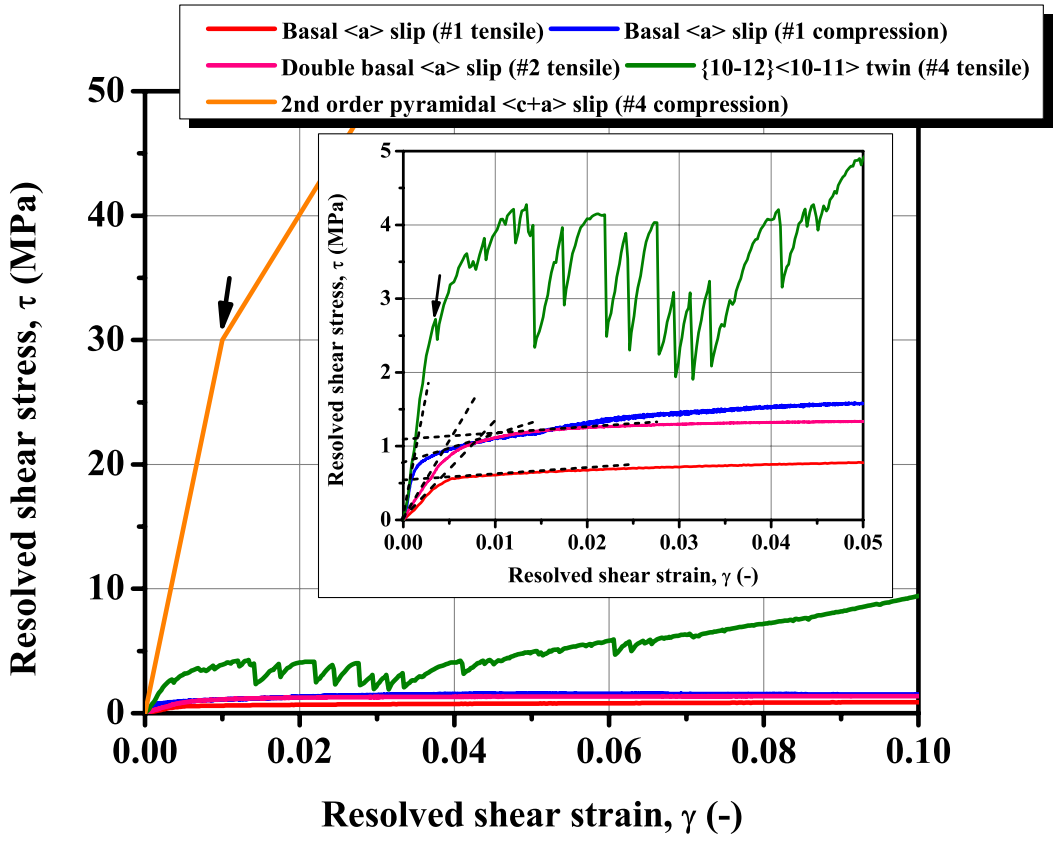

Figure 6.1: Comparisons of resolved shear stress – resolved shear strain characteristic of Mg single crystals oriented for basal $< a >$ slip, 2^{nd} order pyramidal $< c + a >$ slip, and $\{10\bar{1}2\} < 10\bar{1}1 >$ twin systems during initial stage of plastic flow at 295K. CRSS values are depicted in the figure for corresponding orientations of crystals.

The CRSS for basal $< a >$ slip obtained in current studies was 0.70MPa for a crystal #1. Bhattacharya and Niewczas (2011) have pointed out that various sensitive parameters such as metal purities, sample size, initial crystallographic orientation,

influence τ - γ characteristics of Mg single crystals. The CRSS values for basal $< a >$ slip of Mg single crystals at 295K reported by different researchers are in the range between 0.5MPa-1.1MPa e.g., 1MPa was reported by Basinski (1960), 0.8-0.9MPa by Yoshinaga and Horiuchi (1962), ∼0.5MPa by Hirsch and Lally (1965), 0.7MPa by Lavrentev *et al.* (1973),and ∼1.1MPa by Bhattacharya and Niewczas (2011). It is clear that the present data represent the lower range of CRSS values measured in the literature. The CRSS for basal $< a >$ slip obtained from compression test of crystal #1 was 0.92MPa, slightly higher than the tensile test. In Cu single crystals oriented for single slip, the CRSS for compressive deformation is almost twice higher than for tensile deformation (Takeuchi, 1975).

The CRSS observed in the tensile test of crystal #2 oriented for double basal $< a >$ slip, was somewhat higher than the tensile and compression tests of crystal #1 (single basal $< a >$ slip orientation). When both slip systems BI and BII operate simultaneously, the stress axis moves towards $[1\bar{1}00]$, the direction given by the sum of the two slip directions, $\frac{1}{3}[2\bar{1}\bar{1}0]+\frac{1}{3}[1\bar{2}10]=[1\bar{1}00]$. Such a crystallographic orientation evolution is considered to be unstable. Stress serrations accompanied $\{10\bar{1}2\} < 10\bar{1}1 >$ twinning was observed in the middle of deformation in the double basal $< a >$ slip orientation crystals. However, the double coplanar basal $< a >$ slip was active at least at the beginning of deformation, and it was associated with slightly higher CRSS. The present results agree with the observations of Edwards *et al.* (1953), who reported the increase of CRSS in double basal $< a >$ orientation of Zn single crystal in comparison with crystals oriented for single basal $< a >$ slip.

The CRSS for 2^{nd} order pyramidal $< c + a >$ slip system observed in the c-axis

[0001] compression test of crystal #4 was 30MPa. The values of CRSS for 2^{nd} order pyramidal $< c + a >$ slip reporting by Ando *et al.* (2010) were slightly different between the c-axis compression tests and the a-axis tensile tests. Ando *et al.* (2010) explained the differences by sample size between the both tests, argumenting that activation of 2^{nd} order pyramidal $< c + a >$ slip systems depend on aspect ratio of the specimens. Apart from the sample size difference, several other factors may also affect the CRSS for 2^{nd} order pyramidal $< c + a >$ slip. As shown in Table 6.2, for the [0001] compression test, all the six slip systems, II.Py1-II.Py6, had the highest Schmid factor value of 0.45 and the multiple slip can be induced during plastic flow of these crystals. On the other hand in the $[2\bar{1}\bar{1}0]$ single crystals, two slip systems, II.Py3 and II.Py6 had 0.45 Schmid factor, wheres other slip systems had low Schmid factor values, about 0.11 (Table 6.2), making II.Py3 and II.Py6 slip systems dominant mechanisms of plastic flow.

Table 6.2: Difference of Schmid factors for 2^{nd} order pyramidal $< c+a >$ slip systems between [0001] and $[2\bar{1}\bar{1}0]$ orientaions.

Deformatin modes	Notation	Miller-Bravais index	Schmid factor	
			[0001]	$[2\bar{1}\bar{1}0]$
2^{nd} order pyramidal $< c + a >$ slip	II.Py1	$(11\bar{2}2)[\bar{1}\bar{1}23]$	0.45	0.11
	II.Py2	$(\bar{1}2\bar{1}2)[1\bar{2}13]$	0.45	0.11
	II.Py3	$(\bar{2}112)[2\bar{1}\bar{1}3]$	0.45	0.45
	II.Py4	$(\bar{1}\bar{1}22)[11\bar{2}3]$	0.45	0.11
	II.Py5	$(1\bar{2}12)[\bar{1}2\bar{1}3]$	0.45	0.11
	II.Py6	$(2\bar{1}\bar{1}2)[\bar{2}113]$	0.45	0.45

The CRSS for $\{10\bar{1}2\} < 10\bar{1}1 >$ twinning obtained from the c-axis [0001] tensile

test of crystal #4 was 2.72MPa. The data agree with the CRSS for $\{10\bar{1}2\} < 10\bar{1}1 >$ twinning reported by Koike (2005), who observed CRSS values in the range ∼2-3MPa independent of deformation temperatures and strain rate.

6.1.2 Work hardening behaviour of Mg single crystals

Fig. 6.2 - Fig. 6.5 show comparisons of the $\sigma - \epsilon$ curves and the $\Theta - \epsilon$ plots for tensile and compressive deformation tests of Mg single crystals #1 - #4 at 295K. In the tensile tests, work hardening rate for crystal #4 with the perfect $\{10\bar{1}2\} < 10\bar{1}1 >$ twin orientation was about an order of magnitude higher than other crystals oriented for basal $< a >$ slip. Although both basal $< a >$ slip and $\{10\bar{1}2\} < 10\bar{1}1 >$ twin were activated simultaneously in crystal #3 from the beginning of deformation, the work hardening rate was almost at the same level as in crystal #1 and #2. Under the compression tests, the work hardening rate of crystal #4 oriented for 2^{nd} order pyramidal $< c + a >$ slip was significantly higher than other crystals.

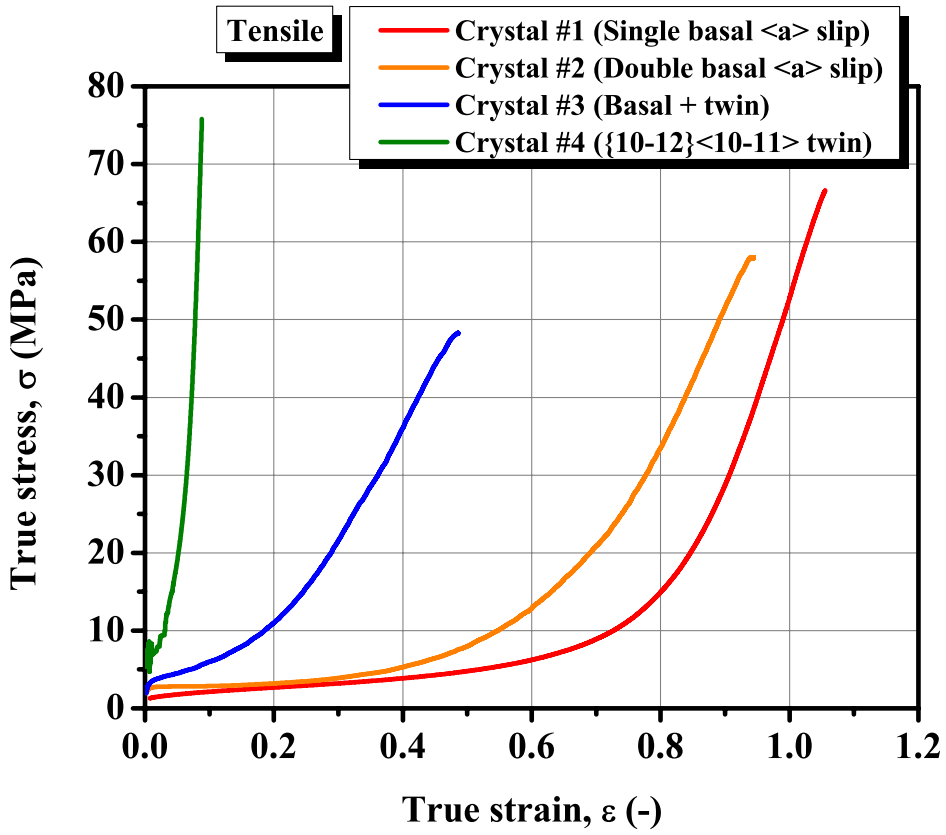

Figure 6.2: Comparisons of $\sigma - \epsilon$ curves for Mg single crystals #1 - #4 deformed in tension at 295K.

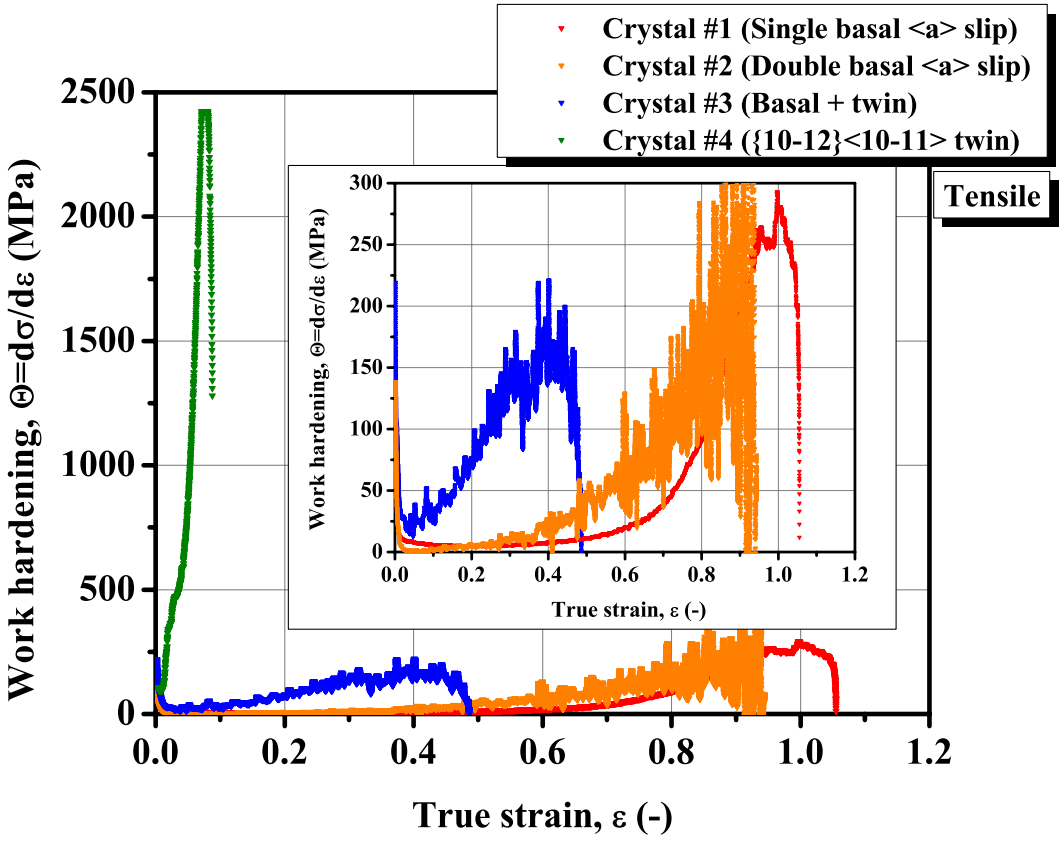

Figure 6.3: Comparisons of $\Theta - \epsilon$ plots for Mg single crystals #1 - #4 deformed in tension at 295K.

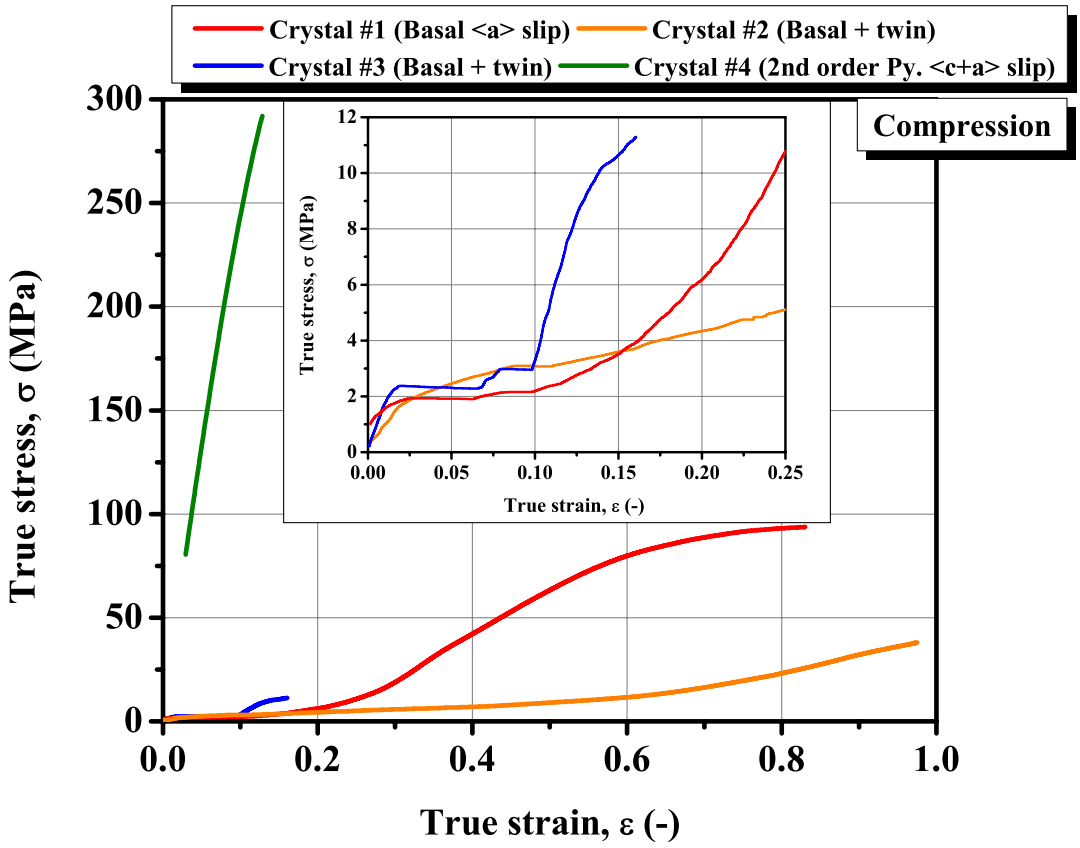

Figure 6.4: Comparisons of $\sigma - \epsilon$ curves for Mg single crystals #1 - #4 deformed in compression at 295K.

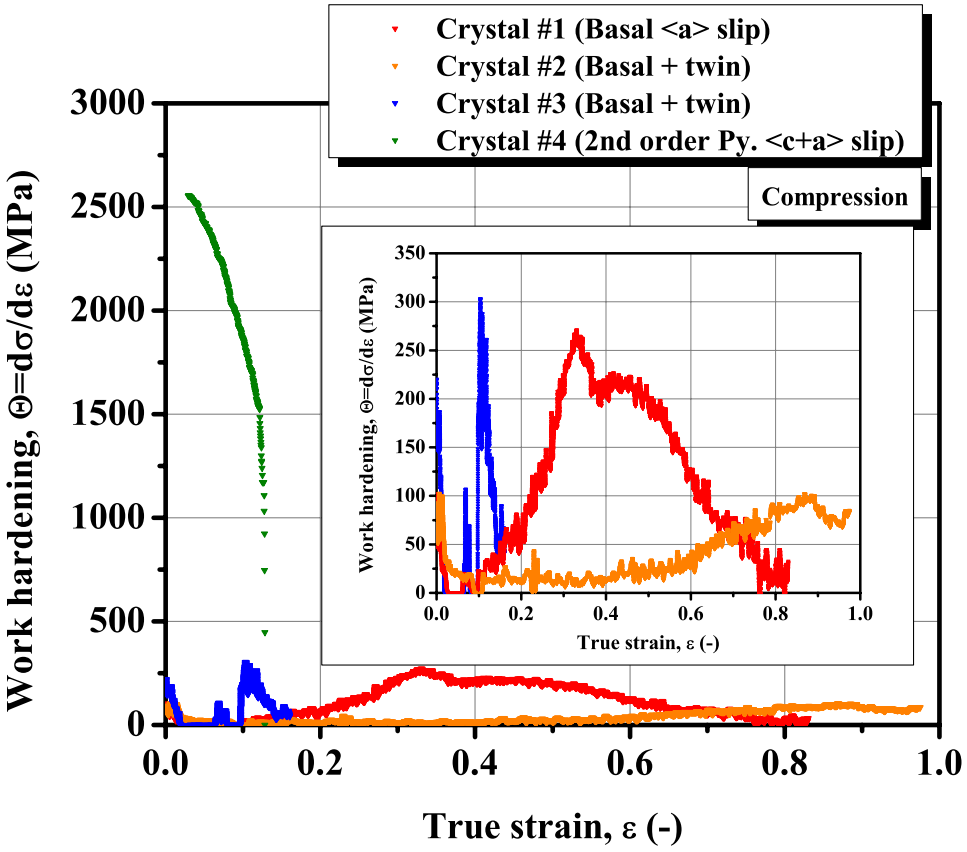

Figure 6.5: Comparisons of $\Theta - \epsilon$ plots for Mg single crystals #1 - #4 deformed in compression at 295K.

We now discuss the work hardening behaviour of Mg single crystals under different deformation modes. Fig. 6.6 and Fig. 6.7 show comparisons of the $\tau - \gamma$ curves and the $\theta/\mu - \tau/\mu$ plots for basal $< a >$ slip, 2^{nd} order pyramidal $< c+a >$ slip, and $\{10\bar{1}2\} < 10\bar{1}1 >$ twin orientations in Mg single crystals. The work hardening behaviour is strongly orientation dependent and the work hardening rate of the crystal #4 deformed in compression (2^{nd} order pyramidal $< c+a >$ slip orientation) shows the highest value among all the single crystal orientations studied here.

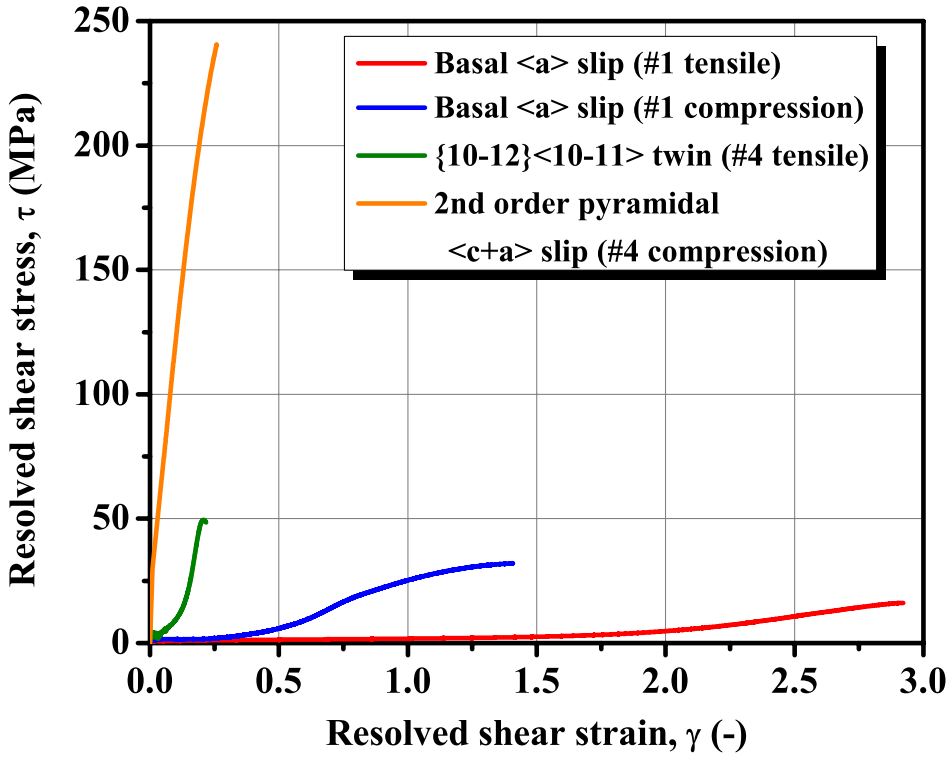

Figure 6.6: Comparisons of $\tau - \gamma$ curves for basal $< a >$ slip, 2^{nd} order pyramidal $< c+a >$ slip, and $\{10\bar{1}2\} < 10\bar{1}1 >$ twin orientations in Mg single crystals at 295K.

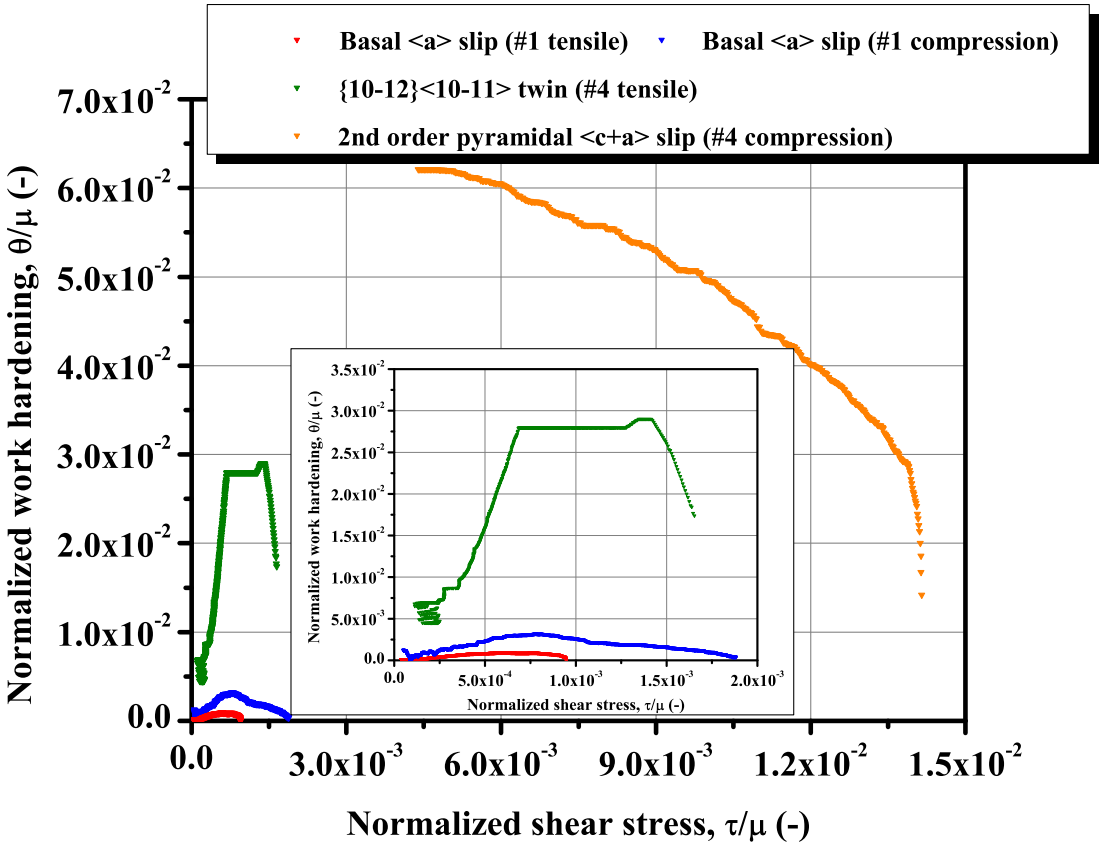

Figure 6.7: Comparisons of $\theta/\mu - \tau/\mu$ plots for basal $< a >$ slip, 2^{nd} order pyramidal $< c+a >$ slip, and $\{10\bar{1}2\} < 10\bar{1}1 >$ twin orientations in Mg single crystals at 295K.

The analysis of the work hardening behaviour using Kocks and Mecking method (Kocks and Mecking, 2003) provides further information about dislocations storage and recovery during plastic flow. The Kocks-Mecking analysis was carried out on deformed Mg polycrystals (Cáceres and Blake, 2007; Cáceres *et al.*, 2008; Cáceres and Lukáč, 2008; Noble, 2011; Jia, 2013) and Mg-RE binary alloys (Noble, 2011; Jia, 2013). For Mg single crystals, Cáceres *et al.* (2008) and Bhattacharya and Niewczas (2011) have analyzed the Kocks-Mecking's $\tau\theta$ plots based on the data available in

the literatures and their own experimental results for: basal $< a >$ slip orientation (Akhtar, 1968; Akhtar and Teghtsoonian, 1968a; Lavrentev and Pokhil, 1975b; Bhattacharya, 2006; Bhattacharya and Niewczas, 2011), prism $< a >$ slip orientation (Akhtar, 1968), and 2^{nd} order pyramidal $< c + a >$ slip orientation (Obara *et al.*, 1973; Tonda and Ando, 2002; Ando *et al.*, 2003). In this thesis, the Kocks-Mecking analysis is carried out for Mg single crystals oriented for basal $< a >$ slip, 2^{nd} order pyramidal $< c + a >$ slip and $\{10\bar{1}2\} < 10\bar{1}1 >$ twining, the results will be compared and contrasted with the data in the literature.

When the plastic flow is governed by dislocations interactions, the resolved shear stress is expressed as a function of dislocation densities,

$$\tau - \tau_0 = \alpha \mu b \rho^{1/2} \tag{6.1}$$

where τ_0 is the critical resolved shear stress, α is a constant $\sim$0.2-0.35 for most metals, μ is the shear modulus, b is the magnitude of the Burgers vector of the dislocations, and ρ is the dislocation densities stored in the material. The rate of dislocation accumulation with the shear strain, γ can be expressed as:

$$\frac{d\rho}{d\gamma} = \frac{1}{bL} \tag{6.2}$$

where L stands for dislocations mean free path and if we assume a similitude relationship between mean free path and dislocation density:

$$L = \beta \rho^{-1/2} \tag{6.3}$$

where β is a constant, eq. (6.2) can be rearranged such that:

$$\frac{d\rho}{d\gamma} = \frac{\sqrt{\rho}}{\beta b}. \tag{6.4}$$

Differentiating eq. (6.1) and inserting eq. (6.4) yields:

$$(\tau - \tau_0)\frac{d\tau}{d\gamma} = \frac{(\alpha\mu b)^2}{2}\frac{d\rho}{d\gamma}. \tag{6.5}$$

Combining eq. (6.4) with the definition of work hardening one obtains:

$$(\tau - \tau_0)\,\theta = \frac{(\alpha\mu)^2}{2}\frac{b}{L}. \tag{6.6}$$

Finally, rearrangements of eqs. (6.1), (6.4), and (6.6) leads to

$$\frac{\theta}{\mu} = \frac{\alpha}{2\beta}. \tag{6.7}$$

Eqs. (6.6) and (6.7) imply that the Kocks-Mecking's $\tau\theta$ plot should be a straight line through the origin, when the work hardening is governed by the dislocation interactions and accumulations. This concept can also apply to polycrystaline materials by using the appropriate Taylor factor. For the polycrystals, Eqs. (6.6) can be transformed into:

$$(\sigma - Y)\frac{d\theta}{d\epsilon} = (\sigma - Y)\left[\Theta_h - \Theta\left(\sigma, \dot{\epsilon}, T\right)\right]. \tag{6.8}$$

where σ is the flow stress, Y is the yield strength, ϵ is the strain, Θ_h is the work hardening rate in polycrystals, equivalent to θ_h in single crystals, and Θ_r is the recovery term due to dislocation annihilation.

Fig. 6.8 shows a schematic plot of the Kocks-Mecking's $\tau\theta$ plot (Kocks and Mecking, 2003; Cáceres and Lukáč, 2008; Cáceres *et al.*, 2008) represented by eq. (6.8). When gliding dislocations interact with grain boundaries, twin boundaries, and other dislocation, the dislocation mean free path becomes:

$$\frac{1}{L} = \frac{1}{D_0} + \frac{1}{D} + \frac{\rho^{1/2}}{\beta} \tag{6.9}$$

where D_0 is the initial grain size and D is the mean twinning space. When a mean free path is a constant, $\sigma\Theta$=*const.*, indicated by dash line 1 in the Fig. 6.8. In turn, when the mean free path is proportional to the dislocation spacing, i.e., athermal forest hardening, $\sigma\Theta$ increases with stress (line 2). The solid line 3 predicts work hardening behaviours when the two effects occur simultaneously.

In addition, one must consider the effects of deformation twinning on strain-hardening of polycrystalline HCP materials. It has been suggested that profuse mechanical twins substantially increase the work hardening during deformation through at least three independent hardening mechanism, described in the literature review section, i.e., (i) dynamical Hall-Petch effect, (ii) texture hardening/softening, and (iii) the Basinski mechanism (Cáceres *et al.*, 2008). The Kocks-Mecking's analysis enables us to analyse the twinning effect on the work hardening for the following reasons. Grain segmentation by the deformation twinning shifts line 1 up to line 4, because the mean free path decreases. Point A predicts that the hardening by dynamical Hall-Petch effect is over and twinning saturates. Gross dislocation plasticity is dominant after this point, shown by line 5. Line 6 is the superimposition of two mechanisms, indicating that deformation twinning influences the strain hardening during the onset of plastic deformation.

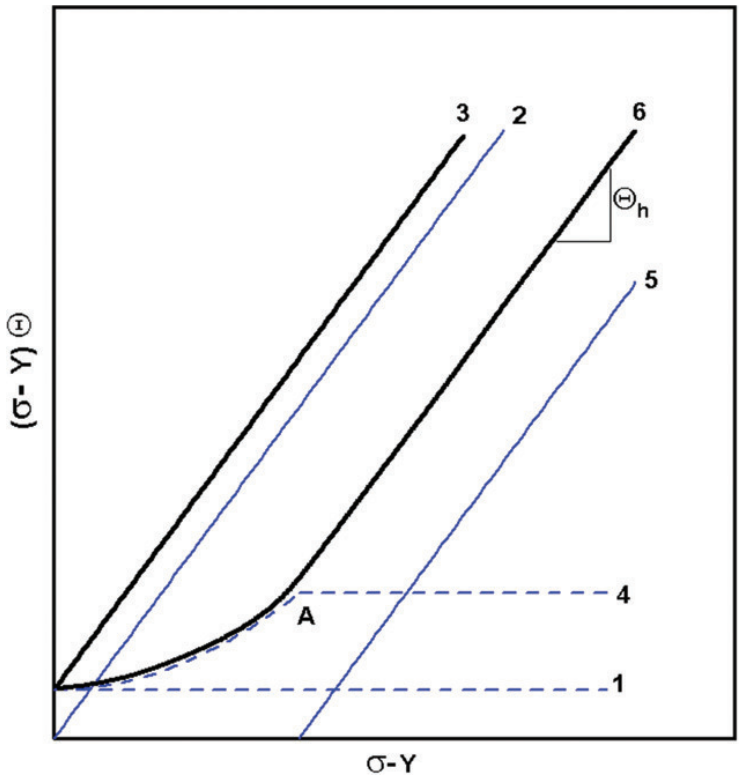

Figure 6.8: A schematic plot of the Kocks-Mecking's $\tau\theta$ plot (Cáceres *et al.*, 2008).

Fig. 6.9 shows the Kocks-Mecking's $\tau\theta$ plots, i.e., $(\tau - \tau_0)\theta$ vs. $(\tau - \tau_0)$ plots of Mg single crystals oriented for single basal $< a >$ slip (crystal #1 tension and compression), $\{10\bar{1}2\} < 10\bar{1}1 >$ twin orientation (crystal #4 tension), and 2^{nd} order pyramidal $< c+a >$ slip (crystal #4 compression). $\tau_0 = 0.70$MPa, 0.92MPa, 2.72MPa and 30MPa have been used as CRSS for basal $< a >$ slip system during tensile and compressive deformation, $\{10\bar{1}2\} < 10\bar{1}1 >$ twinning and 2^{nd} order pyramidal $< c + a >$ slip, respectively.

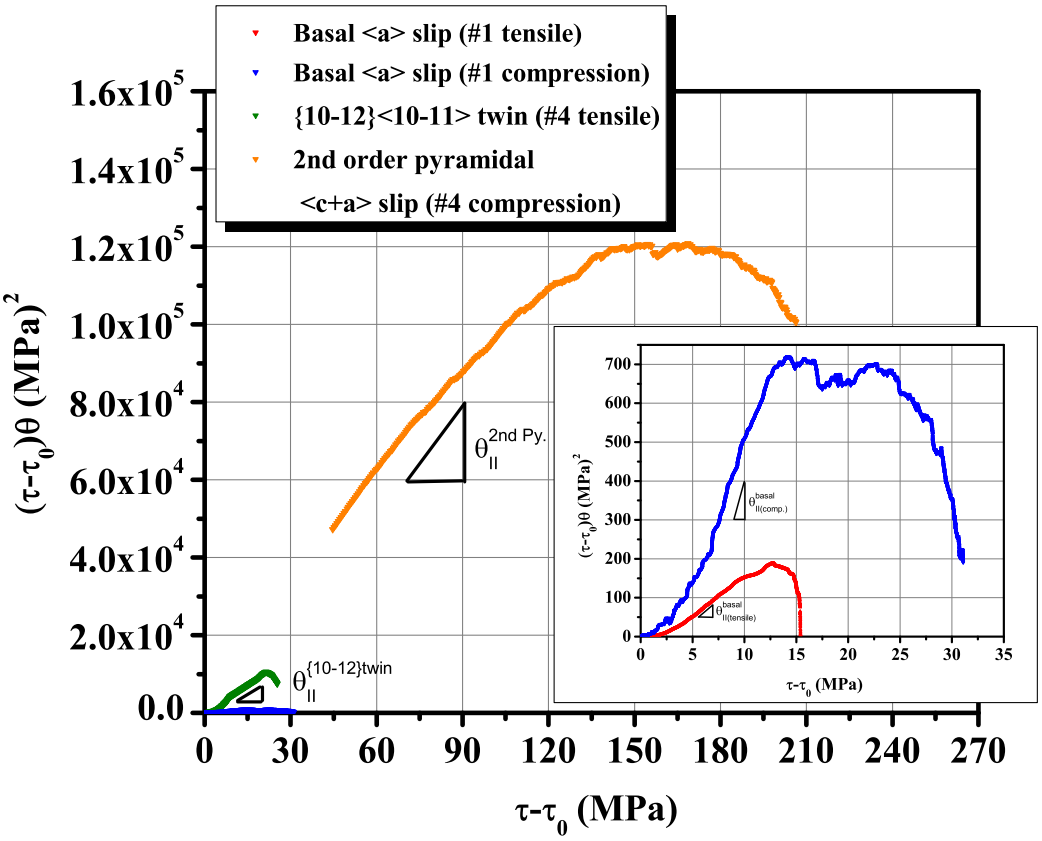

Figure 6.9: Comparison of Kocks-Mecking's $\tau\theta$ plots of Mg single crystals oriented for single basal $< a >$ slip (crystal #1 tension and compression), $\{10\bar{1}2\} < 10\bar{1}1 >$ twin orientation (crystal #4 tension), and 2^{nd} order pyramidal $< c+a >$ slip (crystal #4 compression).

The $\tau\theta - -\tau$ plots for basal $< a >$ slip orientations exhibit upwards curvature during the transition from stage I to stage II of the deformation and then follow a linear relation in stage II, for both tensile and compressive deformation tests. An abrupt fall in the $\tau\theta - \tau$ curve in the tensile test of crystal #1 was observed after the linear region, while the dynamic recovery stage due to dislocation annihilation

was observed in the compression test after stage II (Fig. 6.9). Such features on $\tau\theta$-τ characteristics were also reported by Bhattacharya and Niewczas (2011)'s and Cáceres *et al.* (2008)'s. Cáceres and Blake (2007) pointed out that when dislocation slip and mechanical twin systems operate simultaneously, the Kocks-Mecking's $\tau\theta$ plot show an upward curvature, which is peculiar to deformation of HCP metals. This behaviour contrasts the $\tau\theta$-τ behaviour during stage II in FCC metals characterized by forest dislocation interactions. Mecking and Kocks (1981) have analyzed $\tau\theta$ plots for $< 541 >$ Ag single crystals and showed that $\tau\theta$ values are proportional to the flow stress or dislocation densities during the forest hardening region.

The work hardening rate in stage II of compressive deformation of crystal #1, $\theta_{II(C)}^{Basal}$∼100MPa was somewhat higher than the tensile deformation of crystal #1, $\theta_{II(T)}^{Basal}$∼50MPa. Apart from small difference in CRSSs, the difference in the work hardening rate is observed between tensile and compressive deformation. This is probably in part due to the factors discussed earlier such as sample size, or the friction effect during the compression test, but it may also be caused by different contribution of operating slip systems.

The effect of grain refinement by $\{10\bar{1}2\} < 10\bar{1}1 >$ twinning on work hardening behaviour of random and textured Mg polycrystals was analyzed by means of the Kocks-Mecking method by Cáceres and Blake (2007); Cáceres *et al.* (2008); Cáceres and Lukáč (2008). However, there has been no data on the influence of $\{10\bar{1}2\} < 10\bar{1}1 >$ twinning on the hardening behaviour of Mg single crystals and the current studies represent the first analysis of this kind in Mg single crystals deformed by $\{10\bar{1}2\} < 10\bar{1}1 >$ twinning mode. Fig. 6.10 shows the Kocks-Mecking's $\tau\theta$ plot

of Mg single crystal #4 deformed in tension at 295K, where τ_0 is the CRSS. The $\tau\theta$-τ characteristics of the tensile deformation in crystal #4 can be divided into two regions, depicted region I and region II in Fig. 6.10.

In the region I, a positive curvature related to the $\{10\bar{1}2\} < 10\bar{1}1 >$ twinning deformation is observed. The stage I characterized by the profuse twinning deformation extended over to 3-4% true strain marked by the point A. The profuse twinning region is also seen in polycrystalline Mg in the first 6-8% strain. Cáceres *et al.* (2008) demonstrated that the quasi Hall-Petch hardening associated with grain segmentation by $\{10\bar{1}2\} < 10\bar{1}1 >$ twin in polycrystalline Mg has relatively small effect on hardening. For textured-polycrystals, the authors attributed this effect to the small value of the Hall-Peach constants. For randomly oriented grains the fraction of grains undergoing twinning is small, despite the larger Hall-Petch constant. As a result, the twinning has a minor contribution to the hardening of polycrystals.

During the profuse twinning region in Mg single crystals, work hardening, θ_I was low, ∼400MPa. After the twinning stage ends at point A, a deformation proceeds by gross dislocation plasticity (region II), characterized by slip/slip, twin/slip, and twin/twin dislocation interactions and the creations of higher order $\{10\bar{1}2\} < 10\bar{1}1 >$ twins of much finer size. The work hardening in the region II, $\theta_{II}^{T.twin}$ ∼500MPa is higher than observed earlier.

In the Kocks-Meckng's analysis (Cáceres *et al.*, 2008), the gross hardening stage continues smoothly with the same level of the hardening rate after the onset of profuse twinning (dash line in Fig. 6.8). However, the work hardening rate θ_{II} observed in the present work is more moderate than one could expect. This is probably because the activity of basal $< a >$ slip becomes more enhanced due to lattice rotation during

deformation. Slip trace analysis on the surfaces of crystal #4, show the traces from the basal plane together with the traces from different twin variants. The slip traces were tilted a few degree (at most 8°) from the basal plane due to the lattice rotation during the tensile deformation and it caused gross hardening associated with twin - slip, twin - twin dislocations interactions between basal $< a >$ slip and $\{10\bar{1}2\} < 10\bar{1}1 >$ twin in late stage of deformation, 4-9% strain.

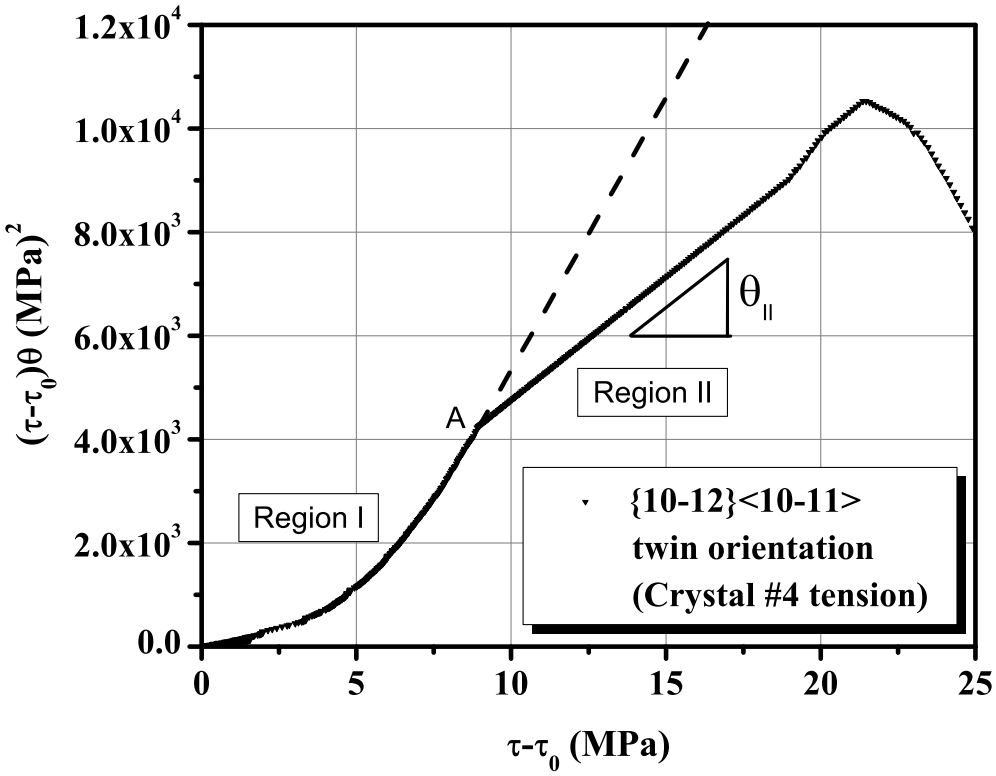

Figure 6.10: The Kocks-Mecking's $\tau\theta$ plot of Mg single crystal #4 deformed in tension at 295K.

Work hardening in stage II in the crystal #4 deformed in tension, $\theta_{II}^{T,twin}$ ∼500MPa

is one order of magnitude higher than crystal #1, $\theta_{II(T)}^{Basal}$ ∼50MPa. This is attributed to the difference in volume fraction of twins created during deformation. In the crystal #4 oriented for twinning, a high density of $\{10\bar{1}2\} < 10\bar{1}1 >$ twin interfaces is created during the onset of twinning and they act as strong obstacles and contribute to higher work hardening rate of the material. On the other hand, volume fraction of twins in Mg single crystal oriented for basal $< a >$ slip deformed to fracture was at maximum ∼20%, according to the X-ray texture analysis by Bhattacharya and Niewczas (2011). These results agree with the current EBSD analysis in the tensile specimen #1, as shown in Fig. 5.13.

In the c-axis compression, a linear hardening stage on $\tau\theta$ versus τ characteristics was observed, due to the athermal forest hardening between the 2^{nd} order pyramidal $< c + a >$ slip systems. This stage shows similarity to $\tau\theta$–τ behaviour during stage II in FCC metals (Asaro, 1975), probably because 2^{nd} order pyramidal $< c + a >$ slip systems contains five independent slip systems and they may interact together. The work hardening rate in stage II of crystal #4 deformed in compression showed the highest value, $\theta_{II}^{II.Py.}$∼1000MPa, among all single crystal orientations studied. The work hardening rate was approximately at the same level as reported by Obara *et al.* (1973), ∼1150MPa, for Mg single crystals compressed along the c-axis.

The work hardening behaviour of Mg single crystals oriented for $< c + a >$ slip is very complex. The magnitude of the Burgers vector $< c + a >$ is large compared to interatomic spacing and the pyramidal planes are atomically rough. The $< c + a >$ dislocations tend to reduce its energy by dissociation and/or decomposition. Therefore, it seems that the effects of dislocations core splitting and dislocation mobility of

$< c + a >$ dislocations are responsible for the initial rapid hardening stage observed in $\tau\theta - \tau$ characteristics of single crystals more than the effect of the forest hardening for 2^{nd} order pyramidal $< c + a >$ slip systems.

TEM observations of Mg foils in the a-axis orientation deformed a few percent in the microscope (Ando *et al.*, 1992), indicate that the $< c + a >$ dislocations were observed occasionally, typically in conjunction with perfect $< a >$ and $< c >$ dislocations. The theoretical calculations verified that these dislocations are stable in the screw orientation but unstable in the edge orientation (Ando *et al.*, 1992).

The core structures of $< c + a >$ edge dislocation have been studied by molecular dynamics (MD) simulations (Minonishi *et al.*, 1981b, 1982a; Bacon and Liang, 1986; Liang and Bacon, 1986a,b; Ando *et al.*, 1996, 2002). However, there are difficulties in the interpretation of the simulation results because the particular type of core structure depends sensitively on the initial position of the core, the interatomic potential, and the relaxation technique used. The simulation results by Ando *et al.* (1996, 2002) suggest that the $< c + a >$ edge dislocation has two stable core structures at 0K: one type is the perfect dislocation and the other type consist of two $\frac{1}{2} < c + a >$ partial dislocations. The core of $< c + a >$ edge dislocation becomes sessile due to the core structure change, in which the core extends parallel to the basal plane, as temperature increases, resulting in very low mobility of the $< c + a >$ edge dislocation. The core structures of $< c + a >$ screw dislocation has also been simulated by MD technique (Minonishi *et al.*, 1981a, 1982b). These calculations indicate that the screw cores may split on multiple slip planes, the pyramidal and the basal planes and the $< c + a >$ screw dislocations are likely to cross-slip on the basal planes. The calculation results are supported by TEM observations (Ando *et al.*, 1992).

6.1.3 Ductility, instability, and fracture mechanisms

According to the Considère criterion, a tensile specimen would undergo stable deformation up to the point where the work hardening is equal to the true stress, $\frac{d\sigma}{d\epsilon} = \sigma$. Necking or localized deformation begins at the maximum load where the increase in the flow stress due to the decrease in the cross sectional area of the specimen, becomes greater than the increase in the load carrying ability of the metal due to the strain hardening. However, many metals and alloys exhibit a sudden onset of strain localization before the samples satisfy this criterion. Basinski *et al.* (1997b) reported this kind of instability in Cu and Cu alloy single crystals and in order to describe this phenomenon quantitatively, these authors introduced the Considère ratio (CR), a ratio of the work hardening rate and the flow stress at the fracture,

$$CR = \frac{\frac{d\sigma_F}{d\epsilon_F}}{\sigma_F} = \frac{\Theta_F}{\sigma_F}. \tag{6.10}$$

When CR$\leq$1 the Considère criterion is met and if CR>1, the criterion is not satisfied. In this thesis, the CRs are calculated for Mg single crystals with various orientations and their ductility, instability, and fracture mechanisms are discussed.

As seen in Fig. 6.2 - Fig. 6.5, ductility of the specimens exhibits strong orientation dependence. We discuss first the ductility, instability and fracture mechanisms of tensile deformed Mg single crystal samples #1-4. Single crystals #1 and #2 with initial basal $< a >$ slip orientations exhibited good ductility over 100% of true strain, during room temperature tensile deformation. As the Schmid factor for basal $< a >$ slip decreases and the activation of $\{10\bar{1}2\} < 10\bar{1}1 >$ twin increases, ductility of

single crystals decreases. In the case of tensile deformation of crystal #4 at 295K with $\{10\bar{1}2\} < 10\bar{1}1 >$ twin orientation, the crystal had fractured just after about 8.8% of true strain. This suggests that interfaces introduced during onset of twinning decrease ductility.

In Table 6.1, the Considère ratio (CR) for all the crystals tested in the present works is considerably larger than unity (CR>1), i.e., the work hardening decreases suddenly at certain stress level after stage II. The CR for crystal #1 oriented for basal $< a >$ slip is 3.06, while the CR for crystal #4 oriented for $\{10\bar{1}2\} < 10\bar{1}1 >$ twinning under tension, reached quite a large number, 16.9. The Kocks-Mecking analysis indicates that $\{10\bar{1}2\} < 10\bar{1}1 >$ twinning contributes to the strength of these materials. At the same time, the $\{10\bar{1}2\} < 10\bar{1}1 >$ twin interfaces act as the favourable sites of crack nucleation. Many $\{10\bar{1}2\} < 10\bar{1}1 >$ twins were observed in crystal #1 deformed in tension until fracture at 295K, as shown in Fig. 5.12 and Fig. 5.13. However, according to the Kocks-Mecking analysis of crystal #4, the gross hardening stage proceeded at least another 5% of true strain, after the profuse twinning hardening stage was over.

The combined Kocks-Mecking analysis and the CR permits to gain an insight into the operating mechanisms, which lead to fracture of the crystal. The interaction of the $\{10\bar{1}2\} < 10\bar{1}1 >$ twin interfaces with operating slip modes is believed to be one of the main reasons for the premature failure of the crystal. SEM fracture surface observations of Mg single crystals oriented for single basal $< a >$ slip at 295K showed a ductile type of fracture mode and cleavage along non-basal planes in some areas (Bhattacharya and Niewczas, 2011). Therefore, the results suggest that increase in non-basal $< a >$ slip activities in stage II and the $\{10\bar{1}2\} < 10\bar{1}1 >$ twin interactions

with basal $< a >$ and non-basal $< a >$ slip dislocations promotes failure of the crystals in the tensile samples #1, #2, and #3. For the tensile sample #4, in contrast, there is little possibility of the activations of non-basal $< a >$ slip systems. Optical microscopy observation of the tensile sample #4 after fracture revealed evidence of the slip traces from basal $< a >$ slip together with multiple $\{10\bar{1}2\} < 10\bar{1}1 >$ twins. Lattice rotations in deformed matrix area by SEM/EBSD analysis was only a few degree from the initial positions. This indicates that much higher frequency of $\{10\bar{1}2\} < 10\bar{1}1 >$ twin interactions with basal $< a >$ slip dislocation causes failure of the crystals in the tensile samples #4.

The crystal orientation influences strongly not only the work hardening behaviour and the ductility but also instability and fracture mechanisms of the specimens. The CRs for Mg single crystals at 295K obtained in the current studies are quite higher than CRs for Cu single crystals. Cu single crystals oriented for single slip show CR$\sim$1.1-1.8, these oriented for multiple slip, $\sim$1.0, and Cu polycrystals exhibit CR$\sim$1.0 (Basinski *et al.*, 1997b). The results indicate therefore that multiple slip Cu single crystals and polycrystalline Cu obey the classical Considère criterion (Basinski *et al.*, 1997b).

We turn our attention to the properties of Mg single crystals under compression and discuss the ductility, instability, and fracture mechanisms of compressed sample #4. The compression sample #4 oriented for 2^{nd} order pyramidal $< c + a >$ slip systems fractured by shear after about 12% of true strain. Mg single crystal deformed in the c-axis compression at 295K presents poor ductility. Similarly poor ductility

shows crystal with $\{10\bar{1}2\} < 10\bar{1}1 >$ twin orientation. However, the CR for compression sample #4C, 3.82 is almost at the same level as for basal $< a >$ slip orientation (CR$\sim$3.06). It was difficult to analyzed the shear fracture area by EBSD, because the fracture area was heavily distorted and the image quality was very low. As Obara *et al.* (1973) pointed out, the fracture mechanisms may be due to the activation of $\{10\bar{1}1\} < 10\bar{1}2 >$ twin and rapid accumulations of basal $< a >$ dislocations at the twin boundaries.

The conclusions obtained from the current deformation studies suggest that in order to improve the ductility of Mg single crystals it is necessary to enhance the activity of the non-basal $< a >$ slip systems in the expense of $\{10\bar{1}2\} < 10\bar{1}1 >$ twinning. The same should be true to improve ductility and formability of more complex Mg alloys at/near room temperature.

Koike and Maruyama (2004) have studied grain size dependence of deformation modes in Mg alloys. For coarse-grained Mg alloys ($\sim$20-30μm), basal $< a >$ slip and $\{10\bar{1}2\} < 10\bar{1}1 >$ twin are dominant modes in the first stage of deformation. For fine-grained Mg alloys (grain size $<$10μm), the activity of $\{10\bar{1}2\} < 10\bar{1}1 >$ twinning is suppressed, whereas the activities of non-basal $< a >$ slip systems are enhanced. Grain refinement is a valuable materials processing also from a different perspective, e.g. ductility and fracture toughness. In coarse-grained Mg alloys, deformation twins form at the very beginning stage of deformation and crack propagation occurs through the twin boundaries (Somekawa *et al.*, 2009). However, recently, Somekawa *et al.* (2010) studied fracture mechanisms in a fine-grained Mg alloys (grain size $\sim$1-3μm) and found different fracture mechanisms from these observed in the coarse-grained

alloys. The authors have reported that in the fine-grained Mg alloys, deformation twins were suppressed, causing higher ductility and fracture toughness of alloys with the ductile fracture occurring by void formation. Another way of improving ductility of Mg is to add small amounts of alloy elements, e.g. Ce is known as the one of the effective solute strengthening elements, which makes Mg cold-workable (Barnett *et al.*, 2004a). Discussion of theses aspects is beyond the scope of the present thesis.

6.2 Latent hardening behaviours under the conditions of self- and coplanar interactions on the basal plane

6.2.1 Coplanar interactions on the basal plane

For the coplanar interactions between BI/BIII slip systems, the LHRs were always higher than in the case of BI/BI self-interactions and LHRs showed linear increase from 1.0-1.6 in the range of 0-49% primary shear strain studied here. The results are in good agreement with latent hardening experiments on Mg single crystals under pure shear by Phillips (1961), which revealed that LHRs increase linearly with the shear strain of parent crystals, up to the value of $\sim$1.24, in the range of 0-7.5% shear strain values.

However, the observed latent hardening behaviour on the coplanar system in Mg is significantly different from that of FCC single crystals such as Cu and/or Al single crystals. Most researchers reported the LHRs for the coplanar systems in FCC crystals between 1.0 and 1.2 (Basinski and Basinski, 1979), but the experimental results

of deferent research groups showed significant discrepancies. Later, more precise experiments by Franciosi *et al.* (1980) revealed that the LHRs on the coplanar B4/B2 system in Al and Cu behave in a similar way as LHRS for the forest interactions between B4/A6 and B4/A2 systems. The LHRs increase from unity to maximum values between 0 to 0.2% of primary shear strain (early stage I) and then, the they decrease rapidly with increasing primary shear strain, in the transition from stage I to stage II. Finally, the LHRs saturate at approximately constant values later in Stage II of deformation.

Classical forest hardening theory can be used to understand the difference in latent hardening behaviour between FCC and HCP crystals. In the forest hardening theory (Jackson and Basinski, 1967), the flow stresses of both the primary and latent systems can be described by:

$$\tau_p = \alpha_p \mu \left(\rho_f\right)^{1/2} \tag{6.11}$$

and

$$\tau_f = \alpha_f \mu \left(\rho_p + \rho_f\right)^{1/2} \tag{6.12}$$

where ρ is the density of dislocations, with the subscripts f and p referring to the density of dislocations in the forest and primary slip systems. μ is the shear modulus, b is the Burgers vector, α_p and α_f are interaction coefficients. Wessels and Jackson (1969) suggested that when the primary shear strain is large enough, the values of LHRs are approximately expressed as:

$$LHR = \frac{\tau_f}{\tau_p} \approx \left(1 + \frac{\rho_p}{\rho_f}\right)^{1/2} \tag{6.13}$$

The eq. (6.13) suggests that the LHR is approximately proportional to the square

root of the ratio of the dislocation density in the primary system to that in the latent system. Mecking and Bulian (1976) measured the dislocation densities on primary and forest planes in Al and Cu single crystals deformed in tension at 295K and plotted the square root of the ratio of primary to forest dislocation densities against the shear stress, i.e., $(\rho_p/\rho_f)^{1/2}$ versus τ plots. The $(\rho_p/\rho_f)^{1/2}$ versus τ plots showed similar characteristics as the LHRs versus τ plots and the approximate expression for LHR given by the eq. (6.13) was considered to be valid (Mecking and Bulian, 1976).

For Mg single crystals oriented for single basal $< a >$ slip system, deformed in tension or in pure shear at 295K, measurements of dislocation densities on the primary and forest systems were carried out by etch-pit counts (Sułkowski and Mikułowski, 2012) and by TEM observations (Hirsch and Lally, 1965). These experimental measurements revealed that the dislocation densities on the basal plane and the non-basal plane, ρ_b and ρ_f have a linear relationship with shear strain or stress. A remarkable observation is that the basal $< a >$ dislocation density is at least one order of magnitude higher than the forest dislocation density in crystals, even before rupture. This experimental evidence suggests that the LHRs for co-planar system are proportional to the dislocation densities on the basal plane, ρ_b. Therefore, when the classical forest hardening theory is applied to the current latent hardening studies in Mg, the LHRs should be expressed as a function of $\rho_b^{1/2}$ because $\rho_b \gg \rho_f$ during stage I of deformation. We believe that this is the reason that the latent hardening behaviour of Mg single crystals with HCP structure shows a different behaviour from that observed in FCC single crystals.

TEM studies of dislocation substructures in deformed Mg single crystals with single basal $< a >$ slip orientation revealed that other basal $< a >$ slip systems

operate together with original primary basal $< a >$ slip in the transition from stage I to II (Hirsch and Lally, 1965; Sharp *et al.*, 1965; Lavrentev and Pokhil, 1975b). These coplanar interactions, which can be expressed by the reaction between two basal $< a >$ dislocations: $[2\bar{1}\bar{1}0]+[\bar{1}2\bar{1}0]=[11\bar{2}0]$, are at least partially responsible for hardening rate change from stage I to stage II. Another effect might be the increase activity of the non-basal slip systems with increasing the flow stress.

The experiments with single crystals oriented for double basal $< a >$ slip (crystal #2) support the latent hardening results of single basal $< a >$ slip orientation crystals. As a result of BI and BII slip systems operating mutually, as discussed in section 6.1.1, the CRSS and the work hardening rate for basal $< a >$ slip observed in a double basal $< a >$ slip orientation was a bit higher, at the level of $\sigma_0 \sim 1.27$MPa and $\theta \sim 2.35 - 6.48x10^{-5}\mu$ (stage I) and $\theta \sim 7.18 - 8.25x10^{-4}\mu$ (stage II), than in a single basal $< a >$ slip orientation ($\sigma_0 \sim 0.70$ MPa, $\theta \sim 4.70 - 8.30x10^{-5}\mu$ (stage I) and $\theta \sim 8.35 - 9.05x10^{-4}\mu$ (stage II)). This is a fingerprint of the contribution of the coplanar slip system to the flow stress and work hardening.

6.2.2 Self-interactions in the basal slip plane

Present results reveal that LHRs for the self-interactions between BI/BI slip system were independent on the primary strain and the values were closed to unity. Easy glide stage is characterized by dominant single basal $< a >$ slip. TEM studies of Mg single crystals deformed in stage I indicate that the main features of dislocation substructure and the work hardening in stage I in Mg single crystals are as follows: (Hirsch and Lally, 1965; Sharp *et al.*, 1965; Lavrentev and Pokhil, 1975b): (i) the dislocations from the sources operating simultaneously trap one another and form

dipole bands for edges and screws. The screw dislocations cross-slip and annihilate leaving the edge dislocation and the excess of the screws of the same sign. (ii) the flow stress in stage I is controlled by the internal stress field from edge clusters, residual screw dislocations and dislocations with non-primary Burgers vectors. (iii) the work hardening rate in stage I is very low because most of the dislocations annihilate or form dipoles, which have relatively small interaction radii with the mobile dislocation and therefore contribute little to the hardening effect. (iv) the density of the obstacles in stage I rises very slowly as the deformation proceeds. This suggests that basal $< a >$ dislocations on BI system generated during deformation do not constitute the strong obstacles to mobile basal $< a >$ dislocations on the same BI system and the LHRs for BI/BI interactions does not change with the primary deformation and assumes the values $\sim$1.0.

6.2.3 The effect of extrinsic parameters on latent hardening behaviour

The results of latent hardening experiments under the conditions of self- and coplanar interaction in Mg single crystals, indicate an increase in the yield stress of secondary specimens due to latent hardening effect (the LHR>1), when the coplanar slip system is active during secondary deformation. However, the experimental results showed spread of data and in some secondary tests one observes latent softening (LHR<1). Also, when the secondary specimens are reloaded, the yield stress is slightly lower than the final flow stress of a primary samples (#a1-no.1, #b1-no.2 and 3, #c1-no.1 and 3, #d1-no.3, and #e1-no.1). The latent hardening experiments involve unloading of primary crystals, resting during sample cutting and sample preparation at room

temperature and reloading of the secondary samples during subsequent test. These processes induce some stress recovery in the secondary deformation. In the following, we discuss extrinsic parameters that may influence the stress recovery phenomena observed in the secondary samples.

Lattice rotation during tensile deformation

During uniaxial tensile test of a single crystal, the tensile axis rotates towards the slip direction. The crystallographic orientations after 22, 38, 55, 85% shear strain of Mg single crystal oriented for single basal $< a >$ slip deformed at 295K were determined by the X-ray Laüe technique, whereas the orientation after 200% shear strain was determined by SEM/EBSD technique from relatively flat area of the specimen. Fig. 6.11 shows the orientation evolutions during the uniaxial tensile tests on the (0001) stereographic projection. In the figure, black triangle marked by 1, 2, and 3 indices, shows the initial orientation of tensile axis face, wide face, and side face of the single crystal. Similarly, red, pink, orange, blue, and green triangles represent corresponding orientations after 22, 38, 55, 85, and 200% shear strains. Orientation of the lattice evolves in such a way that the tensile axis rotates towards $[2\bar{1}\bar{1}0]$ direction during the deformation. The importance is to determine whether the orientation of the tensile axis after the primary deformation is still located in the range of homogeneous basal $< a >$ slip orientations. If the new tensile axis shifts to non-basal $< a >$ slip orientations, non-basal $< a >$ slip and $\{10\bar{1}2\} < 10\bar{1}1 >$ twinning may be activated and it may influence basal $< a >$ dislocations interactions. As a result, higher CRSS values or work hardening rate would be expected.

According to the X-ray Laüe analysis, the new tensile axis of deformed single crystals was still located within the range of homogeneous basal $< a >$ slip orientations. Since current latent hardening experiments were performed in the range of 0-49% primary shear strain, the effect of lattice rotation during the primary tests was very small. The work hardening rate of all the secondary samples was almost at the same level as the work hardening rate in stage I of parent single crystals, which indicates that single basal slip system was active during secondary deformation.

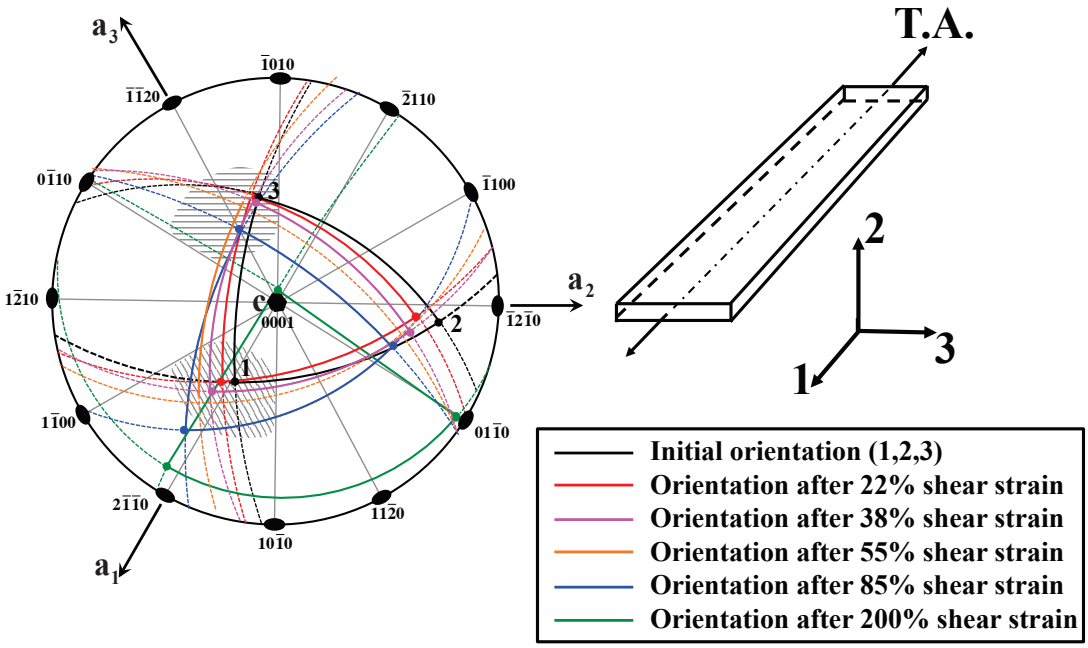

Figure 6.11: Orientaion evolutions during a uniaxial tensile test in Mg single crystal with a single basal $< a >$ slip orientation.

Size effect

The sample size may also influence latent hardening behaviours of crystals. Parent and secondary samples had different dimensions: $\sim 3 \times 26 \times 120 \mathrm{mm}^3$ (parent crystals) and $\sim 3 \times 3 \times 15 \mathrm{mm}^3$ (child crystals), which raises the question how the material properties depend on the sample size. Mg single crystals with different dimensions and the tensile axis $[2\bar{1}\bar{1}2]$ were prepared and deformed in tension with the strain rate $1 \times 10^{-4} \mathrm{s}^{-1}$, to determine their mechanical behaviour. Fig. 6.12 shows true stress-engineering strain curves for both specimens during initial stage of deformation. It was found that the difference of sample size gave rise to the marked elasto-plastic transition region in small samples, whereas large samples exhibited sharp elasto-plastic transition. The yield stress of large samples was smaller by $\sim$0.1MPa than small samples. The difference is attributed to the error in determination of the cross-sectional area of the samples. However, the work hardening rate during the onset of plastic flow was the same in both samples. Consequently, the effect of sample size on the latent hardening results was found to be insignificant.

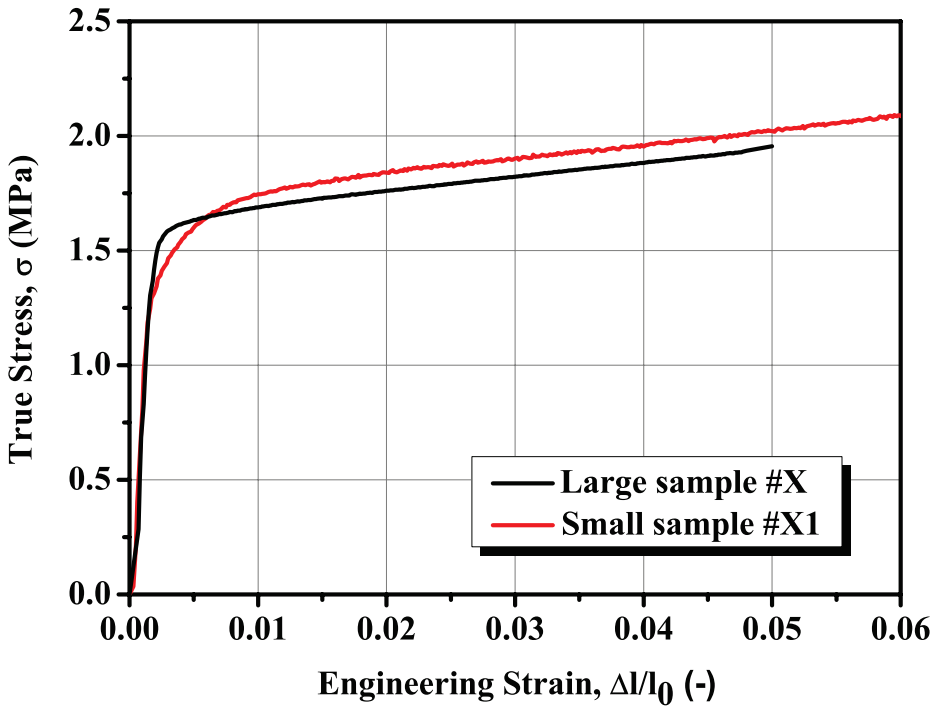

Figure 6.12: Sample size effects on mechanical properties of Mg single crystals.

Unloading/reloading and annealing effects

Different yield drop phenomena have been observed in metals during plastic deformation arising form the temperature change and/or strain-rate change (Argon, 2008). A small yield-point effect due to the work softening has been found to occur in a pre-hardened crystal when deformation temperature is increased or a strain rate of deformation is changed. Cottrell and Stokes (1955) discovered this phenomenon during tensile deformation of Al single crystals when the deformation temperature was

increased form 90K to 196K and 293K. The work softening behaviour has been extensively studied in FCC metals. Although the work softening phenomena in FCC crystals is open to some debate, the softening mechanism is interpreted mainly in terms of: (i) the interaction between dislocations and impurities or vacancies, (ii) the rapid breakdown of a metastable dislocation substructure that was formed during deformation at either a lower temperature or a faster strain rate, and (iii) the cross-slip avoiding obstacles such as the Lomer-Cottrell (LC) locks formed at the previous deformation process.

However, Haasen and Kelly (1957) found that a small yield point deformation is observed in Ni and Al single crystals, when the samples are deformed, unloaded and reloaded at the same temperature. The stress recovery due to the unloading/reloading was also observed in Cu single crystals (Marin, 1958). Currently, the Haasen-Kelly effect is explained by a different mechanism then the work softening effect (Brown, 2010). The mechanism can briefly be explained as follows. During unloading process, dislocations anchors themselves. The dislocation locking prevents stress reversal and causes the yield jump on reloading process.

A work softening behaviour has been observed not only in FCC single crystals but also in Mg single crystals, when deformation temperature and the strain rate of deformation are changed (Basinski, 1960; Sakui *et al.*, 1966a,b). In contrast, there has been no report about the Haasen-Kelly effect in Mg single crystals. For unloading/reloading tests in Al, Ni, and Cu single crystals (Haasen and Kelly, 1957; Marin, 1958), $\Delta\sigma$ was measured by the maximum divergence of the flow curves in reloading tests from that found by joining the curves obtained before and after reloading. In this

case $\Delta\sigma$ expresses a degree of the Hassen-Kelly effect. However, similar yield stress jump has not been seen in Mg single crystals in Bhattacharya's work (Bhattacharya, 2006) and in the current studies during the intermittent deformation/annealing experiments and during the latent hardening experiments. Therefore, one should expect different mechanisms responsible for the stress recovery phenomena observed in Mg single crystals studied here.

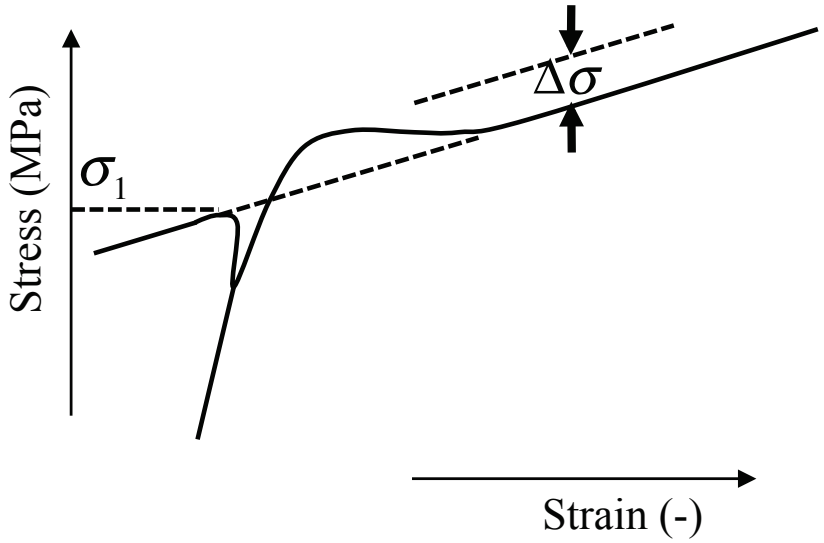

Figure 6.13: The definition of the observed yield point, $\Delta\sigma$ in FCC single crystals (Haasen and Kelly, 1957).

Recent in-situ neutron diffraction experiments during cyclic unloading-reloading of Mg alloys, reveal that a partial reversal of $\{10\bar{1}2\} < 10\bar{1}1 >$ twinning, i.e. detwinning during unloading process, is observed (Cáceres *et al.*, 2003). Detwinning causes a strong inelastic response during unloading and the effective elastic modulus during unloading is smaller than the Youngs modulus of the material. In addition, Koike *et al.* (2008) suggested that the inelastic behaviour cannot be explained solely by the

detwinning during the unloading and the basal $< a >$ slip should also affect the inelastic behaviour from his calculations. According to crystal plasticity finite-element simulations by Hama and Takuda (2011), the basal $< a >$ slip and $\{10\bar{1}2\} < 10\bar{1}1 >$ twin are active during both the loading and unloading. On the other hand, non-basal slip systems such as prismatic $< a >$ slip and 2^{nd} order pyramidal $< c+a >$ slip were activated only during loading. The results obtained from the cyclic loading/unloading tests can provide an insight into the stress recovery mechanisms in Mg single crystals.

Various researchers assume that the activity of basal $< a >$ slip during the unloading process affect the stress recovery in Mg single crystals. When the shear direction changes from the forward direction to the fully reversed direction, the softened onset of plastic deformation, i.e., the quasi-Bauschinger effect has been observed in pure shear deformation tests of Cd, Mg, and Zn single crystals (Edwards *et al.*, 1953; Edwards and Washburn, 1954; Phillips, 1961). Asaro (1975) reported the microscopic Bauschinger effect in dispersion-strengthened Cu single crystals and attributed it to the Orowan loops around dislocations or other polarized dislocation structures, which induce the macroscopically observed softer initial stress under reloading. Asaro (1975) argue that such a softening mechanism should also operate in pure single crystals with long-range stress field. In Mg single crystals the stress recovery in stage I (e.g. points A-C in Fig. 5.52) can also be understood in terms of the quasi-Bauschinger effect. As can be seen in Fig. 5.52, the stress recovery in the unloading-reloading tests is constant, about 0.2MPa up to true stress of 8MPa. At larger stress regions, $\{10\bar{1}2\} < 10\bar{1}1 >$ detwinning may also influence the stress recovery.

The intermittent deformation/annealing experiments with electrical resistivity

measurements were carried out in Cu single crystals with (111)[$\bar{1}$10] single slip orientations (Niewczas *et al.*, 2001) and in Mg single crystals with various orientations, e.g. basal $< a >$ slip, 2^{nd} order pyramidal $< c + a >$ slip and $\{10\bar{1}2\} < 10\bar{1}1 >$ twin orientations (Bhattacharya, 2006). The electrical resistivity measurements during the intermittent deformation/annealing experiments revealed that there exist recoverable and unrecoverable resistivity components in both Cu and Mg single crystals. The recoverable resistivity has been attributed to the annealing of point defects generated during deformation and unrecoverable resistivity has been ascribed as due to dislocations. The annealing of point defects from the microstructure may occur by various mechanisms, e.g. Niewczas *et al.* (2001) suggested pipe diffusion in dislocation dipoles in Cu single crystals. In Mg single crystal studied by Bhattacharya (2006) the concentration of point defects induced by deformation is proportional to the plastic work and agrees with the Saada theory of defect production (Saada, 1965), i.e.,

$$C_v \sim \int \tau d\gamma \tag{6.14}$$

where C_v is the concentration of vacancies, τ is the shear stress, and γ is the shear strain. A relevant review paper about this topic is available (Niewczas, 2014). Such a stress recovery phenomenon happens when material is deformed at very low temperatures and then is annealed at room temperature. However, the current experimental results reveal that the stress recovery occurs when Mg single crystals is deformed at 295K and then annealed at 295K.

In the conclusion of this section we suggest that the effects of lattice rotation and sample size difference are considered to be small and do not contribute a large error

in determination of LHRs. On the other hand the effect of unloading and reloading on the ultimate tensile stress are relatively large. This kind of stress relaxation effect is also observed in FCC single crystals. In the case of FCC single crystals, e.g. in Cu single crystals oriented for (111)[$\bar{1}$01] single slip, the CRSS is somewhat higher than in Mg single crystals oriented for basal $< a >$ slip. However, in the case of the FCC crystals, the stress recovery effect is small in comparison to the flow stress and the error in evaluating the LHRs without considering the stress recovery effect is small. In contrast, the CRSS for basal $< a >$ slip in Mg single crystals is only $\sim$0.5-1.0MPa and stage I continues to over 120% shear strain (Fig. 5.6). As it can be seen in Table 5.3, the flow stress of parent crystal deformed to 49% shear strain #e was 1.26MPa and the error in determination of the LHRs due to the stress recovery, cannot be ignored. Therefore, the stress recovery phenomena have to be taken into account while analyzing the latent hardening behaviour in Mg single crystals.

6.3 Latent hardening behaviour under condition of basal $< a >$ slip/$\{10\bar{1}2\} < 10\bar{1}1 >$ twin dislocation interactions and $\{10\bar{1}2\} < 10\bar{1}1 >$ twin/basal $< a >$ slip dislocation interactions

6.3.1 $\{10\bar{1}2\} < 10\bar{1}1 >$ twinning stress

The $\{10\bar{1}2\} < 10\bar{1}1 >$ twinning stress in the secondary samples #x', in the range 1.28 – 3.01MPa, lies in the range of CRSS values observed in crystal #4 during [0001]

tensile test (2.72MPa) and in the range of CRSS values reported in the literatures, $\sim$2 – 3MPa (Koike, 2005).

Fig. 6.14 shows schematic illustration of the selection of secondary samples. The crystallographic orientation of single crystals after the primary deformation was measured by the X-ray Laüe technique to determine exact position of the lattice at a given stage of deformation. Fig. 6.15 shows the orientations of as-grown crystal and the same single crystal after primary deformation where the orientation was measured at the middle part of the sample. In the figure, (1, 2, 3) denote the initial orientation of the tensile axis and lateral faces respectively, whereas (1',2',3') denote the orientation of the tensile axis and lateral faces of crystal #x after primary deformation. The results show that during primary deformation, the tensile axis rotated $2-3^{\circ}$ towards the $[2\bar{1}\bar{1}0]$ slip direction.

For the conditions of self- and coplanar dislocation interactions, a few degree lattice rotation had little influence on latent hardening results, because single basal $< a >$ slip orientations are widely spread in the orientation space and the basal $< a >$ slip systems are dominant deformation mechanisms. In contrast, under conditions of zero Schmid factor for the basal $< a >$ slip systems, BI, BII, and BIII, the Schmid factor values for $\{10\bar{1}2\} < 10\bar{1}1 >$ twin variants, A'1'-F'6', are 0.50 and they are limited only to the exact c-axis tensile test.

The Schmid factors for slip and twinning systems after primary deformation in sample #x are listed in Table 6.3. The Schmid factor for basal $< a >$ slip systems, BII (or BIII) was 0.11, which predicts that the activation of basal $< a >$ slip will be more favoured compared to the exact c-axis tensile test. However, the Schmid factor

values for six variants of $\{10\bar{1}2\} < 10\bar{1}1 >$ twinning, A'1'-F'6' were still ~ 0.49. Nevertheless, the orientation of the crystals permit to study latent hardening behaviour due to basal $< a >$ and $\{10\bar{1}2\} < 10\bar{1}1 >$ twin dislocation interactions. Fig. 5.58 shows that all secondary samples #x'-No.1-No.4 yielded by $\{10\bar{1}2\} < 10\bar{1}1 >$ twinning.

The tensile axis of the parent crystal #x was paralleled to $[5\bar{1}\bar{4}1(5/\lambda^2)]$, with the Schmid factor for BI system 0.37, a little bit far from an ideal homogeneous basal $< a >$ slip orientation, $[2\bar{1}\bar{1}2]$. In this case the homogeneous deformation by basal $< a >$ slip would not occur and inhomogeneous basal $< a >$ dislocation distributions would be induced during the primary deformation of the parent crystal.

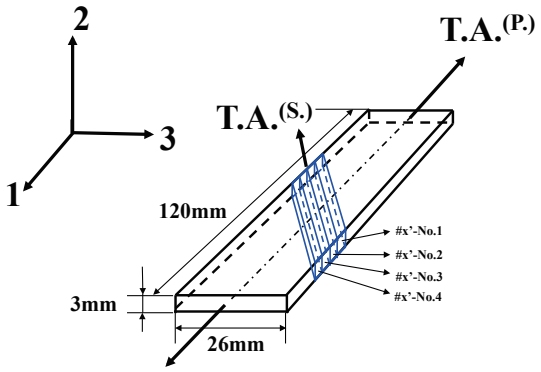

Figure 6.14: Schematic illustration of the selection of secondary samples #x'.

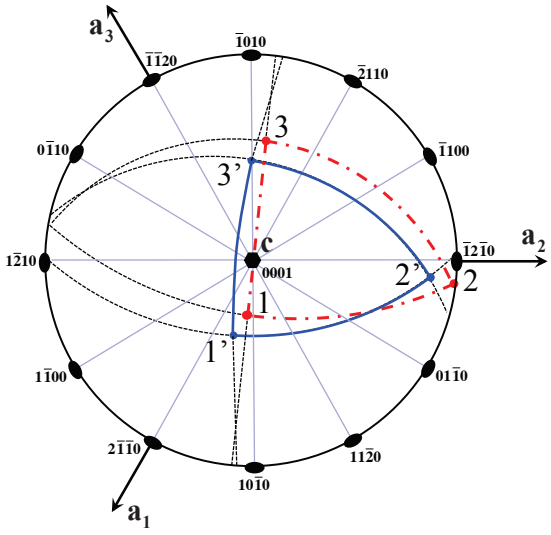

Figure 6.15: Crystallographic orientations of the single crystal #x before and after about 10% strain. (1, 2, 3) denote the initial orientation of the tensile axis and two faces; (1', 2', 3') denote the orientations of the tensile axis and two faces after 10% deformation.

Different elasto-plastic slopes were observed in mechanical characteristics of crystals in Fig. 6.16, which are attributed to different amount of basal slip activated during secondary deformation of single crystals. The results reveal that the slopes correlate with the twinning stress; sample #x'-No.2 with the lowest elasto-plastic slope showed the lowest twinning stress, conversely, crystal #x'-No.1 or No.4 having the steepest slope showed higher twinning stress. The slope of #x'-No.2 sample was close to that observed in the parent crystal #x. One observes a linear relationship between the slopes and LHR*, as shown in Fig. 6.17, suggesting that LHR* depend on the density of basal dislocations ρ_{basal} and scales as $1/\rho_{basal}$. The results indicate

that the state of initial basal $< a >$ dislocation substructure and a local orientation of the crystals influence the $\{10\bar{1}2\} < 10\bar{1}1 >$ twinning stress.

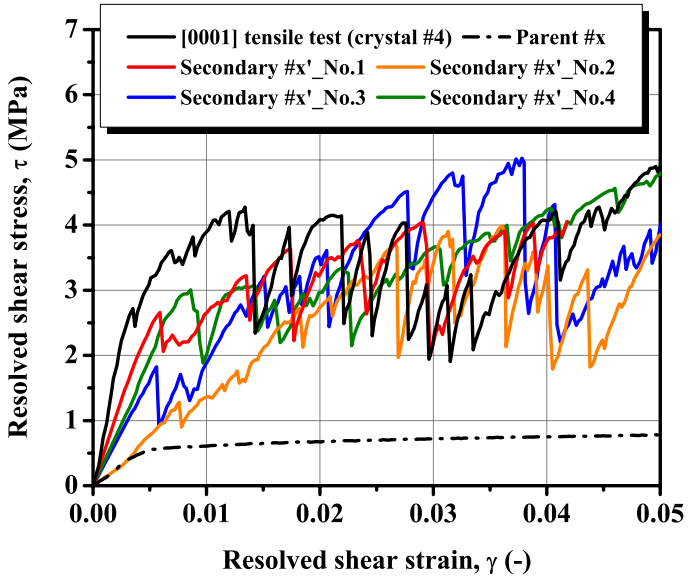

Figure 6.16: Comparisons of elastic-plastic slope for parent crystal #x and secondary samples #x'-No1 to 4.

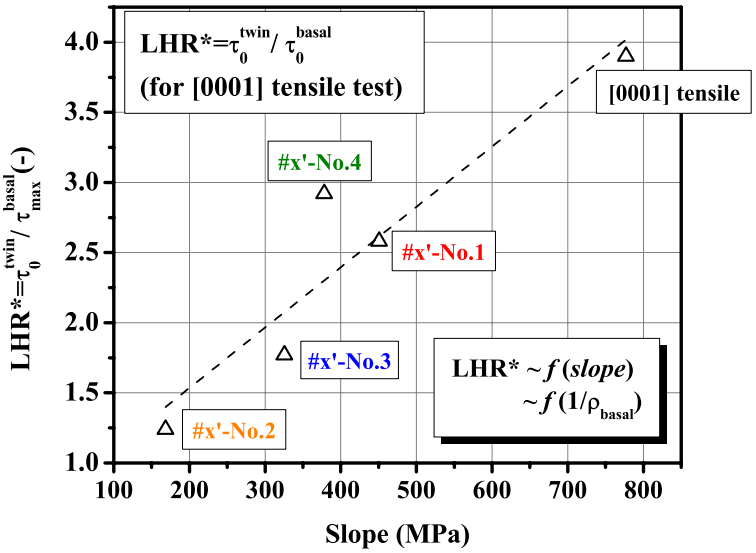

Figure 6.17: LHR plots as a function of the slope in Fig. 6.16.

In the follwing we discuss $\{10\bar{1}2\} < 10\bar{1}1 >$ twinning stress and the role of $\{10\bar{1}2\} < 10\bar{1}1 >$ twin during the secondary compression tests #x". In general, the twin types formed in HCP crystals depend on the internal stress state develop in the crystal during external loading. In the case of Mg, it is expected that $\{10\bar{1}2\} < 10\bar{1}1 >$ twins are formed when tensile stress is applied along the c-axis, while $\{10\bar{1}1\}<10\bar{1}2>$ twins are formed when compression stress is applied along the c-axis (Partridge, 1967; Yoo, 1981). Deformation twinning of ductile HCP metals such as Ti and Zr is known to obey this geometrical condition (Yoo, 1981). However, Mg does not satisfy this criteria. Wonsiewicz and Backofen (1967) observed $\{10\bar{1}2\} < 10\bar{1}1 >$ twin in compressive deformation tests of Mg single crystals. $\{10\bar{1}2\} < 10\bar{1}1 >$ twins are also formed in polycrystalline Mg and Mg alloys without any relationship to the loading

Table 6.3: Schmid factors for basal $< a >$ slip and 2^{nd} order pyramidal $< c+a >$ slip systems in secondary sample #x' (#x") calculated from the initial orientation and the new orientation after the primary deformation.

Deformatin modes	Notation	Miller-Bravais index	Schmid factors	
			#x'	#x'
Basal $< a >$ slip	BI	$(0001)[2\bar{1}\bar{1}0]$	0	0
	BII	$(0001)[\bar{1}2\bar{1}0]$	0	0.11
	BIII	$(0001)[\bar{1}\bar{1}20]$	0	0.11
2^{nd} order pyramidal $< c+a >$ slip	II.Py1	$(11\bar{2}2)[\bar{1}\bar{1}23]$	0.45	0.39
	II.Py2	$(\bar{1}2\bar{1}2)[1\bar{2}13]$	0.45	0.39
	II.Py3	$(\bar{2}112)[2\bar{1}\bar{1}3]$	0.45	0.44
	II.Py4	$(\bar{1}\bar{1}22)[11\bar{2}3]$	0.45	0.48
	II.Py5	$(1\bar{2}12)[\bar{1}2\bar{1}3]$	0.45	0.48
	II.Py6	$(2\bar{1}\bar{1}2)[\bar{2}113]$	0.45	0.44
$\{10\bar{1}2\} < 10\bar{1}1 >$ twin	A'1'	$(10\bar{1}2)[\bar{1}011]$	0.50	0.49
	B'2'	$(01\bar{1}2)[0\bar{1}11]$	0.50	0.49
	C'3'	$(\bar{1}102)[1\bar{1}01]$	0.50	0.49
	D'4'	$(\bar{1}012)[10\bar{1}1]$	0.50	0.49
	E'5'	$(0\bar{1}12)[01\bar{1}1]$	0.50	0.49
	F'6'	$(1\bar{1}02)[\bar{1}101]$	0.50	0.49
	Remarks		initial orientation	new orientation

direction, e.g. (Barnett *et al.*, 2004b; Yang *et al.*, 2004). In the latent compression tests, all twins observed in the microstructure were the $\{10\bar{1}2\} < 10\bar{1}1 >$ tensile twin systems, despite the fact that the compressive axes were only a few degree off the exact [0001] orientation. This clearly suggests that the primary dislocation microstructure facilitates nucleation of tensile twins over the compression twins. However, it is seen that the the twinning stress is not much different from that of tensile deformation tests.

6.3.2 Hardening mechanism due to $\{10\bar{1}2\} < 10\bar{1}1 >$ twin in Mg

In HCP metals, deformation twinning contributes to the material strengthening during a deformation process. $\{10\bar{1}2\} < 10\bar{1}1 >$ twin in Mg has the second smallest CRSS, 2-3MPa (Koike, 2005), next to the basal CRSS and it is known as a predominant twinning mode, contributing to the ductility and the strength of Mg and Mg alloys. So far, three independent hardening mechanisms due to the $\{10\bar{1}2\} < 10\bar{1}1 >$ twin in Mg have been suggested: (i) Dynamical Hall-Petch effect, (ii) texture strengthening/weakening, and (iii) the Basinski mechanism (Cáceres *et al.*, 2008; Bhattacharya and Niewczas, 2011). In the following, we discuss the hardening effects due to $\{10\bar{1}2\} < 10\bar{1}1 >$ twinning in Mg in the current latent hardening experiments using hardness measurements.

Dynamic Hall-Petch effect due to $\{10\bar{1}2\} < 10\bar{1}1 >$ twinning in Mg

In section 6.1.2, the dynamical Hall-Petch effect in Mg single crystals and polycrystals was discussed using the Kocks-Mecking analysis. Additionally, the latent hardening experiments ware carried out to investigate $\{10\bar{1}2\}<10\bar{1}1>$ twin/basal <a> slip dislocation interactions. Mechanical properties of Mg single crystal with twin boundaries induced during primary deformation were investigated in order to understand the effect of twin boundaries (crystals #y, #y'1 and #y'2) on the flow stress and deformation behaviour. The work hardening ratio (WHR) of crystal #y'2 during twin-basal interactions, is about 7 times higher than that of parent crystal #y. SEM/EBSD analysis in the secondary sample #y'2 revealed the formation of 2^{nd} and 3^{rd} order $\{10\bar{1}2\} < 10\bar{1}1 >$ twins during the plastic deformation. Basal slip traces were also seen in the matrix, primary twin and secondary twin regions. The results indicate that such a high work hardening of the secondary sample #y'2 was caused by the effective grain size refinement due to formation of higher order $\{10\bar{1}2\} < 10\bar{1}1 >$ twins and the reduction of the dislocation mean free path and slip/slip, slip/twin, and twin/twin dislocation interactions. The plastic flow was associated with the gross plastic deformation stage in the c-axis tensile deformation of Mg single crystal #4.

The Basinski hardening and texture hardening/softening due to $\{10\bar{1}2\} < 10\bar{1}1 >$ twinning in Mg

The hardness of $\{10\bar{1}2\} < 10\bar{1}1 >$ twins was analyzed from the perspective of Basinski hardening mechanism. The present results of micro- and nano-hardness measurements did not confirm this strengthening effect, instead following results have been obtained:

- In the latent samples #x', the hardness showed orientation dependence resulting from the texture hardening/softening due to the $\{10\bar{1}2\} < 10\bar{1}1 >$ twinning.
- In the tensile deformed crystal #1, the hardness measurements revealed that small decrease in the twinned regions.

The formation of $\{10\bar{1}2\} < 10\bar{1}1 >$ twins occurs to accommodate the stress concentration or the strain incompatibility caused by localized basal $< a >$ dislocations (Yang *et al.*, 2004; Koike, 2005; Koike *et al.*, 2008) and vice versa, the local shape change caused by the $\{10\bar{1}2\} < 10\bar{1}1 >$ twin is accommodated by kinks (Kadiri and Oppedal, 2010). When the localized deformation is accommodated by the kink band formation, a part of slip dislocations is emitted, resulting in dislocation rearrangement and formation of low-angle symmetrical tilt grain boundaries. The kink bands tilted more than 30° from the matrix orientation reported in Mg single crystals (Yoshinaga and Horiuchi, 1962). The latter process is called "accommodation effects". As a result of it, the dislocation densities in the matrix increase to accommodate formation of twins induced by slip dislocations (Kadiri and Oppedal, 2010).

Fig. 6.18 shows (a) SEM image, (b) image quality (IQ) map, (c) inverse pole figure (IPF) map, and (d) pole figures (PFs) constructed from EBSD data at twin interfaces in the secondary sample #x'-No.3. From Fig. 6.18 (c) and (d), the twinning type was $\{10\bar{1}2\}<10\bar{1}1>$. Image quality (IQ) map constructed from electron backscatter diffraction data provides useful visualizations of the microstructure by including phase, strain, topography, and information about the type of grain boundaries. The darker colours in the IQ map are the regions where dislocations accumulate. As can be seen in Fig. 6.18 (b), the interior of the $\{10\bar{1}2\} < 10\bar{1}1 >$ twins is coloured in

lighter grey than corresponding matrix regions, indicating that the dislocation densities in the interior of the twin are smaller than the matrix. These results may be related to the accommodation effects of the $\{10\bar{1}2\} < 10\bar{1}1 >$ twin.

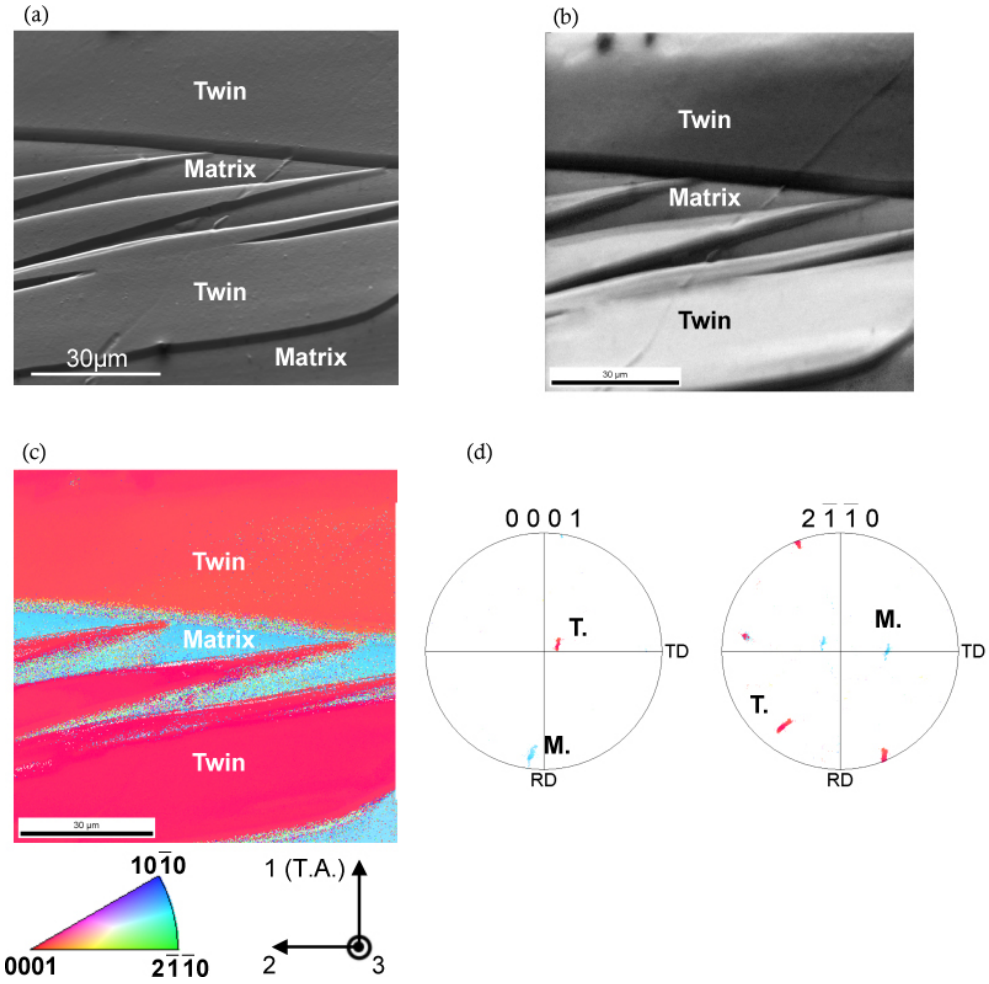

Figure 6.18: (a) Relatively high magnification SEM image, (b) image quality (IQ) map, (c) inverse pole figure (IPF) map, and (d) pole figures (PFs) constructed from EBSD data at the matrix and $\{10\bar{1}2\} < 10\bar{1}1 >$ twins area in the secondary sample #x'-No.3.

In the studies of Mg single crystals with single basal $< a >$ slip orientations, e.g. (Sharp *et al.*, 1965; Hirsch and Lally, 1965), stage II was characterized in terms of twinning formation and dislocation accumulation around twin boundaries. However, recently Bhattacharya and Niewczas (2011) estimated volume fraction of the deformation twins was ∼13-22% by X-ray texture analysis and they suggested that the twinning contributes weakly to the rapid hardening of the crystals and forest dislocation interactions between basal and non-basal slip systems are responsible for the stage II. TEM observations indicate that activations of the non-basal slip occurs relatively early during deformation and they contribute to the development of dislocation networks (Lavrentev and Pokhil, 1975b; Bhattacharya, 2006). In the current EBSD analysis, primary twins of relatively large size were observed in inhomogeneously deformed areas, as shown in Fig. 5.13 (a), Fig. 5.13 (c), and Fig. 5.15 (b). It is expected therefore that the nano-hardness measurements of tensile deformed crystal #1 probed the accommodation effects in these areas. In consequence, hardness in twin regions were slightly lower than the matrix regions, although the basal Schmid factors for matrix and twin regions were very similar and both matrix and twin had a harder orientation.

The secondary sample #x' had a $\{10\bar{1}2\} < 10\bar{1}1 >$ twin orientation and thereby deformation by profuse twinning occurred from the beginning. One can expect that in the gross plasticity stage, $\{10\bar{1}2\} < 10\bar{1}1 >$ twin played an important role in work hardening. In that sample, the primary function of $\{10\bar{1}2\} < 10\bar{1}1 >$ twin is to cary out the deformation and the contribution to the work hardening occurs mainly through dynamical Hall-Petch and texture hardening/softening mechanisms. The effect of Basinski hardening in $\{10\bar{1}2\} < 10\bar{1}1 >$ twinning was too small to be

detectable by nano-indentation measurements.

In either case, the indentation results have not confirmed the Basinski hardening effect inside $\{10\bar{1}2\} < 10\bar{1}1 >$ twins in Mg. This is in contradiction to the results of nano-indentation studies on polycrystalline α-Ti. In that case, deformation twins were always harder than the matrix regardless of the twins' size (Salem *et al.*, 2006). The micro-hardness measurements from matrix and twin regions in Cu-8at.% Al single crystal (Basinski *et al.*, 1997b) also revealed the Basinski hardening effect. In Cu-8at.% Al single crystal, the value of micro-hardness in twin area is almost twice higher than the adjacent matrix region.

One of the reasons why the Basinski hardening effect might be not detectable is that $\{10\bar{1}2\} < 10\bar{1}1 >$ twins in Mg nucleate at low CRSS and their growth may involve transformation of a small dislocation density. The mechanical twinning in FCC systems including Cu and Cu-alloys, occurs at high stresses and low temperatures and the twinning proceeds after the onset of gross deformation stage, because the flow stress must be raised up to the level required for the twin formation. However, $\{10\bar{1}2\} < 10\bar{1}1 >$ twin in Mg can be activated from the early stage of deformation without any prior dislocation glide and so the amount of preexistent dislocations incorporated in the twin lattice may not be large.

A correspondence matrix calculations (Niewczas, 2010) indicate that during $\{10\bar{1}2\} < 10\bar{1}1 >$ twinning in Mg, (0001) basal plane in the parent should transform into $\{10\bar{1}2\}$ prism plane inside the twin lattice. This indicates that basal $< a >$ dislocation would lie on the harder prism planes, whereas prism $< a >$ dislocations would lie on softer basal planes after the occurrence of twinning. TEM observations inside

$\{10\bar{1}2\} < 10\bar{1}1 >$ twins in 2% deformed polycrystalline Mg revealed dislocation characteristic only of the mechanical twin (Morozumi *et al.*, 1976), which included: $\frac{1}{3}[\bar{2}110]$ ($< a >$ dislocation), [0001] (<c> dislocation), $\frac{1}{3}[2\bar{1}\bar{1}3]$ ($< c+a >$ dislocation), $\frac{1}{6}[20\bar{2}3]$ (Schockley partial dislocations), stacking fault in the vicinity of the twin boundaries and dislocation loop. Among all these dislocations, the <c> dislocation is the sessile. However, the density of <c> sessile dislocations, observed by TEM, was very small. Furthermore, the screw component of basal $< a >$ dislocation on the twin lattice can move onto basal plane in the twin via cross-slip mechanism. Thus, after dislocation transmutation occurs as a result of the twinning, the dislocations may loose their identity due to various escape or annihilation mechanisms.

6.4 Latent hardening behaviour under the condition of basal $< a >$ slip/2^{nd} order pyramidal $< c + a >$ slip dislocation interactions

The present work attempted to study latent hardening behaviour under the conditions of basal $< a >$ slip/2^{nd} order pyramidal $< c + a >$ slip dislocation interactions, by means of the latent hardening experiments using a combination of $[2\bar{1}\bar{1}2]$ tensile test in the primary deformation followed by [0001] compression test of the secondary samples. It became eventually evident that the activity of the basal $< a >$ slip made it difficult to measure the strength of basal $< a >$ slip/2^{nd} order pyramidal $< c+a >$ slip interactions. During the primary deformation, crystal #x experiences the lattice rotation. The Schmid factors for 2^{nd} order pyramidal $< c + a >$ slip calculated after the primary deformation were high, as shown in Table 6.3, however, basal $< a >$ slip

and $\{10\bar{1}2\} < 10\bar{1}1 >$ twin modes were active during secondary deformation.

Stohr and Poirier (1972) have pointed out that the control of the very accurate initial orientation is required to obtain pure 2^{nd} order pyramidal $< c + a >$ slip in Mg single crystals. According to their reports, basal $< a >$ slip occurs in the c-axis compression test in spite of a very small Schmid factor (<0.035) and in order to obtain pure conditions of 2^{nd} order pyramidal $< c + a >$ slip, the angle between the applied stress and the c-axis must be set less than 5 arc minutes (Stohr and Poirier, 1972). For these reasons no successful latent hardening characteristics on forest systems in Mg have been determined so far, which has been recognized as an important problem open for future studies.

6.5 Application of latent hardening data to model plasticity of Mg

In this study, the semi-quantitative hardening parameters that can be used in the modelling of plasticity of Mg and its alloys were measured by means of the Jackson & Basinski type latent hardening experiments. In the crystal plasticity models the interaction coefficients between the basal $< a >$ slip, the prismatic $< a >$ slip and the 2^{nd} order pyramidal $< c + a >$ slip systems, and the $\{10\bar{1}2\} < 10\bar{1}1 >$ twin can expressed as 18 ×18 matrix, as shown schematically in Fig. 6.19. Since other non-basal slip systems such as 1^{st} order pyramidal $< a >$ and $< c + a >$ slip systems and the c-axis contraction $\{10\bar{1}1\} < 10\bar{1}2 >$ twin modes have not been reported in Mg, their interaction coefficients are not included in the interaction matrix in in Fig. 6.19.

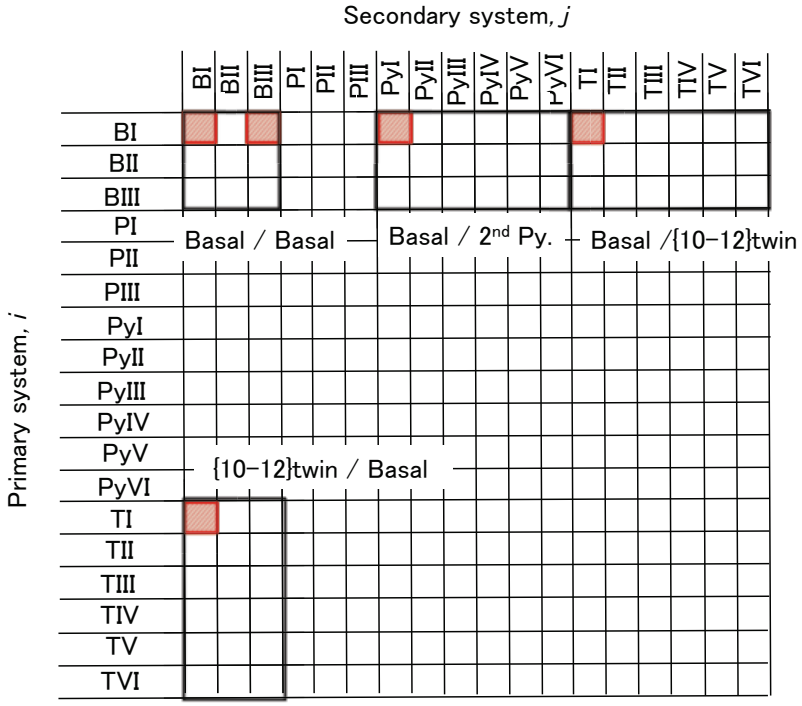

Figure 6.19: Interaction coefficients between various slip and twinning systems determined in the present work.

For matrix components accounting for basal $< a >$ / basal $< a >$ interactions, the current experimental data can be directly used. The self-hardening parameters, BI/BI, BII/BII, and BIII/BIII should be set as 1, independent of the strain or stress. The current experimental studies reveal that the LHRs for the coplanar interaction in Mg scale as: $LHR \sim 1.1\gamma_p$ or $LHR \sim 1.5\tau_p^2$ (Hiura and Niewczas, 2015). This suggests that the coplanar hardening parameters for BI/BII, BI/BIII, and BII/BIII interactions depend on degree of deformation and should be expressed as a function of stress $LHR = f(\tau_p^2)$, strain $LHR = f(\gamma_p)$ or dislocation density $LHR = f(\rho)$.

For basal $< a >$ / $\{10\bar{1}2\} < 10\bar{1}1 >$ twin interactions, the LHR* vary from 1.24

– 2.92 depending on the density of preexisting basal $< a >$ dislocations and the amount of micro-yielding that the crystals experiences, in this case, the LHR* can be expressed as a function of the elastic-plastic slopes and the inverse of basal dislocation densities. The results suggest that the interaction coefficients between basal $< a >$ and $\{10\bar{1}2\} < 10\bar{1}1 >$ should assume the values slightly lower than unity because basal $< a >$ slip dislocations can assist in twin nucleation and growth. In contrast, for $\{10\bar{1}2\} < 10\bar{1}1 >$ twin / basal $< a >$ interactions, the twin boundaries are found to be weak obstacles for active basal $< a >$ slip, because the LHR** are less than 1, ~ 0.9. However, one has to consider the dynamical Hall-Petch hardening effects at larger deformation stages, i.e., effective grain refinements and reduction of mean free path with the progress of deformation.

For basal $< a >$ / 2^{nd} order pyramidal $< c + a >$ slip interactions, the LHR* cannot be measured because of the activations of basal slip and $\{10\bar{1}2\} < 10\bar{1}1 >$ twin. As discussed in chapter 2, the HCP structure with highly anisotropic mechanical properties and the ease of the basal $< a >$ slip have made it difficult to measure the strength of interactions between forest systems in Mg. On the other hand, theoretical calculations and discrete dislocation dynamics (DDD) simulations which are capable to extract interaction parameters between non-basal $< a >$ slip systems in Mg, should be useful to provide data about these interactions. Flow stress, τ_f depends on the forest dislocation density, ρ_f by the known equation: $\tau_f = \alpha\mu b\rho_f^{1/2}$. According to the theoretical calculations by Lavrentev and Pokhil (1975a); Lavrentev *et al.* (1976), constant value α for forest interactions in Mg was estimated as ~ 2.6, relatively large compared to typical FCC metals which show $\alpha\sim$ 0.3 – 0.9. Very recently, Bertin *et al.* (2014) determined the strength of forest dislocation interactions and their effects on

latent hardening by means of the DDD simulations. They found that collinear forest interactions contribute the most to the latent hardening. Basal $< a >$ / 2^{nd} order pyramidal $< c + a >$ interactions are also found to be strong, while interactions involving 2^{nd} order pyramidal $< c + a >$ primary dislocations appear to be the weakest ones.

Nevertheless, the $LHR^{\star}_{basal/\{10\bar{1}2\}}$∼1.95 determined in the present experiments under secondary compression tests can be used to describe basal $< a >$ / $\{10\bar{1}2\}$ $< 10\bar{1}1 >$ twin interactions in Mg poly-crystals.

Table 6.4: Different types of dislocation interactions in Mg (Bertin *et al.*, 2014).

Interaction #	Designation
S1	Basal self-interaction
S2	Prismatic self-interaction
S3	Pyramidal $< c + a >$ self-interaction
1	Coplanar basal / basal
2	Coplanar prismatic / prismatic
3	Collinear basal / prismatic
4	Non-collinear basal / basal
5	Collinear prismatic / basal
6	Non-collinear prismatic / basal
7	Semi-collinear basal / pryramidal $< c + a >$
8	Non-collinear basal / pryramidal $< c + a >$
9	Semi-collinear prismatic / pryramidal $< c + a >$
10	Non-collinear prismatic / pryramidal $< c + a >$
11	Semi-collinear pyramidal $< c + a >$ / basal
12	Non-collinear pyramidal $< c + a >$ / basal
13	Semi-collinear pyramidal $< c + a >$ / prismatic
14	Non-collinear pyramidal $< c + a >$ / prismatic
15	Semi-collinear pyramidal $< c + a >$ / pyramidal $< c + a >$
16	Non-collinear pyramidal $< c + a >$ / pyramidal $< c + a >$

Chapter 7

Summary and Conclusions

In the first part of this thesis, room temperature tensile and compressive deformation characteristics of Mg single crystals with four different orientations of the tensile axis were investigated. Crystal #1 was oriented for single basal $< a >$ slip, crystal #2 for double basal $< a >$ slip, crystal #3 had crystallographic orientation to induce basal and twinning deformation under tension and crystal #4 was oriented for $\{10\bar{1}2\} < 10\bar{1}1 >$ twin under tension and 2^{nd} order pyramidal $< c+a >$ slip under compression. The work hardening behavior of Mg single crystals with basal $< a >$, 2^{nd} order pyramidal $< c + a >$ slip and $\{10\bar{1}2\} < 10\bar{1}1 >$ twin orientations was analyzed by the Kocks-Mecking method. The Considère ratios (CRs) given by eq. (6.10) were calculated in Mg single crystals for each orientation and their ductility, instability and fracture mechanisms were discussed. From the experimental results a following conclusions can be drawn:

1. Mg single crystals oriented for single basal $< a >$ slip (crystal #1 tension) show CRSS $\sim$ 0.7 MPa. Work hardening behaviour exhibits two stages: easy

glide stage ($\theta \sim 4.70 - 8.30x10^{-5}\mu$) and rapid hardening stage ($\theta \sim 8.35 - 9.05x10^{-4}\mu$). Stage I and transition between stage I and II extends much longer compared to FCC single crystals. Stage II is relatively short followed by fracture occurring suddenly before the Considère criterion is satisfied at CR $\sim$ 3.06.

2. Mg single crystals oriented for double basal $< a >$ slip (crystal #2 tension) show CRSS $\sim$ 1.27 MPa and work hardening rate $\theta \sim 2.35 - 6.48x10^{-5}\mu$ (stage I) and $\theta \sim 7.18 - 8.25x10^{-4}\mu$ (stage II). Slightly higher CRSS value and the work hardening rate in comparison to basal $< a >$ orientation is attributed to the effect of double coplanar basal $< a >$ dislocation interactions.

3. Mg single crystals oriented for $\{10\bar{1}2\} < 10\bar{1}1 >$ twining (crystal #3 tension) show CRSS $\sim$ 2.72 MPa. Work hardening behaviour of crystal exhibit two stages: profuse twinning stage with $\theta \sim 4.48x10^{-3} - 8.70x10^{-2}\mu$ and gross crystal plasticity stage with $\theta \sim 2.80x10^{-2}\mu$. Specimen fracture occurs suddenly after stage II with CR $\sim$ 16.9. This suggests that the interaction of the $\{10\bar{1}2\} < 10\bar{1}1 >$ twin interfaces with operating slip modes is one of the main reasons for the failure of the Mg single crystal.

4. Mg single crystals oriented for 2^{nd} order pyramidal $< c+a >$ slip systems (crystal #4 compression) show CRSS $\sim$ 30 MPa. Only a rapid hardening stage was observed in the c-axis compression test of single crystal. The work hardening was the highest among all orientations studied, at the level of $\theta \sim$ 1000 MPa, corresponding to $\theta \sim 4.48x10^{-3} - 8.70x10^{-2}\mu$.

In the second part of the thesis, the Jackson-Basinski type latent hardening experiments in Mg single crystals at 295K have been carried out under different types of dislocation interactions, which included: (i) the self-interactions, (ii) the co-planar interactions on the basal plane, (iii) basal $< a >$ slip/$\{10\bar{1}2\} < 10\bar{1}1 >$ twin dislocation interactions, (iv) $\{10\bar{1}2\} < 10\bar{1}1 >$ twin/basal $< a >$ slip dislocation interactions and (v) basal $< a >$ slip/2^{nd} order pyramidal $< c + a >$ slip dislocation interactions.

5. The LHRs for self-interactions are close to unity, regardless of the amount of pre-strain. For coplanar interactions, the LHRs depend on the amount of strain and stress, they linearly increase from 1.0 to 1.6 within the range of 0-49% primary shear strains and quadratically with primary shear stress.

6. Latent softening (the LHR<1) was observed in some secondary specimens after the secondary reloading. The unloading and resting produces the recovery of the flow stress in the secondary samples, which has to be taken into account while analyzing the latent hardening behaviour of single crystals. The amount of the recovered stress increases during initial deformation and then saturates at the value of about 30% for higher pre-strain stresses.

7. In both intermittent annealing and deformation experiments and cyclic unloading-loading tests in Mg single crystals at 295K, stress recovery, $\Delta\sigma$ increases linearly with the stress. The results have been attributed to the quasi Bauschinger effect and anneal-out of point defects created during deformation.

8. Under the conditions of the basal $< a >$ slip/$\{10\bar{1}2\} < 10\bar{1}1 >$ twin dislocation interactions, latent hardening ratios (LHR*s) given by eq. (5.4) and $\{10\bar{1}2\} < 10\bar{1}1 >$ twin stress were measured. The $\{10\bar{1}2\} < 10\bar{1}1 >$ twinning stress,

in the range of 1.28-3.01 MPa, scales linearly with the slope of the elasto-plastic transition. This effect is attributed to the influence of the primary basal $< a >$ dislocation substructure on the $\{10\bar{1}2\} < 10\bar{1}1 >$ twinning, which provides heterogeneous nucleation sites for $\{10\bar{1}2\} < 10\bar{1}1 >$ twins, decreasing the twinning stress.

9. The activity of basal $< a >$ slip and $\{10\bar{1}2\} < 10\bar{1}1 >$ twinning during the secondary compressive deformation made it difficult to measure the strength of basal $< a >$ slip and 2^{nd} order pyramidal $< c + a >$ slip interactions. The $\{10\bar{1}2\} < 10\bar{1}1 >$ twinning stress observed in the secondary compressive deformation of sample #x" was at similar level of 2-3MPa as observed in tensile deformation tests.

10. For $\{10\bar{1}2\} < 10\bar{1}1 >$ twin/basal $< a >$ slip dislocation interactions, the hardening effect due to the twin boundaries and the twin development during plastic deformation has been confirmed. The microstructure and micro-texture observations of secondary samples by SEM/EBSD technique revealed that formation of higher order $\{10\bar{1}2\} < 10\bar{1}1 >$ twins inside the primary twin region. The secondary samples showed high level of work hardening, influenced by the density of higher order $\{10\bar{1}2\} < 10\bar{1}1 >$ twins. The mechanical properties and the work hardening behaviour of the secondary samples are interpreted in terms of dynamical Hall-Petch effect arising from effective grain refinement and the reduction of the dislocation mean free path due to formation of higher order twins.

Finally, possible hardening mechanisms due to the $\{10\bar{1}2\} < 10\bar{1}1 >$ twin in Mg, (i) dynamic Hall-Petch effect, (ii) the Basinski hardening, and (iii) texture hardening/softening have been investigated by combination of orientation-imaging microscopy (OIM) and micro- and nano-indentation measurements on $\{10\bar{1}2\} < 10\bar{1}1 >$ twin and matrix regions in twinned Mg single crystals (secondary sample #x' and tensile sample #1).

12. The micro- and nano-indentation hardness measurements on $\{10\bar{1}2\} < 10\bar{1}1 >$ twins and matrix regions in the secondary sample #x' showed no experimental evidence for the Basinski hardening mechanism. Instead, the hardness values show orientation dependence, following the Schmids law in both matrix and twins regions, regardless of the twin's variants and size.

13. In stage II of the tensile sample #1, the accommodation $\{10\bar{1}2\} < 10\bar{1}1 >$ twins were developed in the locally heterogeneous areas. The volume fraction of $\{10\bar{1}2\} < 10\bar{1}1 >$ twins was small at the level 20%, in a fractured sample. The hardness measurements on the crystal showed somewhat higher hardness values in the matrix regions than in $\{10\bar{1}2\} < 10\bar{1}1 >$ twins regions. The results suggest that the main role of $\{10\bar{1}2\} < 10\bar{1}1 >$ twins developed during transition range and stage II of plastic deformation is the accommodation of the lattice distortions.

Appendix A

Basic Crystallography for the Hexagonal System (Okamoto and Thomas, 1968)

A.1 Basic definitions

The lattice parameters for the hexagonal crystal system are given by $\{a, a, c, 90, 90, 120\}$. The choice of the unit cell is not unambiguous, because one can select any one of the three cells, shown in Fig. A.1. First, we can use the standard basis vectors, $\boldsymbol{a}_1, \boldsymbol{a}_2$, and $\boldsymbol{c}$ to express direction and Miller indices of planes. Now, we denote the three index components of a lattice vector, $\boldsymbol{r}$ by the symbol $[u'v'w']$:

$$\boldsymbol{r} = u\boldsymbol{a}_1 + v\boldsymbol{a}_2 + w\boldsymbol{c}. \tag{A.1}$$

In the case of the direct lattice in terms of four index notation, this is done by introducing a third symmetric axis, $\boldsymbol{a}_3 = -(\boldsymbol{a}_1 + \boldsymbol{a}_2)$, and an arbitrary crystal vector, $\boldsymbol{r}$ is written in the form:

$$\boldsymbol{r} = u\boldsymbol{a}_1 + v\boldsymbol{a}_2 + t\boldsymbol{a}_3 + w\boldsymbol{c}, \tag{A.2}$$

with

$$u + v + t = 0 \tag{A.3}$$

,as usual. From eqs. (A.1)-(A.3), the correct transformation relations from the three to the four index notations can easily be given by:

$$u' = u - t = 2u + v, \tag{A.4}$$

$$v' = v - t = 2v + u, \tag{A.5}$$

$$w' = w. \tag{A.6}$$

The inverse relations are:

$$u = \frac{1}{3}(2u' - v'), \tag{A.7}$$

$$v = \frac{1}{3}(2v' - u'), \tag{A.8}$$

$$t = -\frac{1}{3}(u' + v') = -(u + v), \tag{A.9}$$

$$w = w'. \tag{A.10}$$

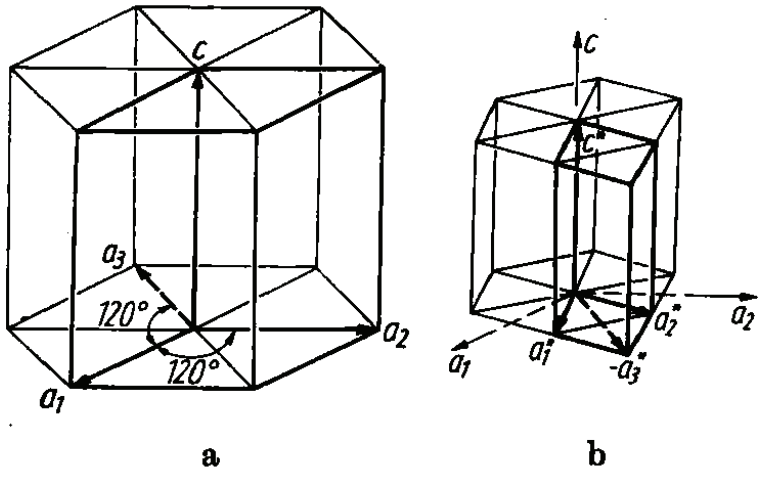

Figure A.1: (a) The conventional unit cell of the direct hexagonal lattice and (b) the conventional reciprocal lattice (Okamoto and Thomas, 1968).

According to the usual definition, the conventional reciprocal lattice points is indexed by using Miller indices based on the primitive reciprocal lattice vectors, $\boldsymbol{a}_1^*$, $\boldsymbol{a}_2^*$, and $\boldsymbol{c}^*$.

$$\boldsymbol{a}_1^* = \frac{\boldsymbol{a}_2 \times \boldsymbol{c}}{V} = \frac{2(2\boldsymbol{a}_1 + \boldsymbol{a}_2)}{3a^2}, \tag{A.11}$$

$$\boldsymbol{a}_2^* = \frac{\boldsymbol{c} \times \boldsymbol{a}_1}{V} = \frac{2(\boldsymbol{a}_1 + 2\boldsymbol{a}_2)}{3a^2}, \tag{A.12}$$

$$\boldsymbol{c}^* = \frac{\boldsymbol{a}_1 \times \boldsymbol{a}_2}{V} = \frac{\boldsymbol{c}}{c^2}, \tag{A.13}$$

where $\boldsymbol{a}_1$, $\boldsymbol{a}_2$, and $\boldsymbol{c}$ are the primitive vectors of the direct lattice, and V is the volume of the unit cell,

$$V = \boldsymbol{a}_1 \cdot (\boldsymbol{a}_2 \times \boldsymbol{c}) = \frac{\sqrt{3}a^2 c}{2}. \tag{A.14}$$

However, the problem is that the conventional reciprocal lattice vectors, $\boldsymbol{a}_1^*, \boldsymbol{a}_2^*$, and $\boldsymbol{c}^*$ do not define a conventional hexagonal unit cell, i.e. the introduction of a third axis, $\boldsymbol{a}_3^* = -(\boldsymbol{a}_1^* + \boldsymbol{a}_2^*)$, will not have the same geometrical relation as its analogue in the direct lattice. Therefore, we should introduce more convenient choice, defined as $\boldsymbol{A}_1^*, \boldsymbol{A}_2^*, \boldsymbol{A}_3^*$, and $\boldsymbol{C}^*$, chosen in such a way that th usual Miller to Miller-Bravais transformation of reciprocal lattice points is retained, $[hkl]^* \rightarrow [hkil]^*$ or

$$h\boldsymbol{a}_1^* + k\boldsymbol{a}_2^* + l\boldsymbol{c}^* \rightarrow h\boldsymbol{A}_1^* + k\boldsymbol{A}_2^* + i\boldsymbol{a}_3^* + l\boldsymbol{C}^* \tag{A.15}$$

where $h + k + i = 0$ as usual. Substituting eqs. (A.11) - (A.14) into the left-hand side of eq. (A.15) and using the definitions $i = -(h + k)$ and $\boldsymbol{a}_3 = -(\boldsymbol{a}_1 + \boldsymbol{a}_2)$ yields

$$\boldsymbol{A}_1^* = \frac{2}{3a^2}\boldsymbol{a}_1, \tag{A.16}$$

$$\boldsymbol{A}_2^* = \frac{2}{3a^2}\boldsymbol{a}_2, \tag{A.17}$$

$$\boldsymbol{A}_3^* = \frac{2}{3a^2}\boldsymbol{a}_3, \tag{A.18}$$

$$\boldsymbol{C}^* = \frac{1}{c^2}\boldsymbol{c}. \tag{A.19}$$

These basis vectors define a hexagonal lattice whose sixfold symmetry, shown in Fig. A.2, is identical in orientation with that of the direct lattice.

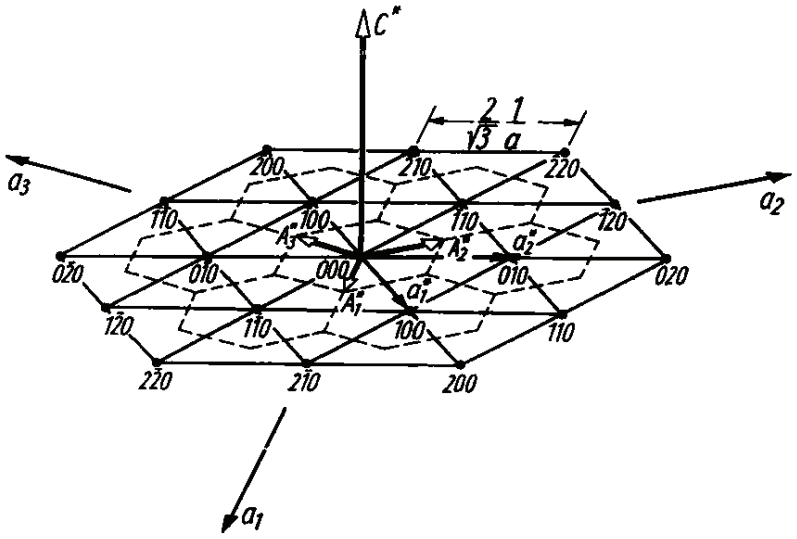

Figure A.2: The 0001 reciprocal lattice plane. The reciprocal lattice points are indexed using Miller indices based on the three and the four axis hexagonal reciprocal basis vectors (Okamoto and Thomas, 1968).

A.2 The relation between the crystal plane ($hkil$) and its normal [$uvtw$]

Unlike cubic crystals, a situation is more complex to express the relation between the crystal plane and its normal due to the four-index notation in the case of hexagonal crystals. In hexagonal crystals, the direction $[uvtw]$ normal to the plane $(hkil)$ is simply the reciprocal lattice vector $[hkil]^*$ expressed in terms of the direct lattice

coordinate system, i.e.

$$u\boldsymbol{a}_1 + v\boldsymbol{a}_2 + t\boldsymbol{a}_3 + w\boldsymbol{c} = h\boldsymbol{A}_1^* + k\boldsymbol{A}_2^* + i\boldsymbol{A}_3^* + l\boldsymbol{C}^* \tag{A.20}$$

and by substituting Eq. A.20 into the right-hand side to get

$$u\boldsymbol{a}_1 + v\boldsymbol{a}_2 + t\boldsymbol{a}_3 + w\boldsymbol{c} = \frac{2}{3a^2}\left(h\boldsymbol{a}_1 + k\boldsymbol{a}_2 + i\boldsymbol{a}_3 + \frac{1}{\lambda^2}\boldsymbol{c}\right), \tag{A.21}$$

where

$$\lambda^2 = \frac{2}{3}\left(\frac{c}{a}\right)^2. \tag{A.22}$$

Therefore, the direction $[uvtw]$ normal to the plane $(hkil)$ can be expressed as:

$$[uvtw] = [hki(l\lambda^{-2})]. \tag{A.23}$$

Conversely, the plane $(hkil)$ normal to the direction $[uvtw]$ is given by:

$$(hkil) = (uvt(w\lambda^2)). \tag{A.24}$$

A.3 The dot product of a reciprocal lattice vector and a direct lattice vector, of two direct lattice vectors, and of two reciprocal lattice vectors

Now, let $\boldsymbol{g} = [hkil]^*$ and $\boldsymbol{r} = [uvtw]$. Then the dot product of a reciprocal lattice vector and a direct lattice vector becomes:

$$\boldsymbol{g} \cdot \boldsymbol{r} = (h\boldsymbol{A}_1^* + k\boldsymbol{A}_2^* + i\boldsymbol{A}_3^* + l\boldsymbol{C}^*) \cdot (u\boldsymbol{a}_1 + v\boldsymbol{a}_2 + t\boldsymbol{a}_3 + w\boldsymbol{c}) \,. \tag{A.25}$$

Eq. (A.25) may be expanded and written in the form:

$$\boldsymbol{g} \cdot \boldsymbol{r} = [hkil] \left\| \begin{array}{cccc} \boldsymbol{A}_1^* \cdot \boldsymbol{a}_1 & \boldsymbol{A}_1^* \cdot \boldsymbol{a}_2 & \boldsymbol{A}_1^* \cdot \boldsymbol{a}_3 & \boldsymbol{A}_1^* \cdot \boldsymbol{c} \\ \boldsymbol{A}_2^* \cdot \boldsymbol{a}_1 & \boldsymbol{A}_2^* \cdot \boldsymbol{a}_2 & \boldsymbol{A}_2^* \cdot \boldsymbol{a}_3 & \boldsymbol{A}_2^* \cdot \boldsymbol{c} \\ \boldsymbol{A}_3^* \cdot \boldsymbol{a}_1 & \boldsymbol{A}_3^* \cdot \boldsymbol{a}_2 & \boldsymbol{A}_3^* \cdot \boldsymbol{a}_3 & \boldsymbol{A}_3^* \cdot \boldsymbol{c} \\ \boldsymbol{C}^* \cdot \boldsymbol{a}_1 & \boldsymbol{C}^* \cdot \boldsymbol{a}_2 & \boldsymbol{C}^* \cdot \boldsymbol{a}_3 & \boldsymbol{C}^* \cdot \boldsymbol{c} \end{array} \right\| \left[\begin{array}{c} u \\ v \\ t \\ w \end{array} \right] . \tag{A.26}$$

The matrix elements can be expanded by Eq. (A.25), i.e.

$$(\boldsymbol{A}_i^* \cdot \boldsymbol{a}_j) = \frac{1}{3} \left\| \begin{array}{cccc} 2 & \bar{1} & \bar{1} & 0 \\ \bar{1} & 2 & \bar{1} & 0 \\ \bar{1} & \bar{1} & 2 & 0 \\ 0 & 0 & 0 & 3 \end{array} \right\| , \tag{A.27}$$

and finally we can get:

$$\boldsymbol{g} \cdot \boldsymbol{r} = hu + kv + it + lw. \tag{A.28}$$

For the case of two direct lattice vectors, $\boldsymbol{r}_1 = [u_1 v_1 t_1 w_1]$ and $\boldsymbol{r}_2 = [u_2 v_2 t_2 w_2]$,

$$\boldsymbol{r}_1 \cdot \boldsymbol{r}_2 = [u_1 v_1 t_1 w_1] \left(\boldsymbol{a}_i \cdot \boldsymbol{a}_j\right) \begin{bmatrix} u_2 \\ v_2 \\ t_2 \\ w_2 \end{bmatrix}, \tag{A.29}$$

where

$$\left(\boldsymbol{a}_i \cdot \boldsymbol{a}_j\right) = \frac{a^2}{2} \begin{Vmatrix} 2 & \bar{1} & \bar{1} & 0 \\ \bar{1} & 2 & \bar{1} & 0 \\ \bar{1} & \bar{1} & 2 & 0 \\ 0 & 0 & 0 & 3\lambda^2 \end{Vmatrix}. \tag{A.30}$$

Therefore,

$$\boldsymbol{r}_1 \cdot \boldsymbol{r}_2 = \frac{3a^2}{2} \left(u_1 u_2 + v_1 v_2 + t_1 t_2 + \lambda^2 w_1 w_2\right). \tag{A.31}$$

Similarity, for the case of two reciprocal lattice vectors, $\boldsymbol{g}_1 = [h_1 k_1 i_1 l_1]^*$ and $\boldsymbol{g}_2 = [h_2 k_2 i_2 l_2]^*$,

$$\boldsymbol{g}_1 \cdot \boldsymbol{g}_2 = [h_1 k_1 i_1 l_1] \left(\boldsymbol{A}_i^* \cdot \boldsymbol{A}_j^*\right) \begin{bmatrix} h_2 \\ k_2 \\ i_2 \\ l_2 \end{bmatrix}, \tag{A.32}$$

where

$$\left(\boldsymbol{a}_i \cdot \boldsymbol{a}_j\right) = \frac{2}{9a^2} \begin{Vmatrix} 2 & \bar{1} & \bar{1} & 0 \\ \bar{1} & 2 & \bar{1} & 0 \\ \bar{1} & \bar{1} & 2 & 0 \\ 0 & 0 & 0 & 3\lambda^{-2} \end{Vmatrix}. \tag{A.33}$$

Therefore,

$$\boldsymbol{g}_1 \cdot \boldsymbol{g}_2 = \frac{2}{3a^2}\left(h_1h_2 + k_1k_2 + i_1i_2 + \lambda^{-2}l_1l_2\right). \tag{A.34}$$

A.4 The magnitude of a reciprocal lattice vector and a direct lattice vector

The magnitude of vectors follows directly from eq. (A.31) and (A.34). For the case of a direct and a reciprocal lattice vector, $\boldsymbol{r}$ and $\boldsymbol{g}$,

$$|\boldsymbol{r}|^2 = \frac{3^2}{2}\left(u^2 + v^2 + t^2 + \lambda^2 w^2\right) \tag{A.35}$$

and

$$|\boldsymbol{g}|^2 = \frac{2}{3a^2}\left(h^2 + k^2 + i^2 + \lambda^{-2}w^2\right). \tag{A.36}$$

A.5 Interplanar and interdirectional angles

These can be derived directly from eqs. (A.31),(A.34)-(A.36). The angle between two direct lattice vectors is calculated from:

$$cos(\boldsymbol{r}_1, \boldsymbol{r}_2) = \frac{\boldsymbol{r}_1}{|\boldsymbol{r}_1|} \cdot \frac{\boldsymbol{r}_2}{|\boldsymbol{r}_2|} = \frac{u_1u_2 + v_1v_2 + t_1t_2 + \lambda^2 w_1w_2}{\left(u_1^2 + v_1^2 + t_1^2 + \lambda^2 w_1^2\right)^{1/2}\left(u_2^2 + v_2^2 + t_2^2 + \lambda^2 w_2^2\right)^{1/2}}. \tag{A.37}$$

Similarly, the angle between two planes corresponding to the reciprocal lattice vectors is given by:

$$cos(\boldsymbol{g}_1, \boldsymbol{g}_2) = \frac{\boldsymbol{g}_1}{|\boldsymbol{g}_1|} \cdot \frac{\boldsymbol{g}_2}{|\boldsymbol{g}_2|} = \frac{h_1h_2 + k_1k_2 + i_1i_2 + \lambda^{-2}l_1l_2}{\left(h_1^2 + k_1^2 + i_1^2 + \lambda^{-2}l_1^2\right)^{1/2}\left(h_2^2 + k_2^2 + i_2^2 + \lambda^{-2}l_2^2\right)^{1/2}}. \tag{A.38}$$

A.6 Application to Schmid factor calculations for hexagonal crystals

Although it is very important to consider Schmid factor for the investigation of slip and twin activities, the calculation of Schmid factor is not well known for hexagonal crystals, because of the $\frac{c}{a}$ ratio and the use of four Miller index notation, in comparison to FCC materials. The Schmid factor for HCP crystals can be calculated in the following way. Consider the tensile axis of the specimen is oriented with respect to the crystal, as shown in Fig. A.3. In the figure, the angle φ and λ denote the relative orientation of the tensile axis and the normal to the slip plane and the relative orientation of the tensile axis and the slip direction within the slip system. The resolved shear stress, τ_{rss} can be expressed by projecting the traction vector, $\boldsymbol{t}^{(n)}$ on the plane with normal $\boldsymbol{n}$ on the slip direction:

$$\tau_{rss} = \boldsymbol{s} \cdot \sigma \boldsymbol{n} = \cos\varphi \cos\lambda \sigma_0 = m\sigma_0 \tag{A.39}$$

where $\boldsymbol{s}$ is a unit vector in the slip direction and σ_0 is the magnitude of the externally applied tensile load. The factor, $m = \cos\varphi\cos\lambda$, is called Schmid factor (Schmid and Boas, 1935).

From the geometrical relations, it is necessary to calculate the inner product of loading axis and slip direction and the loading axis and slip plane normal. We have already obtained the interplanar angle between two directional lattice vectors, eq. (A.37). When the load applied paralleled to the direction, $\boldsymbol{r}_1$=$[u_1v_1t_1w_1]$, the slip plane normal, $\boldsymbol{p}_1$=$[h_1k_1i_1l_1]$, and slip direction, $\boldsymbol{r}_2$=$[u_2v_2t_2w_2]$, Schmid factor, m is

given by:

$$m = \cos(\boldsymbol{r}_1, \boldsymbol{r}_2)\cos(\boldsymbol{r}_1, \boldsymbol{p}_1) = \left(\frac{\boldsymbol{r}_1}{|\boldsymbol{r}_1|} \cdot \frac{\boldsymbol{r}_2}{|\boldsymbol{r}_2|}\right)\left(\frac{\boldsymbol{r}_1}{|\boldsymbol{r}_1|} \cdot \frac{\boldsymbol{p}_1}{|\boldsymbol{p}_1|}\right). \tag{A.40}$$

For example, when the single crystal is deformed in uniaxial tension paralleled to $[11\bar{2}2]$, the Schmid factor for basal slip system $(0001)[2\bar{1}\bar{1}0]$ is 0.25 by eq. (A.40). The Schmid factors for other slip systems can be also calculated using eq. (A.40).

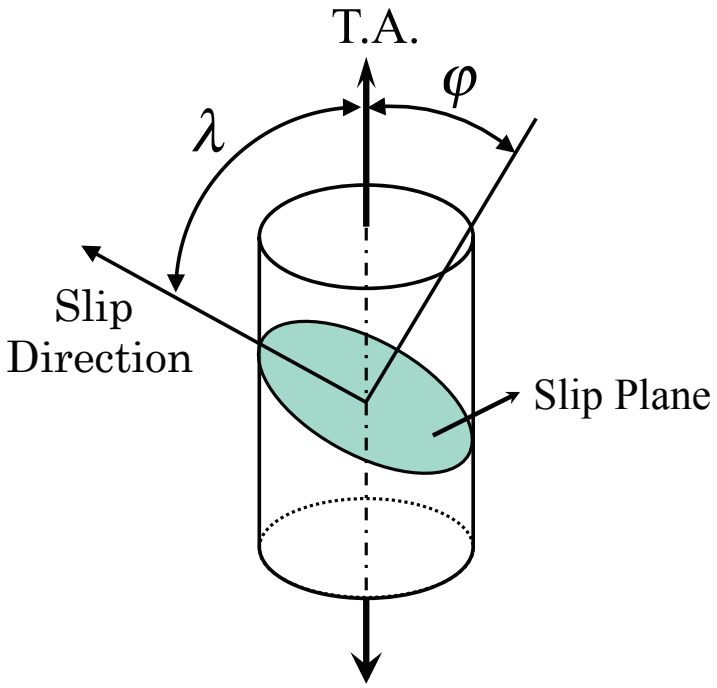

Figure A.3: Schematic illustration of angles between tensile axis and slip direction and slip plane normal.

Appendix B

Deformation Modes in Mg

B.1 Slip modes

Possible slip systems in HCP crystals are shown in Fig. C.5 and are listed in Table B.1. In HCP crystals, the (0001) basal plane is closed-packed and the closed-packed directions are . The shortest lattice vectors are , which corresponds to the unit cell a-vectors in the basal plane. Therefore, the most common slip systems in HCP crystals are basal <a> slip. However, none of the metals known is ideally close-packed and the lattice parameter ratio c/a, usually deviates from ideal c/a = $(8/3)^{\frac{1}{2}}$= 1.633, as shown in Table B.2. This suggests that directionality occurs in inter-atom bonding. In support of this, it is found that some metals such as titanium and zirconium undergo deformation by slip mainly in prism <a> system.

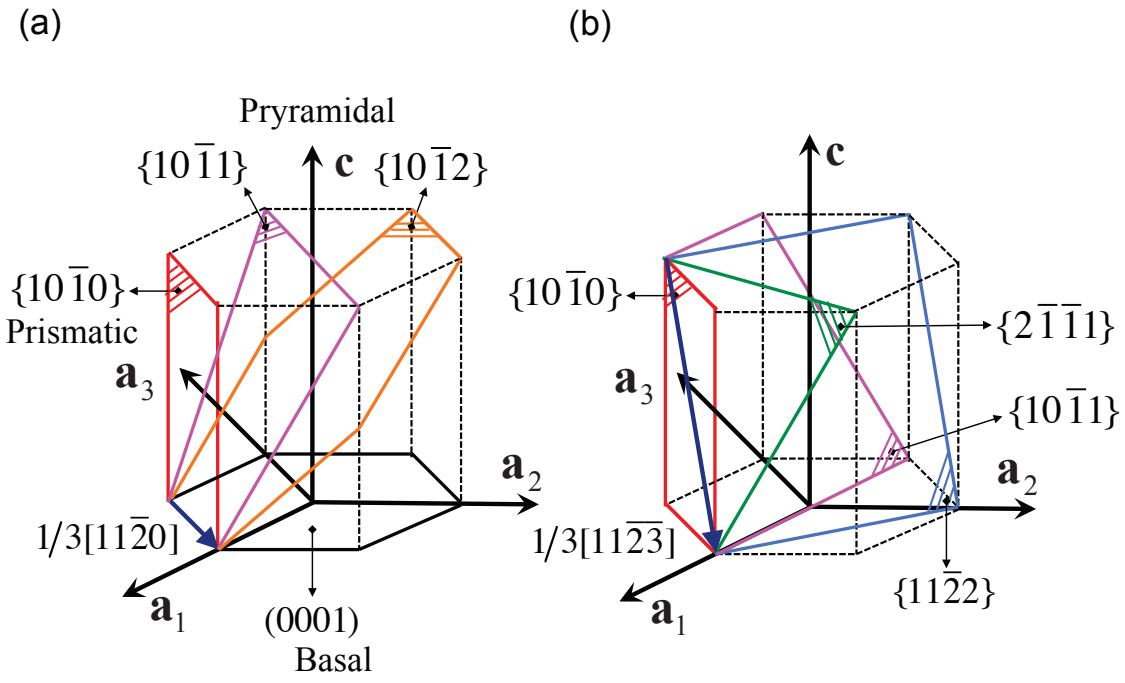

Figure B.4: (a) Basal, prismatic, and pyramidal slip systems with <a> Burgers vector, and (b) four possible pyramidal slip planes with <c+a> Burgers vector (Yoo, 1981).

In polycrystalline metals, basal <a> slip and prism <a> slip do not supply sufficient slip modes to satisfy the Von Mises criterion (Von Mises, 1928) that every grain should be able to plastic deformation generally to meet the shape changes imposed by its neighbors. According to the Von Mises criterion, five independent slip systems are necessary. In FCC crystals, the twelve slip systems provide five independent systems and satisfy the condition and so do the slip systems in BCC crystals. However, either basal <a> slip or prism <a> slip is strongly preferred in HCP crystals. If the two common slip systems are activated simultaneously, they offer only four independent modes between them. Five independent slip systems must be available to carry on

Table B.1: Independent modes of deformation in HCP crystals (Yoo, 1981).

Direction	Plane	Crystallographic elements	# of independent mode
<a>	Basal	$(0001)\langle 11\bar{2}0\rangle$	2
	Prismatic	$\{10\bar{1}0\}\langle 11\bar{2}0\rangle$	2
	Pyramidal	$\{10\bar{1}l\}\langle 11\bar{2}0\rangle$	4
<c>	-	$\{hki0\}[0001]$	-
<c+a>	Pyramidal	$\{hkil\}\langle 11\bar{2}3\rangle$	5
Twinning	-	$\{K_1\}\langle \eta_1\rangle$	0-5

Table B.2: Properties of some HCP metals at 300K (Hull and Bacon, 2011).

Metal	Be	Ti	Zr	Mg	Co	Zn	Cd
c/a ratio	1.568	1.587	1.593	1.623	1.628	1.856	1.886
Preferred slip	basal	prism	prism	basal	basal	basal	basal
plane for $\boldsymbol{b}$=$\boldsymbol{a}$	(0001)	$\{10\bar{1}0\}$	$\{10\bar{1}0\}$	(0001)	(0001)	(0001)	(0001)

arbitrary deformation of a material otherwise, grain-boundary sliding, twinning, or fracture of the crystal will occur. Consequently, non-basal slip systems play an important role in the plastic deformation in HCP crystals, because they provide missing deformation modes to fulfill the von Mises criterion and requirements for five independent slip systems (Hirth and Lothe, 1992). In Mg and Mg alloys, the activations of basal <a> slip, prism <a> slip, and 2nd order pyramidal <c+a> slip are mainly reported. The values of the CRSS for basal <a> slip, prism <a> slip, and 2nd order

pyramidal <c+a> slip in magnesium are plotted in Fig. C.6 as a function of temperatures available in the literatures (Reed-Hill and Robertson, 1957; Sheely and Nash, 1960; Ward Flynn *et al.*, 1961; Yoshinaga and Horiuchi, 1962, 1963c; Wonsiewicz and Backofen, 1967; Akhtar and Teghtsoonian, 1968a,b, 1972; Stohr and Poirier, 1972; Obara *et al.*, 1973). Basal <a> slip dominantly actives in the range from very low to evaluated temperatures. The non-basal slip systems such as prism <a> slip and 2nd order pyramidal <c+a> slip in Mg show very strongly temperature dependence and the CRSS for non-basal systems are decreasing rapidly as temperature rises. At high temperatures, prism <a> slip, and 2nd order pyramidal <c+a> slip can also be activated as secondary slip systems, in addition to basal <a> slip. In fact, for example, Miura *et al.* (2005) reported the activations of basal <a> slip, prism <a> slip and 2nd order pyramidal <c+a> slip in Mg single crystals with single basal orientations deformed in tension at evaluated temperatures, 473-673K.

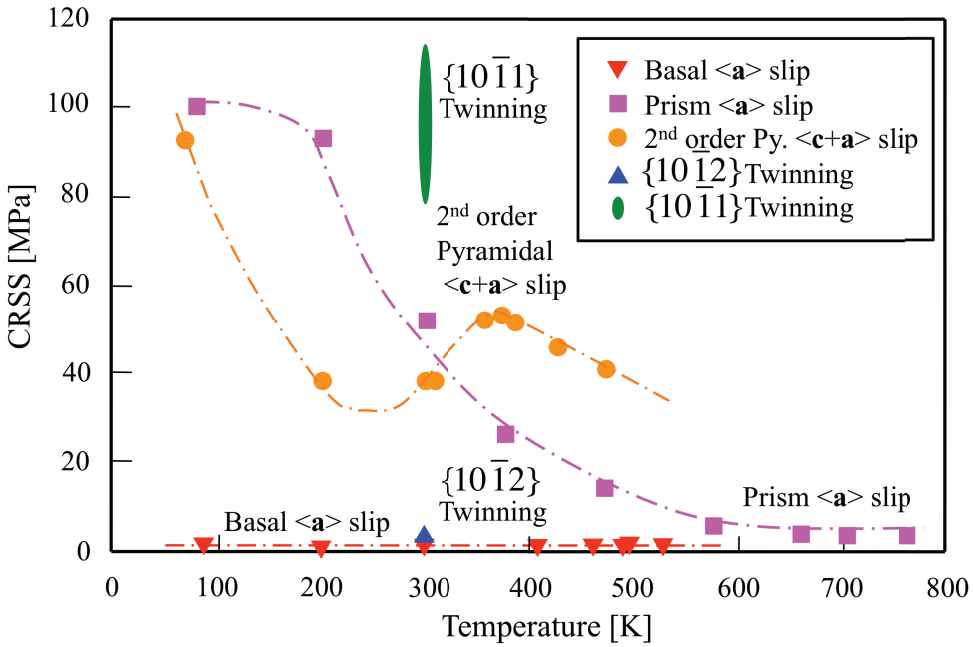

Figure B.5: CRSS plots as a function of temperatures for basal <a> slip, prism <a> slip and 2nd order pyramidal <c+a> slip (Hiura, 2010).

B.2 Deformation twinning

Twinning is a particularly important deformation mechanism when there are only a limited number of slip systems in HCP crystals. At the beginning, the crystallography elements of deformation twinning will be introduced. In the classical theories, which are reviewed in the literature (Christian, 1965), deformation twins can be formed by homogeneous shear, s, in the original (parent) lattice. As a result, the product (twinning) lattice has the same crystal structure as the original one and the two lattices have specific crystallographic relationships. Deformation twins are characterized as

the parameters of K_1, K_2, η_1, and η_2, called twinning elements, as depicted in Fig. C.7. K_1 is the invariant plane of twinning shear and η_1 is the shear direction. From the geometrical relations in the figure,the amount of shear, s is given by:

$$s = 2\cot 2\varphi \tag{B.41}$$

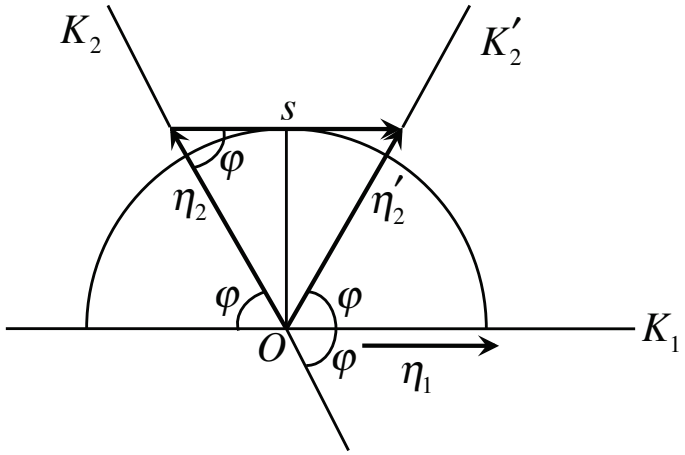

Figure B.6: Geometric relationship between twinning elements (Christian, 1965).

The amount of twinning shear is plotted as a function of the axial ratio for six possible twinning modes in HCP materials and $D0_{19}$ inter metallic compounds in Fig. C.8 (Yoo and Lee, 1991). In the figure, twinning modes having a positive slope cause contraction along the c-axis, while modes indicating a negative slope cause extension along the c-axis. For example, $\{10\bar{1}2\} < 10\bar{1}\bar{1} >$ twin is a contraction twin for Cd and Zn ($\gamma < \sqrt{3}$), whereas a tension twin for the rest materials ($\gamma > \sqrt{3}$), since the shear direction for the $\{10\bar{1}2\} < 10\bar{1}\bar{1} >$ twin reverses at $\gamma = \sqrt{3}$. Table C.3 summarizes twinning parameters for four twinning modes commonly observed in HCP crystals: (i) $\{10\bar{1}2\} < 10\bar{1}\bar{1} >$ well occurred during compressive deformation in Cd and Zn and

tensile deformation in Co, Mg, Zr, Ti, and Be; (ii) $\{10\bar{1}1\} < 10\bar{1}\bar{2} >$ in compressive deformed Mg and Ti; (iii) $\{11\bar{2}2\} < 10\bar{2}\bar{3} >$ in compressive deformed Ti and Zr; and (iv) $\{11\bar{2}1\} < \bar{1}\bar{1}26 >$ in tensie deformed Co, Re, and Zr and in compressive deformed Ti (Niewczas, 2010). Fig. C.8 represents schematic illustrations on their twinning modes.

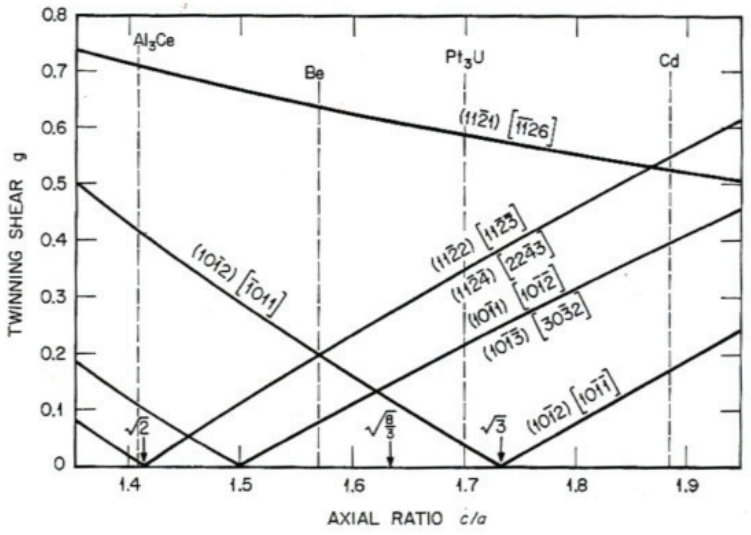

Figure B.7: The amount of twinning shear as a function of the axial ratio in HCP metals and $D0_{19}$ inter metallic compounds (Yoo and Lee, 1991).

Table B.3: Crystallographic elements and parameters of twin systems in HCP crystals (Yoo, 1981).

K_1	K_2	η_1	η_2	shear plane	shear	metal
$\{10\bar{1}2\}$	$\{10\bar{1}\bar{2}\}$	$\pm < 10\bar{1}\bar{1} >$	$\pm < 10\bar{1}1 >$	$\{1\bar{2}10\}$	$\frac{\lvert\gamma^2-3\rvert}{\sqrt{3}\gamma}$	Co, Mg, Zr, Ti, Be
$\{10\bar{1}1\}$	$\{10\bar{1}3\}$	$< 10\bar{1}\bar{2} >$	$< 30\bar{3}2 >$	$\{1\bar{2}10\}$	$\frac{4\gamma^2-9}{4\sqrt{3}\gamma}$	Mg, Ti
$\{11\bar{2}2\}$	$\{11\bar{2}\bar{4}\}$	$\frac{1}{3} < 10\bar{2}\bar{3} >$	$\frac{1}{3} < 22\bar{4}3 >$	$\{1\bar{1}00\}$	$\frac{2\left(\gamma^2-2\right)}{3\gamma}$	Ti, Zr
$\{11\bar{2}1\}$	(0002)	$\frac{1}{3} < \bar{1}\bar{1}26 >$	$\frac{1}{3} < 11\bar{2}0 >$	$\{1\bar{1}00\}$	$\frac{1}{\gamma}$	Co, Re, Ti, Zr

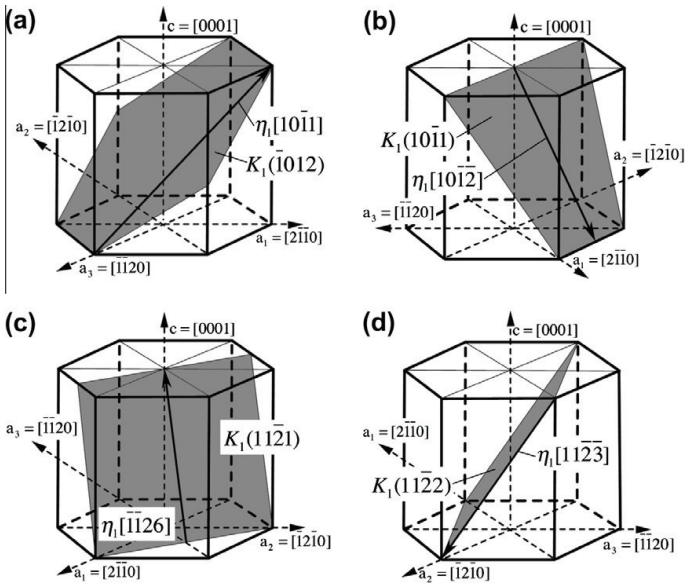

Figure B.8: Geometric relationship between twinning elements: (i) $\{10\bar{1}2\} < 10\bar{1}\bar{1} >$; (ii) $\{10\bar{1}1\} < 10\bar{1}\bar{2} >$; (iii) $\{11\bar{2}2\} < 10\bar{2}\bar{3} >$; and (iv) $\{11\bar{2}1\} < \bar{1}\bar{1}26 >$(Niewczas, 2010).

Appendix C

Stacking-fault energies in some materials (Hirth and Lothe, 1992)

Table C.4: Stacking-fault energies in some close-packed materials (in mJ/m^2) (Hirth and Lothe, 1992).

Materials	Type	Γ_{SFE}	Materials	Type	Γ_{SFE}
Al	FCC	200	Ni	FCC	400
Ag	FCC	17	Pd	FCC	180
Au	FCC	55	Pt	FCC	95
Be	HCP	230	Rh	FCC	750
Cd	HCP	160	Si	Diamondo cubic	69
Cu	FCC	73	Th	FCC	750
Mg	HCP	125	Zn	HCP	230

Bibliography

Advanced industrial science and technology (AIST) (2008). A new rolled magnesium alloy with excellent formability at room temperature.

Akhtar, A. (1968). *Solid solution strenthening of magnesium*. Ph.D. thesis, The University of British Columbia (UBC), BC, CANADA.

Akhtar, A. and Teghtsoonian, E. (1968a). Solid solution strengthening of magnesium single crystals - i alloying behavior in basal slip. *Acta Metallurgica*, **17**, 1339.

Akhtar, A. and Teghtsoonian, E. (1968b). Solid solution strengthening of magnesium single crystals - ii the effect of solute on the ease of prismatic slip. *Acta Metallurgica*, **17**, 1351.

Akhtar, A. and Teghtsoonian, E. (1972). Substitutional solution hardening of magnesium single crystals. *Philosophical Magazine*, **25**, 897.

Andersson, P., Cáceres, C., and Koike, J. (2003). Hall-petch parameters for tension and compression in cast mg. *Materials Science Forum*, **419-422**, 123.

Ando, S. and Tonda, H. (2000). Non-basal slip in magnesium-litium alloy single crystals. *Materials Transactions, JIM*, **41**, 1188.

Ando, S., Nakamura, K., Takashima, K., and Tonda, H. (1992). $\{11\bar{2}2\}\langle\bar{1}\bar{1}23\rangle$ slip in magnesium single crystal. *Journal of The Japan Institute of Light Metals*, **42**(12), 765.

Ando, S., Takashima, K., and Tonda, H. (1996). Molecular dynamics simulation of c+a edge dislocation core structure in hcp crystal. *Materials Transactions, JIM*, **37**(3), 319.

Ando, S., Gotoh, T., and Tonda, H. (2002). Molecular dynamics simulation of c+a dislocation core structure in hexagonal-close-packed metals. *Metallurgical and materials transactions*, **33A**, 823.

Ando, S., Tanaka, M., and Tonda, H. (2003). Pyramidal slip in magnesium alloy single crystals. *Materials Science Forum*, **419-422**, 87.

Ando, S., Ikejiri, Y., Iida, N., Tsushida, M., and Tonda, H. (2006). Orientation dependence of fatigue crack propagation in magnesium single crystals. *Journal of Japan Institute of Metals*, **70**(8), 634.

Ando, S., Tsushida, M., and Kitahara, H. (2010). Deformation behavior of magnesium single crystal in c-axis compression and a-axis tension. *Materials Science Forum*, **654-656**, 699.

Ando, S., Kodera, A., Fukushima, K., Tsushida, M., and Kitahara, H. (2014). Tensile deformation of magnesium and magnesium alloy single crystals. *Materials Science Forum*, **783-786**, 341.

Argon, A. (2008). *Strengthening mechanisms in crystal plasticity*. Oxford series on materials modelling. Oxford University Press.

Asada, H. and Yoshinaga, H. (1959). Temperature and orientation dependence of the plasticity of magnesium single crystals. *Journal of the Japan Institute of Metals*, **23**, 649.

Asaro, R. (1975). Elastic-plastic memory and kinematic-type hardening. *Acta Metallurgica*, **23**, 1255.

Bacon, D. and Liang, M. (1986). Computer simulation of dislocation cores in h.c.p. metals i. interatomic potentials and stacking-fault stability. *Philosophical Magazine A*, **53**, 163.

Baird, J. and Gale, B. (1965). Attractive dislocation intersections and work hardening in metals. *Philosophical Transactions of the Royal Society A*, **257**, 553.

Barnett, M., Nave, M., and Bettles, C. (2004a). Deformation microstructures and textures of some cold rolled mg alloys. *Materials Science and Engineering A*, **386**, 205.

Barnett, M., Keshavarz, Z., Beer, A., and Atwell, D. (2004b). Influence of grain size on the compressive deformation of wrought mg–3al–1zn. *Acta Materialia*, **52**, 5093.

Basinski, S. and Basinski, Z. (1979). *Plastic deformation and work hardening*, volume 4 of *Dislocations in Solids*. North Holland.

Basinski, Z. (1959). Thermally activated glide in face-centred cubic metals and its application to the theory of strain hardening. *Philosophical Magazine*, **4**, 393.

Basinski, Z. (1960). The influence of temperature and strain rate on the flow stress of magnesium single crystals. *Australian Journal of Physics*, **13**, 284.

Basinski, Z., Szczerba, M., and Embury, J. (1997a). Tensile instability in face-centred cubic materials. *Philosophical Magazine A*, **76**(4), 743.

Basinski, Z., Szczerba, M., Niewczas, M., Embury, J., and Basinski, S. (1997b). The transformation of slip dislocations during twinning of copper-aluminum alloy crystals. *Revue de Métallurgie*, **94**, 1037.

Bertin, N., Tomé, C., Beyerlein, I., Barnett, M., and Capolungo, L. (2014). On the strength of dislocation interactions and their effect on latent hardening in pure magnesium. *International Journal of Plasticity*, **62**, 72.

Bhattacharya, B. (2006). *Plastic deformation behavior of pure magnesium in the temperature range 4.2K-300K*. Ph.D. thesis, McMaster University, ON, CANADA.

Bhattacharya, B. and Niewczas, M. (2011). Work-hardening behaviour of mg single crystals oriented for basal slip. *Philosophical Magazine*, **91**, 2227.

Brown, L. (2010). An interpretation of the haasen-kelly effect. *Philosophical Magazine*, **90**, 4147.

Burke, E. and Hibbard, W. (1952). Plastic deformation of magnesium single crystals. *Transactions AIME*, **194**, 295.

Cáceres, C. and Blake, A. (2007). On the strain hardening behaviour of magnesium at room temperature. *Materials Science and Engineering A*, **462**, 193.

Cáceres, C. and Lukáč, P. (2008). Strain hardening behaviour and the taylor factor of pure magnesium. *Philosophical Magazine*, **88**(7), 977.

Cáceres, C., Sumitomo, T., and Veidt, M. (2003). Pseudoelastic behaviour of cast magnesium az91 alloy under cyclic loading–unloading. *Acta Materialia*, **51**, 6211.

Cáceres, C., Lukáč, P., and Blake, A. (2008). Strain hardening due to $\{10\bar{1}2\}$ twinning in pure magnesium. *Philosophical Magazine*, **88**(7), 991.

Capolungo, L. (2011). Dislocation junction formation and strength in magnesium. *Acta Materialia*, **59**, 2909.

Catoor, D., Gao, Y., Geng, J., Prasad, M., Herbert, E., Kumar, K., G., P., and George, E. (2013). Incipient plasticity and deformation mechanisms in single-crystal mg during spherical nanoindentation. *Acta Materialia*, **61**, 2953.

Christian, J. (1965). *The theory of transformations of metals and alloys.* Oxford Pergamon Press.

Cottrell, A. and Stokes, R. (1955). Effects of temperature on the plastic properties of aluminium crystals. *Proceedings of the Royal Society*, **A233**, 17.

Couret, A. and Caillard, D. (1985a). An in situ study of prismatic glide in magnesium - i. the rate cotrolling mechanism. *Acta Metallurgica*, **33**, 1447.

Couret, A. and Caillard, D. (1985b). An in situ study of prismatic glide in magnesium - ii. microscopic activation parameters. *Acta Metallurgica*, **33**, 1455.

Edwards, E. and Washburn, J. (1954). Strain hardening of latent slip system zinc crystals. *Transactions AIME*, **200**, 1239.

Edwards, E., Washburn, J., and Parker, E. (1953). Some observations on the work hardening of metals. *Transactions AIME*, **197**, 1525.

Franciosi, P. (1985). The concepts of latent hardening and strain hardening in metallic single crystals. *Acta Metallurgica*, **33**(9), 1601.

Franciosi, P. and Zaoui, A. (1982). Multislip in f.c.c. crystals a theoretical approach compared with experimental data. *Acta Metallurgica*, **30**, 1627.

Franciosi, P., Berveiller, M., and Zaoui, A. (1980). Latent hardening in copper and aluminium single crystals. *Acta Metallurgica*, **28**, 273.

Frank, F. and Nicholas, J. (1953). Cxxviii. stable dislocations in the common crystal lattices. *Philosophical Magazine*, **44**, 1213.

Gilormini, P., Bacroix, B., and Jonas, J. (1988). Overview no. 64 theoretical analyses of (111) pencil glide in b.c.c. crystals. *Acta Metallurgica*, **36**(2), 231.

Gouldstone, A., Chollacoop, N., Dao, M., Li, J. Minor, M., and Shen, Y. (2007). Indentation across size scales and disciplines: Recent developments in experimentation and modeling. *Acta Materialia*, **55**, 4015.

Graff, S., Brocks, W., and Streglich, D. (2007). Yielding of magnesium: From single crystal to polycrystalline aggregates. *International Journal of Plasticity*, **23**, 1957.

Haasen, P. and Kelly, A. (1957). A yield phenomenon in face-centered cubic single crystals. *Acta Metallurgica*, **5**, 192.

Hama, T. and Takuda, H. (2011). Crystal-plasticity finite-element analysis of inelastic behavior during unloading in a magnesium alloy sheet. *International Journal of Plasticity*, **27**, 1072.

Hauser, F., Landon, P., and Dorn, J. (1956). Deformation mechanisms in polycrystalline aggregates of magnesium. *Transactions of the ASM*, **48**, 986.

Hirsch, P. and Lally, J. (1965). The deformaton of magnesium single crystals. *Philosophical Magazine*, **12**(117), 595.

Hirth, J. and Lothe, J. (1992). *Theory of dislocations (2nd edition)*. Krieger.

Hiura, F. (2010). *Latent hardening behavior in magnesium single crystals*. Master's thesis, McMaster University, ON, CANADA.

Hiura, F. and Niewczas, M. (2015). Latent hardening effect under self- and coplanar dislocation interactions in mg single crystals. *Scripta Materialia*.

Hull, D. and Bacon, D. (2011). *Introduction to dislocations (5th edition)*. Butterworth-Heinemann.

Jackson, P. and Basinski, Z. (1967). Latent hardening and the flow stress in copper single crystals. *Canadian Journal of Physics*, **45**, 707.

Jia, X. (2013). *Solid solution strengthening and texture evolution in Mg-Y alloys*. Master's thesis, McMaster University, ON, CANADA.

Johnston, W. (1962). Yield points and delay times in single crystals. *Journal of Applied Physics*, **33**, 2716.

Kadiri, H. and Oppedal, A. (2010). A crystal plasticity theory for latent hardening by glide twinning through dislocation transmutation and twin accommodation effects. *Journal of the Mechanics and Physics of Solids*, **58**, 613.

Kainer, K. (2003). *Magnesium Alloys and Technologies*. Wiley-VCH.

Kalidindi, S., Salem, A., and Doherty, R. (2003). Role of deformation twinning on strain hardening in cubic and hexagonal polycrystalline metals. *Advanced Engineering Materials*, **5**(4), 229.

Kelly, A., Groves, G., and Kidd, P. (2000). *Crystallography and crystal defects (revised edition)*. WILEY.

Kelly, E. and Hosford, W. J. (1968a). The deformation characteristics of textured magnesium. *Transactions of the Metallurgical Society of AIME*, **242**, 654.

Kelly, E. and Hosford, W. J. (1968b). Plane-strain compression of magnesium and magnesium alloy crystals. *Transactions of the Metallurgical Society of AIME*, **242**, 5.

Klimanek, P. and Pötzsch, A. (2002). Microstructure evolution under compressive plastic deformation of magnesium at different temperatures and strain rates. *Materials Science and Engineering A*, **324**, 145.

Kocks, U. (1964). Latent hardening and secondary slip in aluminum and silver. *Transactions of the Metallurgical Society of AIME*, **230**, 1160.

Kocks, U. (1970). The relation between polycrystal deformation and single-crystal deformation. *Metallurgical Transactions*, **1**, 1121.

Kocks, U. and Brown, T. (1966). Latent hardening in aluminum. *Acta Metallurgica*, **14**, 87.

Kocks, U. and Mecking, H. (2003). Physics and phenomenology of strain hardening: the fcc case. *Progress in Materials Science*, **48**, 171.

Kocks, U., Tomé, C., and Wenk, H. (1998). *Texture and Anisotropy, Preffered orientations in polycrystals and their effect on materials properties*. Cambridge University Press.

Koike, J. (2005). Enhanced deformation mechanisms by anisotropic plasticity in polycrystalline mg alloys at room temperature. *Metallurgical and materials transactions A*, **36A**, 1689.

Koike, J. and Maruyama, K. (2004). Microscopic mechanisms of plastic deformation in polycrystalline magnesium alloys. *Journal of Japan Institute of Light Metals*, **54**(11), 460.

Koike, J., Sato, Y., and Ando, D. (2008). Origin of the anomalous $\{10\bar{1}2\}$ twinning during tensile deformation of mg alloy sheet. *Materials Transactions, JIM*, **49**(12), 2792.

Kubin, L. (2013). *Dislocations, mesoscale simulations and plastic flow*. Oxford series on materials modelling. Oxford University Press.

Kubin, L., Devincre, B., and Hoc, T. (2008). Modeling dislocation storage rates and mean free paths in face-centered cubic crystals. *Acta Materialia*, **56**, 6040.

Lake, J. and Craig, G. (1972). Latent hardening of aluminium deformed in tension. *Scripta Metallurgica*, **6**, 1023.

Lavrentev, F. and Pokhil, Y. (1975a). Effect of forest dislocations in the $\{11\bar{2}2\}\langle\bar{1}\bar{1}23\rangle$ system in hardening in mg single crystals under basal slip. *Physica Status Solidi a*, **82**, 227.

Lavrentev, F. and Pokhil, Y. (1975b). Relation of dislocation densitiy in different slip sytems to work hardening parameters for magnesium crystals. *Materials Science and Engineering*, **18**, 261.

Lavrentev, F., Pokhil, Y., and Startsev, V. (1973). Critical shear stress temperature and rate dependence in mg single crystals. *Problemy Prochnosti*, **10**, 60.

Lavrentev, F., Pokhil, Y., and Zolotukhina, J. (1976). Theoretical analysis of basal-pyramidal interaction of dislocations and calculation of its contribution to work hardening of magnesium crystals. *Materials Science and Engineering*, **23**, 69.

Li, T., Gao, Y., Bei, H., and George, E. (2011). Indentation schmid factor and orientation dependence of nanoindentation pop-in behavior of nial single crystals. *Journal of the Mechanics and Physics of Solids*, **59**, 1147.

Liang, M. and Bacon, D. (1986a). Computer simulation of dislocation cores in h.c.p. metals ii. core structure in unstressed crystals. *Philosophical Magazine A*, **53**, 181.

Liang, M. and Bacon, D. (1986b). Computer simulation of dislocation cores in h.c.p. metals iii. the effect of applied shear strain. *Philosophical Magazine A*, **53**, 205.

Marin, M. (1958). Unloading effects in the plastic properties of copper single crystals. *Philosophical Magazine*, **3**, 287.

Mecking, H. and Bulian, G. (1976). Correlations between stress, strain and dislocation arrangement in weakly deformed copper single crystals. *Acta Metallurgica*, **24**, 249.

Mecking, H. and Kocks, U. (1981). Kinetics of flow and strain-hardeinng. *Acta Metallurgica*, **29**, 1865.

Mendelson, S. (1970). Dislocation dissociations in hcp metals. *Journal of applied physics*, **41**, 1893.

Minonishi, Y., Ishioka, S., Koiwa, M., Morozumi, S., and Yamagichi, M. (1981a). The core structure of a $\frac{1}{3} < \bar{1}\bar{1}23 >$ screw dislocation in h.c.p. metals. *Philosophical Magazine A*, **44**, 1225.

Minonishi, Y., Ishioka, S., Koiwa, M., Morozumi, S., and Yamagichi, M. (1981b). The core structure of $\frac{1}{3} < \bar{1}\bar{1}23 > \{11\bar{2}2\}$ edge dislocations in h.c.p. metals. *Philosophical Magazine A*, **43**, 1017.

Minonishi, Y., Ishioka, S., Koiwa, M., Morozumi, S., and Yamagichi, M. (1982a). The core structures of a $\frac{1}{3} < \bar{1}\bar{1}23 > \{11\bar{2}2\}$ edge dislocation under applied shear stresses in an h.c.p. model crystal. *Philosophical Magazine A*, **45**, 835.

Minonishi, Y., Ishioka, S., Koiwa, M., and Morozumi, S. (1982b). Motion of a $\frac{1}{3} < \bar{1}\bar{1}23 >$ screw dislocation in a model h.c.p. lattice. *Philosophical Magazine A*, **46**, 761.

Miura, H., Yang, X., Sakai, T., Nogawa, H., Miura, S., Watanabe, Y., and Jonas, J. (2005). High temperature deformation and extended plasticity in mg single crystals. *Philosophical Magazine*, **85**(30), 3553.

Miyamoto, M., Funami, K., and Uehara, M. (1977). Latent hardening in aluminum single crystal. *Journal of the Faculty of Engineering, The University of Tokyo(B)*, **34**(2), 349.

Morozumi, S., Kikuchi, M., and Yoshinaga, H. (1976). Electron microscopy observation in and around $\{1\bar{1}02\}$ twins in magnesium. *Transactions of the Japan Institute of Metals*, **17**, 158.

Munroe, N., Tan, X., and Gu, H. (1997). Orientation dependence of slip and twinning in hcp metals. *Scripta Materialia*, **36**(12), 1383.

Niewczas, M. (2007). *Dislocations and twinning in Face Centered Cubic Crystals*, volume 13 of *Dislocations in Solids*. Elsevier.

Niewczas, M. (2010). Lattice correspondence during twinning in hexagonal close-packed crystals. *Acta Materialia*, **58**, 5848.

Niewczas, M. (2014). Intermittent plastic flow of single crystals: central problems in plasticity: a review. *Materials Science and Technology*, **30**(7), 739.

Niewczas, M., Basinski, Z., Basinski, S., and Embury, J. (2001). Deformation of copper single crystals to large strains at 4.2k i. mechanical response and electrical resistivity. *Philosophical Magazine A*, **81**(5), 1121.

Noble, K. (2011). *Origins of Strength and Ductility in Mg-RE Binary Alloys*. Master's thesis, McMaster University, ON, CANADA.

Nye, J. (1985). *Physical properties of crystals*. Oxford University Press.

Obara, T., Yoshinaga, H., and Morozumi, S. (1973). $\{11\text{-}22\}\langle 11\text{-}23\rangle$ slip system in magnesium. *Acta Metallurgica*, **21**, 845.

Okamoto, P. and Thomas, G. (1968). On the four-axis hexagonal reciprocal lattice and its use in the indexing of transmission electron diffraction patterns. *Physica Status Solidi*, **25**, 81.

Oliver, W. and Pharr, G. (1992). An improved technique for determining hardness and elastic modulus using load and displacement sensing indentation experiments. *Journal of Materials Research*, **7**(6), 1564.

Oliver, W. and Pharr, G. (2004). Measurement of hardness and elastic modulus by instrumented indentation: Advances in understanding and refinements to methodology. *Journal of Materials Research*, **19**(1), 3.

Onaka, S., Kato, H., Hashimoto, S., and Miura, S. (1995). Crystal orientation and yield strength of pure magnesium continuously cast with a heated mold. *Journal of Japan Institute of Metals*, **59**(6), 607.

Partridge, P. (1967). The crystallography and deformation modes of hexagonal close-packed metals. *Metallurgical Reviews*, (118), 169.

Phillips, W. (1961). Shear deformation of magnesium and zinc single crystals. *Transactions of the ASM*, **54**, 50.

Ramaswami, B., Kocks, U., and Chalmers, B. (1965). Latent hardening in silver and ag-au alloy. *Transactions of the Metallurgical Society of AIME*, **233**, 927.

Reed-Hill, R. and Robertson, W. (1957). Deformation of magnesium single crystals by nonbasal slip. *Transactions AIME*, **209**, 496.

Roberts, E. and Partridge, P. (1966). The accomodation around $\{10\bar{1}2\}\langle 10\bar{1}1\rangle$ twins in magnesium. *Acta Metallurgica*, **14**, 513.

Saada, G. (1965). Sur la nature des défauts ponctuels crées par le croisement des dislocations. *Acta Metallurgica*, **9**, 965.

Sakui, S., Mori, T., and Sato, K. (1966a). Sharp yielding due to work softening of dynamically prestrained single crystals of magnesium. *Journal of Japan Institute of Metals*, **30**, 412.

Sakui, S., Sato, K., and Mori, T. (1966b). Work softening induced yielding in magnesium single crystals. *Journal of Japan Institute of Metals*, **30**, 984.

Salem, A., Kalidindi, S., Doherty, R., and Semiatin, S. (2006). Strain hardening due to deformation twinning α-titanium: mechanism. *Metallurgical and materials transactions A*, **37A**, 259.

Sambasiva Rao, G. and Prasad, Y. (1982). Grain boundary strengthening in strongly textured magnesium produced by hot rolling. *Metallurgical and materials transactions A*, **13**, 2219.

Schmid, E. and Boas, W. (1935). *Kristallplastizität*. Julius Springer.

Sharp, J., Markin, M., and Christian, J. (1965). Dislocation structure in deformed single crystals of magnesium. *Physica Status Solidi*, **11**, 845.

Sheely, W. and Nash, R. (1960). Institute of metals division - mechanical properties of magnesium monocrystals. *Transactions AIME*, **218**, 416.

Slutsky, L. and Garland, W. (1957). Elastic constants of magnesium from 4.2k to 300k. *Physical Review*, **107**(4), 972.

Somekawa, H., Singh, A., and Mukai, T. (2009). Fracture mechanism of a coarse-grained magnesium alloy during fracture toughness testing. *Philosophical Magazine Letters*, **89**(1), 2.

Somekawa, H., Nakajima, K., Singh, A., and Mukai, T. (2010). Ductile fracture mechanism in fine-grained magnesium alloy. *Philosophical Magazine Letters*, **90**(11), 831.

Stofel, E. and Wood, D. (1967). *Razrusheniye Tverdykh Tel, Metallurgiya (Moscow)*, page 318.

Stohr, P. and Poirier, J. (1972). Etude en microscopie electronique du glissement pyramidal {11-22}⟨11-23⟩ dans le magnesium. *Philosophical Magazine*, **25**, 1313.

Sułkowski, B. and Mikułowski, B. (2012). Work hardening of magnesium single crystals deformed to stage b at room temperature. *Acta Physica Polpnica A*, **122**(3), 528.

Sułkowski, B., Chulist, R., Beausir, B., Skrotzki, W., and Mikułowski, B. (2011). Stage b work-hardening of magnesium single crystals. *Crystal Research and Technology*, **46**(5), 439.

Syed, B., Geng, J., Mishra, R., and Kumar, K. (2012). [0001] compression response at room temperature of single-crystal magnesium. **67**, 700.

Takeuchi, T. (1975). Work hardening of copper single crystals with multiple glide orientations. *Transactions of the Japan Institute of Metals*, **16**, 629.

Taylor, G. and Elam, C. (1925). The plastic extension and fracture of aluminium crystals. *Proceedings of the Royal Society*, **A108**, 28.

Tonda, H. and Ando, S. (2002). Effect of temperature and shear direction on yield stress by $\{11\bar{2}2\}\langle\bar{1}\bar{1}23\rangle$ slip in hcp metals. *Metallurgical and materials transactions A*, **33A**, 831.

Von Mises, R. (1928). Mechanik der plastischen formänderung von kristallen. *ZAMM - Journal of Applied Mathematics and Mechanics / Zeitschrift für Angewandte Mathematik und Mechanik*, **8**(3), 161.

Ward Flynn, P., Mote, J., and Dorn, J. (1961). On the thermally activated mechanism of prismatic slip in magnesium single crystals. *Transactions of the Metallurgical Society of AIME*, **221**(1148).

Washburn, J. and Parker, E. (1952). Kinking in zinc single crystal tension specimens. *Journal of metals*, **4**, 1076.

Wessels, E. and Jackson, P. (1969). Latent hardening in copper-aluminium alloys. *Acta Metallurgica*, **17**, 241.

Wessels, E. and Nabarro, F. (1971). The hardening of latent glide systems in single crystals of copper-aluminium alloys. *Acta Metallurgica*, **19**, 903.

Wilson, D. and Chapman, A. (1963). Effects of preferred orientation on the grain size dependence of yield strength in metals. *Philosophical Magazine*, **8**, 1543.

Wonsiewicz, B. and Backofen, W. (1967). Plasticity of magneisum single crystals. *Transactions of the Metallurgical Society of AIME*, **239**, 1422.

Wu, H., Przystupa, M., and Ardell, A. (1997). Latent hardening behavior of monocrystalline al-mg solid solution. *Metallurgical and materials transactions A*, **28A**, 2353.

Yang, P., Yu, Y., Chen, L., and Mao, W. (2004). Experimental determination and theoretical prediction of twin orientations in magnesium alloy az31. *Scripta Materialia*, **50**, 1163.

Yoo, M. (1981). Slip, twinning, and fracture in hexagonal close-packed metals. *Metallurgical Transactions A*, **12A**, 409.

Yoo, M. and Lee, J. (1991). Deformation twinning in h.c.p. metals and alloys. *Philosophical Magazine A*, **63**(5), 987.

Yoo, M., Morris, J., Ho, K., and Agnew, S. (2002). Nonbasal deformation modes of hcp metals and alloys: Role of dislocation source and mobility. *Metallurgical and materials transactions A*, **33A**, 813.

Yoshinaga, H. (2009). Crystal plasticity of magnesium. *Journal of Japan Institute of Light Metals*, **59**, 450.

Yoshinaga, H. and Horiuchi, R. (1962). Work hardening characteristics of the basal slip of magnesium single crystals. *Materials Transactions, JIM*, **3**(4), 220.

Yoshinaga, H. and Horiuchi, R. (1963a). Deformation mechanisms in magnesium single crystals compressed in the direction parallel to hexagonal axis. *Transactions of the Japan Institute of Metals*, **4**, 1.

Yoshinaga, H. and Horiuchi, R. (1963b). On the flow stress of α solid solution mg-li alloy single crystals. *Transactions of the Japan Institute of Metals*, **4**, 134.

Yoshinaga, H. and Horiuchi, R. (1963c). On the nonbasal slip in magnesium single crystals. *Materials Transactions, JIM*, **5**, 14.

Yoshinaga, H., Obara, T., and Morozumi, S. (1973). Twinning deformation in magnesium compressed along the c-axis. *Materials Science and Engineering*, **12**, 255.

Zhou, Y., Neale, K., and Tóth, L. (1993). A modified model for simulating latent hardening during the plastic deformation of rate-dependent fcc polycrystals. *International Journal of Plasticity*, **9**, 961.